MARTIN MARIETTA ENERGY SYSTEMS LIBRARIES
3 4456 0060957 1

CENTRAL RESEARCH LIBRARY
DOCUMENT COLLECTION

cy. 2

ORNL-4720
UC-41 – Health and Safety

HEALTH PHYSICS DIVISION
ANNUAL PROGRESS REPORT
FOR PERIOD ENDING JULY 31, 1971

OAK RIDGE NATIONAL LABORATORY
CENTRAL RESEARCH LIBRARY
DOCUMENT COLLECTION
LIBRARY LOAN COPY
DO NOT TRANSFER TO ANOTHER PERSON
If you wish someone else to see this document, send in name with document and the library will arrange a loan.
UCN-7969
(3 3-67)

OAK RIDGE NATIONAL LABORATORY
operated by
UNION CARBIDE CORPORATION
for the
U.S. ATOMIC ENERGY COMMISSION

Printed in the United States of America. Available from
National Technical Information Service
U.S. Department of Commerce
5285 Port Royal Road, Springfield, Virginia 22151
Price: Printed Copy $3.00; Microfiche $0.95

This report was prepared as an account of work sponsored by the United States Government. Neither the United States nor the United States Atomic Energy Commission, nor any of their employees, nor any of their contractors, subcontractors, or their employees, makes any warranty, express or implied, or assumes any legal liability or responsibility for the accuracy, completeness or usefulness of any information, apparatus, product or process disclosed, or represents that its use would not infringe privately owned rights.

INTRA-LABORATORY CORRESPONDENCE

OAK RIDGE NATIONAL LABORATORY

ORNL-4720
Errata

HEALTH PHYSICS DIVISION ANNUAL PROGRESS REPORT

FOR PERIOD ENDING JULY 31, 1971

The titles for Table 12.4, page 88, and Table 12.5, page 89, were inadvertently switched. The attached corrected titles are printed on gummed stock and may be cut and pasted directly on the pages.

Bev
12/20/71

UCN-430
(3 5-61)

INTRA-LABORATORY CORRESPONDENCE

OAK RIDGE NATIONAL LABORATORY

ORNL-4720
Errata

HEALTH PHYSICS DIVISION ANNUAL PROGRESS REPORT

FOR PERIOD ENDING JULY 31, 1971

Fig. 13.12, page 103, and Fig. 14.1, page 107, were inadvertently switched. The attached corrected figures are printed on gummed stock and may be pasted directly on the pages.

BEW
10/26/71

UCN-430
(3 5-61)

ORNL-4720
UC-41 — Health and Safety

Contract No. W-7405-eng-26

HEALTH PHYSICS DIVISION ANNUAL PROGRESS REPORT

For Period Ending July 31, 1971

K. Z. Morgan, Director

W. S. Snyder, Assistant Director
E. G. Struxness, Assistant Director

OCTOBER 1971

OAK RIDGE NATIONAL LABORATORY
Oak Ridge, Tennessee 37830
operated by
UNION CARBIDE CORPORATION
for the
U.S. ATOMIC ENERGY COMMISSION

Reports previously issued in this series are as follows:

ORNL-2384	Period Ending July 31, 1957
ORNL-2590	Period Ending July 31, 1958
ORNL-2806	Period Ending July 31, 1959
ORNL-2994	Period Ending July 31, 1960
ORNL-3189	Period Ending July 31, 1961
ORNL-3347	Period Ending July 31, 1962
ORNL-3492	Period Ending July 31, 1963
ORNL-3697	Period Ending July 31, 1964
ORNL-3849	Period Ending July 31, 1965
ORNL-4007	Period Ending July 31, 1966
ORNL-4168	Period Ending July 31, 1967
ORNL-4316	Period Ending July 31, 1968
ORNL-4446	Period Ending July 31, 1969
ORNL-4720	Period Ending July 31, 1970

.156p

Contents

SUMMARY vii

PART I. RADIOACTIVE WASTE DISPOSAL

1. FATE OF TRACE ELEMENTS AND RADIONUCLIDES IN TERRESTRIAL ENVIRONMENT 1

Evaluation of Zonal Centrifugation Techniques 1

Applications of Zonal Centrifugation 3

Heavy Metal Distribution in Streams and Rivers 7

Walker Branch Watershed Studies 9

2. DISPOSAL BY HYDRAULIC FRACTURING 11

Investigations at Oak Ridge 11

Investigations in New York State 11

3. DISPOSAL IN NATURAL SALT FORMATIONS 14

Stratigraphy and Structure of the Rocks at the Proposed Federal Repository, Lyons, Kansas 14

4. ENGINEERING, ECONOMIC, AND SAFETY EVALUATIONS 20

Siting and Operation of Nuclear Facilities 20

5. DOSE ESTIMATION STUDIES RELATED TO PEACEFUL USES OF NUCLEAR EXPLOSIVES AND OTHER RADIONUCLIDE RELEASES 23

Utilization of Natural Gas from Nuclearly Stimulated Wells 23

Development of Radiation Safety Guides for Environmental Releases of Radioactivity 24

A General Model to Estimate Dose to Man from Radionuclide Deposition 26

The Transfer of Tritium to Man after Wet Deposition 28

PART II. RADIATION PHYSICS

6. THEORETICAL RADIATION PHYSICS 30

Effect of Lateral Scattering on Dose from 400-MeV Protons and Neutrons 30

Semiclassical Estimation of Neutron Stopping Power 31

Z_1^3 Effect in the Stopping Power of Matter for Charged Particles 31

MARTIN MARIETTA ENERGY SYSTEMS LIBRARIES

3 4456 0060957 1

Contribution of Surface Losses to the Stopping Power of Matter for Charged Particles 33
Dosimetric Field Quantities in Health Physics 34
What Is "Energy Imparted"? 34
Reexamination of Scattering by a Pair of Fixed Dipolar Charges 34
Critical Binding of an Electron to a Rotationally Excited Dipolar System 35
Unlocalized Energy Losses by Charged Particles in Matter 37
Electron Slowing-Down-Cascade Spectra in Solids 37
Volume Plasmon Decay 39
Photon Interactions at a Rough Metal Surface 40
Dosimetry of Pion Beams 40

7. INTERACTION OF RADIATION WITH LIQUIDS AND SOLIDS 42
Optical Properties of Rubidium above the Plasma Energy 42
Optical Properties of Uranium Mononitride 43
Study of the Optical Properties of Solids by Ellipsometry 44
High-Energy X-Ray Satellites of the L_{23} Emission Bands of Na, Mg, Al, and Si 46
Soft X-Ray Emission Spectra of MgO and MgF_2 47
Photoelectron Attenuation Lengths in Aluminum 48
Photoelectric Manifestation of the Optical Plasmon Resonance in Magnesium 50

8. PHYSICS OF TISSUE DAMAGE 51
Electron-Slowing-Down Studies 51
Optical Properties of Organic Liquids 52

9. ELECTRON AND ION COLLISION PHYSICS 56
Electron Impact Excitation and Ionization of the Rare Gases 56
Thermal and Near-Thermal Electron Attachment Rate and Transport Coefficients for Oxygen with a Modified Time-of-Flight Method 57
Electron Interactions with Carbonyl Compounds 60
Ionic Processes in Boron Halides 62
Collisional Ionization of Cesium by O_2, NO_2, and N_2O: Determination of Electron Affinities 63
FSU-ORNL Chemical Accelerator 67

10. ATOMIC AND MOLECULAR RADIATION PHYSICS 69
Swarm-Determined Electron Attachment Cross Sections as a Function of Electron Energy 69
Cross-Section Functions for Electron Attachment Resonances with Cross Sections Increasing Sharply at Thermal Energies 71

Dissociative Electron Attachment to Halogenated Aliphatic Hydrocarbons 72

Electron Capture of Molecules Forming "Moderately Short-Lived" Negative Ions under High-Gas-Pressure Conditions 72

Lifetimes of Long-Lived Polyatomic Negative Ions 73

Scattering of Slow Electrons by π-Electron-Containing Organic Molecules 73

Threshold Electron Excitation of Molecules; Location of Triplet and Compound Negative-Ion States 73

Quasi-Equilibrium Theory of Unimolecular Decompositions 73

Ionic Fragmentation through Centrifugal Barriers 74

Linking of Existing Data on Electron Attachment in Gases with Those in the Liquid Phase 74

Photophysical Studies of Organic Liquids and Solutions; Emission Spectra from Higher Excited π-Singlet States of Aromatic Hydrocarbons in Solution 76

11. GRADUATE EDUCATION AND VOCATIONAL TRAINING 78

Part III. RADIATION DOSIMETRY RESEARCH

12. DOSIMETRY FOR HUMAN EXPOSURES AND RADIOBIOLOGY 80

Japanese Dosimetry Program 80

Calculations of Dose and LET Distributions for Neutrons and Gamma Rays 81

Measurements of Dose Distributions 90

13. APPLIED DOSIMETRY RESEARCH 95

TSEE Research 95

Thermoluminescence Dosimetry 103

Nuclear Track Etching Studies 104

14. INTERACTION OF CHARGED PARTICLES WITH MATTER 107

15. SPECTROMETRY RESEARCH AND DEVELOPMENT 110

Organic Scintillator Research 110

A Voltage-to-Frequency Converter 110

Health Physics Research Reactor Timer 111

16. HPRR AND ACCELERATOR OPERATIONS 112

Health Physics Research Reactor Operations 112

Intercomparison Studies 112

Accelerator Operations 114

A Self-Replenishing Tritium Target 114

PART IV. INTERNAL DOSIMETRY

17. PRELIMINARY INDICATIONS OF THE AGE VARIATION OF THE SPECIFIC ABSORBED FRACTION FOR PHOTONS 116

18. DOSE TO A DEVELOPING FETUS FROM A GAMMA EMITTER IN THE BLADDER 119

19. ABSORBED FRACTIONS FOR INTERNAL EMITTERS 121

20. DEPTH-DOSE RATES IN REFERENCE MAN FROM ELECTRONS AND BETA PARTICLES IN A RADIOACTIVE CLOUD 125

21. ESTIMATES OF MICROCURIE-DAYS RESIDENCE, DOSE EQUIVALENT, AND $(MPC)_W$ FOR THORIUM-232 IN MAN USING A MAMMILLARY MODEL 128

THESES, PAPERS, PUBLICATIONS, AND LECTURES

THESES 132

PAPERS 133

PUBLICATIONS 138

LECTURES 148

Summary

PART I. RADIOACTIVE WASTE DISPOSAL

1. Fate of Trace Elements and Radionuclides in Terrestrial Environment

The development and application of zonal centrifugation to soil and sediment analyses were continued. Adsorption of polyvinylpyrrolidone on montmorillonite interlayers was demonstrated. Gypsum was segregated and identified in a calcareous Holtsville soil from California. The sensitivity of the zonal centrifugation technique to quantifying minerals in soils is illustrated for the clay fraction of a Dodge soil. Bottom sediments of White Oak Lake could be banded by zonal centrifugation without appreciable dissolution of radionuclides, but the suspended sediments lost appreciable amounts in the less than 2-μ fraction.

Heavy metals were determined in the water and suspended sediments of several samples taken from a stream draining a mineralized zone. The bulk of the metal is transported in the dissolved state in the 1- to 25-ppb range. The concentration per unit weight of solid is about an order of magnitude higher in the particulates than in the dissolved solids.

2. Disposal by Hydraulic Fracturing

Almost no work was done with hydraulic fracturing at Oak Ridge during the reporting period. Work in New York consisted in making three "tagged" injections, each of 100,000 gal of water, at depths of 1450, 1226, and 1010 ft. All three injections formed horizontal fractures, but the third injection at 1010 ft also broke vertically downward about 400 ft and then moved horizontally out to the east. The formation of a vertical fracture was not unexpected. The pressure-decay curve from the first injection was unsatisfactory because only a poor gage was available. The analysis of the pressure-decay curve for the second injection showed a break at a pressure equal to the weight of the overburden. The pressure-decay curve from the third injection has not yet been analyzed.

3. Disposal in Natural Salt Formations

Geologic and hydrologic investigations at the proposed repository site have revealed that the rocks are all of sedimentary origin and, for the most part, are flat-lying. Rock salt, interbedded with clay shale and anhydrite stringers, lies between about 800 and 1100 ft below the surface. This salt section is capped with impermeable shales, while a thick sequence of shale and interbedded anhydrite lies directly beneath it. Two distinct freshwater aquifers are known to exist at depths of about 100 and 300 ft below the surface at the site.

4. Engineering, Economic, and Safety Evaluations

Investigation has continued of factors involved in the siting and operation of nuclear facilities. The influence of parent decay and daughter buildup on the potential radiation exposures downwind from a gaseous effluent illustrates the versatility of the atmospheric release computer code. From our search for potentially critical radionuclides at reactors, fuel reprocessing plants, and waste management facilities, a comprehensive nuclear data base has evolved. Computer codes permit rapid access and manipulation of the Nuclide and Biological Information System.

5. Dose Estimation Studies Related to Peaceful Uses of Nuclear Explosives and Other Radionuclide Releases

Studies of doses from the hypothetical use of Gasbuggy gas in areas served by El Paso Natural Gas Company were very nearly completed the past year, while similar investigations related to the Rulison project, the second experiment designed to test the nuclear stimulation concept, were just getting started at the end of the year.

An experiment was performed in a small natural gas processing plant near Barnhardt, Texas, in cooperation with El Paso Natural Gas Company to study the

distribution of tritiated hydrocarbons among plant products and to evaluate exposures that plant personnel may receive during the processing of natural gas containing tritium and ^{85}Kr. The maximum dose commitment received by plant personnel during the test was 0.7 millirem, and this was attributed to the handling of tritium for instrument calibration rather than breathing diluted plant fuel gas combustion products. Analysis of liquid and gas hydrocarbon samples, taken during and soon after the test, is not complete.

The Cumulative Exposure Index concept is being developed to facilitate realistic assessment of environmental releases of radioactivity. The aim of the concept is to assess the releases on the basis of time-integrated radionuclide concentrations measured in suitable environmental sampling media. Environmental pathway models and dose models are used to convert the measured environmental radionuclide concentrations into estimates of radiation dose to man. To complete the assessment, the estimates of dose are compared with basic radiation safety standards.

The methodology under development for assessing environmental radioactivity involves dynamic modeling techniques or systems simulations. A generalized model was constructed to simulate selected terrestrial pathways by which fallout radioactivity can be transferred to man. The model is intended for preliminary predictions of radionuclide intakes by man through consumption of milk, beef, and plant parts contaminated directly by fallout as well as by uptake from the soil. The model is sufficiently versatile that it can be applied to many terrestrial environments and to all radionuclides.

A specific model was developed to simulate the transfer of tritium to man after wet deposition. Tritium movement through the soil is simulated as a diffusion process. The model supports the conclusion that, except for the desert, the time-dependent concentration of tritium in the soil compartment is primarily determined by the rainfall after deposition, and it is essentially independent of the assumed compartment depth. A simple chart facilitates estimation of the total dose to man from a given wet deposition source and the subsequent rainfall rate.

PART II. RADIATION PHYSICS

6. Theoretical Radiation Physics

A classical impact parameter approach has been used to calculate a stopping-power correction term which depends on the sign of the charge of the incident particle.

An equation has been derived which may be used to estimate the energy loss due to the presence of foil surfaces and hence the relative contribution of surface losses to experimental measurements of stopping power.

The electron density fluctuation generated by a swift charged particle in a condensed medium has been investigated in order to elucidate the ultimate spatial distribution of initially unlocalized energy loss events. Electron slowing-down-cascade spectra generated by uniformly distributed high-energy electron sources in various solids are being determined theoretically in a program paralleling the experimental research being carried out in the Radiation Physics Section. The decay rate of volume plasmons in a nearly free-electron-like system has been determined using many-body perturbation theory techniques. The diffuse scatter and plasmon creation probability of photons incident on a rough bounding surface of a free electron gas has been studied theoretically.

Calculations were made to show the effects of lateral scattering on depth-dose curves for 400-MeV protons and neutrons. Also, an estimate of the stopping power of matter for neutrons shows that this quantity is expected to be smaller than that for protons by a factor of about 10^5. A Monte Carlo program was completed for the calculation of depth-dose curves from pion beams. Good agreement was obtained between calculated and experimental curves in water. The program is being used to study the effects of various beam characteristics of interest for cancer radiotherapy with negative pions.

The nature of critical electron binding by a rotationally excited dipolar system has been elucidated, and critical dipole moments have been determined for the first four rotational states of the electron-dipole system.

Contrary to results obtained by earlier investigators, the total scattering cross section for charged particles scattering from a finite stationary dipolar system has been shown to be divergent. The contradictions and the gross underestimate in total and momentum transfer cross sections in earlier theoretical treatment of the problem were shown to be due to truncation errors in a divergent series.

7. Interaction of Radiation with Liquids and Solids

The electronic response of solids to electromagnetic radiation has been studied further by measuring the optical properties of Rb and UN in the vacuum

ultraviolet region of the spectrum and of In and Sn by ellipsometric techniques in the visible region. Soft x-ray emission of the L_{23} core level of Mg in MgO and MgF_2 and the high-energy satellites in Na, Mg, Al, and Si have been investigated. Finally, the attenuation length of low-energy electrons in Al and the plasma energy in Mg have been measured by photoelectric techniques.

8. Physics of Tissue Damage

Comparison of the electron-slowing-down spectrum in a semiconductor and a metal has shown very little difference, suggesting that biological materials may be approximated by low-Z metals for studies of this type. The electron flux has been measured for silicon beta particles slowing down in silicon as well as the Auger cascade electrons from thulium slowing down in ytterbium.

Optical absorption k has been obtained for several organic liquids and silicone pump oils over the energy region from 4.0 to 10.65 eV. These data were obtained using a transmission cell with liquid samples as thin as 500 Å.

9. Electron and Ion Collision Physics

Absolute cross sections for the production of slow electrons (0 to ~1 eV) upon electron impact ionization of He, Ne, and Ar have been measured in the incident electron energy range from 0 to 500 eV. For incident electron energies from 100 to 500 eV the slow electron production cross sections fall off in the same manner as the total ionization cross sections for all of the rare gases. The measured slow electron production cross sections are useful in describing electron-slowing-down spectra in gases.

Negative-ion processes were studied in the boron halides BF_3 and BCl_3 using both electron beam and electron swarm techniques. The thermal energy electron attachment rate for BF_3 was found to be quite small, if not zero, and F^- was found to occur at the anomalously high incident electron energy of 11.5 eV. These studies have been related to the operation of BF_3 in neutron dosimeters.

Electron impact excitation and negative-ion formation have been studied in a series of carbonyl compounds. New electronic states and negative-ion states have been discovered. The energy positions of the negative-ion states are in agreement with the electron withdrawing and donating effects of the various substituents.

Electron attachment and diffusion coefficients have been determined for O_2 in the difficult thermal energy range. This work is the first measurement of electron transport properties of thermal electrons in molecular oxygen. Previous measurements have been obscured by attachment.

Ion products from the collisions of fast cesium atoms with O_2, NO_2, and N_2O have been mass-identified from the reaction threshold to approximately 40 eV in the laboratory system. Accurate measurements of the threshold for ion pair production yield electron affinities of 0.46 ± 0.05, 2.09 ± 0.2, and $\sim 0 \pm 0.3$ eV for O_2, NO_2, and N_2O, respectively. The experiment will be used to determine greatly needed information on electron affinities of organic molecules.

10. Atomic and Molecular Radiation Physics

A new technique has been established which allows direct determination of electron attachment cross sections as a function of electron energy from high-pressure electron swarm data alone. This technique has been tested and shown to be uniquely suited for electron attachment resonances with cross sections increasing sharply at thermal energies. Results are presented for a number of molecules. The results of a study on dissociative electron attachment to halogenated aliphatic hydrocarbons are presented also, and preliminary data on electron capture by molecules forming "moderately short-lived" negative ions under high-gas-pressure conditions are outlined. Lifetimes τ of long-lived polyatomic negative ions have been measured for a number of organic molecules, and the dependence of τ on electron energy has been accurately determined. The presence of π electrons in organic molecules has been found to enhance the scattering of slow electrons from such systems. Threshold electron excitation spectra for a number of molecules have been studied and revealed new compound negative-ion states. A formalism of quasi-equilibrium theory of unimolecular decomposition based on microscopic reversibility has been developed and applied to unimolecular dissociation of excited ions. Preliminary results of our effort to link existing data on electron attachment in gases with those in the liquid phase are presented. Optical emission spectra from the second excited π-singlet state of six organic molecules in solution have been clearly observed. Photophysical studies of organic liquids and solutions indicate that such emissions from higher π-singlet states of aromatic hydrocarbons are not uncommon.

11. Graduate Education and Vocational Training

Six AEC Fellows were trained at ORNL in applied health physics. Nineteen students were enrolled in the health physics courses taught by the Division at Vanderbilt University and The University of Tennessee. Seventeen schools were visited by staff members to discuss health physics research and educational activities. Twenty-one students conducted thesis research in the Division leading to the M.S. or Ph.D. degree. A great deal of assistance was given to ORAU in conducting numerous USAEC-sponsored programs.

PART III. RADIATION DOSIMETRY RESEARCH

12. Dosimetry for Human Exposures and Radiobiology

The medical applications of ^{252}Cf sources and the special dosimetric problems encountered by medical physicists continue to be of interest in the program of calculating distributions of dose with depth in a tissue-equivalent phantom. During this report period, emphasis has been placed on calculations for gamma rays from the source as well as secondary gammas. An extensive evaluation and analysis of previous calculations has been completed. This analysis was intended to reveal the reactions of importance for given neutron energies, as well as the percentage of total dose for each reaction. Extensive measurements of neutron and gamma-ray dose as a function of depth in a tissue-equivalent phantom have been completed for radiation fields from the HPRR and from a 14-MeV neutron generator. Liaison with the Atomic Bomb Casualty Commission has continued in an effort to assign dose to the 1100 remaining individuals for whom shielding histories exist. Studies related to the determination of dose for persons exposed in reinforced concrete buildings in Japan have been intensified.

13. Applied Dosimetry Research

Major emphasis in the solid state dosimetry program this year was placed on the role of activators in TSEE detectors, sensitizing ceramic BeO detectors, identifying damage mechanisms and trapping centers, and improving chambers for reading out the exoelectrons. It was found that ceramic BeO, Thermalox 995, is most sensitive after a heat treatment at 1400°C for several hours. Silicon, which is the major impurity in 995 BeO, was found to be the activator responsible for the 325°C peak in the exoelectron distribution. It is believed that Si^{4+} in place of Be^{2+} acts as an electron trap because of its excess positive charge with respect to the normal lattice sites. The effect of other parameters such as Li^+ activation and deuteron bombardment on the detectors and their dosimetric implications were also studied. Experiments on the properties of phosphors such as $CaSO_4$:Dy, $CaSO_4$:Tm, CaF_2:Dy, and LiF:Mg,Ti as thermoluminescence dosimeters were performed in a tropical environment. These studies were directed at determining sensitivity of the detectors and signal fading under various conditions. Nuclear track etching studies were continued with emphasis given to the application of track detectors to personnel dosimetry, in particular to the use of small quantities of ^{237}Np.

14. Interaction of Charged Particles with Matter

A major effort is being made to determine the energy pathways involved when charged particles interact with gases. A six-in-one experiment is being conducted using the ORNL 3-MV Van de Graaff: radiation intensities as a function of wavelength and pressure for pure noble gases, quenching of electromagnetic radiation by additive gases, *W* values for the pure gases, *W* values for the gas mixture (Jesse effects), lifetimes of continuous and resonance radiations, and absolute intensities of radiation into the vacuum ultraviolet region. These studies have led to the formation of graphic models for the emission processes from helium and argon molecules. The emission model for argon appears to explain the fact that quenching of the 1250-Å emission involves a kinetic scheme which is more complicated than the Jesse effect. Separate studies of the resolved radiation at 1048 Å, the 1100-Å continuum, and the 1250-Å continuum should provide an interpretation of the detailed ways in which quenching collisions intercept the energy flow.

15. Spectrometry Research and Development

Much of the research in spectrometry has been directed toward the purification of organic scintillators. For *para*-quaterphenyl purified by zone refining, most of the impurities which limit light output were removed. This purified material has about the same emission for gammas as anthracene. *Para*-sexiphenyl purification is accomplished through a process of recrystallization. Preliminary measurements made on the single crystals of *para*-sexiphenyl reveal that the optical index of refraction lies above 1.64, that the crystals are completely transparent to visible light, and that the fluorescence spectrum indicated a single large

peak at 450 nm. It is expected that for better purification the peak should shift to near the theoretical maximum of 430 nm. In the area of instrumentation, a voltage-to-frequency converter was built to digitize the output of an electrometer so that the digital signal could be summed with a scaler. Integrated circuits are used for amplification of input voltages, as a variable current source for the relaxation oscillator, and for output pulse shaping. It was designed to operate in an NIM power unit.

16. HPRR and Accelerator Operations

The HPRR was operated routinely and without fault, and no change has been noted in any of the systems or core components. In May 1971, the eighth intercomparison of nuclear accident dosimetry systems was conducted. This study was cosponsored by the International Atomic Energy Agency, and representatives from 11 foreign countries participated. The HPRR was used to provide three radiation fields to simulate nuclear accidents with three different neutron spectra. Studies of the energy pathways involved when charged particles interact with matter were done using the 3-MV Van de Graaff. The DOSAR Low-Energy Accelerator was used in support of depth-dose studies in tissue-equivalent phantoms. A new target using a Pd-Ag foil to pass ^{3}H from a reservoir to the target area has been tested successfully. This target was operated for 10 hr at an average yield of 3×10^{10} neutrons/mA-sec.

PART IV. INTERNAL DOSIMETRY

The specific absorbed fraction of photon energy is known to be much greater for younger children than for adults; hence, the dose per unit activity to a target organ from a photon emitter in a source organ is correspondingly greater for individuals of younger ages. The fact that organs in the young are closer to each other than in the adult and the inverse square law for variation of dose with distance are the bases for the expected increase of dose, but quantitative data correlating absorption factors with age have been lacking. The data in the first study reported by the Internal Dose Estimation Section are a first step toward filling this gap. While the data are preliminary, they demonstrate the expected increase of dose at younger ages as well as a means of supplying the dose estimates for various age groups. Such estimates are of great importance in nuclear medicine and in obtaining reliable estimates of dose for population exposure.

The report on "Dose to a Developing Fetus from a Gamma Emitter in the Bladder" is a first effort to fill another gap in the dosimetry of internally deposited radionuclides. When gamma emitters are present in an organ of the body, the fetus will be irradiated to some extent, and the bladder is of particular importance because it lies close to the fetus and also because many radionuclides are excreted through the bladder. The results reported here make it possible to obtain a realistic estimate of dose for this case. The study has obvious application in nuclear medicine as well as for estimating population exposure.

Realistic estimates of absorbed fractions of energy have been obtained using the Monte Carlo technique and have been published in MIRD Pamphlet No. 5. However, there are many cases where the statistical uncertainty of these estimates is so great that a blank was left in the table. The gonads represent a case of particular interest where estimates are lacking. In the study on "Specific Absorbed Fractions for Internal Emitters," the Monte Carlo estimates of MIRD Pamphlet No. 5 are compared with estimates calculated for an infinite homogeneous medium of tissue. The results suggest that estimates obtained in this way do not differ by more than a factor of 2 from those obtained in the finite nonhomogeneous phantom and, on the average, are not more than 20 to 30% in error. Since errors of this magnitude will frequently be found due to individual characteristics, the use of specific absorbed fractions calculated for the infinite medium seems appropriate for those cases where the more precise Monte Carlo estimates are not available.

The estimation of dose to the skin and subcutaneous tissues from an atmosphere containing a radioactive aerosol is a problem of considerable importance for purposes of estimation of dose to the population living near a nuclear plant. In the past, only an estimate of "surface dose" has been used, and this did not adequately represent the dose to subcutaneous tissues such as testes, lenses of the eyes, etc. Using data of Berger (MIRD Pamphlet No. 8) on dose at a distance from a point source, a computer code has been developed for estimating depth dose in tissue from a uniform "cloud" of radioactive material present in the air surrounding the body. The estimates can be obtained either for monoenergetic electrons or for beta rays emitted by the radionuclide.

Data from the literature have been analyzed to obtain practical models for metabolism of ^{232}Th. The data as published only provide an indication of the various "pools" or compartments and some indications of exchange rates between these compartments. From these indications, metabolic models are obtained which can then be tested with other data, particularly that relating to the naturally occurring isotope.

Part I. Radioactive Waste Disposal

K. E. Cowser

1. Fate of Trace Elements and Radionuclides in Terrestrial Environment

Tsuneo Tamura
W. P. Bonner F. S. Brinkley
C. W. Francis E. R. Eastwood
R. M. Perhac[1]

EVALUATION OF ZONAL CENTRIFUGATION TECHNIQUES

Zonal centrifugation consists in preparing a continuous density-gradient solution in a tube, layering the test sample on the gradient solution, and centrifuging the tubes to allow each component to collect at its isodensity, or isopycnic, point. The density-gradient solution consists of varying proportions of tetrabromoethane (TBE) and ethyl alcohol (EtOH), the latter containing 10% by weight of polyvinylpyrrolidone (PVP) as a dispersant for the clays. The development of this system and some preliminary results of separating mixed mineral suites have been published.[2,3]

During the course of further investigations, it was noted that in some samples of soils or clays the recovery of the sample exceeded the initial amount applied. It soon became apparent that the weight gain was mainly associated with the clay mineral montmorillonite, which is commonly referred to as bentonite (Table 1.1), and adsorption of PVP by this mineral. Thus soils containing montmorillonite showed the higher-weight recoveries.

Emphasis in the early part of the work concerned the use of appropriate washing solvents which would remove PVP from the system. Solvents used were acetone, 190 and 200 proof EtOH, dioxane, 1% sodium pyrophosphate, 0.1 *N* sodium hydroxide, 1 *N* strontium chloride, and water. The number of washings was varied as well as the method of dispersion. Listed in Table 1.1 are the quantities of PVP remaining on the clays after various methods were used to desorb the PVP.

Acetone and dioxane are definitely inferior to ethanol in their ability to remove PVP from bentonites. The use of six or seven ethanol washings results in slightly greater PVP desorption than three washings; however, the advisability of using a greater number of washings for routine operation is questionable. Intermittent ultrasonic treatment resulted in slightly lower weights (treatment 13); but, compared with ethanol washings, this treatment is not warranted.

Desorption of PVP by H_2O and ethanol from illite and kaolinite is complete. Both illite and kaolinite are

1. University of Tennessee, Knoxville.
2. W. P. Bonner, T. Tamura, C. W. Francis, and J. W. Amburgey, Jr., "Zonal Centrifugation – A Tool for Environmental Research," *Environ. Sci. Technol.* **4**, 821–25 (1970).
3. C. W. Francis, T. Tamura, W. P. Bonner, and J. W. Amburgey, Jr., "Separations of Clay Minerals and Soil Clays Using Isopycnic Zonal Centrifugation," *Soil Sci. Soc. Amer. Proc.* **34**, 351–52 (1970).

Table 1.1. Adsorption of polyvinylprrolidone on reference clay minerals

Treatment number	Clay mineral	Sample size (mg)	Method of cleanup (number of 50-ml washings)	Weight gain (mg PVP per 100 mg clay)	Comments
1	Wyoming bentonite, API No. 26	250	3 (190-proof EtOH) 2 (H_2O)	14.2	
2	Wyoming bentonite, API No. 26	100	6 (190-proof EtOH) 1 (H_2O)	12.9	
3	Wyoming bentonite	100	3 (acetone) 1 (H_2O) 2 (1 N $SrCl_2$) 3 (EtOH-H_2O – 50:50)	36.6	Na-saturated clay
4	Wyoming bentonite, API No. 23	100	3 (acetone) 1 (H_2O) 2 (1 N $SrCl_2$) 3 (EtOH-H_2O – 50:50)	33.2	K-saturated clay
5	Wyoming bentonite, API No. 23	100	3 (acetone) 1 (H_2O) 2 (1 N $SrCl_2$) 3 (EtOH-H_2O – 50:50)	39.2	Cs-saturated clay
6	Wyoming bentonite, API No. 23	100	3 (acetone) 1 (H_2O) 2 (1 N $SrCl_2$) 3 (EtOH-H_2O – 50:50)	31.5	Mg-saturated clay
7	Wyoming bentonite, API No. 23	100	3 (acetone) 1 (H_2O) 2 (1 N $SrCl_2$) 3 (EtOH-H_2O – 50:50)	27.2	Ca-saturated clay
8	Mississippi bentonite, API No. 22a	250	3 (dioxane) 2 (H_2O)	27.8	Dispersed in ice bath
9	Mississippi bentonite, API No. 22a	250	3 (dioxane) 2 (H_2O)	28.4	Dispersed without ice bath
10	Mississippi bentonite, API No. 22a	250	3 (190-proof EtOH) 2 (H_2O)	16.6	
11	Mississippi bentonite, API No. 22a	250	7 (200-proof EtOH)	12.8	
12	Mississippi bentonite, API No. 22a	250	3 (200-proof EtOH) 2 (H_2O)	16.4	
13	Mississippi bentonite, API No. 22a	250	3 (200-proof EtOH)	10.6	Ultrasonically dispersed between each washing for 1 min

nonexpanding layer-lattice silicates, whereas bentonite (montmorillonite) has an expanding layer-lattice structure. Hence it might be concluded that the PVP, which is difficult to desorb, is associated with the interlayer positions of the latter-type minerals. To further investigate the specific adsorption sites of PVP, the clay fraction (2 μ) of Wyoming bentonite, hydrobiotite ("Zonolite") from Libby, Montana, and "African vermiculite" were saturated with various cations, suspended in 1% PVP solution in water, and x-rayed after drying on glass slides.

The 001 or c-axis spacings are presented in Tables 1.2 and 1.3. The large c spacings (ca. 27 Å at 100°C) associated with sodium and potassium bentonite dried from the 1% PVP solution are proof of interlayer adsorption of PVP. Continued heating treatments of the other saturated montmorillonite (cesium, magnesium, calcium, and barium) indicate probable monolayer adsorption. If 15.5 Å is chosen to represent the spacings associated with the alkaline-earth-saturated samples at 110°C, the height of the monolayer would be approximately 6 Å (15.5 – 9.5 = 6.0 Å). The height of such a

Table 1.2. Parallel oriented x-ray spacings of Wyoming bentonite, API No. 26[a]

Saturating cation	Temperature			
	Room	110°C	300°C	450°C
Dried from 1% PVP aqueous solutions				
Na	29.4	26.7	22.4	12.8
K	28.5	26.7	23.2	10.4
Cs	14.7	15.2	I[b]	I[b]
Mg	16.0	15.0	14.2	12.6
Ca	16.0	15.8	14.8	12.8
Ba	15.8	15.2	14.2	12.8
Dried from H_2O				
Na	12.6		10.1	9.6
K	12.4		10.1	9.8
Cs	12.3		11.9	11.6
Mg	15.5		9.9	9.5
Ca	15.2		14.7	9.6
Ba	15.2		12.3	11.8

[a]*c*-axis distance in angstroms, ½-hr heating intervals.
[b]I = irregular interstratified material.

Table 1.3. Parallel oriented x-ray spacing of Zonolite[a]

Saturating cation	Temperature			
	Room	110°C	300°C	450°C
Dried from 1% PVP aqueous solutions				
Na	14.5	12.1	10.0	9.85
K	11.0	10.4	10.0	10.0
Cs	10.5	10.9	10.5	10
Mg	14.1–12.4	14.2–12.4	11.8	11.0
Ca	14.7–12.6	14.5–12.6	11.9–I[b]	9.3
Ba	12.3–11.6	11.3	10.8	10.4
Dried from H_2O				
Na	14.7	12.1	9.93	9.82
K	10.3	10.1	10.1	10.1
Cs	10.6	10.6	10.5	10.4
Mg	14.2–12.6	14.5–12.6	14.5–12.4	10.0
Ca	14.7–12.6	14.7–12.6	14.7–9.8	9.82
Ba	12.3–11.3	11.0	10.6	10.4
Mg + glycerol	14.0–12.3		14.2–12.4	

[a]*c*-axis distance in angstroms, ½-hr heating intervals.
[b]I = irregular interstratified material.

monolayer is not known, although one would expect it to be greater than the 5.2-Å (14.7 − 9.5 = 5.2 Å) spacing observed with monolayer adsorption of polyvinyl alcohol in dried calcium-saturated montmorillonite.[4]

4. D. G. Greenland, "Adsorption of Polyvinyl Alcohols by Montmorillonite," *J. Colloid Sci.* **18**, 647–64 (1963).

Data in Table 1.3 indicate that the interlamellar adsorption of PVP does not take place in Zonolite vermiculite regardless of cation saturation. For example, Zonolite dried from 1% PVP in water showed essentially the same spacings as that dried from water. Although controls (samples dried from water) were not used for comparison in African vermiculite, the maximum *c* spacings of samples dried from 1% PVP were very nearly the same as that found in Zonolite.

The absence of PVP adsorption in the interlamellar region of vermiculites is of considerable significance in relation to identification of clay minerals after removal from density gradients containing PVP. Normally in soil clay mineral identification, behavior of the *c* spacing with heat treatment is used to differentiate vermiculite, pedogenic chlorite, and chlorite. If PVP had been adsorbed in interlamellar positions, then heating the clay to 300°C could in all likelihood show a 14-Å spacing when x-rayed, and doubt would exist whether the mineral was originally a vermiculite, pedogenic chlorite, or chlorite. Without PVP, 14-Å spacing after heating is interpreted as being due to chlorite.

APPLICATIONS OF ZONAL CENTRIFUGATION

Separation and Identification of Gypsum in Soils

Holtsville soil, a calcareous slightly weathered soil from the Imperial Valley in California, was obtained to evaluate the potential of zonal centrifugation techniques for mineral identification of soils different from the acidic noncalcareous soils of the east. During the course of evaluation, it was found that some of the samples, when x-rayed, produced a 7.5-Å maximum in the band removed at 2.3 g/cc. The low density of the mineral precluded the presence of iron-rich chlorites, and the high spacing rejected it as being kaolinite (7.2 Å). Furthermore, as kaolinite did occur in the soil, a separate spacing of 7.2 Å was observed for this mineral.

Part of the difficulty of identifying the mineral as gypsum ($CaSO_4 \cdot 2H_2O$) of 2.3 g/cc density was due to the pretreatments given the sample prior to x-ray diffraction. In some samples the pretreatment included contact with water, in which case the gypsum would dissolve, and the amount dissolved depended on the volume of water and contact time; hence, the 7.5-Å spacing would not occur in some of the samples, which led to suspicion that it was an impurity in those samples which showed the spacing. However, after it was realized that the mineral was gypsum and every effort was made to avoid water, the spacing consistently occurred in the samples. The x-ray diffractogram shows the major peak of gypsum in this sample (Fig. 1.1). The

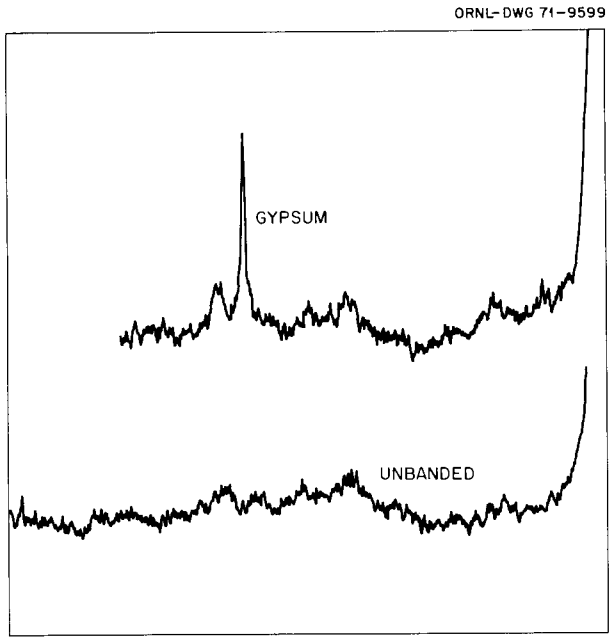

Fig. 1.1. X-ray diffractogram of unbanded Holtsville soil and the component identified as gypsum from band recovered after rotor zonal centrifugation.

diffractogram of an unbanded soil sample is also shown to illustrate that this component would not have been identified without prior banding. Presently, gypsum content in soils is determined by the destructive technique of initially dissolving the mineral in water.[5] The separation thus would permit study of this mineral as it occurs in the soil and offers the potential of studying the role of the mineral in reclamation, for example, of alkali soils. Furthermore, it is of great importance in controlling the behavior and fate of phosphorus fertilizer through its high solubility in water.

Mineral Quantification

The identification of specific minerals in the clay fraction of soils is normally carried out through the procedures of Jackson.[6] Depending on the degree of accuracy desired, many different analyses are used to make mineral allocations. Whereas the final allocation depends upon the different analyses, the mineral identification depends largely on x-ray diffraction analysis. Since clay-size particles exert the greatest influence on the chemical and physical properties of soil, mineral analysis is focused in this size range.

5. L. A. Richards (ed.), *Diagnosis and Improvement of Saline and Alkali Soils,* U.S. Department of Agriculture Handbook No. 60, Washington, D.C., 1954.

6. M. L. Jackson, *Soil Chemical Analysis – Advanced Course* (Fifth Printing, 1969), published by the author, Department of Soil Science, University of Wisconsin, Madison, 1951.

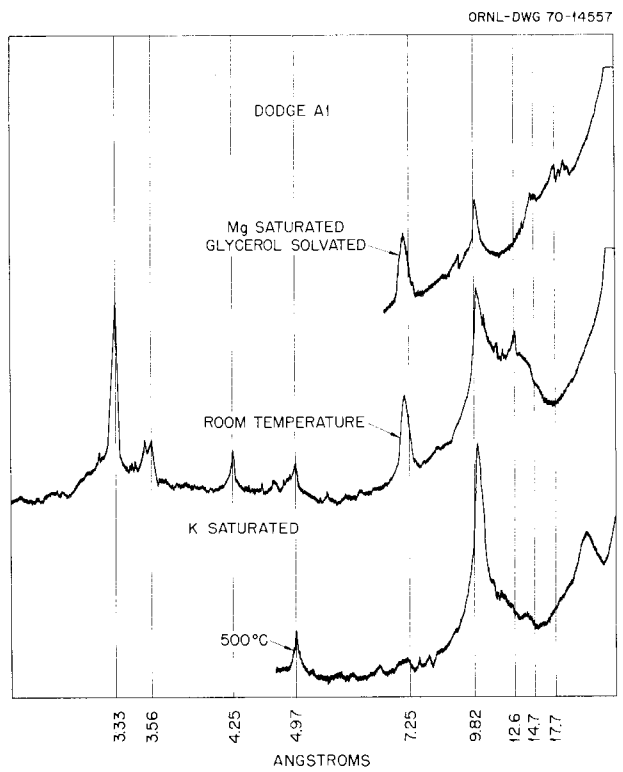

Fig. 1.2. Classical x-ray diffraction diagrams in clay distribution.

In Fig. 1.2 is shown the x-ray diffraction patterns of the A1 horizon of the Dodge soil (<2 μ size) which are normally obtained. The different saturation and heat

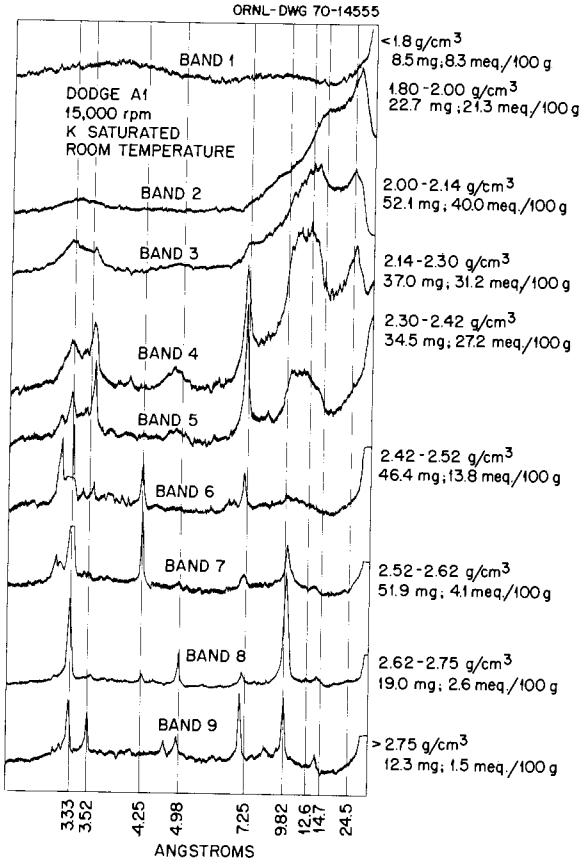

Fig. 1.3. X-ray diffractograms of the bands in the zonal centrifugation of the clay fraction of a Dodge silt loam.

treatments are used to aid in the identification of the minerals. From these data, the following minerals are identified: montmorillonite, vermiculite, illite or mica, kaolinite, quartz, and possibly feldspar.

After banding the same sample of the Dodge soil, nine bands are recovered. The recovered bands were x-rayed at room temperature and potassium saturation; the diffractograms are shown in Fig. 1.3. Since potassium saturation collapses the *c* spacings of vermiculite (Table 1.3), its presence cannot be determined in these samples; hence, separate samples of bands 2, 3, 4, and 5 were x-rayed with magnesium saturation and glycerol solvation. These bands were selected since vermiculites normally band at the 2.2- to 2.3-g/cc range. Vermiculite was identified in bands 3, 4, and 5. The minerals identified in the sample were montmorillonite, vermiculite, kaolinite, illite, alkali feldspar, plagioclase feldspar, mica, quartz, chlorite, and amphibole. In addition, the amorphous component was separated from the crystalline minerals.

Table 1.4. Quantitative estimation of specific minerals in the clay fraction of a Dodge silt loam (A1 horizon)

Mineral	Occurrence (band No.)	Estimated percentage	Weight (mg)	Fraction (%)
Amorphous	1	100	18	3
Montmorillonite	2	100	23	17
	3	50	26	
Vermiculite	3	50	26	19
	4	60	22	
	5	20	7	
Kaolinite	4	30	11	12
	5	60	20	
	6	10	5	
Illite	4	10	3	4
	5	10	3	
	6	10	5	
Alkali feldspar	5	10	3	8
	6	45	21	
Plagioclase feldspar	7	10	5	2
Quartz	6	45	21	22
	7	80	42	
Mica	7	10	5	9
	8	90	17	
	9	25	3	
Chlorite	8	10	2	3
	9	60	7	
Amphibole	9	15	2	1
			287	100

Table 1.4 presents the quantitative estimate of the specific minerals in the clay fraction of the Dodge soil (A1 horizon). The amounts are based on visual estimates of the diffraction intensity and the weight of material in the bands. Especially noteworthy is the estimate of illite and mica. Without the banding, the 10-Å maximum would have been assigned totally to illite; because of the more intense reflection due to mica, a higher percentage allocation than the 13% (illite plus mica) would have been ascribed to illite. Note, too, that chlorite makes up about 20% of the 7-Å maximum; normally, all the 7-Å maximum would have been assigned to kaolinite. The presence of chlorite in the A1 soil infers that this is a "youthful" soil. In addition to providing an estimate of the amorphous component (3%), it was possible to definitely detect the amphibole even though the amount is almost negligible (1%).

Lake Sediment Studies

In a previous report the radionuclide distribution of sediments from White Oak Lake Bed and White Oak

Creek was given.[7] Data in that report showed that about 10% of the radiocesium was lost during the banding process of zonal centrifugation. It was thus desirable to verify this observed loss from the bottom sediment and to evaluate the possible loss from suspended solids.

The lake bed sediment was collected in the same portion of the lake as the sample taken last year. The suspended solid sample was taken at the permanent sampling station which monitors the effluent over White Oak Dam. The 5-gal sample of water (collected during the week of July 27 to August 3) was passed through a continuous flow centrifuge and two size fractions collected – greater than 2-μ-diam (coarse) and 2- to 0.01-μ-diam (fine) particles. The sample received no pretreatment prior to size segregation; thus, the separation represents the size distribution found in the natural state. The particle size distribution obtained from a total of 0.659 g per 5 gal was 91% coarse and 9% fine particles.

The density range, mineralogical composition, weight percent, and the distribution of ^{137}Cs and ^{60}Co in the sediment sample are given in Table 1.5. The original concentration of ^{137}Cs and ^{60}Co is 16,200 and 2330 dis min^{-1} g^{-1}, respectively. The data in Table 1.5 show that 88% of the ^{137}Cs and 77% of the ^{60}Co occur in bands 3 and 4, which contain 86% of the sample weight. Bands 3 and 4 are the clay bands; the clay consists primarily of illite and kaolinite with small amounts of quartz.

The percentages of ^{137}Cs and ^{60}Co released during banding and subsequent leaching with 1 N solutions of $CaCl_2$ and HNO_3 are given in Table 1.6. These data show that the ^{137}Cs in the sediment is resistant to leaching by $CaCl_2$ and only slightly leachable by HNO_3. The bands which released the highest percent of activity were bands 1 and 5. Although the percentage released is

7. K. Z. Morgan et al., *Health Phys. Div. Annu. Progr. Rep. July 31, 1970,* ORNL-4584, pp. 1–10.

Table 1.5. Characteristics of White Oak Lake sediment after banding in a 1.8- to 2.8-g/cc density gradient

Band	Density range (g/cc)	Weight distribution (%)	^{137}Cs distribution (%)	^{60}Co distribution (%)	Mineralogical composition
1	<1.81	0.92	1.01	3.93	Amorphous
2	1.81–2.27	3.3	4.96	6.29	Quartz, amorphous
3	2.27–2.40	40.64	60.95	50.39	Illite, kaolinite, quartz
4	2.40–2.52	45.49	27.73	26.77	Illite, kaolinite, quartz
5	2.52–2.58	7.77	4.79	8.66	Calcite, quartz
6	2.58–2.67	0.61	<1.0	1.57	Mica, quartz
7	2.67–>2.75	1.23	0.51	2.36	Dolomite, anatase, quartz, and mica

Table 1.6. Percent of nuclide in each band lost during indicated treatment

Band	^{137}Cs			^{60}Co		
	Banding solution	1 N $CaCl_2$	1 N HNO_3	Banding solution	1 N $CaCl_2$	1 N HNO_3
White Oak Lake sediment						
1		<1	43		40	<1
2		<1	<1		10	3
3		<1	4		<1	61
4		<1	15		<1	49
5		<1	33		70	<1
6		<1	<1		100	<1
7		<1	<1		60	<1
Sum	8	<1	8	<1	11	45
Unbanded		<1	9		5	65
White Oak Lake suspended solids						
>2 μ	<1	11	9	<1	12	22
<2 μ	37	15	7	49	27	12

high, the bands contained less than 6% of the total ^{137}Cs. The relative ease of removal of ^{137}Cs from these two bands is attributed to the presence of amorphous (primarily organic) material in band 1 and calcareous material in band 5, both of which tend to decompose in acid media. The release of 15% of the ^{137}Cs from band 4 by the HNO_3 is surprising, particularly since earlier studies showed that less than 1% of the ^{137}Cs was released from White Oak Lake sediment by 1 *N* HNO_3.[8] In addition, the presence of illitic material in bands 4 and 5 suggests that ^{137}Cs would be very difficult to remove if it were associated with this material.[9]

Cesium-137 appears to be more easily removed from the suspended solids than from the sediment. Although the percentage leached by HNO_3 is approximately the same for the sediment and each size fraction of the suspended solids, that removed by $CaCl_2$ is much greater for the suspended solids than the sediment (sediment, less than 1%; suspended solids, 11–15%).

Collectively, the data show that ^{137}Cs is much more readily leached from the suspended solids than from the sediments. In addition, the removal of 37% of the ^{137}Cs and 49% of the ^{60}Co from the fine fraction of the suspended solids during banding seems noteworthy. These data suggest that the smaller particulates may be one of the more important sources of these nuclides to the food chain.

Separation of Mercury-Contaminated Sediment

Simple food-chain laboratory models (microcosms) are being used to study the uptake of mercury. These studies, being conducted in the Ecological Sciences Division, utilize different sediments and water. Radioactive mercury in the form of $^{203}Hg(NO_3)_2$ was added to the water in contact with the sediment; analyses have shown that greater than 90% of the mercury is associated with the sediment within 24 hr. With the rapid depletion of the mercury from the water phase, it was deemed desirable to determine the distribution of the mercury in the solid phase. One of the sediments, which had been obtained from the outfall of a municipal sewage treatment plant, was subjected to zonal centrifugation. The distribution of mercury among the solids in the six bands, as well as the gradient solution in which each band occurred, is presented in Table 1.7.

Table 1.7. ^{203}Hg distribution in a banded sediment and the gradient medium associated with each band

Band	Sample weight distribution (%)	^{203}Hg	
		Solids (%)	Liquid (%)
1	5.81	9.24	50.28
2	5.12	2.57	11.38
3	14.38	5.55	16.90
4	10.71	0.39	2.33
5	61.29	0.17	0.91
6	2.68	0.08	0.18
Sum	99.99	18.00	81.98

The data show that approximately 82% of the mercury was recovered in the gradient solution and only 18% in the sediment. Although about 50% of the mercury was recovered in the liquid portion of band 1 (which contained only 5.8% of the sample weight), this amount is not necessarily derived from the solid recovered in the fraction. Since sample pretreatment included subjecting the sample to ultrasonics for 15 min in 7 ml of 1.8 g/cc gradient solution, it is possible that amorphous precipitates of mercury hydroxides were broken into small particles and peptized to prevent movement through the gradient. In addition, if HBr should be present in the slightly acid tetrabromoethane, it could have complexed the mercury kept in the ionic form. Further speculation regarding the higher percentage of mercury in the liquid than in the solids of each band is not warranted at this time; however, the data do suggest that most of the mercury, when synthetically applied in this manner, may be solubilized or complexed by the components of the gradient medium. It would be interesting to test mercury's behavior in naturally contaminated sediments in the same gradient medium.

HEAVY METAL DISTRIBUTION IN STREAMS AND RIVERS

The literature abounds with data on the chemical composition of natural waters. Most papers, however, deal only with the composition of the dissolved phase or with gross analyses of the total solids. Few data are available on the partitioning of heavy metals among dissolved and suspended solids (particulates). Research was started, therefore, to measure the metal content of the dissolved solids and of two sizes of particulates –

8. T. F. Lomenick and D. G. Gardiner, "The Occurrence and Retention of Radionuclides in the Sediments of White Oak Lake," *Health Phys.* **11**, 567–77 (1965).

9. T. F. Lomenick and T. Tamura, "Naturally Occurring Fixation of Cesium-137 on Sediments of Lacustrine Origin," *Soil Sci. Soc. Amer. Proc.* **29**, 383–87 (1965).

greater than 0.15-μ-diam (coarse) and 0.15- to 0.013-μ-diam (colloid) particles. The data should be useful for pollution studies and for ore genesis problems.

The basic approach of this study consisted of: (1) sampling natural streams, some samples being taken in an area of known metallic mineralization; (2) recovering from the water the coarse particulates and then the colloids by continuous flow centrifugation; (3) recovering the dissolved solids by evaporation; and (4) analyzing the solids for selected heavy metals.

Five water samples were taken at four sites in two streams (Fig. 1.4). Samples 1, 2a, 2b, and 3 were collected from Joe Mill Creek in Northeast Tennessee. Sample 4 was taken from Valley Creek, about 12 miles east of Joe Mill Creek, and it represents water from a nonmineralized area. Sample 1 was taken about 3700 ft above the mineralized zone, samples 2a and 2b were taken 100 ft downstream from the mineralized zone, and sample 3 was taken 3500 ft downstream from the mineralized zone. All samples except 2b were collected in July 1970 toward the end of a summer dry spell. Sample 2b was taken at the same site as 2a in August 1970 following a period of summer rains.

In Table 1.8 the solid content of the water is given for the samples. The data show that nearly all solid matter in the water occurs in the dissolved state; only minute traces occur as colloids. It should be mentioned that the

ORNL-DWG 71-9600

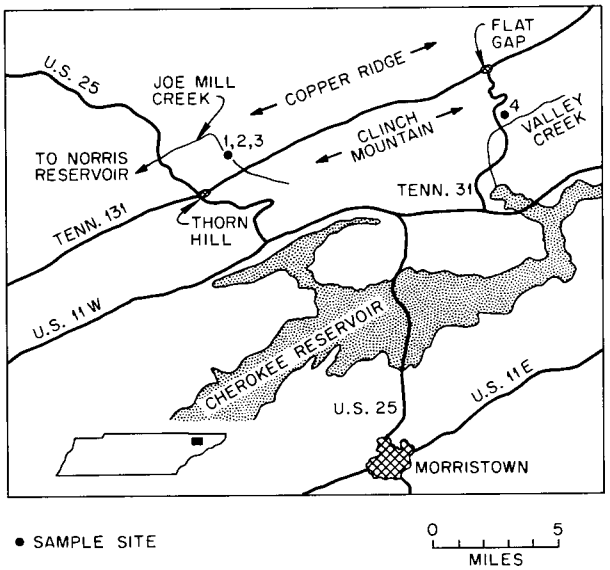

Fig. 1.4. Sample locations for heavy metal content.

Table 1.8. Solid content of water

Sample site	Dissolved solid	Coarse particulate	Colloid
	Solid in water (ppm)		
1	251	8.146	0.105
2a	192	3.279	0.0081
2b	197	5.786	0.0904
3	183	2.487	0.179
4	118	10.431	0.0571
	Fraction of total solid (%)		
1	96.8	3.1	0.04
2a	98.3	1.7	0.004
2b	97.1	2.9	0.04
3	98.6	1.3	0.10
4	91.8	8.1	0.04

Table 1.9. Total heavy metal transported in dissolved and particulate phases (μg/liter $\times$ 10^2)

Sample	Fraction	Cd	Co	Cu	Fe	Mn	Ni	Pb	Zn
1	Dissolved solid	300	800	1800	2,800	275	1100	1900	1040
	Coarse particulate	12	33	70	12,000	910	38	100	185
	Colloid	2.4	1.9	27	250	5	2.3	0.7	<0.5
2a	Dissolved solid	260	530	2100	2,060	230	800	1600	2440
	Coarse particulate	13	20	90	10,600	705	27	58	70
2b	Dissolved solid	280	400	2200	2,000	530	900	1480	1640
	Coarse particulate	12	26	90	13,700	735	40	125	1430
	Colloid	1.5	2.6	43	230	8.5	3	25	17
3	Dissolved solid	165	420	1780	2,380	150	700	1540	2470
	Coarse particulate	6	15	160	5,950	590	17	160	200
	Colloid	1.2	3	28	530	53	7	50	24
4	Dissolved solid	160	350	2000	6,700	220	425	1140	1020
	Coarse particulate	14	75	125	24,900	1830	75	130	270
	Colloid	9	9	27	140	2.7	2.7	<4.8	5.0

particulates were separated under natural conditions with no dispersion treatments. It is thus likely that the coarse fractions could contain aggregates of colloidal material.

The total heavy metal transported in dissolved and particulate phases is summarized in Table 1.9. The bulk of the metal is transported in the dissolved state, because the dissolved solids comprise nearly all the total solid (Table 1.8). Except for zinc, no marked metal enrichment shows up, which is as expected, since the major ore mineral is sphalerite (ZnS). Both iron and manganese are higher in the coarse particulates than in the dissolved solids, which is understandable, since these metals are easily hydrolyzed in the water to form insoluble oxide hydrates. It should also be noted that the analysis represents the total metal content; at this stage the distribution of the elements as exchangeable, fixed, or lattice ions is not known.

WALKER BRANCH WATERSHED STUDIES

This section represents contributions from the Health Physics Division to the Ecological Sciences Division's joint cooperative projects. Only the summary of the findings is reported here; the more detailed report will be found in the Ecological Sciences Division Annual Report.[10]

10. S. I. Auerbach et al., *Ecological Sciences Div. Annu. Progr. Rep. July 31, 1971* (to be published).

Table 1.10. Weight distribution and mineralogical composition of the banded particulates from the East and West Fork of Walker Branch

Band[a]	East Fork		West Fork	
	Particulates (μg/liter)	Mineralogical composition	Particulates (μg/liter)	Mineralogical composition
		February–May 1970, >2 × 10^6 S[b]		
1	130	Amorphous	70	Amorphous, quartz
2	790	Kaolinite, quartz	660	Kaolinite, quartz
3	100	Kaolinite, quartz, dolomite, feldspar	210	Quartz, feldspar, dolomite
Sum	1020		940	
		February–May 1970, 100 ≤ 2 × 10^6 S		
1	150	Amorphous, quartz, kaolinite	520	Amorphous, quartz
2	1690	Amorphous, quartz, kaolinite	370	Kaolinite, quartz
3	17	Feldspar	20	Feldspar, quartz
Sum	1857		910	
		June–September 1970, >2 × 10^6 S		
1	250	—[c]	110	—
2	4	—	80	—
3	2	—	120	—
Sum	256		310	
		June–September 1970, 100 ≤ 2 × 10^6 S		
1	490	—	540	—
		October 1970–Jauary 1971, >2 × 10^6 S		
1	470	Amorphous, quartz	290	Amorphous, quartz
2	370	Kaolinite, quartz	1480	Quartz, calcite, amorphous
3	70	Quartz	390	Calcite, quartz
Sum	910		2160	
		October 1970–January 1971, 100 ≤ 2 × 10^6 S		
1	150	Amorphous	260	Amorphous, feldspar, quartz

[a]Band 1 = <1.8 g/cc density; band 2 = 1.8 to 2.2 g/cc density; and band 3 = 2.2 to 2.8 g/cc density.
[b]S = Svedberg coefficient.
[c]— = not determined.

Studies were made to determine: (1) the concentration of particulates in the water of both the East Fork and West Fork, (2) the mineralogical composition of the particulates, and (3) the forms and concentrations of inorganic phosphates in the solids.

The particulate content of the water ranged from 0.7 to 2.9 mg/liter, with the maximum observed in the winter and spring and the minimum in the fall (Table 1.10). During the spring season, the presence of a slightly milky cast was observed to occur in the East Fork, especially after rainfall following a period of subfreezing temperatures. From x-ray diffraction analysis, it is suspected that the white cast is due to dolomite. Although dolomite is noted in both forks of the stream, the intensity of the dolomite diffraction maxima was about three times higher in the East Fork sample. In general, however, the diffraction maxima were of low intensity; it is suspected that substantial amounts of the solids are amorphous.

The concentration of the various forms of inorganic phosphates was determined in each fraction of the sample banded by zonal centrifugation. The sum of the phosphate forms varied from 2.6 to 5.4 μg/liter. For both forks the maximum concentration occurred during the winter, which is to be expected, because plant uptake is minimal during this season. The highest concentration was found in the aluminum phosphate form, the average percentage was 62% of the total, and the range was between 39 and 91%.

2. Disposal by Hydraulic Fracturing

Wallace de Laguna
K. E. Cowser
Tsueno Tamura
O. M. Sealand

INVESTIGATIONS AT OAK RIDGE

Operational waste injection ILW-7, made September 23, 1970, consisted of 146,000 gal of slurry comprised of 83,000 gal of waste, 25,000 gal of water, and the solid ingredients that formulate the mix. The waste contained 45,000 Ci of ^{137}Cs, 2800 Ci of ^{90}Sr, 200 Ci of ^{106}Ru, and 70 Ci of ^{60}Co. No further waste injections were made at Oak Ridge during FY 1971. A detailed analysis and report on disposal by fracturing was prepared, and presumably disposal operations will begin again in the coming year.

INVESTIGATIONS IN NEW YORK STATE

On June 26, 1970, a second injection of about 100,000 gal of water was made into the slot at a depth of 1450 ft at our test site in western New York state. This time the injection was tagged with 2.7 Ci of ^{95}Zr-^{95}Nb added at the wellhead, and about $^1/_{10}$ lb of Grundite (illite) clay was added to the water as a carrier for the radioactive tag. Logging of three of the four observation wells showed that the fracture that formed had been horizontal. The eastern observation well could not be logged, as the lower part of the well, below 1390 ft, was plugged with cement left over from the cementing in of the casing. Figure 2.1 shows the pressure decay curve obtained from this injection. However, the pressure gage used on this occasion was not sufficiently sensitive or accurate for the service, and the pressure decay curve (Fig. 2.2) shows irregularities due to the gage. The plot of log of rate of pressure change against the log of time was a straight line and so provided no information on the nature of the fracture.

On August 17, 1970, a similar injection of 100,000 gal of tagged water was made at a depth of 1226 ft into rock rated as "good for the production of horizontal

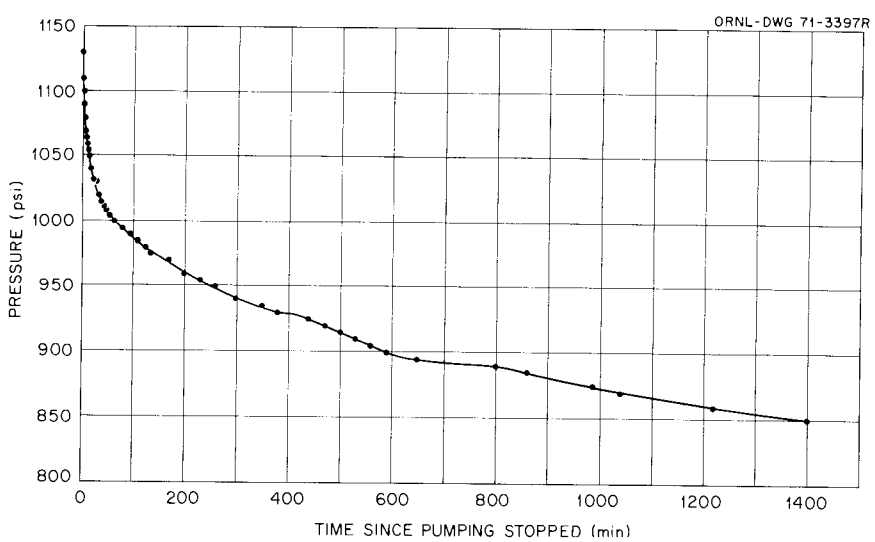

Fig. 2.1. West Valley, New York, second fracture at 1450 ft, June 26, 1970.

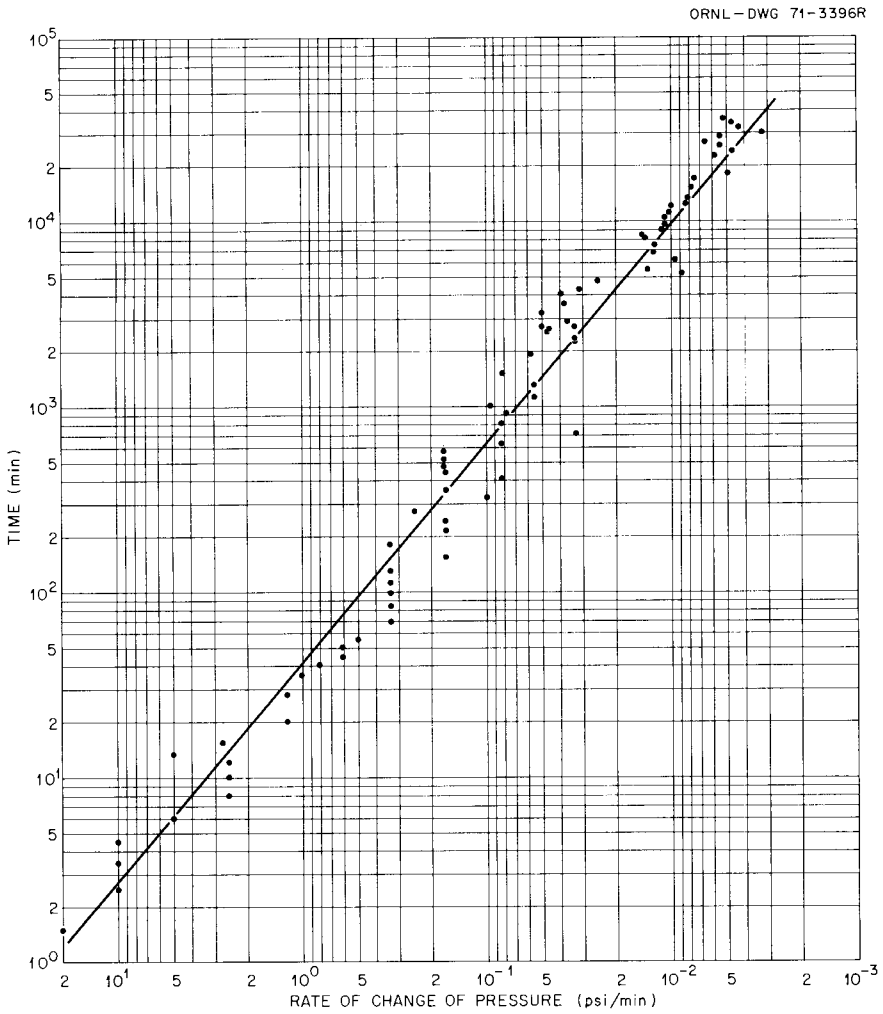

Fig. 2.2. West Valley, New York, second fracture at 1450 ft, June 26, 1970.

fractures" from an examination of the cores. An examination of the logs in all four of the observation wells showed that this fracture had indeed been horizontal and that it had spread out in all directions from the central well to a distance of at least 150 ft.

Figure 2.3 was made from readings taken with a much better pressure gage than had previously been available, and shows a smooth curve. The plot of the log of rate of pressure change against the log of time (Fig. 2.4) shows a marked break in slope at time 110 min, at which time the pressure was 806 psi. This pressure is exactly equal to the calculated weight of the overburden at the depth of the fracture, and so indicates a horizontal fracture.

On May 10, 1971, another similar injection of 100,000 gal of tagged water was made into a fracture at a depth of 1010 ft, into a hard brittle massive siltstone that had been rated as "poor for horizontal fractures" from an examination of the cores. Subsequent logging in all four observation wells showed that a paper-thin horizontal fracture had been formed which intersected all four observation wells. However, a large peak in the gamma-ray log in the east well at a depth of 1375 ft showed that the main fracture had been vertically downward nearly 400 ft, at which depth the fracture had moved out to the east. No analysis has yet been made of the pressure-decay data from this injection.

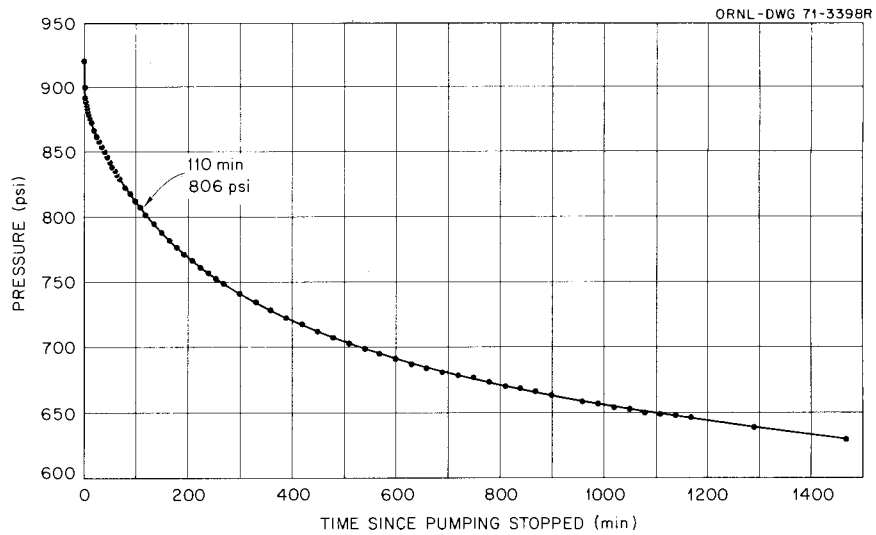

Fig. 2.3. West Valley, New York, fracture at 1226 ft, Aug. 17, 1970.

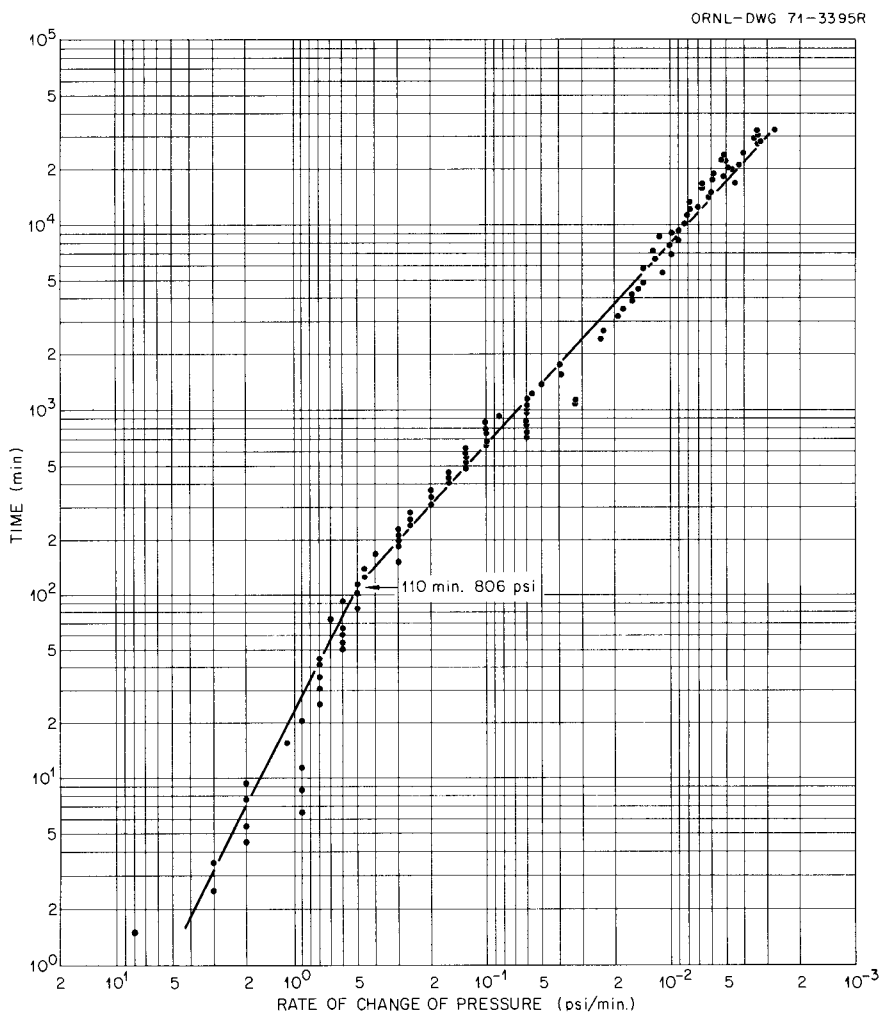

Fig. 2.4. West Valley, New York, fracture at 1226 ft, Aug. 17, 1970.

3. Disposal in Natural Salt Formations

F. M. Empson T. F. Lomenick
T. W. Hodge, Jr. W. C. McClain
H. J. Wyrick

Following the completion of the field experiment called Project Salt Vault[1] demonstrating the concept of radioactive waste disposal in underground salt mines, a number of feasibility, siting, and conceptual design studies were undertaken.[2,3] Based on the results of these studies, the AEC announced on June 17, 1970, the tentative selection of a site near Lyons, Kansas, for an initial salt mine repository for the demonstration of long-term storage of solid high-level and long-lived low-level radioactive wastes. Also announced at the same time was the Commission's intention of seeking Congressional authority for initiation of the project during fiscal year 1972. The purpose of this demonstrational project will be to provide technical data and experience on operational methods and costs of long-term storage of solidified high-level wastes. These wastes are generated by commercial reprocessing plants that remove waste fission products from fuel that has been used in nuclear power stations. In addition, the waste management facility will provide long-term storage of solid materials contaminated with low-level radiation, principally the transuranium elements such as plutonium, generated at AEC installations.

As a consequence of the decisions embodied in this announcement, the effort on this long-standing research and development program has been considerably broadened and enlarged to include: (1) development of a conceptual design for the entire facility (performed largely under contract by Kaiser Engineers); (2) survey of the sources and characteristics of the wastes, especially the transuranium-contaminated materials, and experimental investigations leading to the establishment of various design criteria; (3) research and analysis in support of the various safety evaluations required for establishment of the facility; and (4) detailed examinations of the site geology, hydrology, and ecology. While the Health Physics Division has participated to some extent in virtually all phases of this program, the major responsibilities have been centered on the site investigations and that portion of the safety analysis related to the geologic effects of the repository and the evaluation of the long-term geologic containment.

The following sections summarize the geologic and hydrologic characteristics of the Lyons site which have so far been produced by these investigations.

STRATIGRAPHY AND STRUCTURE OF THE ROCKS AT THE PROPOSED FEDERAL REPOSITORY, LYONS, KANSAS

General

To determine and define the geological and hydrological conditions at the site and its immediate surroundings, an investigative program has been initiated that includes surface mapping, core drilling, auger and rotary drilling, geophysical well logging, hydrologic testing, and measurements of the physical, chemical, and thermal properties of the rocks. To date two core holes about 1300 ft deep have been completed at the northeast (test hole 1) and southeast (test hole 2) corners of the site. In addition, four 300-ft hydrologic test holes have been drilled at the approximate corners of the site, and a series of some 45 auger borings have been made within a nine-square-mile area centered on the repository site to aid in delineating the unconsolidated surface sediments and in appraising the shallow

1. R. L. Bradshaw and W. C. McClain, *Project Salt Vault: A Demonstration of the Disposal of High Activity Solidified Wastes in Underground Salt Mines,* ORNL-4555 (March 1969).

2. *Health Phys. Div. Annu. Progr. Rep. July 31, 1969,* ORNL-4446, pp. 12–14.

3. R. L. Bradshaw, W. C. McClain, and J. O. Blomeke (internal memorandum), *Radioactive Waste Disposal in Salt: Preliminary Cost Estimates and Comparison of Alternative Sites,* ORNL-CF-69-6-69.

ORNL-DWG 71-1787

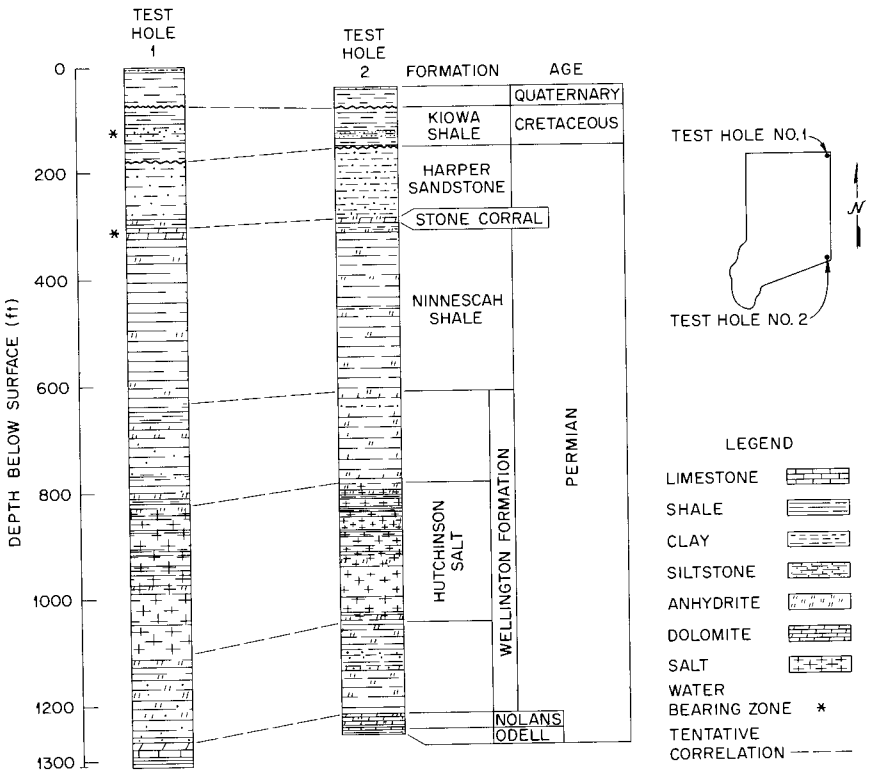

Fig. 3.1. Generalized stratigraphic sections at test holes 1 and 2. Data obtained from cores and logs of core borings performed for USAEC by U.S. Army Corps of Engineers, August–November 1970.

groundwater aquifers. Data from this test program, coupled with the mine workings maps, oil and gas well logs, and previous geologic and hydrologic studies of the county, will provide, when complete, the necessary knowledge to establish the suitability of the site for the safe operation of the facility and for the long-term confinement of the radioactive wastes.

Stratigraphy

The stratigraphic section at the site as revealed by the first two core holes is shown in Fig. 3.1. The uppermost material in both holes (71 ft in test hole 1 and 35 ft in test hole 2) consists mostly of lean, stiff, moist, light-brown clay that is occasionally silty and contains sporadic nodules of caliche or calcium-cemented silt. According to Angino,[4] this material blankets the surface of the repository site and much of the surrounding area. The rather wide variation in thickness of the aeolian or wind-blown sediments is not unexpected, since the underlying Cretaceous rocks were subjected to a long period of erosion that created an irregular topographic surface before deposition of the Pleistocene deposits. This old erosional surface was found by Angino to consist of a thin zone of clay mixed with residual gravels and a thin layer of caliche. Outside the boundaries of the repository in sediment-filled stream valleys, the Pleistocene deposits consist of fluvial or water-lain materials of clay, silt, sand, and gravel. These unconsolidated sediments range from a few feet in thickness to about 180 ft and are by far the most important water-bearing deposits in the general area.

The Kiowa formation of Cretaceous age underlies the Pleistocene deposits at the site and is the youngest consolidated rock encountered. It consists primarily of weathered, light-brown, fissile, clay shale that contains occasional nodules of phosphate in the upper part and generally dark-gray clay shale with a few thin beds of fossiliferous limestone in the lower part. Low- to high-angle fractures with slickenside surfaces are com-

4. Ernest E. Angino et al., *Preliminary Report on the Geology and Hydrology of the Lyons, Kansas, Radioactive Waste Repository Site,* prepared by the State Geological Survey of Kansas and the University of Kansas Center for Research, Inc., for the U.S. Atomic Energy Commission and Union Carbide Corporation, November 1970.

mon throughout the formation. One of the most outstanding features of the Kiowa is the occurrence of water-bearing sandstone lenses that may range from a few inches to tens of feet in thickness. In test hole 1 a 7.5-ft-thick sandstone bed with another 11 ft of underlying interbedded shale and sandstone occurs near the middle of the 100-ft-thick section of the Kiowa formation. In test hole 2, where the formation is about 74 ft thick, an 8-ft-thick section of shale and interbedded sandstone was encountered near the bottom of the formation. An oscillating shoreline during Kiowa time was probably instrumental in the development of the highly variable sandstone beds of the formation. The variable thickness of the Kiowa throughout the area is accounted for by the irregular nature of its pre-Pleistocene erosional surface at the top and by the similarly uneven erosional surface of the underlying Permian rocks at its base. The Kiowa does not outcrop at the repository site, being completely covered by alluvium; however, surface exposures of the formation occur 1 to 2 miles southeast of the site. Although the Kiowa persists over the repository site, it is not present a few miles to the west, beneath the bed of Little Cow Creek, or to the south in the alluvial valleys of Cow Creek and the Arkansas River, having been eroded completely, probably during the Pleistocene, by these down-cutting streams. Toward the north of the site, the Kiowa formation is complete (approximately 150 ft thick) and is underlain by the Cheyenne sandstone of Cretaceous age and overlain by the Dakota formation, also of Cretaceous age.

Permian-age rocks underlie the Kiowa shale formation at the site (Fig. 3.1). Here, as well as throughout the Permian basin, these rocks reflect the conditions prevailing during this time period. In general the sequence of beds encountered in test holes 1 and 2 include, from the top, red beds, salt, anhydrite, and limestone and shale (Fig. 3.1). The Harper sandstone formation is the youngest Paleozoic-age rock present at the site. This formation is the lowermost member of the Nippewalla group of rocks in Kansas, which is progressively more complete toward the western part of the state. At the close of the Permian age, uplift, followed by a long period of erosion, removed most of the Upper Permian rock section from this part of the state, leaving only the Harper in the Nippewalla group. In both test holes the Harper was found to be about 125 ft thick. The formation is predominantly reddish massive siltstone and reddish silty to clayey shale, except for the uppermost shales and siltstones which are generally soft and gray in color from weathering. The Harper is undoubtedly present beneath the entire repository site; however, it extends only some 10 miles further to the east before being beveled by pre-Cretaceous erosion.

Underlying the Harper sandstone is the Stone Corral formation. This well-known "marker" bed, which is easily identified in well samples and on electric and radioactivity logs, is seen to be about 18 ft thick in test holes 1 and 2. It is mainly white to light-gray anhydrite and dolomite with a few thin beds of varicolored clay shale. The formation contains numerous gypsum-filled vugs and fractures throughout and, in the upper half, some open fractures. The Stone Corral is probably consistent in thickness and lithology beneath the repository, although some changes occur in the formation throughout its extent in western Kansas. It is the uppermost formation of the Sumner group of rocks in Kansas which, like the Nippewalla group mentioned above, consists mainly of red beds and evaporites. The Ninnescah shale and the Wellington formation comprise the two remaining formations of the Sumner group.

Red beds of the Ninnescah formation unconformably underlie the Stone Corral formation and conformably overlie the Wellington salt formation at the repository site, as well as throughout south-central Kansas. As seen in Fig. 3.1 the formation is about 300 ft thick in test holes 1 and 2. The Ninnescah shale here is predominantly reddish silty shale that frequently shows red and green mottling. Fracture fillings of gypsum are numerous throughout the formation as are bands, partings, and thin beds of gypsum, anhydrite, and dolomite. In some places the bedding is nondistinct, and the shale is massive in appearance. Although all fractures appear to be filled or tightly sealed, slickenside surfaces are present in some parts of the formation.

The Wellington formation is the lowermost member of the Sumner group of rocks and consists, in general, of a gray and red shale sequence at the top with rock salt beds in the middle and anhydrite and shale at the base. These members are approximately 185, 260, and 170 ft thick, respectively, at the site as revealed by test holes 1 and 2 (Fig. 3.1). The upper member of the formation consists largely of silty gray shales at its top and base, separated by a rather prominent red shale zone. Thin beds and partings of anhydrite occur frequently in the lower shales, but are less common in the upper gray shales, which also contain some blue clays, and in the red shales. Fractures in the upper gray shale and the red shale zone are usually filled with gypsum, while in the lower shale fracture fillings are of anhydrite, except near the contact with the underlying salt beds where salt-filled vugs and fractures exist.

Rock salt, interbedded with clay shale and anhydrite stringers, comprises the rock section from a depth of

755 to 1084 ft below the land surface in test hole 1 and for an approximately comparable depth in test hole 2. Owing to the complexities of the depositional environment of the rock salt deposit, both vertical and horizontal, persistence of the salt and its interbedded impurities is difficult to assess, even over the relatively small area of the repository. However, from the available data, it appears that the section of salt being considered for burial of the wastes is perhaps the least variable within the entire column of salt. A comprehensive discussion of the salt rocks at the site is available in another part of this report.

The predominantly anhydrite rocks that lie immediately below the rock salt comprise the basal member of the Wellington formation. Test holes 1 and 2 have shown that, for the most part, the anhydrite is light to dark gray in color and contains numerous inclusions and partings and clay shale with some interbedded siltstone and dolomite members. The thickness of the member is about 170 ft in test holes 1 and 2 (Fig. 3.1) and is believed to be rather consistent in thickness beneath the entire site.

In contrast to the Sumner group of evaporitic rocks described above, the underlying Chase group consists of a sequence of alternating beds of carbonate rock and shale. Only the upper part of this group (the Nolans limestone and the Odell shale) was encountered in test holes 1 and 2 (Fig. 3.1). The Nolans was found to be about 35 ft thick and, for the most part, consists of interbedded dolomite and shale beds in the upper part with a dense gray limestone bed at its base. Only about 10 ft of Odell shale was penetrated in test holes 1 and 2, and it was observed to consist of variegated, calcareous, hard, and massive shales.

Structure

The rocks beneath the proposed repository site have been subjected to a long and complex history of deformation; the older formations show, as would be expected, a more complicated regime than successively younger beds. Local movements along the central Kansas uplift have been instrumental in fabricating the existing structure, while the inclinations of the rocks at the site have also been affected by broad regional warping of the earth's crust. The repository site lies on the western flank of the Geneseo uplift which extends beneath a large part of the eastern half of Rice County and into the southern tip of Ellsworth County and the southwestern corner of McPherson County. This egg-shaped structure is separated on the west from the genetically related but semidetached main lobe of the central Kansas uplift by a rather sharp syncline, and on the east and northeast by another synclinal structure. Several north-south-trending anticlinal structures, some of which have associated oil and gas fields, are superimposed on the uplift along its western edge. One of these, the Lyons Gas Field structure, is centered a short distance east of the repository site and has been instrumental in establishing the present configuration of the rocks at the site. Some uplift of the Lyons Gas Field structure may have occurred prior to the deposition of Mississippian rocks, but the greatest deformation unquestionably occurred between Mississippian and Pennsylvanian deposition, as evidenced by the erosion of the entire Mississippian section along the crest of the anticline. This structural high remained topographically high during the deposition of succeeding beds which, along with recurrent uplifts, account for the persistence of the structure upward through the geologic column. The regional dip of the pre-Pennsylvanian sediments within the area is southeast, while the Pennsylvanian and Permian beds are west and the Cretaceous rocks are northward. Regional tilting accounts for this discordance in the direction of dip of the various age rocks within the area.

Rock Salt Deposits

The rock salt column beneath the proposed repository site consists generally of a succession of layers of rock salt intercalated with shales and occasionally anhydritic beds. As seen in Fig. 3.2, the principal salt zones can be traced laterally from the northeast corner to the southwest corner of the site, although some irregularities in thickness and in lithology occur. In general, lateral consistency in the column is greatest in the lower to middle part of the columns and least at the extreme bottom and upper part of the formation. As discussed earlier, the salt deposit at Lyons lies in a marginal portion of the Permian basin. In addition, the site lies on the northwest flank of the Lyons Gas Field anticline. With these conditions, some variation in the thickness and lithology of the entire salt sequence as well as individual beds over the site area would be expected. The salt is thickest in the south-central part of the site. The principal uplift associated with the Lyons Gas Field anticline occurred in late Mississippian to early Pennsylvanian time or long before the deposition of salt in the Permian. Nevertheless, through recurrent uplift movements during the deposition of the evaporites or through the prevailing topographic relief at the anticlinal structure during Pennsylvanian and Permian times, some local thickening and thinning of

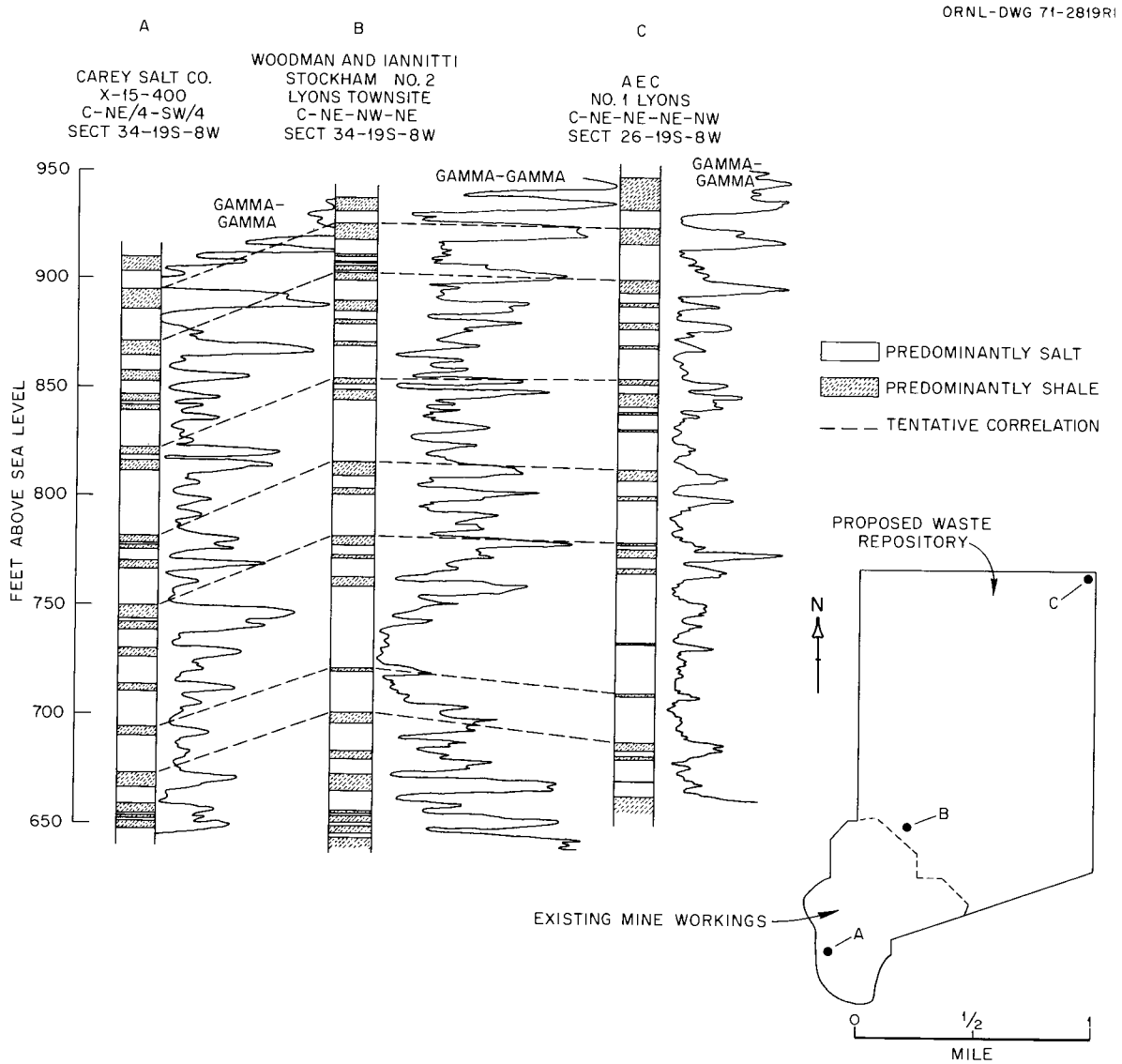

Fig. 3.2. Cross section of the salt rocks at the proposed repository site.

the salt rocks occurred. This explanation as the cause for the measured thinning of the salt is strengthened further by the absence of any observed solutioning and collapse of the overlying shale in the top parts of the salt sections in cores from test holes 1 and 2, which, if present, could account for gross thinning of the salt column.

In the marginal areas of the evaporitic Permian basin, such as at Lyons, it is apparent that the precipitation and deposition of salt was periodically interrupted by the influx of clay-bearing waters from nearby land masses. These local intrusions not only created irregularities in thickness and composition of the sediments but may also have created solution channels and slump features at various stratigraphic levels in the previously deposited salt section. It is likely that the discontinuous zones of brecciated salt observed in test holes 1 and 2 were formed in this manner. Irregularities in the salt section may also be due, in part, to periodic subareal exposure of some areas of the salt resulting from a fluctuating water level within the basin.

The thickest and most persistent salt zone is seen in Fig. 3.2 to occur in the bottom half of the column at a distance of between 673 and 710 ft above sea level in the Project Salt Vault (PSV)[2] charging shaft. A 9-ft-thick bed in the lower part of the zone comprises the mined unit at the Carey Salt Company's workings at the repository site and also at the American Salt Company's

mine a short distance south of the site. This bed of salt is unquestionably the most uniform and the best quality of the entire sequence and is, therefore, the desired location for burial of the wastes.

The salt unit that has been mined in the Lyons mine consists of relatively pure salt that contains minor inclusions of clay and shale. The first 10 to 11 ft of the section below the floor contains between 20 and 40% shale. The shale is present in beds that vary greatly in thickness over relatively short distances and may grade vertically and laterally into zones of salt that contain many pods and irregularly shaped lenses of shale and anhydrite. A second shaly zone, approximately 3 to 4 ft thick, is present, generally from about 19 to 20 ft below the floor. Four separate shaly zones occur in the first 21 ft of the section above the mine roof. The thickest shale bed lies at a minimum distance of about 2 ft above the ceiling of the mine, while other less prominent zones of shale lie between about 11 and 19 ft above the roof. These zones are usually only a few inches thick and contain, in addition to shale, lenses and stringers of anhydrite and salt.

The proposed area to be mined will lie at a level of about 20 ft above the preexisting mine floor and extend upward a distance of about 15 ft. The floor of the newly mined area will be rock salt, while a thin shale parting will mark the roof. A prominent shale bed that varies from a few inches to more than 1 ft in thickness will lie approximately 2½ ft below the floor. Several easily distinguishable shale beds that are about ½ to ¼ in. in thickness will probably persist in the walls of the mined area at distances of about 6½, 7, 10, and 12 ft above the floor. The salt in the proposed excavation area contains numerous blebs of polyhalite that are commonly concentrated along bedding, giving the salt a banded appearance.

Due to the structural attitude of the rocks at the proposed site, some variation in the levels of individual salt and shale beds is apparent. A measure of this level change can be made by determining the attitude of the prominent shale bed that exists as the "high top" or "17-ft" shale in the Carey mine workings and which will lie a few feet below the floor of the proposed working area. This shale bed, which is easily identifiable in cores as well as recognizable in the geophysical logs from the noncored borings, is about 10 ft higher in test hole 1 and 40 ft higher in elevation in test hole 2 than in the vicinity of the PSV charging shaft. Thus a constant rise in the mining level will be experienced from the southwest corner of the site to the southeast corner, while there will be essentially no change in the mining level along the western boundary of the site. From the southwest corner to the northeast, the mining level will rise constantly to the apex of the fold and then show a gradual decrease.

4. Engineering, Economic, and Safety Evaluations

K. E. Cowser
P. G. Fowler[1]
G. S. McNeilly[1]
Mark Reeves III[1]

SITING AND OPERATION OF NUCLEAR FACILITIES

Management and control of radioactive effluents and the need for a coherent model to simulate the dynamic behavior of critical radionuclides in the environment continue to be areas of considerable interest. Our last annual report described progress made in developing computer codes to calculate average annual ground-level air concentrations and ground-surface deposition rates for routine atmospheric releases of radionuclides and the cycling of these radionuclides in food chains.[2]

Application of Atmospheric Release Model

Parameters of the code include atmospheric stability, wind speed, wind direction, stack height, release rate, deposition velocity, washout coefficient, and a decaying chain of radionuclides emitted from the stack. Our principal contribution to the mathematical model was the inclusion, in a general fashion, of radioactive decay and production processes. Here an example is presented to show the relative importance of such effects. For didactic purposes, we apply the code to the Oak Ridge environment.

Stack release rates of noble gas measured at a boiling water reactor are listed in Table 4.1 and are used in these calculations.[3] Use is made of meteorological data collected earlier for the joint frequency of occurrence of various wind speed vectors and atmospheric stability conditions.[4] For this example, washout and fallout of the noble gas fission products and their descendants are assumed to be negligible. Radionuclide concentrations in air are converted to a submersion dose rate as specified by the International Commission on Radiological Protection (ICRP).[5]

Table 4.1. Average release rates of noble gas fission products

Radionuclide	Half-life	Release rate (μCi/sec)
$^{85m}Kr^{a}$	4.4 hr	300
^{85}Kr	10.7 years	0.1
^{87}Kr	76 min	700
$^{88}Kr^{a}$	2.8 hr	500
$^{133m}Xe^{a}$	2.3 days	10
^{133}Xe	5.3 days	300
^{135}Xe	9.1 hr	800
$^{138}Xe^{a}$	17 min	2000
^{88}Rb	18 min	0
^{138}Cs	22 min	0

[a]Parent-daughter considerations: $^{85m}Kr \xrightarrow{0.19} {}^{85}Kr \rightarrow {}^{85}Rb$(stable); $^{88}Kr \rightarrow {}^{88}Rb \rightarrow {}^{88}Sr$(stable); $^{133m}Xe \rightarrow {}^{133}Xe \rightarrow {}^{133}Cs$(stable); $^{138}Xe \rightarrow {}^{138}Cs \rightarrow {}^{138}Ba$(stable).

Source: ref. 3.

The impact of radioactive decay on total submersion dose rate is illustrated by ratios of dose rate, with and without decay. For the northeast direction, radioactive decay reduces the dose rate by a factor of about 5 after 25 km of downwind travel, and by a factor of about 10 after 50 km. Relative dose rates are shown in Fig. 4.1 and illustrate how the changing composition of dispersed material due to decay influences the total dose rate.

1. Mathematics Division.
2. *Health Phys. Div. Annu. Progr. Rep. July 31, 1970,* ORNL-4584, pp. 37–40.
3. Bernd Kahn et al., *Radiological Surveillance Studies at a Boiling Water Nuclear Power Plant,* U.S. Department of Health, Education, and Welfare, Public Health Service, BRH/DER70-1 (March 1970).
4. W. F. Hilsmeier, *Supplementary Data for Oak Ridge,* ORO-199 (Mar. 15, 1963).
5. International Commission on Radiological Protection, *Report of Committee II on Permissible Dose for Internal Radiation,* ICRP Publication 2, Pergamon, London, 1959; *Health Phys.* 3 (June 1960).

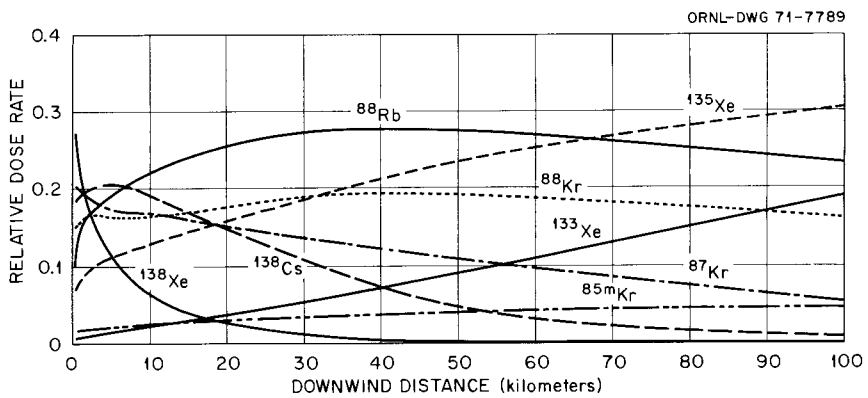

Fig. 4.1. Relative contribution of radionuclides to total submersion dose rate in northeast sector.

Identification of Potentially Critical Radionuclides

The ICRP emphasizes the value of identifying potentially critical radionuclides in the radiological assessment of nuclear facilities.[6] Critical radionuclides are those most likely to present problems in terms of ultimate exposure to man and/or detrimental effects on the environment.

Our search for critical radionuclides is divided into several steps, the first of which is to determine the internal and external dose to man, given a unit exposure.[7] The internal and external dose models used in these calculations have been reported previously.[7-9] These models, and most other aspects of this problem, require comprehensive information of nuclear structure and decay schemes, as well as extensive biological data. Since, for example, a typical core inventory of a nuclear power reactor includes almost 500 nuclides, the volume of necessary data handling is enormous. Consequently, our initial effort has been the development of a comprehensive data base which can be accessed in a flexible and easily modified manner. The data base, which is founded on the Battelle-Northwest Isotopic Data Tape,[10] currently contains information on nearly 200 nuclides and metastable states, as well as biological information necessary to perform calculations of dose equivalents.[5] Data are retrievable by key-word search. As an example, the computer printout in Table 4.2 was produced by requesting the nuclide ^{239}Pu with the key words HALF, BHALF, FRAC, ALPHA, BETA, GAMMA, CAPK, and POSIT. Half-lives are in days and energies in million electron volts. The biological fraction data are those defined by ICRP and are used with the nuclear data to perform dose calculations.

The above Nuclide and Biological Information System (NABIS) is of general utility in managing and retrieving large amounts of necessary data. The specific application currently under way is the generation of input data cards compatible with the internal and external dose computer codes INREM and EXREM.[8,9] This task is complicated by the variety of special cases defined by ICRP Committee II for dose calculations,[5] and by the fact that all decay products of a given parent must be included in calculations of effective energies. In the heavier nuclei approximately 100 possible decay pathways may exist for one parent nuclide; thus capability to automatically generate all possible decay chains from a given parent nuclide has been developed. Prototype dose calculations with the above system are presently being performed, and production dose calculations with large radionuclide inventories are anticipated in the near future.

6. International Commission on Radiological Protection, *Recommendations of the International Commission on Radiological Protection,* ICRP Publication 7, Pergamon, London, 1965.

7. K. E. Cowser, S. V. Kaye, P. S. Rohwer, W. S. Snyder, and E. G. Struxness, *Dose Estimation Studies Related to Proposed Construction of an Atlantic-Pacific Interoceanic Canal with Nuclear Explosives: Phase I,* ORNL-4101 (1967).

8. W. Doyle Turner, S. V. Kaye, and P. S. Rohwer, *EXREM and INREM Computer Codes for Estimating Radiation Doses to Populations from Construction of a Sea Level Canal with Nuclear Explosives,* K-1752 (1968).

9. W. Doyle Turner, *The EXREM II Computer Code for Estimating External Doses to Population from Construction of a Sea Level Canal with Nuclear Explosives,* CTC-8 (1969).

10. R. L. Reynolds, BNWL-551 (1970).

Table 4.2. Computer printout of nuclear and biological data

Z	NUCLIDE	MODE	PERCENT DECAY	ENERGY	HALF
94	PU239	ALPHA	.00032	5.081	8.9084 +6
		ALPHA	.111	5.110	
		ALPHA	.00013	5.013	
		ALPHA	.00021	5.059	
		ALPHA	.159	5.148	
		ALPHA	.72	5.160	
		BETA	NO DATA	NO DATA	
		GAMMA	.079	.0516	
		GAMMA	.0003	.0568	
		GAMMA	.0002	.0688	
		GAMMA	.00013	.0988	
		GAMMA	.99	.0007	
		GAMMA	.187	.013	
		GAMMA	.027	.0386	
		GAMMA	.0003	.0462	
		CAPK	NO DATA	NO DATA	
		POSIT	NO DATA	NO DATA	

BIOLOGICAL HALF LIFE

ORGAN	AGE	VALUE
T.B.	20.0	65000.
KIDNEY	20.0	32000.
BONE	20.0	73000.
LIVER	20.0	30000.

FRAC DATA

ORGAN	AGE	FRAC2	FRACW	FRACA
KIDNEY	20.0	.01	6.0E-7	5.0E-3
BONE	20.0	.9	2.4E-5	.2
T.B.	20.0	1.0	3.0E-5	.25
LIVER	20.0	.07	4.5E-6	.038

5. Dose Estimation Studies Related to Peaceful Uses of Nuclear Explosives and Other Radionuclide Releases

C. J. Barton[1] M. J. Kelly[1]
R. S. Booth[2] P. S. Rohwer
D. G. Jacobs W. S. Snyder
S. V. Kaye[3] E. G. Struxness

UTILIZATION OF NATURAL GAS FROM NUCLEARLY STIMULATED WELLS

C. J. Barton D. G. Jacobs
M. J. Kelly O. M. Sealand

Two experiments, Gasbuggy and Rulison, have been conducted to test the feasibility of using nuclear explosives to recover gas from known reservoirs that cannot produce gas economically under present conditions. These experiments demonstrated that the principal radionuclides remaining in the gas several months after the initial explosion are ^{3}H and ^{85}Kr. A continuing program is under way to assess the probable radiation dose to individuals and populations from the use of gas containing small quantities of radionuclides.

This program has been in a transitional stage during the past year. Major steps were taken to complete the Gasbuggy studies described in previous annual reports, while similar studies related to Project Rulison were just getting under way.

Tritium Tracer Test with Gasbuggy Gas in a Natural Gas Processing Plant

It is important to determine the distribution of tritium in gas from a nuclearly stimulated well among the various plant products and to estimate the doses that plant personnel will receive while operating a natural gas processing plant with gas containing radionuclides.

In February 1971, approximately 40,000 ft^3 of gas from the Gasbuggy well was transported in two tank trucks to a small natural gas processing plant near Barnhardt, Texas. It was then mixed with 1.8 million cubic feet of uncontaminated plant gas during a 12-hr period with the plant operating normally except that the product gas was flared (burned) instead of being sent to consumers.

The major exposure of operating personnel would occur from HTO released in the plant area as the result of fuel combustion in boilers, compressors, and other auxiliary equipment. Because of the low tritium concentration in the diluted Gasbuggy gas, tritium as $^{3}H_2$ was added to the fuel gas line to bring the tritium level before combustion to 3.5 pCi per cubic centimeter of gas so that samples of atmospheric moisture would contain measurable amounts of activity. Atmospheric moisture samples collected during the test showed a maximum tritium concentration of 90 pCi per cubic meter of air. A worker exposed to this concentration during a normal work year (2000 hr) would receive a dose commitment of 0.05 millirem.

The Barnhardt plant extracts butane, propane, and natural gasoline from natural gas prior to sending the remaining methane and ethane to consumers. Samples of all these products and processing liquids were taken both during the Gasbuggy injection period and for the subsequent 18 hr. In addition, on-line tritium analyzers monitored the inlet gas stream and the product gas stream during the test.

Within 15 min after Gasbuggy gas injection was started, radioactivity was noted in the exit gas stream. Within 45 min after the injection was stopped, activity was undetectable in the exit gas stream. This behavior was expected, but it helps to confirm that chemical

1. Reactor Chemistry Division.
2. Instrumentation and Controls Division.
3. Ecological Sciences Division.

exchange of tritium probably does not occur among the hydrocarbons during processing.

Samples of all plant products were returned to ORNL for tritium analysis. A full evaluation of the results cannot be made until all of the sample analyses are available.

A final report of this experiment will be published early in FY 1972.

Comparison of Gasbuggy and Rulison Cavity Gas and Rulison Production Testing

Miniata, the first test of an explosive designed specifically for natural gas stimulation, was conducted near the end of FY 1971 at the Nevada test site. It is of interest, nevertheless, to compare the radionuclide content of gas from the two wells stimulated with nuclear explosives said[4] to represent spillover from the weapons program. The data in Table 5.1 show that the concentration of tritium in Rulison gas is down by a factor of 4 as compared with Gasbuggy, and the total quantity is also less by a factor of about 2. The slightly higher concentration of ^{85}Kr in Rulison gas is of no importance, because whole-body or gonadal doses from this isotope are much less than from the same concentration of airborne HTO.[5,6]

Production testing of the Rulison well has been completed. Although much of the analytical data expected to be produced from the production testing program is not yet available, some significant observations have already been made. Water production has been found to be much greater than from Gasbuggy, presumably because of the higher well temperature. The CO_2 concentration in the gas declined from its initial value of 48% to 22% during the testing program, a much smaller decrease than in the tritium and ^{85}Kr concentrations. This indicates that CO_2 is being evolved in the cavity.

Water and CO_2 are both removed from natural gas during processing, but disposal of the radioactive contaminants (HTO in water and ^{14}C in CO_2) may require some attention.

4. B. C. Groseclose, "Nuclear Explosive Development," *Proceedings of the Symposium on Engineering with Nuclear Explosives, Las Vegas, Nevada, January 14–16, 1970,* CONF-70010, pp. 24–28.

5. H. J. Dunster and B. F. Warner, *The Disposal of Noble Gas Fission Products from the Reprocessing of Nuclear Fuels,* AHSB(RP)101, 1970.

6. M. M. Hendrickson, *The Dose from ^{85}Kr Released to the Earth's Atmosphere,* BNWL-SA-3233A; see also CONF-700810-16.

Table 5.1. Comparison of initial radioactivity in Gasbuggy and Rulison gas

	Gasbuggy	Rulison
Tritium		
Total in gaseous products (Ci)	2400	1100
Initial concentration (pCi/cm)	700	175
Krypton-85		
Total (Ci)	370	960
Initial concentration (pCi/cm)	110	150

DEVELOPMENT OF RADIATION SAFETY GUIDES FOR ENVIRONMENTAL RELEASES OF RADIOACTIVITY

P. S. Rohwer S. V. Kaye
R. S. Booth E. G. Struxness

The Cumulative Exposure Index (CUEX) concept has been extended to include continuous release situations (for example, effluent release from a nuclear power station or nuclear fuel reprocessing plant during routine operation). The following description reflects the extended format and the current stage of development of the suggested guide.

Release of radioactive material to the environment may result in radiation exposure of man, which may occur through any one of a number of exposure modes with each mode, in turn, having any number of subordinate exposure pathways of potential importance. The modes of exposure may be classified into two groups: internal (radiation source within the body, that is, inhalation and ingestion); and external (radiation source outside the body, that is, submersion in contaminated air or water and exposure to a contaminated surface). Adequate assessment of an environmental release of radioactivity requires that consideration be given to possible dose and dose commitment contributions for each of these exposure modes.

The CUEX concept is being developed to facilitate realistic assessment of doses from environmental contamination. The aim of the concept is to assess the release on the basis of time-integrated radionuclide concentrations measured in suitable environmental sampling media. It embodies environmental models and dose models to convert the measured environmental radionuclide concentrations into estimates of radiation dose to man. The final estimate of dose and dose commitment, which includes a contribution for each radionuclide and exposure mode of significance, is

compared with the appropriate radiation safety standard to complete the assessment.

The general structure within the CUEX concept is shown in Fig. 5.1. Starting at the top of the figure, the environmental sample is collected and analyzed to estimate the time-integrated radionuclide input to the environment. That input is quantified in units of μCi-hr/cm^3-year from air and water contamination measurements and in units of μCi/cm^2-year from surface contamination measurements. In the case of land surface concentration, time-integrated radionuclide concentrations in air are converted to estimates of surface concentration by application of a deposition velocity (centimeters per unit time). Integration of environmental input is limited to a period of a year, because the recommended radiation safety standards are annual dose limits. Summation of the dose contributions from all five exposure modes to obtain an estimate of total dose is shown diagrammatically in the lower portion of Fig. 5.1. Assessment of an environmental release of radioactivity is achieved by comparing the estimated total dose and dose commitment with the appropriate annual dose limits.

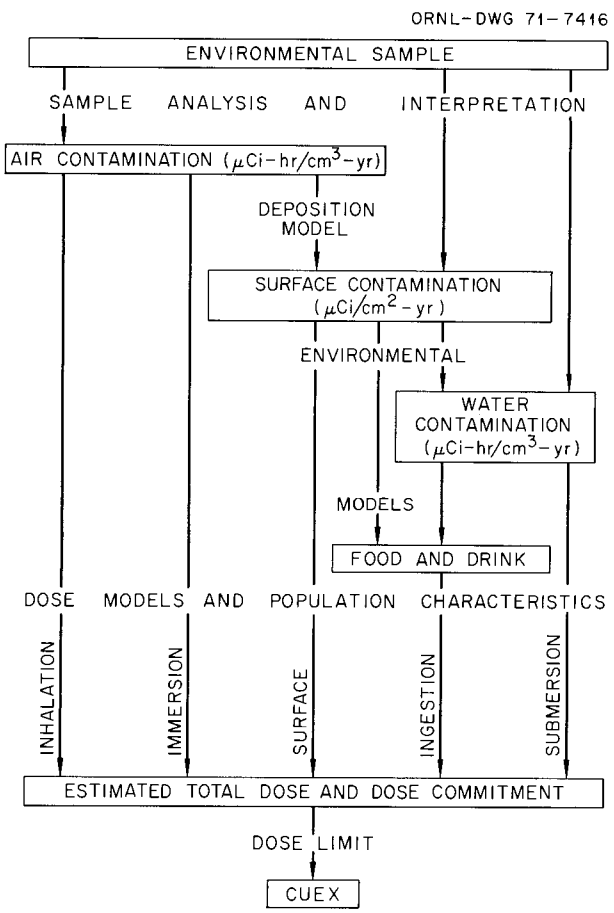

Fig. 5.1. The CUEX concept.

CUEX is defined as that time-integrated radionuclide concentration (μCi-hr/cm^3-year or μCi/cm^2-year) which, if present in the environmental medium sampled under the conditions considered, is estimated to yield a dose or dose commitment, via all exposure modes, equal to the selected annual dose limit. The exposure guide CUEX may be calculated for a single exposure mode or for any combination of exposure modes. The following formulation is used to calculate CUEX for exposure via inhalation only:

$$\mathrm{CUEX}_{ij}^{\mathrm{inh.}} = \frac{R_j}{D_{ij}^{\mathrm{inh.}} \times 8.33 \times 10^5}\ \mu\text{Ci-hr/cm}^3\text{-year}\ , \tag{1}$$

where

$\mathrm{CUEX}_{ij}^{\mathrm{inh.}}$ = exposure guide (μCi-hr/cm^3-year) for the ith radionuclide based on exposure of the jth organ via inhalation only,

R_j = selected annual dose limit (rems/year) for the jth organ,

$D_{ij}^{\mathrm{inh.}}$ = dose commitment to the jth organ per microcurie of the ith radionuclide inhaled (rems/μCi), and

8.33×10^5 = inhalation rate (cm^3/hr).

A dose commitment term ($D_{ij}^{\mathrm{inh.}}$) is used in Eq. (1), rather than a dose rate term, to prevent the radionuclide intake for a given year from placing unreasonable limitations on future years. Each term in Eq. (1) may vary as a function of the age of the individual exposed; therefore, CUEX may be calculated for specific age groups in the population. As the dose and dose commitment contributions for additional modes of exposure are estimated, the single-exposure-mode CUEX is reduced proportionately in the following manner:

$$\mathrm{CUEX}_{ij} = \mathrm{CUEX}_{ij}^{\mathrm{inh.}} \frac{R_j}{R_j + \sum_{k=1}^{n} D_{ijk}}\ \mu\text{Ci-hr/cm}^3\text{-year}\ , \tag{2}$$

where

CUEX_{ij} = exposure guide (μCi-hr/cm^3-year) for the ith radionuclide based on exposure of the jth organ via all exposure modes,

$CUEX_{ij}^{inh.}$ = exposure guide (μCi-hr/cm^3-year) for the ith radionuclide based on exposure of the jth organ via inhalation only,

R_j = selected annual dose limit (rems/year) for the jth organ, and

D_{ijk} = dose commitment (rems/μCi) to the jth organ from the ith radionuclide in the kth exposure mode (k denotes any exposure mode other than inhalation) for an exposure equivalent to $CUEX_{ij}^{inh.}$.

Each CUEX is calculated assuming only one radionuclide is present. As most exposures involve mixtures of radionuclides, the following additional calculation is required to assess the collective dose contribution from all radionuclides against the selected annual dose limit:

$$\sum_{i=1}^{n} \frac{E_i}{CUEX_{ij}} \leqslant 1 , \qquad (3)$$

where E_i is the time-integrated exposure (μCi-hr/cm^3-year) for the ith radionuclide and $CUEX_{ij}$ is the exposure guide (μCi-hr/cm^3-year) for the ith radionuclide based on exposure of the jth organ via all exposure modes. An assessment not satisfying the conditions of Eq. (3) indicates overexposure of the jth organ as a result of the cumulative dose and dose commitment contributions for the mixture of radionuclides considered in the concentrations and exposure conditions specified. The objective in controlling environmental releases of radioactivity on this basis is to reduce the result obtained with Eq. (3) as far below 1.0 as practicable.

A GENERAL MODEL TO ESTIMATE DOSE TO MAN FROM RADIONUCLIDE DEPOSITION

R. S. Booth S. V. Kaye

The methodology being developed for radiological safety assessments of environmental releases of radioactivity involves dynamic modeling techniques or systems simulations. These systems simulations vary from generalized models, which can be applied to many terrestrial locations and all radionuclides, to models applying to individual radionuclides of particular importance in special situations. The model discussed here is an example of the former.

The generalized systems analysis model[7] transferring radionuclides from deposition on to man is shown schematically in Fig. 5.2. Radionuclides are transferred from the source compartment (fallout) to the receptor compartment (man) through food crops, meat, and milk. Fractions s_1, s_2, s_3 of the fallout are deposited on the above-surface food crop, the soil surface, and pasture grass, respectively.

The food crops considered are fruits, vegetables, and grains which are exposed directly to fallout. Radionuclides in this compartment are immediately available for uptake by man. They are removed to the soil surface with an environmental half-time of less than 30 days.[8]

Passage from the soil surface compartment through the subsurface pool to the soil sink can take several years and represents a long-term radionuclide source to man. Coupling between the subsurface pool and the above-surface food is not considered explicitly, but is included in the transfer from the subsurface pool to man.

Radionuclides can be transferred from pasture grass to man through his intake of beef or milk. A feedback loop to the grass through the soil compartment accounts for radionuclide movement into the soil and its subsequent uptake by grass roots.

The milk compartment variable $C(t)$ (μCi/liter) is the concentration of a radionuclide in milk produced by a cow grazing on the contaminated pasture. The radionuclide is transferred from the grass directly to the milk compartment, because the milk of grazing cows can be in transient equilibrium with the forage radioactivity after about two days,[9] and data are not available to prepare a detailed milk-pathway model for many radionuclides.

The beef compartment variable $B(t)$ (μCi/kg) is the radionuclide concentration in the meat of cattle grazing on the contaminated pasture. Again the conservative assumption of the direct transfer of the radionuclide from grass to meat is used, since sufficient data for detailed modeling are not available. The mass in the beef compartment remains constant, since growth and

7. R. S. Booth and S. V. Kaye, *A Preliminary Systems Analysis Model of Radioactivity Transfer to Man from Deposition in a Terrestrial Environment*, ORNL-TM-3135 (1971).

8. J. P. Witherspoon and F. G. Taylor, Jr., "Interception and Retention of Simulated Fallout by Agricultural Plants," *Health Phys.* **19**, 493–99 (1970).

9. R. S. Booth, O. W. Burke, and S. V. Kaye, *Dynamics of the Forage-Cow-Milk Pathway for Transfer of Radioactive Iodine, Strontium, and Cesium to Man*, ORNL-TM-3054 (1971).

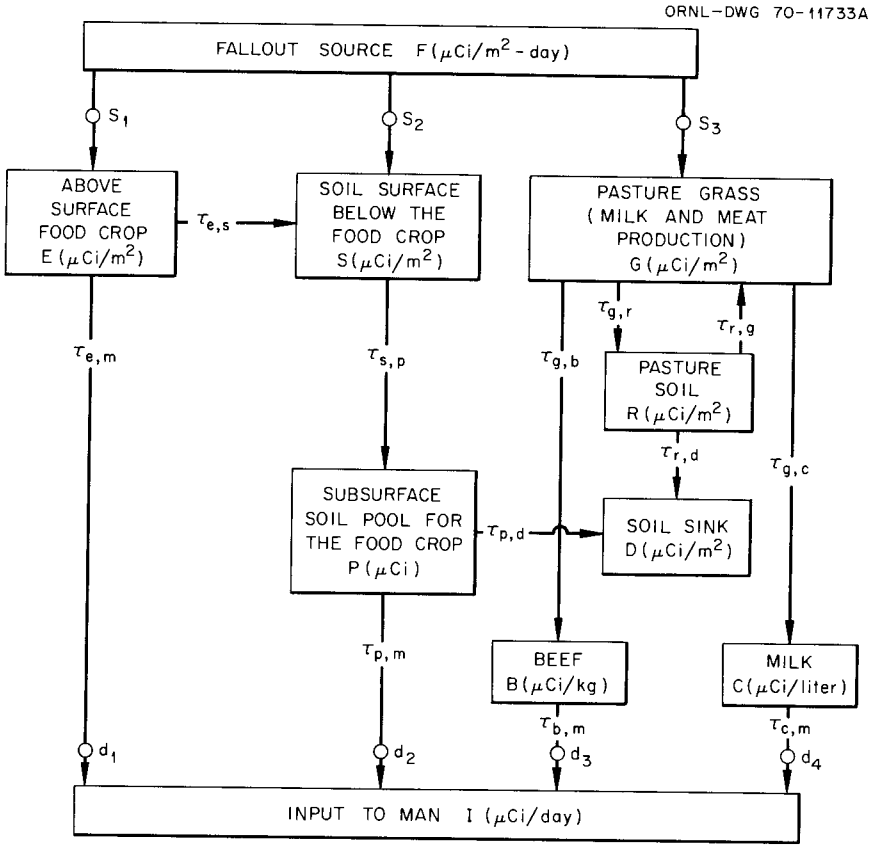

Fig. 5.2. Block diagram of the terrestrial food pathways.

new additions to the herd were assumed to balance slaughter.

The dietary factors d_1, d_2, d_3, and d_4 account for variations in the diet of the exposed population from that of standard man. These variations may be due to age, culture, religious custom, type of agriculture, or any other variation. For example, if milk is not available, d_4 is equal to 0.

The numerical values for the transfer coefficients $\tau_{g,b}$, $\tau_{g,c}$, and $\tau_{p,m}$ are different for each chemical element. These are derived in ref. 7 using refs. 10 and 11.

The other coefficients shown in Fig. 5.2 are assigned constant numerical values for all radionuclides, because (1) data were not available from which unique transfer coefficients could be calculated, (2) the transfer coefficient applied to a biomass that was independent of the radionuclide, or (3) although a unique coefficient could be calculated, it would have a negligible effect on the total input to man.

A 14-day environmental half-time is assumed for the transfer from the grass to the soil and from the food crop to the soil surface ($\tau_{g,r} = \tau_{e,s} = 0.05$ day^{-1}).[12] Feedback of radionuclides from the soil compartment was assumed to be 1% per year ($\tau_{r,g} = 2.74 \times 10^{-5}$ day^{-1}) and the loss to the soil sink 4% per year ($\tau_{p,d}$ =

10. Yook C. Ng et al., *Prediction of the Maximum Dosage to Man from the Fallout of Nuclear Devices: Part IV, Handbook for Estimating the Maximum Internal Dose from Radionuclides Released to the Biosphere,* UCRL-50162 (May 14, 1968).

11. Report of Committee II on Permissible Dose for Internal Radiation, *Recommendations of the International Commission on Radiological Protection,* ICRP Publication 2, Pergamon, 1959.

12. J. D. Zimbrick and P. G. Voilleque' (ed.), *1967 CERT Progress Report, Controlled Environmental Radioiodine Tests at the National Reactor Testing Station,* Progress Report No. 4, IDO-12065 (December 1965).

$\tau_{r,d} = 1.1 \times 10^{-4}$ day^{-1}).[13] The cow udder is emptied twice a day ($\tau_{milk} = 2.0$ day^{-1}), and the fraction of the beef herd slaughtered ($\tau_{beef} = 0.004$ day^{-1}) was assumed constant. The transfer coefficients $\tau_{c,m}$ (1.0 liter/day) and $\tau_{b,m}$ (0.3 kg/day) were taken from ref. 10.

The equations which describe the radionuclide transfer to man are programmed for a digital computer. Complete details on the calculation of all coefficients appear in ref. 7.

In order to use the model to calculate the dose to man, an input source term accounting for the microcuries per square meter of each radionuclide deposited is required. Given these values, the model will facilitate calculation of the total microcuries ingested which, when multiplied by the dose factor expressed in rems per microcurie, will yield the dose commitment.

THE TRANSFER OF TRITIUM TO MAN AFTER WET DEPOSITION

M. J. Kelly R. S. Booth

This model[14] describing environmental movement of tritium considers deposition of the radionuclide as rainfall from a cloud containing both HTO and H_2O. The space- and time-dependent diffusion equation for the movement of tritium in the soil from an initial concentration inserted over a finite depth is solved.[15] Transpiration and evaporation are not accounted for. Subsequent rainfall (H_2O) after the initial deposition of tritium exerts a driving force upon the diffusing concentration. This phenomenon was incorporated into our model by superimposing upon this diffusing concentration a vertical translation into the soil. The velocity of this translation, v_g, is related to the rainfall rate r and the void fraction f by the expression $v_g = r/f$. Average rainfall rates were 1 cm/day for the tropics, 0.35 cm/day for the temperate zone, and 0.05 cm/day for the desert. The value of the diffusion coefficient D selected for arable soil with a 50% void fraction (f = 0.5) was 1×10^{-5} cm^2/sec. The root depth was 50.0 cm in most calculations.

Variation of the depth of the initial tritium pulse from a surface monolayer to 10 cm containing the same total tritium was found to only qualitatively alter the final results for dose to man, although the distribution within the soil box is changed.

The average concentration of tritium in the soil compartment in curies per cubic centimeter is obtained by integrating the tritium concentration from the ground surface to the soil compartment depth and then dividing by this range of integration. This function when multiplied by the intake of water by man in milliliters per day and divided by the void fraction in the soil yields the time-dependent intake of tritium by man, $\bar{C}(t)$, when the equilibrium assumption of the model is applied. The expression for $\bar{C}(t)$ is

$$C(t) = (2000/0.5)(1/d) \int_0^d C(x, t)\, dx\,, \qquad (4)$$

where d is the depth of the soil compartment, $C(x, t)$ is the concentration of tritium in curies per cubic centimeter as a function of depth in the ground x and time t, and the numerical values for f and man's intake of water have been incorporated into the equation.

The cumulative dose to man $Q(T)$ was calculated by multiplying the total input of tritium to time T by the dose conversion factor 0.136 millirem/μCi:

$$Q(T) = 0.136 \times 10^{-6} \int_0^T C(t)\, dt\,, \qquad (5)$$

where the factor 10^{-6} converts curies to microcuries and the units of $Q(T)$ are millirems. The dose to man is an inverse function of v_g.

Values of $Q(\infty)$ may be calculated, and the mathematical expressions for this process are given in Eqs. (4) and (5). The $Q(\infty)$ values can be conservatively approximated, with an accuracy of about 25%, in a simple graphical form as shown in Fig. 5.3. To construct Fig. 5.3 a functional relationship between rainfall rate and $Q(\infty)$ was assumed. Losses by diffusion were ignored. Figure 5.3 applies for the following parameters: the depth of the initial tritium pulse = 10 cm, the diffusion coefficient of water = 1×10^{-5} cm^2/sec, void fraction of the soil = 0.5, and an input to man of 2000 g/day of water from the food he eats.

The accuracy expected from this model depends on the particular environmental condition against which it is tested. The model is believed to be conservative. It agrees qualitatively with existing experimental results and requires only experimentally demonstrable constants. Development of this model for predicting the movement of tritium to man from an initial wet deposition has given insight into the parameters that are most important in this transfer.

13. R. G. Menzel, "Factors Influencing the Biological Availability of Radionuclides for Plants," *Fed. Amer. Soc. Exp. Biol. Proc.* **22**, 1398–1401 (1963).

14. M. J. Kelly and R. S. Booth, *Quarterly Progress Report on Radiological Safety of Peaceful Uses of Nuclear Explosives: Transfer of Tritium to Man from an Initial Wet Deposition*, ORNL-TM-3134 (Jan. 8, 1971).

15. W. Jost, *Diffusion in Solids, Liquids, and Gases*, Academic, New York, 1952.

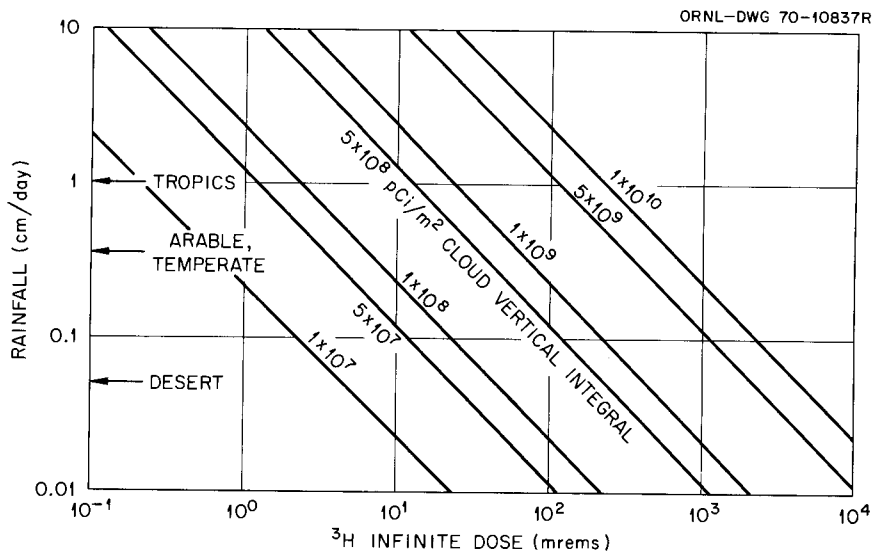

Fig. 5.3. Chart for estimating $Q(\infty)$ from the initial source strength and the subsequent rainfall rate.

Part II. Radiation Physics

R. D. Birkhoff R. H. Ritchie

6. Theoretical Radiation Physics

Jacob Neufeld
R. H. Ritchie

V. E. Anderson[1]
J. C. Ashley
W. Brandt[2]
Julian Crowell[2]
J. M. Elson[3]
Kenneth Fox[2]
W. R. Garrett
R. N. Hamm
Vinod Krishan[4]
H. C. Schweinler
S. Y. Shieh[2]
W. S. Snyder
J. E. Turner
R. B. Vora[5]
H. A. Wright

EFFECT OF LATERAL SCATTERING ON DOSE FROM 400-MeV PROTONS AND NEUTRONS

Most calculations of dose from high-energy protons and neutrons have been reported for an infinite slab. Comparisons which have been made with experimental measurements have generally shown the experimental values to be somewhat less at large depths than the theoretical values.

The question arises as to whether the absorbers used in the experiments are sufficiently large to approximate an infinite slab. Also, in radiological experiments, it is important to determine the region within an absorber in which the dose can be considered uniform.

When a high-energy neutron or proton penetrates matter it may interact with the nucleus of an atom of the target material, creating a cascade in which other nucleons or heavier nuclear fragments are ejected. These secondary particles, which may also have high energy, do not, in general, travel in the same direction as the incident particle. They may, therefore, transport a substantial fraction of the energy some distance laterally from the track of the incident particle. A study has been made of the effects of this lateral scattering on dose distributions.

Detailed Monte Carlo calculations have been made for a pencil beam of 400-MeV protons and neutrons incident at the center of one end of a water cylinder of radius 25 cm and traveling initially along the axis of the cylinder.[6] The energy deposited within the cylinder at various distances from the axis is calculated as a function of depth behind the end of the cylinder on which the particles are incident. It is found that for 400-MeV protons almost 30% of the total energy deposited at a depth of between 29 and 30 cm will be

1. Mathematics Division.
2. Consultant.
3. Oak Ridge Graduate Fellow, University of Kentucky.
4. Graduate student, University of Tennessee. Present address: Dept. of Physics, The University of Alberta, Edmonton 7, Alberta, Canada.
5. World Health Organization Fellow from Bhabha Atomic Research Centre, Bombay-74, India.

6. H. A. Wright, R. N. Hamm, and J. E. Turner, "Effect of Lateral Scattering on Absorbed Dose from 400 MeV Neutrons and Protons," in *Proceedings of International Congress on Protection against Accelerator and Space Radiation* (CERN, Geneva, April 26–30, 1971), to be published.

deposited at a lateral distance of more than 5 cm from the beam. For 400-MeV neutrons, more than half of the energy is deposited over 5 cm from the beam track and more than 25% is deposited over 10 cm away. Furthermore, the dose at a depth of 30 cm in an infinite slab differs by about 10% from the average dose over the 25-cm-radius cylinder for 400-MeV neutrons.

Calculations have also been made for broad beams of 400-MeV neutrons and protons incident uniformly over one end of a water cylinder of radius 15 cm. The average dose in concentric subcylinders of various radii was calculated as a function of depth behind the end of the cylinder on which the beam was incident. It was found that the dose was uniform to within less than 5% for 400-MeV protons and to within 10% for 400-MeV neutrons out to a radius of 10 cm.

The above calculations indicate that lateral scattering of the radiation from the sides of the phantoms used in experiments may account for the major portion of the existing discrepancy between experimental and theoretical results.

SEMICLASSICAL ESTIMATION OF NEUTRON STOPPING POWER

The semiclassical impulse approximation, employed by Bohr[7] to calculate the stopping power for charged particles, has been used to estimate the stopping power of matter for neutrons.[8] The stopping power, which is the rate of neutron energy loss per unit path length traveled, arises in this approximation from the forces due to the coupling of the neutron's magnetic moment to the charge and magnetic moment of the electrons in matter. Effects of nuclear forces are not considered. For most materials the neutron stopping power can be written

$$-\frac{dE}{\rho\, ds} \sim 5 \times 10^{-9}\,(\gamma^2 - 1)(\gamma^2 + 3)\ \text{MeV cm}^2/\text{g}\ ,$$

where $\gamma = (1 - \beta^2)^{-1/2}$ and β is the speed of the neutron relative to the speed of light. This formula is restricted to values $1 < \gamma \lesssim 10$, covering the range from fast neutrons to energies of ~10 GeV. The predicted stopping power for neutrons is smaller than that for protons in the same energy range by a factor of about 10^5. A method of detecting such electronic energy losses by neutrons has been suggested by G. S. Hurst.[8]

7. N. Bohr, *Phil. Mag.* **25**, 10 (1913).

8. R. B. Vora, V. N. Neelavathi, J. E. Turner, T. S. Subramanian, and M. A. Prasad, *Phys. Rev.* **B3**, 2929 (1971).

Z_1^3 EFFECT IN THE STOPPING POWER OF MATTER FOR CHARGED PARTICLES

An account of the early results on the calculation of a Z_1^3 correction to stopping power was described earlier.[9] For a medium of atomic density n_2 with Z_2 electrons per atom, we found the stopping-power correction due to electrons bound isotropically and harmonically with a frequency ω to be given by

$$\Delta\left(-\frac{dE}{dx}\right)_\omega = \frac{4\pi n_2 Z_2 F_\omega \omega}{m^2 v_1^5}\,(Z_1 e^2)^3\, I(\xi)\ ,$$

where m is the electron mass, v_1 is the speed of the incident particle of charge $Z_1 e$, F_ω is the fraction of electrons in the medium bound with frequency ω, and $I(\xi)$, with $\xi \equiv a\omega/v_1$, is a complicated integral which has been evaluated by computer for the range of values of ξ which are of interest.

For a comprehensive study of its v_1 and Z_2 dependence, we evaluate the Z_1^3 term for the statistical model of the target atoms in the Lenz-Jensen (LJ) approximation for the electron density distribution.[10] The total stopping power can then be written in the reduced form

$$\frac{m v_1^2}{4\pi (Z_1 e^2)^2 n_2 Z_2}\left(-\frac{dE}{dx}\right) = x\,S(x) = L(x) + \frac{Z_1}{Z_2^{1/2}\,x^{3/2}}\,F\left(\frac{\eta\chi Z_2^{1/6}}{x^{1/2}}\right)\ ,$$

where $S(x)$ is a dimensionless stopping cross section in terms of the reduced variable $x = v_1^2/v_0^2 Z_2$ with $v_0 = e^2/\hbar$. For $x \gg 1$, $L(x)$ approaches the Bethe-Bloch formula $L(x) = \ln(4\,\text{ry}/K_B)x$, where $\text{ry} = m v_0^2/2 = 13.6$ eV; $K_B = I/Z_2$ is Bloch's constant as determined by the mean excitation potential I of the target. The constant $\chi = 1.29$; η is a parameter of order unity associated with the choice of the minimum impact parameter. The second term on the right-hand side of this equation is the "Z_1^3 correction" term. The function $L(x)$ is shown in Fig. 6.1.

The function $F(w)$, where $w \equiv \eta\chi Z_2^{1/6}/x^{1/2}$, has been evaluated by numerical integration with the result shown in Fig. 6.1.

9. *Health Phys. Div. Annu. Progr. Rep. July 31, 1970*, ORNL-4584.

10. See, for example, P. Gombas, *Die statistische Theorie des Atoms und ihre Anwendungen*, p. 74, Springer-Verlag, Berlin, 1949.

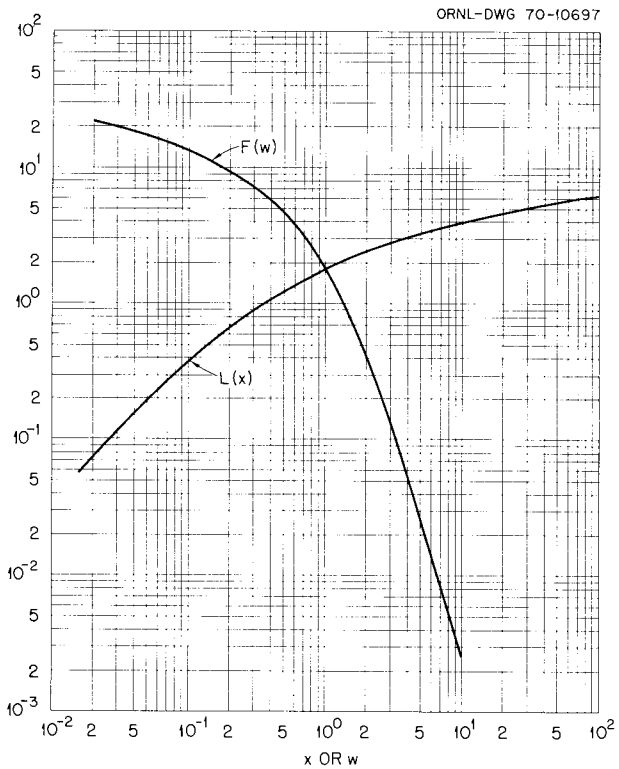

Fig. 6.1. The functions $F(w)$ and $L(x)$ used in the calculation of the $Z_1{}^3$ effect.

The relative change in the stopping power due to the $Z_1{}^3$ effect can then be calculated from the expression

$$\frac{x\,S(x) - L(x)}{L(x)} = \frac{Z_1}{Z_2{}^{1/2}} \frac{F(\eta\chi Z_2{}^{1/6}/x^{1/2})}{x^{3/2}\,L(x)} .$$

The dominant dependence of this correction on particle velocity is proportional to $x^{-3/2}$.

We now compare the theory with the experimental results of ref. 11. In Fig. 6.2 we plot the relative change in stopping power as a function of $\beta = v_1/c$ for $Z_1 = +1$ particles in tantalum ($Z_2 = 73$) with the trial values $\eta = 3/4$ and $\eta = 2/3$. The experimental points are taken from Fig. 1 of ref. 11. A parameter value close to $\eta = 0.7$ gives excellent agreement for the high Z_2 material over the v_1 range. Figure 6.3 shows the comparison for $Z_1 = +1$ particles in aluminum ($Z_2 = 13$) with the trial values $\eta = 2/3$, $\eta = 3/4$, and $\eta = 1$. The experimental points are taken from Fig. 2 of ref. 11. A value close to $\eta = 0.9$ provides an excellent fit. We have also made a calculation of the difference in stopping

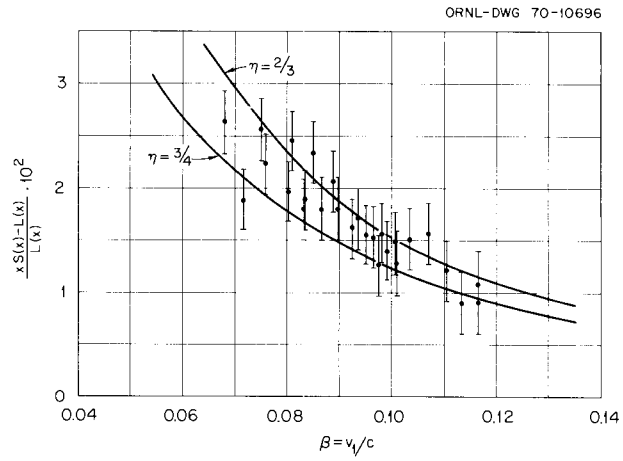

Fig. 6.2. Comparison of theory and experiment for the case of tantalum.

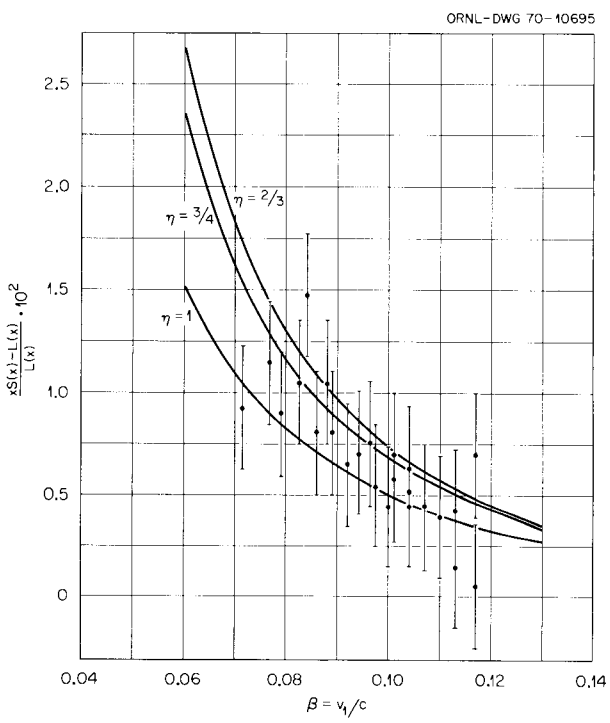

Fig. 6.3. Comparison of theory and experiment for the case of aluminum.

power due to the $Z_1{}^3$ effect between $Z_1 = +1$ and $Z_1 = -1$ particles in emulsion. We find that this effect produces an $\approx$8–9% difference at $\beta = 0.051$ in fair agreement with the estimate derived from π^+ and π^- range data of 14% reported in ref. 12 for this value of β.

11. H. H. Anderson, H. Simonsen, and H. Sørensen, *Nucl. Phys.* **A125**, 171 (1969).

12. H. H. Heckman and P. J. Lindstrom, *Phys. Rev. Lett.* **22**, 871 (1969).

CONTRIBUTION OF SURFACE LOSSES TO THE STOPPING POWER OF MATTER FOR CHARGED PARTICLES

In measurements of stopping power of bulk materials for charged particles, the presence of foil surfaces is usually not considered, or assumed to be quite small. As increasingly precise measurements of stopping power are made, it seems desirable to have a simple method of estimating the contribution of surface losses to the total energy lost by a charged particle in passing through a foil of a given thickness.

Consider a particle of charge ze and nonrelativistic speed v incident normally on a foil of material with plane, parallel surfaces separated by a distance a. The response of the material to fields of frequency ω is assumed to be given by a dielectric function $\epsilon(\omega)$. Using the probability for surface losses,[13] we find the contribution of the surfaces to the stopping power of the medium to be given by

$$\left(-\frac{dE}{ds}\right)_s = \frac{(ze)^2}{a\mathrm{v}}\int_0^\infty d\omega \,\mathrm{Im}\left[\frac{(1-\epsilon)^2}{\epsilon(1+\epsilon)}\right] \equiv \frac{(ze)^2}{a\mathrm{v}}\,\Omega\,.$$

Thus if we know $\epsilon(\omega)$ for all ω for the material of interest, the required integral can be evaluated, and a simple expression results for the surface loss contribution to the stopping power.

One way to approach the evaluation of Ω is through the use of an approximate dielectric function of a general solid. In the absence of damping, the dielectric function is taken to be

$$\epsilon_1(\omega) = 1 + \sum_n \frac{f_n\,\omega_{PT}^2}{\omega_n^2 - \omega^2}\,,$$

where ω_n is an average transition frequency from the nth shell to the ionization continuum, f_n is the fractional oscillator strength of that shell, and $\omega_{PT}^2 = 4\pi NZe^2/m$, where m is the electron mass and N the number of atoms of atomic number Z per unit volume. A dielectric function of this form has been used by Sternheimer in extensive analyses of the "density effect" in stopping power.[14] Contributions to Ω will occur at frequencies such that $\epsilon_1(\omega) = 0$ or $\epsilon_1(\omega) + 1 = 0$. The approximate roots of the equation $\epsilon_1(\omega) = 0$ are given by $\omega^2 \approx \omega_m^2 + f_m\omega_{PT}^2$ for $m = 1, 2, \ldots$, and for $\epsilon_1(\omega) + 1 = 0$, $\omega^2 \approx \omega_m^2 + \frac{1}{2}f_m\omega_{PT}^2$ for $m = 1, 2, \ldots$. Thus Ω is given approximately by

$$\Omega \approx \frac{\pi\omega_{PT}^2}{2}\sum_n f_n\left[\left(\omega_n^2 + \frac{1}{2}f_n\omega_{PT}^2\right)^{-1/2} - \left(\omega_n^2 + f_n\omega_{PT}^2\right)^{-1/2}\right].$$

This sum can be evaluated using the tables of values of ionization energies and oscillator strengths given in ref. 14 for various atoms and molecules. The approximate result here should be expected to give only rough estimates for the value of the integral since the main contribution comes from the outer-shell electrons whose response may be quite different in condensed media as opposed to the situation of isolated atoms. However, using this method we find for graphite $\hbar\Omega$ = 3.3 eV and for aluminum $\hbar\Omega$ = 0.8 eV.

A second method which should give more nearly correct results for Ω consists of using experimentally determined values of $\epsilon(\omega)$ from $\omega = 0$ to the highest value available to evaluate part of the required integral and adding on higher-energy contributions from the inner shells using the harmonic oscillator type of contribution described above. This procedure should give a more realistic result for the contribution of the outer-shell electrons. For graphite a graphical integration using values of $\epsilon(\omega)$ from 0 to ~80 eV and adding a K-shell contribution of $\approx 1.3 \times 10^{-3}$ eV, we find $\hbar\Omega$ = 5.54 eV. For aluminum with values of $\epsilon(\omega)$ from 0 to ~100 eV and adding a K-shell contribution of $\sim 3 \times 10^{-6}$ eV and an L-shell contribution of ~0.22 eV, we find $\hbar\Omega$ = 5.9 eV.

To illustrate the size of the surface loss contribution we consider the case of a graphite layer 100 Å thick of density 2.26 g/cm^3 with electrons normally incident on the layer. Using tabulated values of stopping power of graphite[15] and $\hbar\Omega$ = 5.54 eV, we find the ratio of surface to volume stopping powers, $(-dE/dx)_x/(dE/dx)_{\mathrm{vol}} \equiv r$, for various electron energies to be $r = 0.0045$ at 10 keV, $r = 0.0062$ at 30 keV, $r = 0.0072$ at 50 keV, and $r = 0.0079$ at 70 keV. The values at the higher energies are pushing the limits of validity of our nonrelativistic theory but seem to indicate an effect of less than 1% for this example. For

13. R. H. Ritchie, *Phys. Rev.* **106**, 874 (1957).

14. R. M. Sternheimer, *Phys. Rev.* **88**, 851 (1952).

15. M. J. Berger and S. M. Seltzer, p. 205 in *Studies in Penetration of Charged Particles in Matter*, NAS-NRC Publication No. 1133, 1964.

energies less than 10 keV, r is expected to continue to decrease as v decreases. Calculations for a 100-Å layer of aluminum with $\hbar\Omega = 5.9$ eV yield values of r just slightly larger than those for graphite, but less than a 1% effect is predicted for energies up to 70 keV. A relativistic treatment of the problem is needed to provide a more definitive statement about r at the higher energies.

DOSIMETRIC FIELD QUANTITIES IN HEALTH PHYSICS

A suggestion has been made to introduce in health physics a quantity termed tissue dose, which is to be used instead of absorbed dose and which is based on a volume element Δv different from that specified by the International Commission on Radiation Units and Measurements (ICRU).[16] The assumption made by the ICRU that Δv should "contain many interactions and be traversed by many particles" is not considered to be sufficient for a definition of dosimetric field quantities when a human body or its equivalent is the medium. It has been suggested that a "biologically infinitesimal" volume element $(\Delta v)_b$ and a "biologically infinitesimal" time interval $(\Delta t)_b$ be defined in health physics by analogy with the corresponding "physically infinitesimal" volume elements and time intervals in the macroscopic Maxwell electromagnetic theory. Both $(\Delta v)_b$ and $(\Delta t)_b$ are to be used as a basis for a phenomenologically defined and a macroscopically interpreted system of dosimetric field quantities in health physics.

WHAT IS "ENERGY IMPARTED"?

The purpose of this investigation was to clarify the formulation of a quantity known as "energy imparted," which represents the energy removed from a radiation field but not including that given to increase rest mass. It has been pointed out[17] that by not taking into account the energy of ionizing particles within a volume element in matter, energy imparted has not been, in the current ICRU recommendations, rigorously defined. An attempt has been made to reformulate energy imparted and related dosimetric quantities in a rigorous manner within the framework of a microscopic field theory.[17]

16. Jacob Neufeld, *Health Phys.* (in press).

17. Jacob Neufeld, *Health Phys.* (in press).

REEXAMINATION OF SCATTERING BY A PAIR OF FIXED DIPOLAR CHARGES

In order to better understand the scattering of electrons by polar molecules, a number of studies have been made of scattering by a simple dipolar system. Altshuler[18] determined the cross sections for electron scattering by a point dipole in the Born approximation. Later Mittleman and von Holdt[19] obtained an exact solution to the same problem. In both cases the total cross section diverges, and in the latter case the momentum transfer cross section also diverges for dipole moments greater than the critical $D = 0.639ea_0$.

It is well known that scattering by a spherically symmetric potential with an r^{-2} asymptotic form leads to an infinite total scattering cross section.[20] The general behavior of the total cross section is not due to the strong singularity at the origin but rather to the long-range nature of the interaction. Though it is considerably more complicated because of the angular dependence, the dipolar field has a long-range r^{-2} form; thus it would seem very reasonable that the divergence in the total cross section for a point dipole is also due to the long-range nature of the interaction and not a result of the strong singularity at $r = 0$. However, Takayanagi and Itikawa[21] have obtained results which yielded a finite total cross section for the case of a finite stationary dipole, where no singularity exists. Thus, their results would indicate that the removal of the singularity at $r = 0$ also removes the divergence in the total cross section. We have shown that this is not the case.[22] Instead, the total cross section does diverge, and the finite results obtained by Takayanagi and Itikawa are due to numerical approximation in a nonconvergent series.

The new result has been obtained through two different approaches to the problem of scattering by two fixed dipolar charges. Through a rather involved argument it was shown that the cross sections $\sigma(j \to j')$ for transitions of a rigid rotator dipolar system of internal rotational angular momentum j approached the Born approximation result for the same problem,[22] where the cross sections for transitions $j \to j \pm 1$ diverge

18. S. Altshuler, *Phys. Rev.* **107**, 114 (1957).

19. M. H. Mittleman and R. E. von Holdt, *Phys. Rev.* **140**, A725 (1965).

20. N. F. Mott and H. S. W. Massey, *The Theory of Atomic Collisions*, 3d ed., p. 41, Oxford Press, London, 1965.

21. K. Takayanagi and Y. Itikawa, *J. Phys. Soc. Jap.* **24**, 160 (1968).

22. W. R. Garrett, *Phys. Rev.* (submitted).

in the limit when the moment of inertia $I \to \infty$. Chang and Temkin[23] have recently shown that the expression for elastic scattering in the fixed nuclei approximation averaged over classical orientations of the internuclear axis is equivalent to the sum, in the limit $I \to \infty$, of the cross sections for transitions from a given rotational level j to all final rotational levels j'. Thus,

$$\bar{\sigma} = \lim_{I \to \infty} \sum_{j'} \sigma(j \to j'),$$

where $\bar{\sigma}$ is the elastic cross section in the fixed nuclei approximation. This equation leads to the result that the elastic cross section $\bar{\sigma}$ for scattering from a fixed dipole diverges as do the excitation (and the deexcitation) cross sections for the $I = \infty$ limit of the nonstationary dipole.

In order to elucidate the discrepancy between the results of Takayanagi and Itikawa[21] and those just mentioned, the exact treatment of the problem in prolate spheroidal coordinates was examined closely. It was shown[22] that the set of l spheroidal wave phase shifts diverge as $1/(2l + 1)$, thus leading to a logarithmic divergence in the total cross section. The results of ref. 21 were due to numerical approximation to this nonconvergent series.

CRITICAL BINDING OF AN ELECTRON TO A ROTATIONALLY EXCITED DIPOLAR SYSTEM

In work which has been reported previously,[24] an investigation was made of the critical dipole moment necessary to bind an electron in the ground state of a freely rotating electric dipole, and comparison was made with the more fictitious problem of electron binding to two fixed dipolar charges. The critical binding properties of a nonstationary dipolar system were found to differ quite drastically from those of a fixed charge system.[24] Contrary to these results, Bottcher[25] published an analytical analysis of the nonstationary electron-dipole problem which purportedly showed that the critical dipole moments for electron binding to a freely rotating electric dipole are the same as those for a fixed dipole. In a subsequent note[26] it was shown that the proof given by Bottcher was invalid, with the result that his conclusions hold only for the limiting case of a fixed dipole.

The treatment of the critical binding of an electron to a freely rotating dipolar system has now been extended to include calculations of critical dipole moments for rotationally excited states of the electron-dipole system.[27] Results for the even-parity states with total angular momentum $J = 0, 1, 2, 3$ are given in Table 6.1 for two different dipole lengths R and moments of inertia I. Some of these results are shown graphically in Fig. 6.4. Critical moments for the odd-parity states with $J = 1, 2, 3$ are given in Table 6.2 and shown graphically in Fig. 6.5.

The present results have shown that the minimum dipole moment necessary for the existence of a bound state of an electron-dipole system in a state of total angular momentum J increases with each unit of rotational excitation. The minimum moment D_{min} for the highest rotational state considered here ($J = 3$) is about 50% greater than that for a fixed dipole. A reasonable extrapolation to higher rotational states indicates that for small molecules the minimum mo-

23. E. S. Chang and A. Temkin, *Phys. Rev. Lett.* **8**, 399 (1969).

24. W. R. Garrett, *Chem. Phys. Lett.* **5**, 393 (1970).

25. C. Bottcher, *Mol. Phys.* **19**, 193 (1970).

26. W. R. Garrett, *Mol. Phys.* 20, 751 (1971).

Table 6.1. Critical dipole moments for the first four even-parity rotational states of a dipolar system having charge separation (dipole length) R and moment of inertia I

I*	$R = 0.6672a_0$				$R = 1.0284a_0$			
	$J = 0$	$J = 1$	$J = 2$	$J = 3$	$J = 0$	$J = 1$	$J = 2$	$J = 3$
2×10^8	0.705				0.709			
2×10^7	0.717	0.741				0.751		
2×10^6	0.733	0.768	0.781		0.740	0.780	0.798	
2×10^5	0.754	0.802	0.826	0.837		0.819	0.842	0.860
4×10^4	0.775	0.834	0.862	0.882	0.787	0.856	0.891	0.914
1×10^4	0.796	0.870	0.907	0.935	0.812	0.902	0.944	0.978

*In units of $m_e a_0^2$.

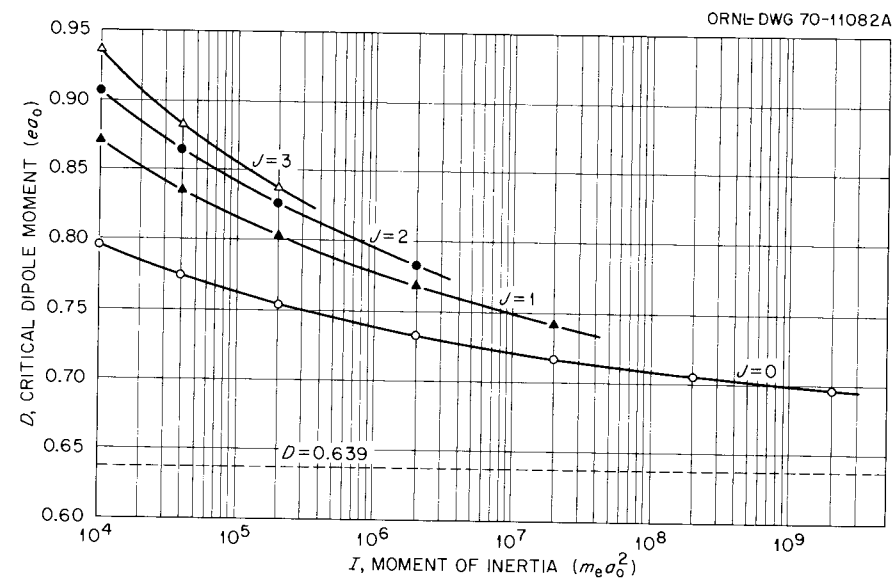

Fig. 6.4. Critical dipole moment as a function of moment of inertia I for the first four even-parity rotational states of a nonstationary electric dipole. Dipole length $R = 0.6672a_0$.

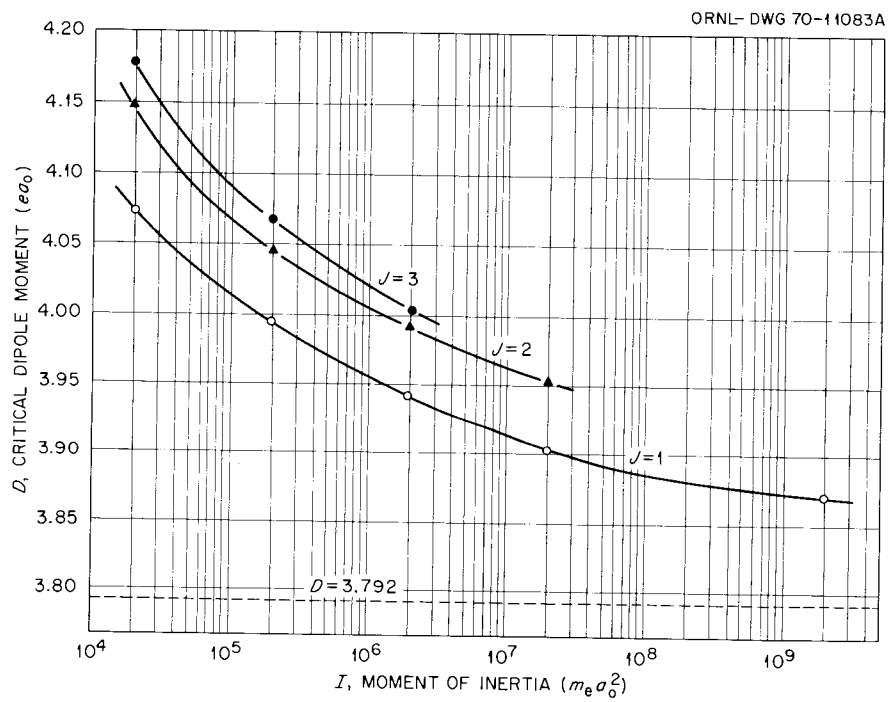

Fig. 6.5. Critical dipole moment as a function of moment of inertia I for the first three odd-parity rotational states of a nonstationary electric dipole. Dipole length $R = 0.6672a_0$.

ment might easily increase by a factor of 2 over that for the fixed dipole in the range $J = 5$–10.

We have also obtained the interesting and very useful result that the minimum critical moments for all rotational states J converge, in the limit as $I \to \infty$, to the two lowest critical moments for the fixed dipole.[27]

The critical binding properties of a nonstationary electric dipole have important implications for problems involving the scattering of low-energy electrons by polar molecules. The existence of a critical moment for

27. W. R. Garrett, *Phys. Rev.* **A3**, 961 (1971).

Table 6.2. Critical dipole moments for the first three odd-parity rotational states of a dipolar system having charge separation (dipole length) R and moment of inertia I

I*	$R = 0.6672a_0$			$R = 1.0284a_0$		
	$J = 1$	$J = 2$	$J = 3$	$J = 1$	$J = 2$	$J = 3$
2×10^9	3.871			3.888		
2×10^7	3.898	3.955				
2×10^6	3.941	3.992	4.005	3.954	4.003	4.020
2×10^5	3.994	4.046	4.067			
2×10^4	4.074	4.151	4.179	4.131	4.206	4.245

*In units of $m_e a_0^2$.

the dipole field has raised considerable speculation as to the behavior of the scattering cross sections of low-energy electrons on polar molecules whose dipole moments lie near $0.639ea_0$. Conflicting theoretical predictions have been made of the presence or absence of a large change in these cross sections for supercritical as compared with subcritical polar molecules.[28–31] Electron swarm data have been reported[32–34] as indicating significantly larger thermal energy scattering cross sections in dipolar gases whose moments lie near $0.639ea_0$ as compared with those with larger or smaller moments, but the nature of available data is such as to leave considerable latitude in its interpretation.

If we consider the scattering of an electron by a dipolar system which is initially in its ground rotational state, then the present results show that (1) each partial wave component in the scattering problem has associated with it a different critical moment, and (2) these critical moments increase with increasing incident angular momentum. Thus, since a large number of partial wave components contribute to the electron scattering cross section even at very low energies, the resonant phase change in one channel would not necessarily result in a dramatic change in the total cross section. Any noticeable change in a cross section would certainly not occur at $D = 0.639ea_0$ but would instead be distributed over moments from a few percent to perhaps a factor of 2 greater than this number.

Thus, one cannot choose a specific dipole magnitude, whether the value chosen is $0.639ea_0$ or some other larger number, and use this as a basis for comparison in relating scattering cross sections between a number of different molecules whose dipole moments cover a specific range of values of D.[22]

UNLOCALIZED ENERGY LOSSES BY CHARGED PARTICLES IN MATTER

Some time ago Fano pointed out that it may not be possible to localize initially certain low-lying excitations of matter caused by swift charged particles. The excitations cannot be localized within a region of the order of several hundred atoms across (1) due to the operation of the uncertainty principle and (2) because of the existence of collective electron oscillations involving the cooperative motion of many thousands of electrons. We have studied the spatial distribution of electron density fluctuations induced in condensed matter in a region through which a fast electron passes. We have shown that the electron density fluctuation $\delta n(\mathbf{r})$ at vector position $\mathbf{r}$ measured from the nominal location of the electron is given by

$$\delta n(\mathbf{r}) = \frac{-1}{2\pi^2} \int d^3k\, e^{i\mathbf{k}\cdot\mathbf{r}} \left(\frac{1}{\epsilon_{\mathbf{k},\, \mathbf{v}\cdot\mathbf{k}}} - 1 \right),$$

where $\mathbf{v}$ is the velocity of the fast electron and $\epsilon_{\mathbf{k},\omega}$ is the diagonal part of the inverse dielectric response matrix of the medium for disturbances having wave vector $\mathbf{k}$ and frequency ω. This equation describes the spreading out of disturbances through the medium due to the dispersive character of collective excitations and, in addition, the effects of the uncertainty principle. In a free-electron-like medium such dispersion results in a Čerenkov-like wake behind a swift classical point charge whose extension depends upon the Fermi velocity and damping processes occurring in the medium. Numerical evaluation of the expression for $\delta n(\mathbf{r})$, using various models for $\epsilon_{\mathbf{k},\omega}$, is being carried out.

ELECTRON SLOWING-DOWN-CASCADE SPECTRA IN SOLIDS[35]

Experimental data on the slowing-down-cascade (sdc) spectrum of electrons generated over a very wide energy

28. J. M. Levy-Leblond and J. P. Provost, *Phys. Lett.* **26B**, 104 (1967).

29. A. Dalgarno, O. H. Crawford, and A. C. Allison, *Chem. Phys. Lett.* **2**, 381 (1968).

30. O. H. Crawford, *Chem. Phys. Lett.* **2**, 461 (1968).

31. Y. Itikawa and K. Takayanagi, *J. Phys. Soc. Jap.* **26**, 1254 (1969).

32. J. A. D. Stockdale, L. G. Christophorou, J. E. Turner, and V. E. Anderson, *Phys. Lett.* **25A**, 381 (1968).

33. L. G. Christophorou and A. A. Christodoulides, *J. Phys.* **B2**, 71 (1969).

34. L. G. Christophorou and D. Pittman, *J. Phys.* **B3**, 1252 (1970).

35. The research reported here was sponsored in part by the Air Force Cambridge Research Laboratories, Office of Aerospace Research, under Contract Y70-837, but the report does not necessarily reflect endorsement by this Agency.

range by uniformly distributed beta-ray sources in metals and semiconductors have been obtained by Birkhoff and co-workers at Oak Ridge National Laboratory. These data agree well with the Spencer-Fano theory for electron energies $\gtrsim$20 keV but are larger by as much as 300% for lower energies. Differences are to be expected, since the Spencer-Fano cross sections are derived from the Møller theory which neglects binding of stopping electrons.

Inelastic electron cross sections for solids at energies lower than a few hundred kilovolts are necessary in order to construct a realistic theory of the sdc spectrum over the requisite energy range. In recent years electron mean free paths in a number of metals and semiconductors have been studied experimentally using photoemission and characteristic energy loss techniques. Certain theoretical models for inelastic interactions[36] have been employed by us in constructing solutions of the Boltzmann equation for sdc spectra. The approximate electron cross sections determined from these models are adjusted to yield agreement with available experimental data on mean free paths and stopping power and to satisfy certain low-order sum rules.

We use cross sections taken from the electron gas model in the case of the conduction band in metals and from the Callaway-Tosatti model for the case of the valence band in semiconductors. Electron energy losses to plasmon excitation, electron-hole pair excitation, and phonon excitation are included. Hole inelastic interactions which give rise to electron-hole pairs are also included. Interaction cross sections of electrons with core electrons in the solid are taken from analytical cross sections for the inner shells of the isolated atoms and, alternatively, from classical models for inner-shell excitation and ionization. The spectrum of electrons arising from Auger cascade filling of inner-shell vacancies is estimated for the solids of interest from the work of Carlson and others.

The energy-dependent Boltzmann equation is solved numerically for source distributions corresponding to those used in the sdc experiments. Since the only independent variable appearing in the appropriate Boltzmann equation is the energy, this equation is solved straightforwardly by the application of standard numerical techniques. In addition, a Monte Carlo code for electron transport in solids, which was written earlier for another application, has been modified to apply to the present situation.

We have compared the results of an ~1-min run for a unit monoenergetic source energy of ten times the Fermi energy in aluminum metal with a numerical solution of the energy-dependent Boltzmann equation describing the sdc process for the same conditions. Figure 6.6 shows the results of this comparison. The solid curve shows the Boltzmann equation solution; the rather sharp peaks are due to (undamped) successive plasmon losses by electrons originally at the source energy. The sharp increase as E/E_F decreases below unity is similar to results obtained analytically and described above.

The histogram gives our Monte Carlo results. Although the energy resolution is not as good as that obtained from the Boltzmann equation solution, it is clear that the results are quite similar and agree well on an absolute basis. Monte Carlo calculations of this type are being carried out for other slowing-down media and for continuous source distributions.

It is possible to obtain an interesting analytical approximation to the sdc spectrum for these model systems in the low-energy range. From this solution and from numerical solutions of the Boltzmann equation, it is expected that the flux of sdc electrons at energy E just above the Fermi level in a metal should be given by a constant, which depends upon the conduction band electron density, times E^{-4}, if E is measured from the Fermi level. The expression for this low-energy flux includes the effects of the complete coupled electron-hole slowing-down cascade. It has been compared with experimental data of Birkhoff and co-workers on several different metals and gives reasonable agreement

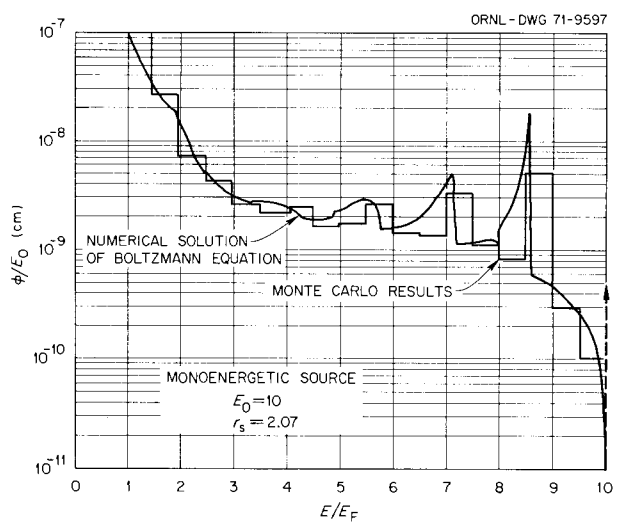

Fig. 6.6. Comparison of sdc spectra in aluminum metal calculated by the Monte Carlo method (histogram) and by numerical solution of the Boltzmann transport equation (solid curve).

36. R. H. Ritchie and V. E. Anderson, to be published.

both in shape and absolute magnitude with the experimental flux.

VOLUME PLASMON DECAY

The volume plasmon is an important "elementary excitation" in condensed media which has received a great deal of attention in recent years, both theoretically and experimentally. Until recently it was thought that the decay of the volume plasmon in a free-electron-like system was explainable in terms of a two-pair (electron-hole pair) momentum-conserving final state and that theory and experiment (in aluminum metal) were in good agreement. Theoretical results of DuBois and co-workers have thrown doubt on earlier results. In view of the importance of understanding such prototypical systems, we have studied the contribution of ionic scatter to volume plasmon decay processes in free-electron-like metals, using a pseudopotential representation for the ionic system.

We have investigated the interaction of plasmons with the ionic system in a metal, using the nearly free electron model in the framework of (1) quantum hydrodynamical theory, (2) semiclassical dielectric theory, and (3) many-body theory. The damping rate of the volume plasmon in a weakly inhomogeneous system due to elastic scatter on static density variations has been calculated from both (1) and (2). The quantum hydrodynamical theory and the semiclassical dielectric theory are comparable under the assumption that the deviation from uniformity of the electron density is closely related to the ionic distribution function of a polycrystalline material. A diagrammatic analysis of certain low-order interactions in the framework of many-body theory has been given also.

The diagonal part of the dielectric response matrix of a nearly free electron gas may be defined by the equation $\epsilon_q = 1 - v_q \Lambda_q$, where v_q is the Fourier-transformed bare Coulomb interaction energy between electrons in the electron gas corresponding to four-momentum $\hbar q = \hbar(\mathbf{q}, \omega)$, $i\Lambda_q$ is the diagonal part of the sum over all proper polarization subdiagrams, and ϵ is the dielectric matrix. In the lowest (or pair) approximation, ionic interactions may be neglected; one obtains the well-known Lindhard dielectric constant. In next order the ionic (pseudo) potential may be included; one then considers diagrams of the structure shown in Fig. 6.7, in which the dashed lines represent interactions with the ionic system. If one designates contributions of this order as $\Lambda_q^{(2)}$, one may show that the damping rate $\gamma_{\mathbf{q}}$ of a plasmon with four-momentum $\hbar q$ is given by $-\omega_{\mathbf{q}} v_{\mathbf{q}}$ Im $\Lambda_q^{(2)}$, where $\omega_{\mathbf{q}}$ is the

ORNL-DWG 71-9598

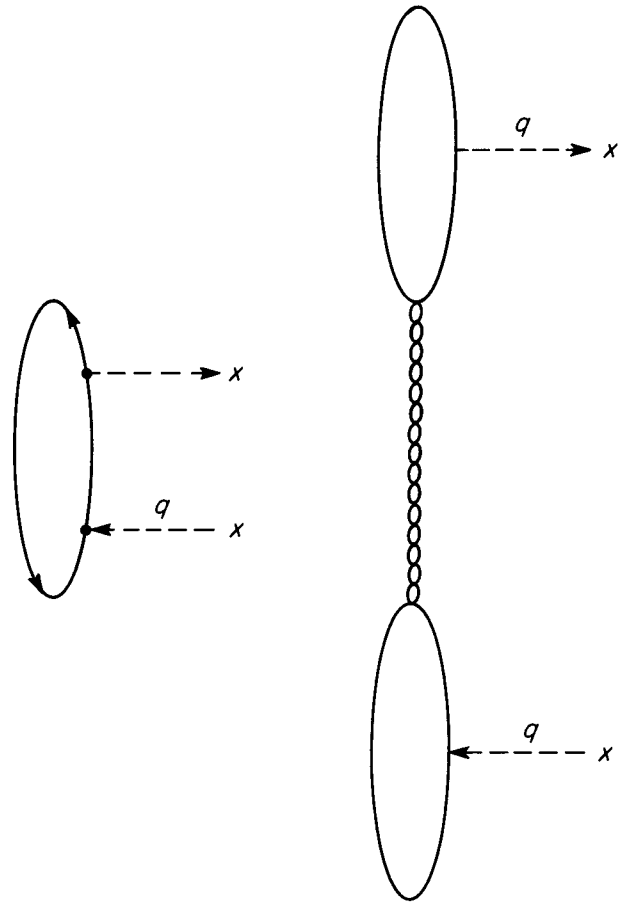

Fig. 6.7. Structure of diagrams contributing to the sum of proper polarization subdiagrams entering the inverse dielectric response matrix to lowest order in the ionic potential.

eigenfrequency of a plasmon with three-momentum $\hbar\mathbf{q}$. Evaluating the contribution from all diagrams having structures shown in Fig. 6.7, one finds

$$\gamma_{\mathbf{q}} = \frac{\pi^2}{2} v_q \omega_{\mathbf{q}} \int \frac{d^3k}{(2\pi)^3} |w_{\mathbf{q}}|^2 \int \frac{d^3p}{(2\pi)^3} \times (1 - n_{\mathbf{p}}) n_{\mathbf{p}-\mathbf{q}-\mathbf{k}} \, \delta(\epsilon_{\mathbf{p}} - \omega_{\mathbf{q}} - \epsilon_{\mathbf{p}-\mathbf{q}-\mathbf{k}}) \, |A - iB \, v_{\mathbf{q}+\mathbf{k}} (\epsilon_{\mathbf{q}+\mathbf{k}}, \omega_{\mathbf{q}})^{-1}|^2 ,$$

where $w_{\mathbf{q}}$ is the Fourier-transformed pseudopotential distribution, $n_{\mathbf{p}}$ is the occupation number of the noninteracting electron gas corresponding to momentum $\hbar\mathbf{q}$, $\epsilon_{\mathbf{p}} = \hbar p^2/2m$, and A and B are rather complicated integrals arising from the triangle diagrams appearing in Fig. 6.7. Evaluation of this complete

expression requires numerical methods which are being explored. Considerable simplification occurs if $\hbar|\mathbf{q}| \ll$ the Fermi momentum of the electron gas; in this case one finds exact agreement with the results of the quantum hydrodynamical treatment and the semi-classical dielectric approach.

PHOTON INTERACTIONS AT A ROUGH METAL SURFACE

The most accurate method of experimental determination of microscopic roughness at solid surfaces presently used involves measurement of the diffuse scatter of photons at the surface. The theory of this process previously employed to interpret such measurements is incomplete, in that it neglects the possibility of scattering resonances and resonance absorption due to the excitation of surface plasmons in intermediate states. Such effects may also influence the values of optical constants inferred from reflectivity measurements.

We have developed a theory of the interaction of photons at a rough solid surface, choosing the solid to be an electron gas to simplify the calculations. A Hamiltonian approach is used; a transformation of coordinates to a nonorthogonal system in which a coordinate surface coincides with the bounding rough surface of the solid is made. The zero-order Hamiltonian is chosen to be that part of the total Hamiltonian expressed in the nonorthogonal system which has the appearance of orthogonality. The residual term of lowest order in the slope of the surface is treated as a perturbing Hamiltonian. The probability of diffuse elastic scatter of an incident photon is calculated by time-dependent perturbation theory. In a similar manner the probability of surface plasmon creation by the incident photon is determined. An ensemble average over surface slope is carried out in order to represent the random character of the surface.

We find that the probability of surface plasmon creation by a photon of frequency $\omega = \alpha\omega_p$ by a normally incident photon is given by

$$P(\omega) = \delta^2 (\omega/c)^4 F(\alpha) g\left[\alpha \frac{\omega_p}{c}\left(\frac{1-\alpha^2}{1-2\alpha^2}\right)^{1/2}\right],$$

where δ^2 is the mean square deviation in the height of the surface, $g(\kappa)$ is the surface scattering function (correlation function), ω_p is the bulk plasma frequency, and

$$F(\alpha) = \frac{\alpha^5 (1-\alpha^2)^2}{(1-2\alpha^2)^{5/2}}\left[1 + 2\left(\frac{1-2\alpha^2}{1-\alpha^2}\right)^{1/2}\right]^2 .$$

The differential probability for scatter of the photon into an s-polarized photon proceeding in a direction measured by the polar angle θ referred to the outward mean normal to the solid and the azimuthal angle ϕ measured from the plane of polarization of the incident photon may be written

$$\frac{dP^{(s)}}{d\Omega} = \frac{\delta^2}{\pi^2} (\omega/c)^4 \cos^2\theta \sin^2\phi\, g\left(\frac{\omega}{c}\sin\theta\right),$$

where $d\Omega = \sin\theta\, d\theta\, d\phi$. Similarly, for p-polarized photons in the scattered field,

$$\frac{dP^{(p)}}{d\Omega} = \frac{dP^{(s)}}{d\Omega} \cot^2\phi \left(\frac{\sin^2\theta - \epsilon}{\sin^2\theta - \epsilon\cos^2\theta}\right) \times \left(1 + \frac{2\sqrt{-\epsilon}}{\sqrt{\sin^2\theta - \epsilon}}\right)^2,$$

where $\epsilon = 1 - (\omega_p/\omega)^2$. The formula for $dP^{(s)}/d\Omega$ agrees exactly with that obtained classically by Davies.[37] However, $dP^{(p)}/d\Omega$ differs considerably from his result; we predict much larger scattering probability in general. We feel that our results should be more accurate than his since we take specific account of the fields associated with surface currents giving rise to p-polarized fields, while the scalar scattering theory of Davies does not distinguish between the two polarizations.

Our results have already been used with good effect by experimenters at Stanford[38] to analyze data on photoelectric emission at rough surfaces and should be very useful in other experimental situations of this general character.

DOSIMETRY OF PION BEAMS

A Monte Carlo computer program has been completed for calculating absorbed dose as a function of depth in a water phantom exposed to a beam of negative or positive pions from typical accelerators. The

37. H. Davies, *Proc. Inst. Elec. Eng.* (*London*) 101, Part IV, 209 (1954).

38. J. G. Endriz and W. E. Spicer, *Phys. Rev.* (to be published).

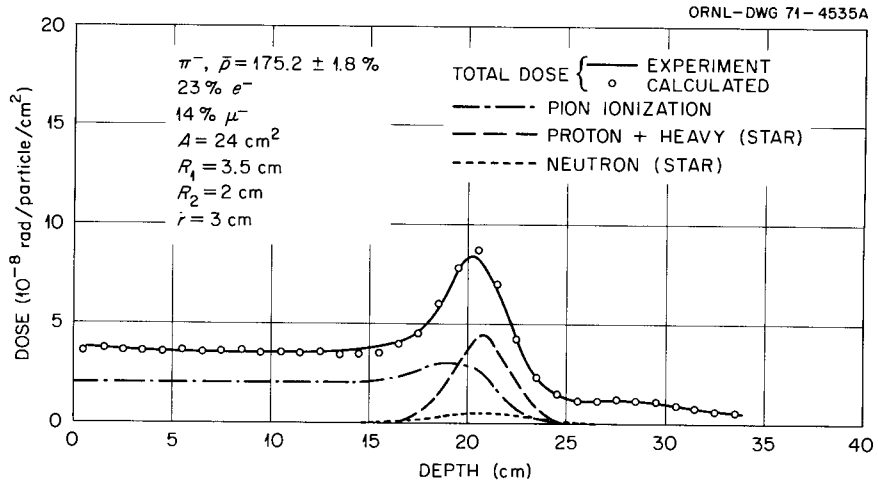

Fig. 6.8. Comparison of calculated and measured depth-dose distribution in water phantom irradiated by negative pion beam.

program takes into account all relevant physical processes, such as inelastic collisions, star production from pion absorption, elastic scattering from hydrogen, multiple Coulomb scattering from nuclei, etc. In addition, specific experimental details are included, such as beam cross section and uniformity, momentum spread of incident particles, detector dimensions, muon and electron contamination in the beam, etc. The calculations have been developed in conjunction with radiobiological experiments with pion beams at the European Organization for Nuclear Research (CERN) in Geneva, Switzerland.[39] A comparison of measured and calculated depth-dose curves for a negative pion beam, incident on a water target, is shown in Fig. 6.8. The solid curve is measured. The beam was approximately elliptic, having a semimajor axis R_1 = 3.5 cm, a semiminor axis R = 2 cm, and an area of 24 cm^2. A cylindrical detector of radius r = 3 cm was used in the measurements and calculations. The calculations (shown by circles) were made by assuming a mean particle momentum of $\bar{p}$ = 175.2 MeV/c, a Gaussian momentum distribution of width 1.8% (i.e., half of the particles have momentum within $\bar{p} \pm 0.018\bar{p}$), and a beam composition of 63% pions, 23% electrons, and 14% muons. The calculated contributions to the total dose from various physical processes are also shown. Systematic studies of the influence of a number of parameters (e.g., beam size and uniformity) on depth-dose distributions are now being made. Continued collaboration with future radiobiological work at CERN will be maintained. An exchange of one staff member from each laboratory, ORNL and CERN, for one year will take place, beginning in August 1971. Future calculations will also be directed toward a study of properties of negative pion beams for cancer radiotherapy.

39. J. E. Turner, H. A. Wright, R. N. Hamm, J. Baarli, J. Dutrannois, and A. H. Sullivan, "Studies in Pion-Beam Dosimetry," in *Proceedings of International Congress on Protection against Accelerator and Space Radiation* (CERN, Geneva, April 26–30, 1971), to be published.

7. Interaction of Radiation with Liquids and Solids

E. T. Arakawa
R. D. Birkhoff
A. J. Braundmeier[1] W. F. Hanson[3]
Barbara G. Brooks[1] J. A. Harter
T. A. Calcott[2] R. A. MacRae[2]
L. C. Emerson Linda R. Painter[2]
T. F. Gesell[1] B. L. Sowers[4]
R. N. Hamm U. S. Whang[2]
Mary W. Williams[2]

OPTICAL PROPERTIES OF RUBIDIUM ABOVE THE PLASMA ENERGY

Recent studies[5–7] of the optical properties of the alkali metals above their plasma energies have been extended to rubidium. Reflectance measurements were analyzed in the same way as for cesium.[7] Transmission measurements were also made in the region 7.7 to 10.6 eV, where the optical absorption is small. Figure 7.1 shows a plot of the real part of the dielectric constant, ϵ_1, as a function of the square of the wavelength λ. The linear relationship predicted by the nearly free-electron model[5] is not obtained, implying the existence of processes such as interband transitions. Assuming the effects on ϵ_1 due to the different processes are additive, we may write

$$\epsilon_1 = 1 + 4\pi\eta_0\alpha_0 - \frac{\eta_0 e^2}{\pi c^2 m_{\text{opt}}}\lambda^2 + \delta\epsilon_1 ,$$

where η_0 is the number of atoms per unit volume, α_0 is the core polarizability, m_{opt} is the average optical effective mass of a conduction band electron, and $\delta\epsilon_1$ is the contribution to ϵ_1 due to processes not included in the nearly free-electron model. Figure 7.2 shows the calculated optical conductivity $\sigma = \epsilon_2 E/(2h)$, where ϵ_2 is the imaginary part of the dielectric constant, plotted as a function of the photon energy E from 3.3 to 10.6 eV. Also plotted are data from the literature.[8–10] Structure is seen in the conductivity centered at 6.8 eV; weaker structure is seen in the vicinity of 3.4 and 10 eV. Structure in σ representing deviations from free-electron-like behavior is responsible for the $\delta\epsilon_1$ contribution to the data in Fig. 7.1. The quantity $\delta\epsilon_1$ was estimated over the whole energy range by means of a Kramers-Kronig analysis. When $\delta\epsilon_1$ was subtracted from the data of Fig. 7.1 a straight line was obtained for ϵ_1 vs λ^2, yielding a volume plasmon energy of (3.40 ± 0.03) eV, an optical effective mass of (1.05 ± 0.02)m_e, and an ion core polarization $4\pi\eta_0\alpha_0$ of (0.26 ± 0.02).

Structure in σ below the plasmon energy has been interpreted previously. Above the plasmon energy the most prominent structure is the peak at 6.8 eV. A possible explanation is in terms of transitions of conduction band electrons from the vicinity of the Fermi level to "*f*-like" levels about 7 eV above the Fermi level.[9] Alternatively, the absorption may be associated in some way with collective oscillations of

1. USAEC Health Physics Fellow.
2. Consultant.
3. Radiological Health Physics Fellow.
4. Oak Ridge Graduate Fellow.
5. J. C. Sutherland and E. T. Arakawa, *J. Opt. Soc. Amer.* **58**, 1080 (1968).
6. J. C. Sutherland, R. N. Hamm, and E. T. Arakawa, *J. Opt. Soc. Amer.* **59**, 1581 (1969).
7. U. S. Whang and E. T. Arakawa, *Phys. Rev. Lett.* **25**, 646 (1970).
8. N. V. Smith, *Phys. Rev.* **2**, 2840 (1970).
9. H. E. Ives and H. B. Briggs, *J. Opt. Soc. Amer.* **27**, 395 (1937).
10. St. von Aufschnaiter (unpublished).

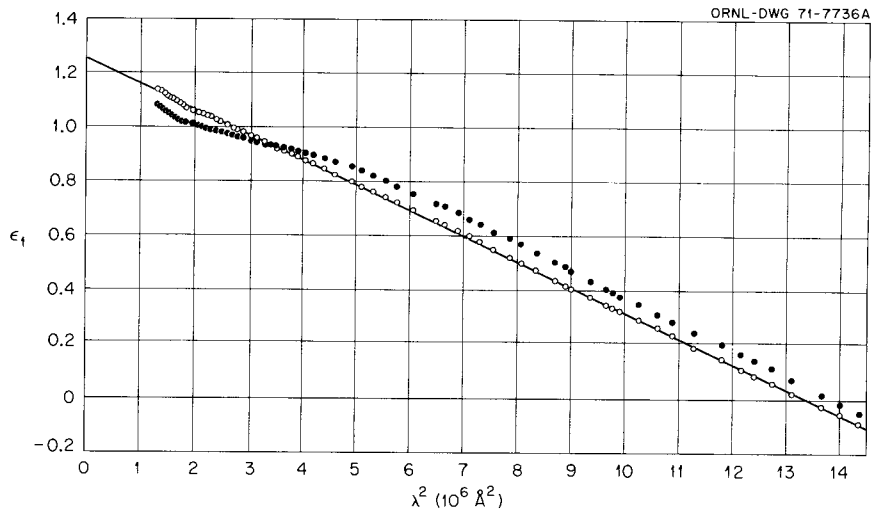

Fig. 7.1. Real part of the dielectric constant of rubidium, ϵ_1, vs λ^2.

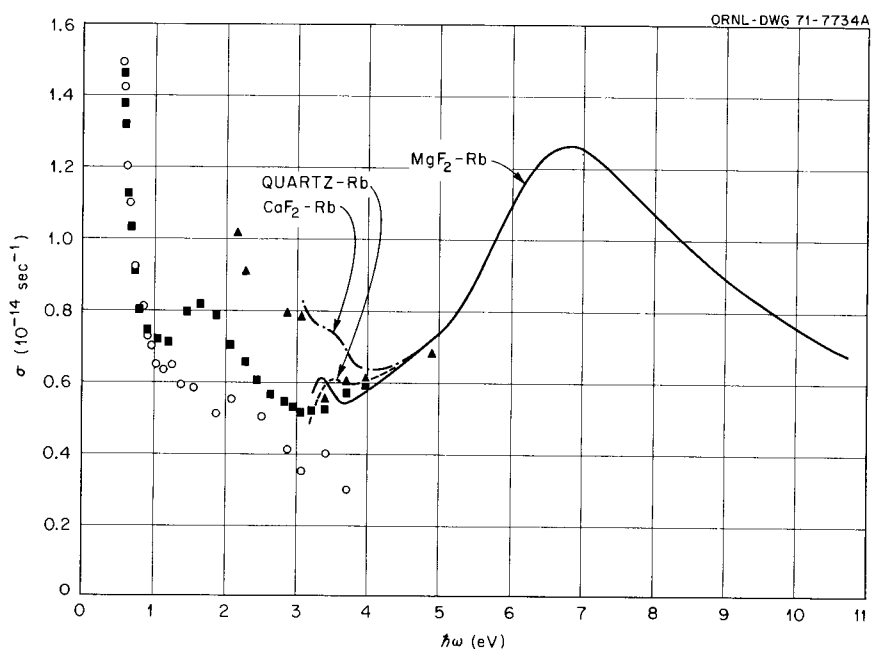

Fig. 7.2. Optical conductivity of rubidium vs photon energy.

the conduction band electrons. However, the predictions of the theory for plasmon-assisted interband transitions[7] do not agree with the observed absorption as well in rubidium as in cesium. With the volume plasmon at 3.4 eV and an interband transition at 1.6 eV, the absorption for plasmon-assisted interband transitions would be expected at 5.0 eV.

OPTICAL PROPERTIES OF URANIUM MONONITRIDE

Uranium mononitride (UN) is an important nuclear reactor fuel candidate which has been studied[11] exten-

11. J. P. Moore, W. Fulkerson, and D. L. McElroy, *J. Amer. Ceram. Soc.* **53**, 76 (1970).

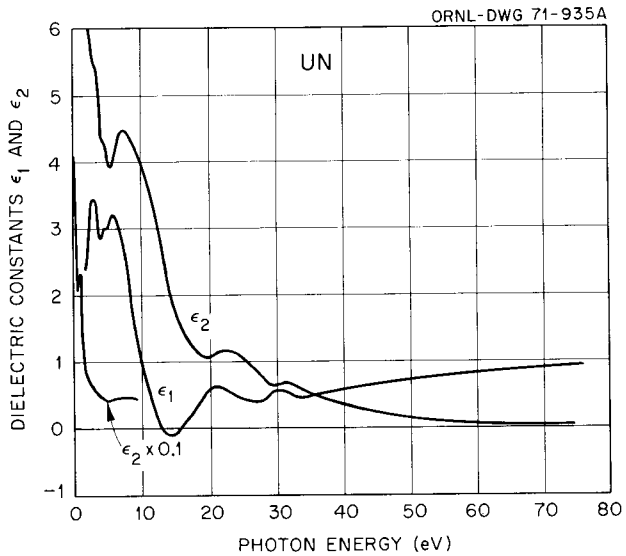

Fig. 7.3. Dielectric constants of polycrystalline UN vs incident photon energy.

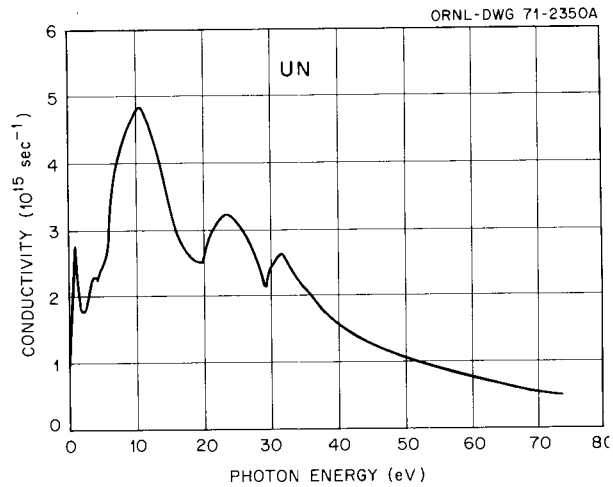

Fig. 7.4. Optical conductivity of polycrystalline UN vs incident photon energy.

sively by the Metals and Ceramics Division of ORNL. The optical properties of a polished arc-melted 100% dense polycrystalline specimen have been obtained from 0 to 74 eV by measuring reflectance as a function of the angle of incidence. The values of ϵ_1 and ϵ_2, the real and imaginary parts of the complex dielectric constant ϵ, obtained from this analysis are shown in Fig. 7.3.

Optical absorptions caused by single electron transitions are identified by relative peaks in the optical conductivity. Thus, the conductivity $\sigma = E\epsilon_2/(2h)$ plotted in Fig. 7.4 indicates strong interband (or single electron) transitions at 10.5, 24.0, and 32.0 eV. Weaker absorption occurs between 0 and 10 eV. In UN the conduction electrons are *f-d* in character and are predominantly localized on the uranium sites with perhaps 2% overlap to the nitrogen sites.[12] The calculated band structure[12] shows a high density of states in the vicinity of the Fermi level. This agrees with the high ϵ_2 values which we obtain at low energies. Furthermore, the band structure for the ΓK direction in k space indicates that single electron transitions should occur from 0 to 1 eV with the onset of strong transitions at 1 eV. This is confirmed by the sharp structure in the conductivity seen at 1 eV (Fig. 7.4). The lack of resolution in our data and uncertainties in band structure calculations make it impossible for us to identify structure in the conductivity between 1 and 10 eV. There is, however, a possible 10.5-eV transition in the ΓK direction corresponding to the peak in the conductivity at this energy.

The peaks in the conductivity at 24.0 and 32.0 eV are thought to be due to excitations of the 6*p* electrons to the vicinity of the Fermi level. X-ray emission data[13] for uranium give strong emission lines for $P_{III} \rightarrow N_I$ and $P_{II} \rightarrow N_I$ transitions that are separated by 7.4 eV. Composite atomic energy levels[14] from x-ray data place the P_{II} and P_{III} levels (42.3 ± 9.0) and (32.3 ± 9.0) eV, respectively, below the Fermi level for uranium with the $P_{II} \rightarrow P_{III}$ separation equal to (10 ± 1) eV (average of values in different tables). It is thought that the present data placing the P_{III} level 24 eV and the P_{II} level 32 eV below the Fermi level give support to the energy difference of 7.4 eV given by the x-ray emission data of Kunzl.[13]

STUDY OF THE OPTICAL PROPERTIES OF SOLIDS BY ELLIPSOMETRY

The optical properties of vacuum-evaporated films of indium and tin have been studied using an ellipsometric technique in the spectral region between 3000 and 8000 Å. The films were prepared on the surface of a strain-free quartz prism at vacuums in the 10^{-9}-torr region. The measurements were then made at the quartz-metal interface, which remained free of any oxide contaminant even after exposure to the atmosphere.

12. H. L. Davis, *Proceedings of the Fourth International Conference on Plutonium and Other Actinides,* Santa Fe, New Mexico, Oct. 5–9, 1970.

13. V. Kunzl, *Cas. Pest. Mat. Fys.* **65**, 179 (1936).

14. J. A. Bearden and A. F. Burr, *Rev. Mod. Phys.* **39**, 125 (1967).

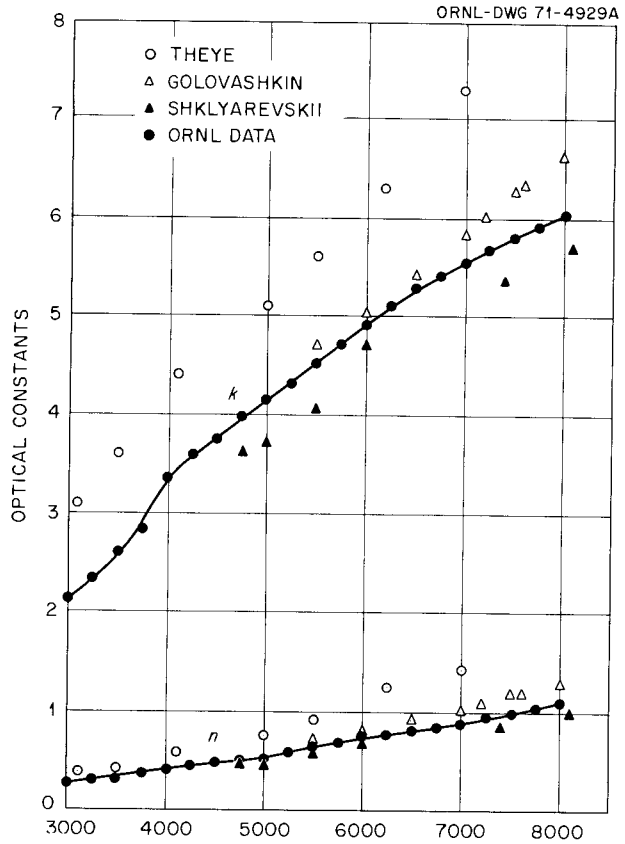

Fig. 7.5. The real and imaginary parts of the complex index of refraction for vacuum-evaporated indium.

The indium data shown in Fig. 7.5 agree reasonably well with the work of Golovashkin and co-workers[15] and of Shklyarevskii and Yarovaya,[16] both of whom obtained their data using opaque films deposited on glass substrates which had been coated with a thin layer of lead. In each case the vacuum was reported to be in the 10^{-5}-torr region. However, the films prepared by Shklyarevskii and Yarovaya were annealed, and the values of n and k were not corrected for the effects of the growth of an oxide film. This possibly accounts for their somewhat lower values of k. The optical constants reported by Theye and Devant[17] are approximately 40% higher than those found in the present study. Their data were obtained on thin semitransparent films using measurements based on both transmittance and reflectance. Again, the influence of an oxide layer was neglected. The data of Lenham and Treherne[18] are also significantly higher than those found here, particularly in the case of n. These authors report data for both hand-polished and electropolished single crystals. At 3000 Å, which represents the long wavelength limit of an earlier ORNL study[19] and the short wavelength limit of the present study, the agreement in the values of n is excellent. However, in the case of k the agreement is poor. The vacuums in the earlier study were in the 10^{-6}-torr range, and some amount of oxide was undoubtedly present, although neither the thickness of the deposit nor its effect on the reflectance is known.

Very few data exist on the optical properties of tin in the spectral region covered in this study, and most of these date from the late 1800's or early 1900's. Thus, the quality of the surfaces in these studies is very much open to question. In any event the agreement with present results is poor in most cases. The n and k values reported by Erokin[20] in 1912 and those reported in an earlier ORNL study[21] are shown in Fig. 7.6, along with the data obtained in the present study. Erokin's data were taken using a molten tin surface and reflect the frequent large changes in k which accompany temperature changes. The tin surfaces studied in the earlier ORNL work were prepared by the same techniques as those used here except that the vacuums were of the order of 10^{-6} torr, whereas the tin surfaces in the present study were prepared at 10^{-9} torr. Nevertheless, in the earlier work the condition of the surface was monitored by comparing the reflectance of the free tin surface with that at the quartz substrate interface. A high-quality surface was reported, so we would expect good agreement with the present data. In the case of k the agreement appears to be quite good, as is that for n below 4000 Å. Above this wavelength the present study gives values which are significantly higher.

As pointed out in the earlier study several workers have indicated the presence of a well-defined interband transition at 1.2 eV. This energy is just below the low-energy cutoff in the present study at 1.5 eV. However, in this same study the possibility of a weak interband transition at about 3 eV was indicated. A plot of the dielectric constants ϵ_1 and ϵ_2 supports this

15. A. L. Golovashkin, I. S. Levchenko, G. P. Motslevich, and A. A. Shubin, *JETP* **24**, 1093 (1967).

16. I. N. Shklyarevskii and R. G. Yarovaya, *Opt. Spectrosc.* 16, 45 (1964).

17. M. L. Theye and G. Devant, *Thin Solid Films* **4**, 205 (1969).

18. A. P. Lenham and D. M. Treherne, *Proc. Phys. Soc.* **85**, 167 (1965).

19. R. H. Huebner, E. T. Arakawa, R. N. Hamm, and R. A. MacRae, ORNL-TM-1104 (1965).

20. P. Erokin, *Ann. Physik* 39, 213 (1912).

21. R. A. MacRae, E. T. Arakawa, and M. W. Williams, *Phys. Rev.* **162**, 615 (1967).

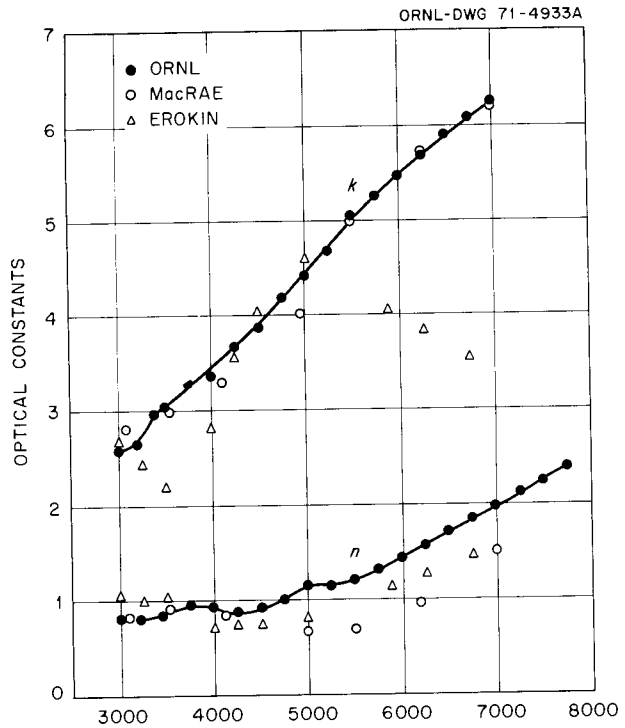

Fig. 7.6. The real and imaginary parts of the complex index of refraction of tin.

conclusion, with some evidence for a weak transition at 3.1 eV.

HIGH-ENERGY X-RAY SATELLITES OF THE L_{23} EMISSION BANDS OF Na, Mg, Al, AND Si

Shmidt[22] has recently postulated that the satellites found on the high-energy side of the L_{23} emission bands of Si and Al may arise from the simultaneous radiative decay of a core ionization state and a volume plasma resonance. An earlier interpretation of similar satellites in the K emission spectra was in terms of a double ionization state, that is, the simultaneous ejection of both a K and L electron.

As part of our program to study collective oscillations in solids a detailed investigation has been made of the high-energy satellites of the L_{23} emission bands of Na, Mg, Al, and Si. Na (Z = 11), Mg (12), and Al (13) are free-electron-like metals with strong plasma resonances, while Si (14) is a semiconductor with a strong plasma resonance.

Bulk samples of each metal were fastened to the target of an x-ray tube. With a pressure in the experimental chamber of $2 \rightarrow 4 \times 10^{-7}$ torr, the surfaces were abraded in situ to expose a clean surface of the metal. The electron energy was varied from 500 to 5000 eV, and the emission spectra recorded.

The spectra reproduced in Fig. 7.7 show the L_{23} emission band and its associated high-energy satellite for each of the metals. By matching characteristic points on the L_{23} emission band with the corresponding points on its satellite the energy difference $\Delta\mathcal{E}$ between each L_{23} band and its satellite has been determined for each metal, and is shown in Table 7.1.

It is seen for Al and Si that the values observed for $\Delta\mathcal{E}$ are approximately equal to the volume plasmon energy E_p, suggesting that for these metals the satellite may arise from the simultaneous decay of an L_{23} ionization and a volume plasmon. However, the $\Delta\mathcal{E}$ values obtained for Na and Mg do not agree with the plasma energies.

The experimental ratio of satellite to parent band emission intensities is shown in Fig. 7.8 as a function of incident electron energy for Mg. Also shown are theoretical curves (A, B, and C) for this ratio, on an arbitrary scale, assuming double ionization with different threshold energies for the satellite. The threshold energies are: (A) the high-energy edge of the L_{23} emission band $\mathcal{E}_1$, (B) $2\mathcal{E}_1 + \Delta\mathcal{E}$, and ($C$) $3\mathcal{E}_1$. In addition, the theoretical ratio on an arbitrary scale, calculated assuming the satellite involves a plasmon interaction,[22] is shown as D. The fit to the experimental data appears best for double ionization with a threshold energy of $2\mathcal{E}_1 + \Delta\mathcal{E}$.

In addition, studies of the shape of the satellite compared with the parent band, the atomic number dependence of the intensity ratio, and the atomic

Table 7.1. Energy difference between the L_{23} band and its satellite

Material	$\Delta\mathcal{E}$(eV) Present results	$\Delta\mathcal{E}$(eV) Previous authors	Plasma energy, E_p (eV)
Na	11.3 ± 0.5	11.9[a]	5.7
Mg	13.6 ± 0.2	13.85[b] 13.5[a]	10.4
Al	15.2 ± 0.3	15.5[c] 15.5[a]	15.0
Si	16.1 ± 0.3	23[a]	16.9

[a]H. W. B. Skinner, *Phil. Trans. Roy. Soc. London* **A239**, 95 (1940).

[b]T. Sagawa, *Sci. Rep. Tohoku Univ.*, First Ser. **45**, 232 (1961).

[c]H. Neddermeyer and G. Weich, *Phys. Lett.* **31A**, 17 (1970).

22. V. V. Shmidt, *Sov. Phys. JETP* **12**, 886 (1961).

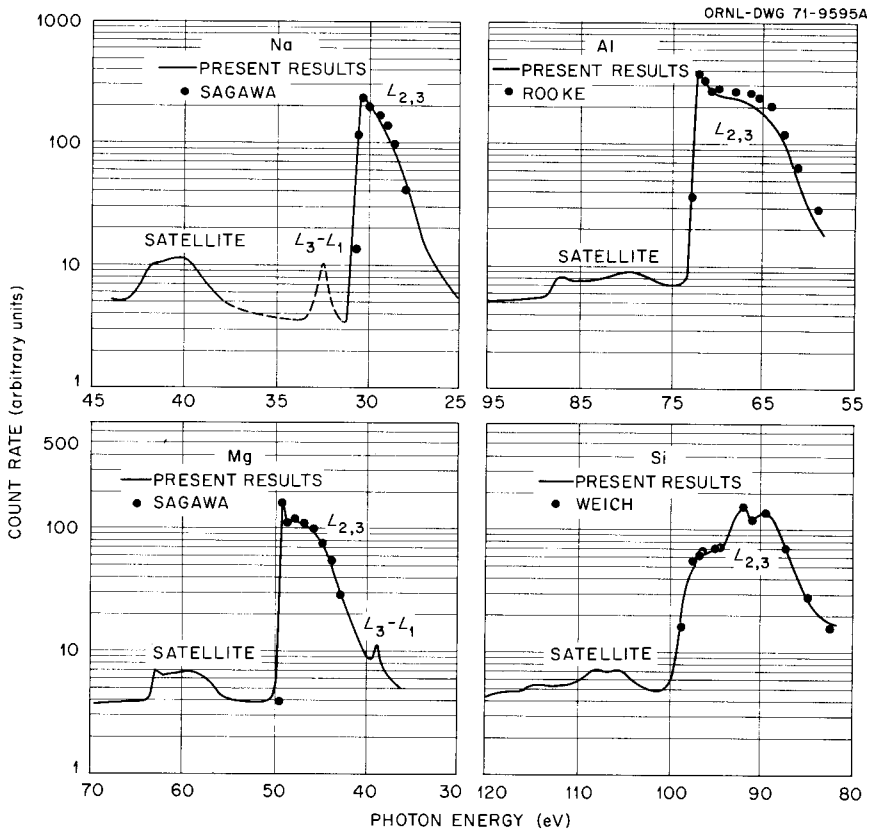

Fig. 7.7. Soft x-ray emission spectra of Na, Mg, Al, and Si in the neighborhood of the L_{23} emission band and its associated satellite.

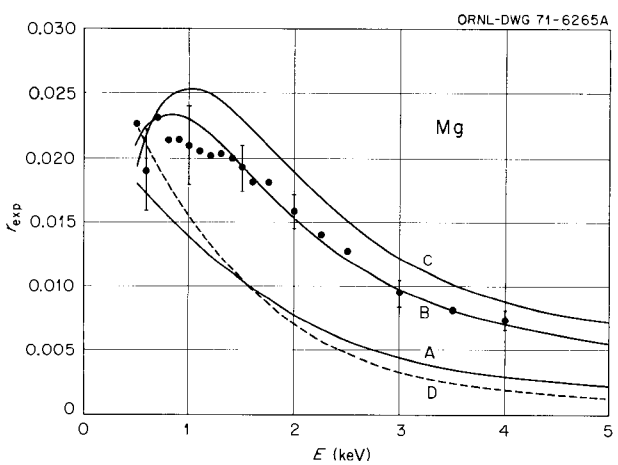

Fig. 7.8. Ratio of satellite emission to parent band emission vs the incident electron energy for Mg.

number dependence of the energy difference $\Delta\mathcal{E}$ were found to agree well with calculations for radiative decay of a doubly ionized atom in which two vacancies are in the L_{23} shell and to agree very poorly with calculations involving plasmon interactions.

SOFT X-RAY EMISSION SPECTRA OF MgO AND MgF_2

Investigations of the optical properties of MgO and MgF_2[23] have been continued. The MgO and MgF_2 crystals used previously were bombarded with 2.5-keV electrons and the emission spectra recorded. The $L_{2,3}$ emission spectra for MgO, MgF_2, and bulk Mg are shown in Fig. 7.9.

The structure (ref. 23, Fig. 9.3) seen in the real part, ϵ_2, of the dielectric constant of MgO between 52 and 60 eV has been identified as being associated with the $L_{2,3}$ level of Mg in MgO. The present emission band spectrum places the Mg $L_{2,3}$ level 46 eV below the top of the valence band. Since the band gap in MgO is 7.9 eV, this sets the $L_{2,3}$ absorption edge at 54 eV. The structure seen between 52 and 54 eV is then interpreted as due to an exciton interaction, while the structure between 54 and 60 eV is due to interband transitions from the $L_{2,3}$ Mg level to the conduction band. The

23. E. T. Arakawa et al., *Health Phys. Div. Annu. Progr. Rep. July 31, 1970,* ORNL-4584, pp. 76–77.

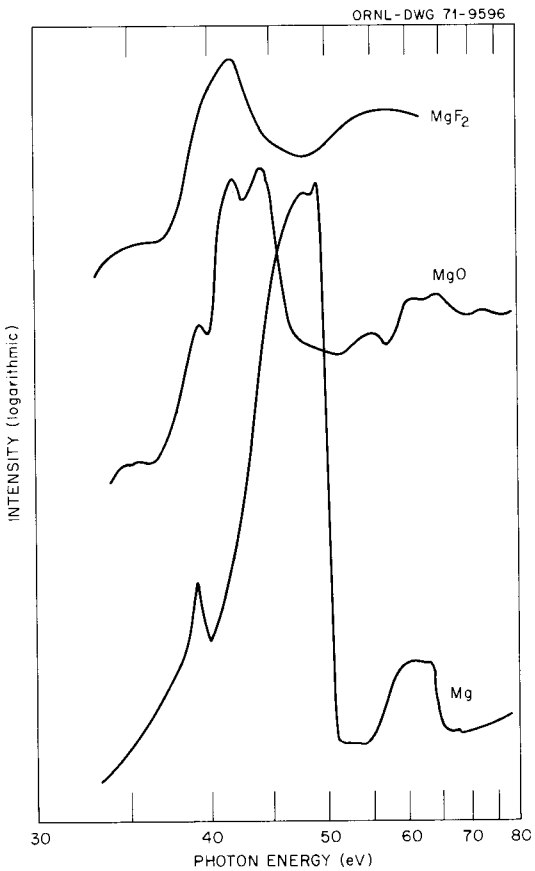

Fig. 7.9. $L_{2,3}$ emission spectra for MgO, MgF_2, and Mg.

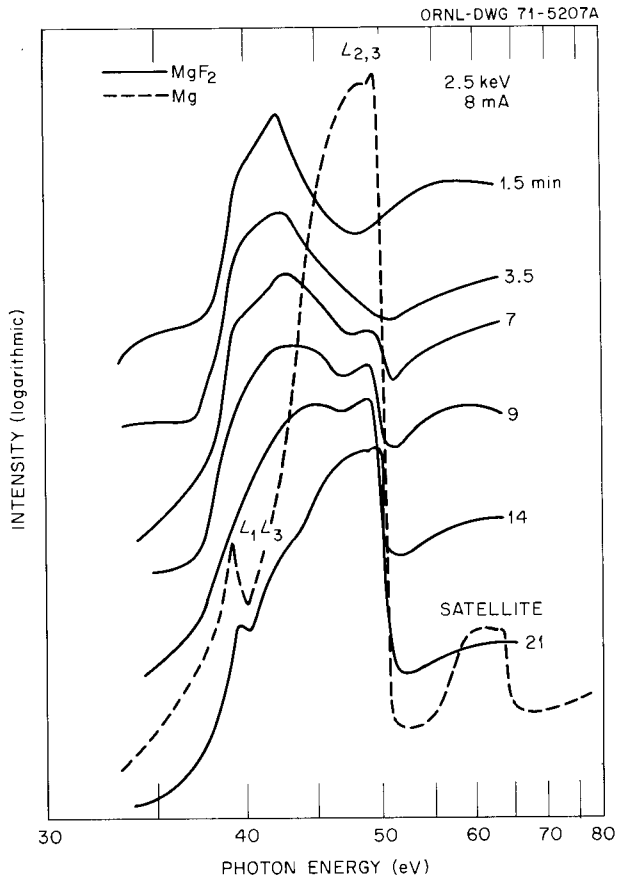

Fig. 7.10. $L_{2,3}$ emission spectrum of MgF_2 as a function of time compared with the $L_{2,3}$ emission spectrum of Mg.

high-energy edge of the $L_{2,3}$ emission band spectrum of Mg in MgF_2 is seen from Fig. 7.9 to be at 43 eV. Since the band gap in MgF_2 is 13 eV, the $L_{2,3}$ absorption edge should be at 56 eV. This confirms the previous identification[23] of the sharp peak in the absorption at 54.6 eV as being associated with an exciton.

Figure 7.10 shows the rapid change in the $L_{2,3}$ emission spectrum of MgF_2 with time. It is seen that within about 20 min of bombardment with 8 mA of 2.5-keV electrons the emission spectrum corresponds essentially to that of bulk Mg. Presumably the phenomenon of metallic coagulation is occurring in the MgF_2 crystal, or the electron bombardment is actually removing fluorine from the crystal leaving a predominantly Mg target. No change was seen in the MgO emission spectrum with time.

PHOTOELECTRON ATTENUATION LENGTHS IN ALUMINUM

Values of the attenuation lengths l of electrons in aluminum reported in the literature vary widely for low electron energies. We present here a new experimental approach to this important problem in which the electron attenuation length is extracted from the angular dependence of the quantum yield of photoelectrons.

Recently Pepper[24] calculated the quantum yield of an arbitrary photoemissive material as a function of the optical constants of the photoemitter and the substrate, the thickness of the photoemitter, the wavelength, the polarization and angle of incidence of the exciting light, and the attenuation length of the electrons. He suggested that measurements of the photoelectric yield as a function of angle might be used to determine the attenuation length of the photoelectrons. We have made these measurements and have determined the attenuation length of photoelectrons excited in aluminum by 21.2-eV photons.

24. S. V. Pepper, *J. Opt. Soc. Amer.* **60**, 805 (1970).

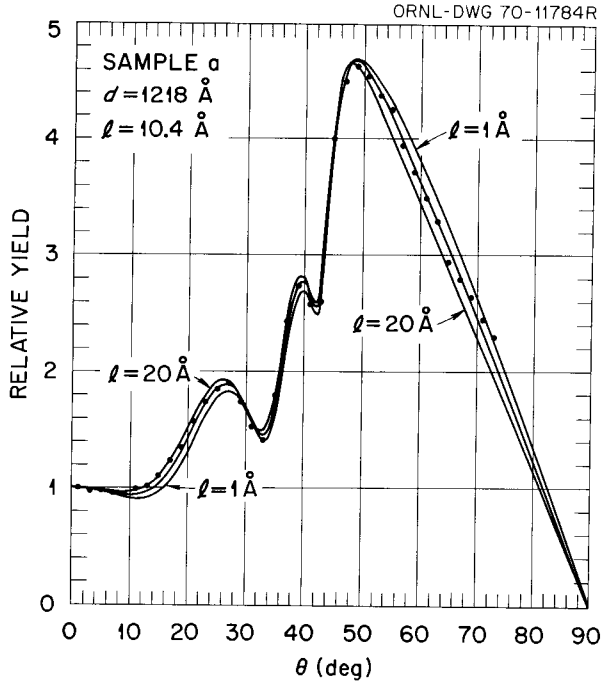

Fig. 7.11. Relative yield for a typical sample, together with the best least-squares fit, plus a calculated curve for l = 1 Å and l = 20 Å for comparison.

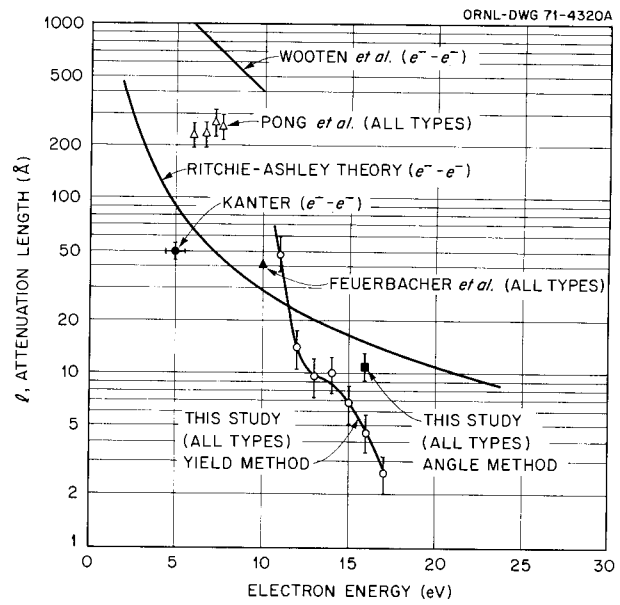

Fig. 7.12. Attenuation lengths for electrons in aluminum as a function of electron energy above the Fermi level obtained from the angle method and the absolute yield method plus the results of other investigators. The types of electron interactions are indicated.

Figure 7.11 shows typical data for the relative yield of one of the samples together with the best fit and calculated results for attenuation lengths of 1 and 20 Å. Results of measurements on five films gave an attenuation length for photoelectrons excited in aluminum by 21.2-eV photons in the range $4 \leqslant l \leqslant 12.8$ Å.

The theoretical calculations of Quinn and of Ritchie et al.[25] as well as the experiments of Kanter,[26] who directly measured the attenuation of an electron beam, indicate that the attenuation length for electrons in aluminum is less than 50 Å for electron energies greater than ~5 eV above the Fermi level. On the other hand, the experiments and analysis of Stuart and Wooten[27] indicate that electrons which are about 9 eV above the Fermi level have a mean free path for electron-electron scattering of ~510 Å and a mean free path for phonon scattering of 130 Å. In support of Stuart and Wooten is the recent work of Pong,[28] who finds an attenuation length of ~230 Å for photoelectrons excited by 7.5- to 11-eV photons. Pong shows that his attenuation length, which includes all types of scattering, is equivalent to the separate e^--e^- and e^--phonon mean free paths of Stuart and Wooten.

Figure 7.12 shows the experimental results for the attenuation length of electrons in aluminum found by others, our results on aluminum using both the absolute yield and the dependence of yield on angle, and the theory for electron-electron scattering of Ritchie and Ashley. The single point obtained from the angle method is plotted at 16 eV, which is the average energy of electrons excited in aluminum by 21.2-eV photons assuming indirect transitions to energy-independent final states. Our photoelectric results give reasonable values of the attenuation length when excitation is made by photons with energy greater than ~12 eV but can be seen to diverge sharply from the theory toward lower energies. It is suggested that data below ~12 eV are complicated by surface plasmon excitation which has not been allowed for in comparing the experimental results with the theory.

25. R. H. Ritchie, F. W. Garber, M. Y. Nakai, and R. D. Birkhoff, in *Advances in Radiation Biology*, ed. by L. G. Augenstein, R. Mason, and M. Zelle (Academic, New York, 1969), vol. 3; R. H. Ritchie and J. C. Ashley, *J. Phys. Chem. Solids* **26**, 1689 (1965).

26. H. Kanter, *Phys. Rev.* **B1**, 522 (1970).

27. R. N. Stuart and F. Wooten, *Phys. Rev.* **156**, 364 (1967).

28. W. Pong, R. Sumida, and G. Moore, *J. Appl. Phys.* **41**, 1869 (1970).

The most important result of this study is the addition of decisive independent experimental evidence for the existence of very short electron attenuation lengths in aluminum.

PHOTOELECTRIC MANIFESTATION OF THE OPTICAL PLASMON RESONANCE IN MAGNESIUM

The dispersion relation for radiative surface plasmons has been studied previously. Feuerbacher and Fitton,[29] investigating the effect by means of measurements of the photoelectric yield as a function of angle of incidence, found an anomalous dispersion for magnesium films ~80 Å thick, whereas Braundmeier et al.,[30] studying the radiative decay of electron-induced resonances in magnesium films ~200 Å thick, found a dispersion as predicted by theory.

The photoelectric yield experiment performed by Feuerbacher and Fitton has been repeated in this laboratory using thicker magnesium films. The results are shown in Fig. 7.13 together with the results of Braundmeier et al. and Feuerbacher and Fitton. The present measurement extrapolates to a value of 10.46 eV for the plasmon energy, which is consistent with the results of Braundmeier (10.43 eV) and somewhat higher than the result of Feuerbacher and Fitton (10.21 eV). The dispersion or slope of the present work is of the correct sign and is consistent with a film thickness of 200 Å if the point at 40° is disregarded. The quartz crystal thickness monitor gave ~200 Å for the thickness of the film, as did a subsequent interferometric measurement.

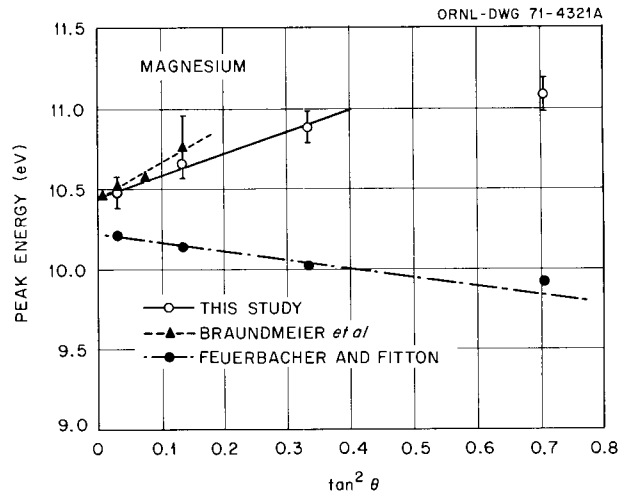

Fig. 7.13. Energy of the peak in the angular dependence of the photoelectric yield as a function of $\tan^2 \theta$ together with the results of other investigators.

29. B. Feuerbacher and B. Fitton, *Phys. Rev. Lett.* **24**, 499 (1970).

30. A. J. Braundmeier, E. T. Arakawa, and M. W. Williams, *Phys. Lett.* **32A**, 241 (1970).

8. Physics of Tissue Damage

E. T. Arakawa
R. D. Birkhoff

L. C. Emerson
R. N. Hamm
L. R. Painter[1]
H. C. Schweinler
B. L. Sowers[2]
M. R. Williams[1]

ELECTRON-SLOWING-DOWN STUDIES[3]

Last year we obtained the electron-slowing-down flux in germanium which decays by *K* capture with 8.2-keV *KLL* and 0.9-keV *LMM* Auger electrons emitted. A preliminary comparison was made at that time with the similar flux from chromium which decays with a 4.3-keV *KLL* Auger electron and a 0.4-keV *LMM* Auger electron. The point of interest here is whether the flux in a semiconductor such as germanium is substantially different from that in a metal, chromium; that is, whether the band gap in the semiconductor influences the electron flux in the irradiated material. This year we made a more quantitative comparison of the fluxes aided by theory, and the results are indicated in Fig. 8.1. Plotted here is the ratio of the absolute flux in germanium to that in chromium, and it is seen that the ratio ranges from about 2 at 4 keV to about 4 at 10 eV. When these fluxes are corrected for the respective densities in the media and the respective stopping powers, assuming that the ratio of these is constant at the value listed in NAS-NRC 1133 for 10-keV electrons, then we get the middle curve with the multiplier of 0.542, this number being the constant multiplier containing the densities and stopping powers. A still more exact comparison may be made if one takes into account the variation of the stopping power in each of the media with energy. We have calculated this stopping power from the Lenz-Jensen statistical model of the atom and used this stopping power for each medium instead of the value mentioned above. When this energy-dependent stopping power is used to correct each set of data, the lower curve results, showing that the fluxes are about the same at 4 keV and differ by about a factor of 1.6 at the lowest energy of 10 eV. Thus we would say that there is very little difference in the fluxes in these two media. Also it would seem that one might, with some confidence, utilize electron fluxes measured in low-*Z* metallic media for calculations in irradiated biological media.

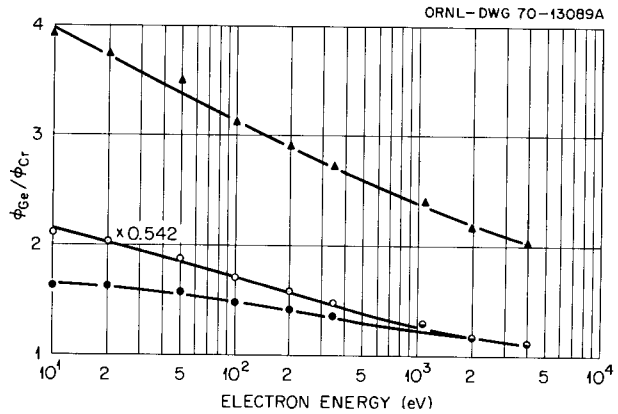

Fig. 8.1. Ratio of electron fluxes in Auger electron irradiated germanium and chromium.

In continuation of our program to measure electron fluxes from monoenergetic sources in order to derive some analytical representations of these, we have measured the electron flux from ^{169}Yb absorbed in ytterbium. Actually, the ytterbium emission spectrum is rather complex, as it has an initial Auger cascade following electron capture decay and a second Auger cascade following internal conversion in the daughter

1. Consultant.
2. Oak Ridge Graduate Fellow.
3. The research reported in this section of the Annual Report was sponsored in part by the Air Force Cambridge Research Laboratories, Office of Aerospace Research, under Contract Y70-837, but the report does not necessarily reflect endorsement by the sponsor.

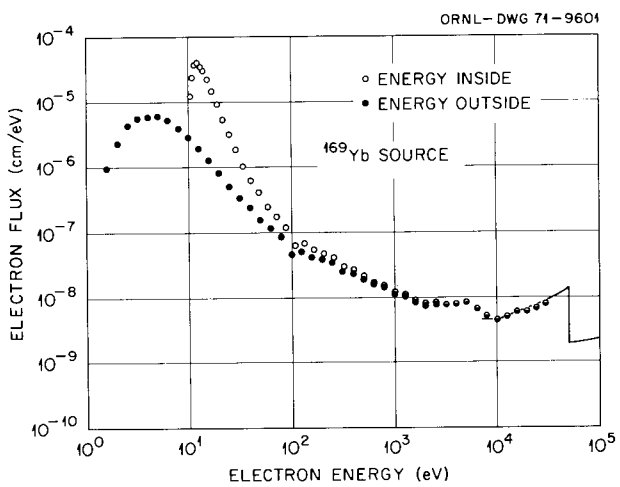

Fig. 8.2. Electron-slowing-down spectra in Auger electron irradiated ytterbium. Fluxes inside and outside the metal are shown at corresponding energies. Solid line, Spencer-Fano theory (arbitrary ordinate scales).

atom. Above 41 keV there are many internal conversion electrons following the formation of the daughter ^{169}Tm in an excited state, but fortunately these are rather low in intensity, contributing only 4% of the total electron yield. At 41 keV the *KLL* Auger electrons contribute 6% of the total, at 6 keV the *LMM* Augers contribute 13%, at 1.5 keV the *MNN* Augers contribute 25%, and at 1.4 keV the *NOO* Auger electrons contribute 52%. Thus we are able to neglect the contribution of the internal conversion component, and we feel that the spectrum above 1.5 keV will be essentially that due to the *KLL* and *LMM* Augers. Spectra are shown in Fig. 8.2. Here we have plotted the electron spectrum emitted from the surface of the ytterbium source (closed circles), and in this case the energy scale represents the energy with reference to the vacuum level. Also plotted is the flux as calculated from our data but on the inside of the metal before passage through the potential barrier at the surface, and here the energy refers to the energy above the bottom of the conduction band. The solid line represents the theory of Spencer and Fano as taken from NBS Circular 597 but adjusted in ordinate to fit the experimental data. It can be seen that the relative agreement is very good between theory and experiment in the relatively high-energy region where the theory can be obtained from this table. The absolute agreement, however, is not nearly so good, and reasons for this discrepancy are under investigation.

This year we also investigated the electron-slowing-down spectrum in silicon. When irradiated in a reactor, silicon produces a 1.48-MeV beta ray with an unfortunately short half-life of 2.6 hr. Nonetheless, we were able to make a source of this isotope and measure the electron-slowing-down spectrum. This is illustrated in Fig. 8.3. It is interesting that the slowing-down spectrum exhibits evidence of some structure near the *KLL* and *L*-shell energies at 1.8 keV and 100 eV, respectively. These results must be considered as tentative, pending additional measurements on a finer energy mesh in the vicinity of these energies. These preliminary results do indicate a possible breakdown in a continuous slowing-down approximation. Such a breakdown, neglected in the theories of Spencer, Fano, and Attic, may be caused by depletion of electrons above and near a shell energy by virtue of their making violent collisions in ionizing the shell. Each electron may lose so much energy in one collision that it drops below the shell energy, failing to populate the flux in this region. Below the shell energy Auger electrons appear, thus accentuating the discontinuity at the shell energy. More careful exploration of these discontinuities will have to await the production of much more radioactive sources such as we will obtain from the High Flux Isotope Reactor. Also, a Monte Carlo calculation of the electron flux spectrum in this important material is under way (see elsewhere in this report), and comparison will be made shortly between the theory and experiment.

OPTICAL PROPERTIES OF ORGANIC LIQUIDS

The study of the optical properties of liquids in the vacuum ultraviolet has continued[4] in order to investigate further the electronic properties of materials in the liquid state. In the past, the optical properties n and k have been determined by reflectance measurements as a function of the angle of incidence using a closed cell with a semicylinder window. Recently a transmission cell has been built which enables samples as thin as 500 Å to be obtained. Using this cell the optical absorption can be determined directly from transmission data over the whole energy range of interest, 4.0 to 10.65 eV.

It is known that the closed-cell method of measuring reflectance involves a loss of accuracy in the determination of n and k when n_{rel}, the relative index of refraction of the liquid with respect to the semicylinder, becomes greater than unity and k is small compared with n. Using the liquid transmission cell with MgF_2 windows, 800-Å samples were consistently obtained giving reliable values for k from the absorption

4. E. T. Arakawa et al., *Health Phys. Div. Annu. Progr. Rep. July 31, 1970*, ORNL-4584, pp. 76–77.

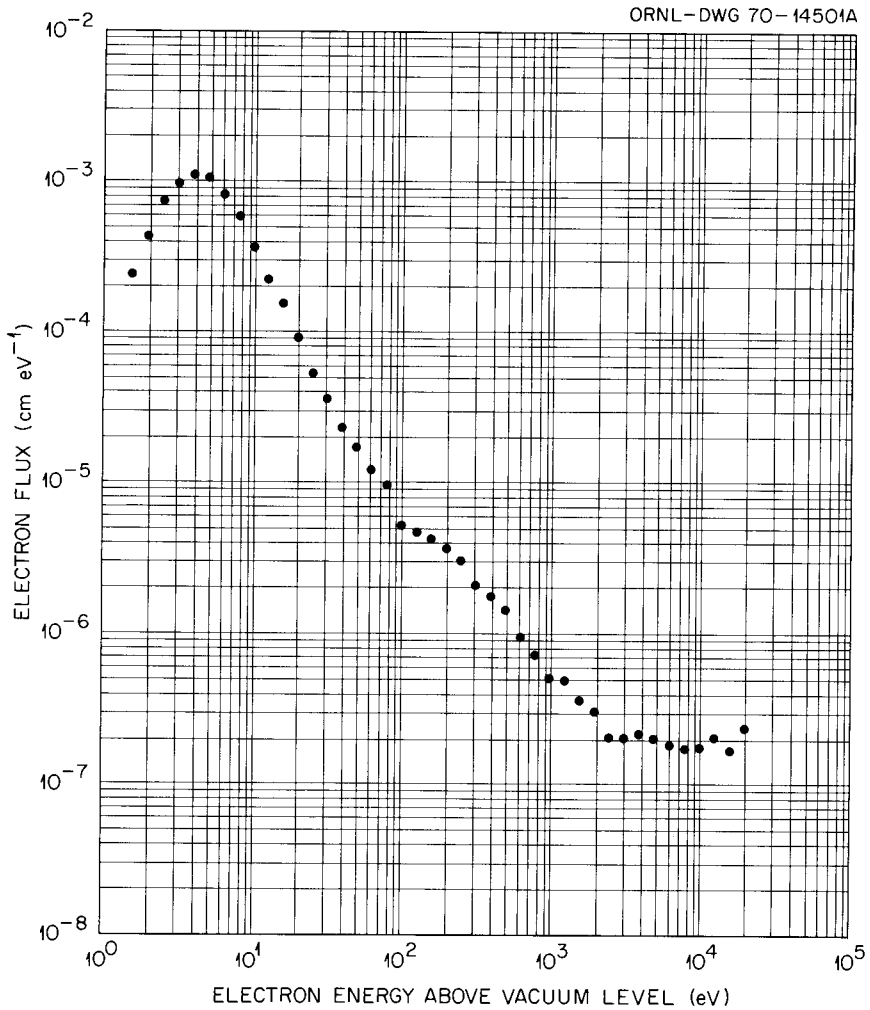

Fig. 8.3. Slowing-down spectrum of electrons in silicon.

edge of the liquid up to the MgF_2 cutoff, 10.65 eV. In some cases samples only 500 Å thick were used, these being a factor of 6 thinner than any liquid samples reported previously and sufficiently thin that absorption measurements can be made for any k in this spectral region. The value of the sample thickness x is not known exactly, so only the quantity $(4\pi k/\lambda)x$ is determined from the transmission data using the Beer-Lambert law,

$$I = I_0 \exp - \left(\frac{4\pi k}{\lambda} x\right) .$$

By using values of k from reflectance data in spectral regions where they are reliable, we compute a set of values of x. These, when averaged, provide a good estimate of the thickness, and k may then be calculated for other wavelengths where reflectance data is less certain.

The optical constants have been reported and discussed previously for several organic liquids.[4,5] Transmission measurements have been made on these materials, and the optical absorption k of a representative group is shown on a semilog plot for these materials in Figs. 8.4–8.7. New peaks are noted for carbon tetrachloride and cyclohexane at around 7 and 6.6 eV, respectively. Structure is seen in k for benzene at 5 eV, and the strange "window" reported previously from reflectance data seems to have disappeared. Thus it is seen that much more reliable absorption values can now

5. E. T. Arakawa et al., *Health Phys. Div. Annu. Progr. Rep. July 31, 1969,* ORNL-4446, pp. 180–82.

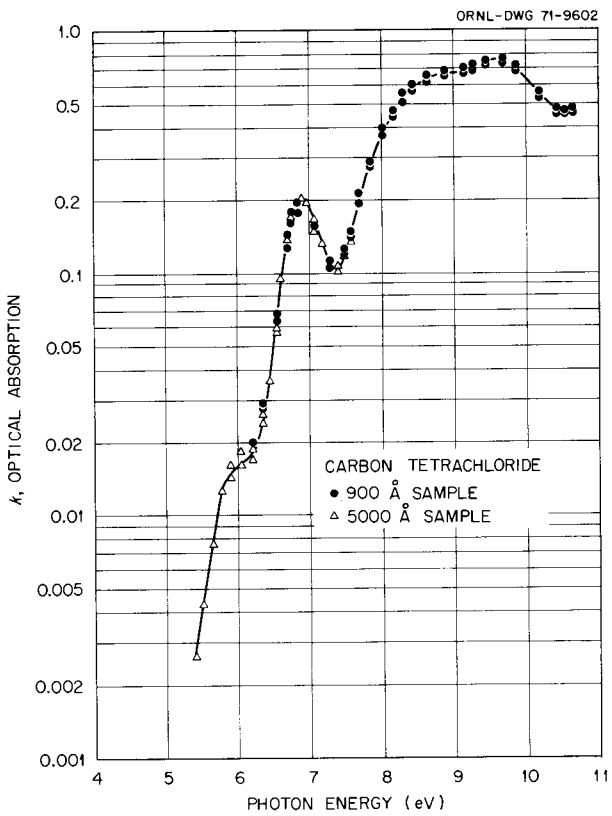

Fig. 8.4. Optical absorption k of carbon tetrachloride as a function of photon energy.

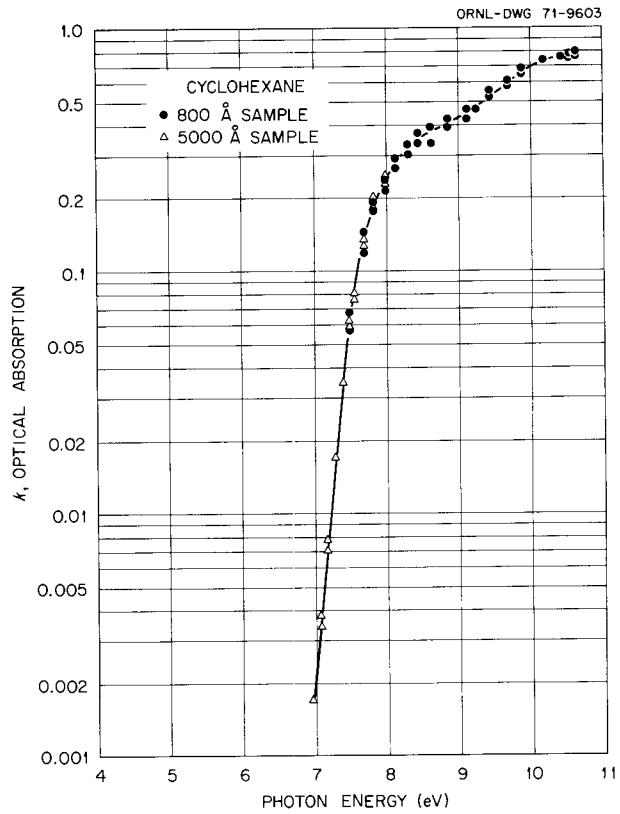

Fig. 8.5. Optical absorption k of cyclohexane as a function of photon energy.

be obtained near the leading edge of structure in k, where n rises sharply and the reflectance method becomes insensitive. Water has also been remeasured using this method; the results are shown in Fig. 8.7 compared with the work of other investigators.[6–8] The present work indicates that the maximum in k that was previously thought to be at 9.5 eV is probably at a somewhat higher energy.

With the use of these two complementary methods, reflectance and transmission, much more accurate values of the optical properties of liquids can now be determined. This increased accuracy should provide a more quantitative basis for explaining the electronic behavior of liquids.

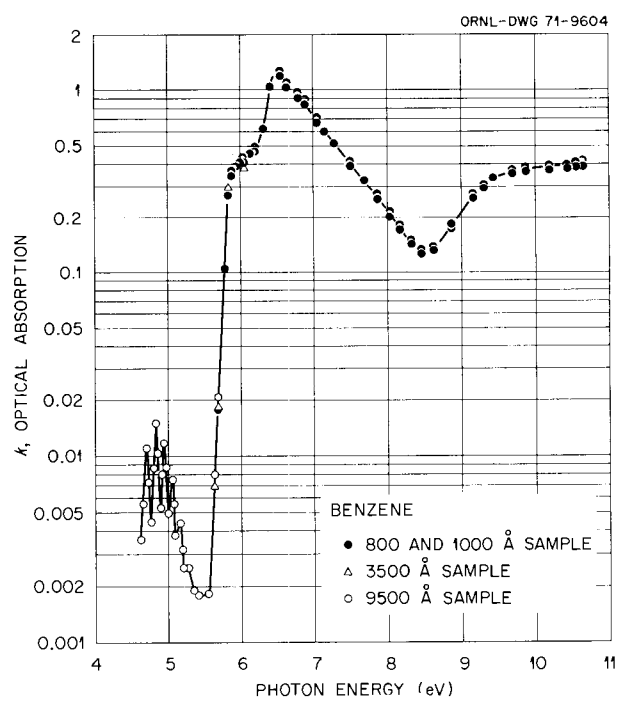

Fig. 8.6. Optical absorption k of benzene as a function of photon energy.

6. L. R. Painter, R. D. Birkhoff, and E. T. Arakawa, *J. Chem. Phys.* **51**, 243 (1969).
7. R. E. Verrall and W. A. Senior, *J. Chem. Phys.* **50**, 2746 (1969).
8. R. Onaka and T. Takahashi, *J. Phys. Soc. Jap.* **24**, 548 (1968).

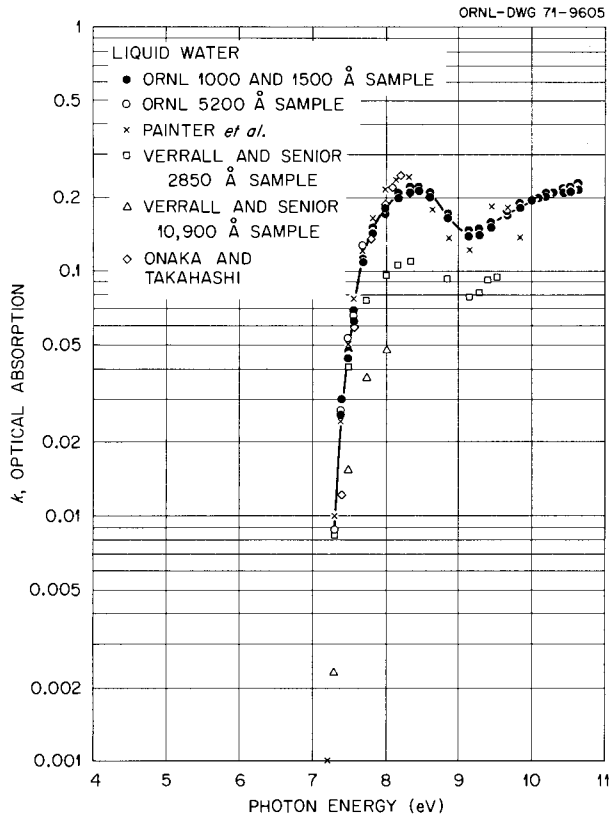

Fig. 8.7. Optical absorption k of water as a function of photon energy.

9. Electron and Ion Collision Physics

R. N. Compton

V. E. Anderson[1]
Ada Carter
C. D. Cooper[2]
F. J. Davis
W. R. Garrett
J. A. Harter
W. T. Naff[3]
S. J. Nalley[4,5]
D. R. Nelson
P. W. Reinhardt
H. C. Schweinler
J. A. Stockdale[6]
J. F. Wilson[4]

ELECTRON IMPACT EXCITATION AND IONIZATION OF THE RARE GASES

The trapped-electron method has been used previously to study autoionizing states and negative-ion resonances in He[7,8] and Ne.[9] The trapped-electron apparatus is also ideally suited for determining absolute cross sections for inelastic electron scattering in which the final electron lies in the range from 0 up to about 1 eV. Such information is important to understanding degradation spectra and energy deposition in gases. The energy distribution of electrons resulting from ionization of atoms and molecules is of primary importance to radiation physics. We have used the trapped-electron apparatus to determine the integral cross section for production of slow electrons in ionizing collisions of electrons with He, Ne, and Ar. Integrated cross sections

$$\int_0^w \sigma(\epsilon, E-\epsilon)\, d\epsilon$$

were measured for secondary electrons from energies from 0 to 1 eV. Figures 9.1 and 9.2 show the integrated cross section with $w = 0.095$ for He and Ne. The slow electron cross sections were observed to rise as the electron energy decreases toward the ionization potential and to undergo a maximum at an energy somewhat below the maximum in the total positive ionization cross section. For energies above ~100 eV the slow electron cross section decreases in the same manner as the total ionization cross section. As a simple theoretical check on the shape of the integral cross sections, Born approximation results for electron impact ionization of hydrogen were used for purposes of comparison. The integral cross sections

$$\int_0^w \sigma(\epsilon, E-\epsilon)\, d\epsilon$$

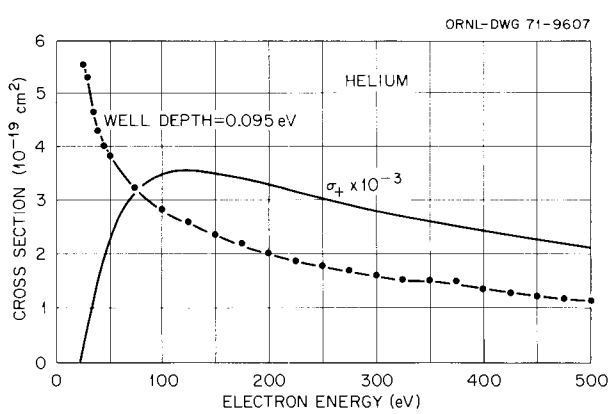

Fig. 9.1. Cross section for production of electrons between 0 and 0.095 eV (circles) and total ionization cross section (solid line) for helium as a function of the incident electron energy.

1. On loan from Computing Technology Center (ORGDP).
2. Consultant (sabbatical leave from University of Georgia to ORNL for 1971–72).
3. Oak Ridge Graduate Fellow, University of Georgia.
4. Radiological Health Physics Fellow, University of Tennessee.
5. Present address: Chattanooga State Technical Institute, 4501 Amnicola Highway, Chattanooga, Tenn.
6. On leave of absence, Guggenheim Fellowship in Art.
7. P. D. Burrow and G. J. Schulz, *Phys. Rev. Lett.* **22**, 1271 (1969).
8. J. T. Grissom, R. N. Compton, and W. R. Garrett, *Phys. Lett.* **30**, 117 (1969).
9. J. T. Grissom, W. R. Garrett, and R. N. Compton, *Phys. Rev. Lett.* **23**, 1011 (1969).

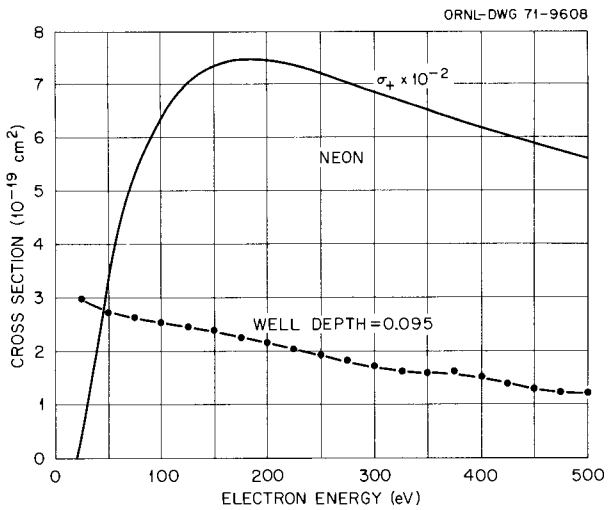

Fig. 9.2. Cross section for production of electrons between 0 and 0.095 eV (circles) and total ionization cross section (solid line) for neon as a function of the incident electron energy.

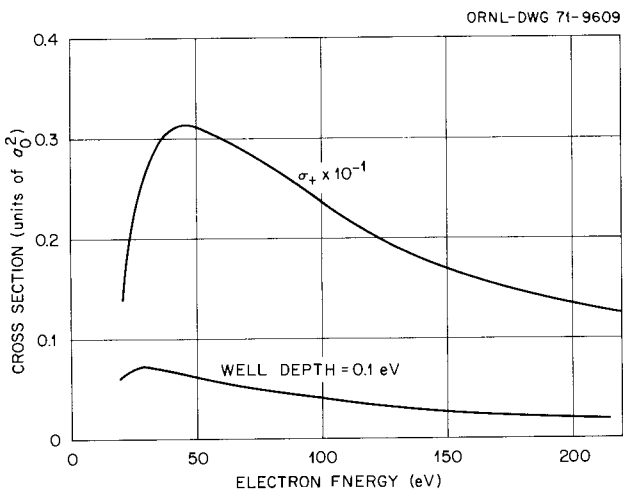

Fig. 9.3. Born approximation calculation for cross section for production of electrons between 0 and 0.1 eV (lower curve) and total ionization cross section (upper curve) for atomic hydrogen as a function of the incident electron energy.

were determined for different energies w corresponding to the experimental values of the well depth. Typical results are shown in Fig. 9.3. We see that the calculated integral cross sections also show a maximum at an energy somewhat below that in the total ionization cross section and show an overall form and relative magnitude quite similar to that observed for the noble gases.

THERMAL AND NEAR-THERMAL ELECTRON ATTACHMENT RATE AND TRANSPORT COEFFICIENTS FOR OXYGEN WITH A MODIFIED TIME-OF-FLIGHT METHOD

The relevance of oxygen to man and the earth's biosphere is unquestioned. Molecular oxygen plays multiple roles in supporting animal and plant life on earth. Despite the obvious importance of oxygen, several areas of research remain where most investigators are not yet satisfied with the available information. One of the areas of primary concern is the determination of electron momentum transfer cross sections Q_m for thermal (zero electric field at ~300°K) and near-thermal energies. The determination of the characteristic energy ϵ_k and the two transport coefficients, drift velocity w and diffusion coefficient D, in electron swarm experiments provides one of the best determinations of the momentum-transfer and inelastic-collision cross sections. However, such electron swarm experiments in O_2 become very difficult due to the large three-body electron attachment process at and near thermal energies. In addition, there is some uncertainty as to the value of the cross section of this electron attachment process at these energies.

In the fields of radiation physics and biophysics, one of the more fundamental processes is the interaction of electrons with the oxygen molecule, especially at thermal energies. For the physicist, the lack of consistent experimental measurements of electron interactions in O_2 at and near thermal energies has meant that no accurate estimate of rotational excitation cross section exists. In addition, the vibrational excitation cross section for electrons in O_2 is in question. Since the vibrational excitation of O_2 is the dominant energy-loss process for electrons in air between 0.2 and 1.7 eV, it is anticipated that the rotational excitation of O_2 will also have a significant contribution to the momentum-transfer and inelastic-collision cross sections for thermal electrons in air. More accurate values of the rotational and vibrational cross sections would provide better estimates of the propagation constants of an electromagnetic wave in weakly ionized dry air which corresponds to ionospheric conditions.

The drift-dwell-drift (DDD) technique previously developed[10] to determine thermal electron diffusion D in nonattaching gases and thermal electron attachment rates αw in attaching gases has been extended to

10. D. R. Nelson and F. J. Davis, *J. Chem. Phys.* **51**, 2322 (1969).

provide a method of determining very low-energy transport coefficients even when there may be a large cross section for attachment. In the original DDD technique the electron swarm was quickly drifted to the center of the experimental drift chamber, whereupon the electric field producing the drift was reduced to zero. Then, after varying periods of dwell time, the swarm was quickly drifted to the detector at the end of the swarm chamber. By measuring either the increasing width of the time-of-flight swarm distribution or the loss of electrons as a function of the dwell time, the thermal electron D or αw coefficients could be respectively determined. In the extended version of the DDD technique the electrons simply dwell in some nonzero field near the center of the drift chamber. The drift velocity w and diffusion D or attachment rate coefficient αw during the dwell period is then determined by essentially the same but more complicated DDD data analysis. The basic reason why the extended DDD technique provides a method for determining values of w and D at low values of E/P (the electric field strength E divided by pressure P) in O_2, even when attachment losses and distortions would normally be very serious at these energies, is that the distortion effects are minimized by pulsing or drifting the electron swarm before and after the dwell period at a judiciously chosen value of E/P.

The DDD time-of-flight technique can be schematically represented in terms of the voltage-time sequence as shown in Fig. 9.4. The voltage V_i, time t_i, partial chamber length l_i, drift velocity w_i, diffusion coefficient D_i, and attachment rate $\alpha_i w_i$ are designated for each distinct ith stage of the drift (swarm input)-dwell-drift (swarm output) technique. The expression for the electron number density after total time $= t_1 + t_2 + t_3$ at some time t_3 of the takeout pulse is

ORNL-DWG 71-9610

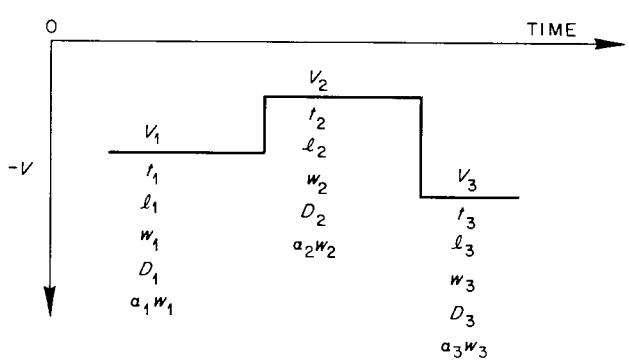

Fig. 9.4. Schematic of the drift-dwell-drift field ring voltage-time pulsing sequence.

$$N(x, t_3) = N_0 \exp\left[-\frac{(x - w_1 t_1 - w_2 t_2 - w_3 t_3)^2}{4(D_1 t_1 + D_2 t_2 + D_3 t_3)} - (\alpha_1 w_1 t_1 + \alpha_2 w_2 t_2 + \alpha_3 w_3 t_3)\right] \times [4\pi(D_1 t_1 + D_2 t_2 + D_3 t_3)]^{-1/2} . \quad (1)$$

Since all the distortions considered here occur only during the takeout pulse or during detection at the boundary $x = L$, substitutions will be made to express (1) only in terms of w_3, D_3, and α_3.

Let

$$D_1 t_1 = D_3 t_1' , \quad (2a)$$

$$D_2 t_2 = D_3 t_2' , \quad (2b)$$

$$\tau = t_1' + t_2' + t_3 , \quad (2c)$$

$$\mathcal{L} = L - w_1 t_1 - w_2 t_2 + w_3 t_2' + w_3 t_1' . \quad (2d)$$

Substituting in (1) and solving for the corresponding expression of the experimental measurement $E(L, \tau)$ gives

$$E(L, \tau) = \frac{aN_0}{2}\left(\frac{\mathcal{L}}{\tau} + w_3\right) \times \frac{e^{-(\mathcal{L} - w\tau)^2/4D_3 - \alpha_3 w_3 \tau - (\text{constant})}}{\sqrt{4\pi D_3 \tau}} . \quad (3)$$

Thus, the DDD time-of-flight experiment has been effectively transformed to the same form of the expression found for the usual time-of-flight experiment. The extended DDD data can, therefore, be analyzed with the same corrections determined for the single drift-diffusion-attachment process provided the length of chamber is modified according to (2d).

The preliminary results of the present oxygen study with the extended DDD technique will be discussed briefly. A three-body thermal electron attachment rate $\alpha w = 2.1 \times 10^{-30}$ cm^6 sec^{-1} was determined, which is in excellent agreement with the most recently reported value of 2.0×10^{-30} cm^6 sec^{-1}. There have been some rather large differences among published results for both the magnitude and the energy dependence of the momentum transport cross section of electrons in O_2. Our mean value for the product of the thermal diffusion coefficient and pressure, $DP = 1.20$ cm^2 μsec^{-1} torr, yields a value of $Q_m = 0.82 \times 10^{-16}$ cm^2

Table 9.1. Oxygen momentum transfer cross section Q_m at ϵ = 0.0258 eV

Q_m (10^{-16} cm^2)	From	Experimental data or method	Reference
2.4	$\nu = 9 \times 10^{-8} N\epsilon$ sec^{-1}	Microwave	Phelps et al. (1951)[a]
2.4	$\nu = 9 \times 10^{-8} N\epsilon$ sec^{-1}	Microwave	Van Lint et al. (1959)[b]
1.9	$\nu = 7 \times 10^{-8} N\epsilon$ sec^{-1}	Microwave	Carruthers (1962)[c]
14.5	$\lambda = 7.5\epsilon^{-1/2}$ cm^{-1} torr^{-1}	Electron mobilities	Heylen (1962)[d]
5.44	$\nu = 1.68 \times 10^{+8}$ sec^{-1} torr^{-1}	Cyclotron resonance	Fehsenfeld (1963)[e]
1.19	$\nu = 4.4 \times 10^{-8} N\epsilon$ sec^{-1}	Microwave	Mentzoni (1965)[f]
3.3	$\mu = 4.1 \times 10^{23}$ (cm-V-sec)$^{-1}$	Electron mobility	Pack and Phelps (1966)[g]
1.24	$\nu = 4.6 \times 10^{-8} N\epsilon$ sec^{-1}	Microwave	Veatch et al. (1966)[h]
0.82	$D_T P = 1.20$ cm^2 μsec^{-1} torr	DDD	Nelson and Davis (1970)[i]

[a]A. V. Phelps, O. T. Fundingsland, and S. C. Brown, *Phys. Rev.* **84**, 559 (1951).

[b]V. A. J. Van Lint, E. G. Wicker, and D. L. Trueblood, General Atomic Division of General Dynamics Corp., Report TR 59-43 (Aug. 31, 1954).

[c]J. A. Carruthers, *Can. J. Phys.* **40**, 1528 (1962).

[d]A. E. D. Heylen, *Proc. Phys. Soc., London* **79**, 284 (1962).

[e]F. C. Fehsenfeld, *J. Chem. Phys.* **39**, 1653 (1963).

[f]M. H. Mentzoni, *J. Res., Radio Sci.* **69D**, 213 (1965).

[g]J. L. Pack and A. V. Phelps, *J. Chem. Phys.* **44**, 1870 (1966).

[h]G. E. Veatch et al., *Bull. Amer. Phys. Soc.* **11**, 496 (1966).

[i]D. R. Nelson and F. J. Davis, *Bull. Amer. Phys. Soc.* **16**, 217 (1971).

(0.0258 eV) when it is assumed that Q_m is proportional to the electron velocity. This thermal value of Q_m is approximately 40% lower than the lowest of previously published values, which range from 1.19 to 14.5 $\times$ 10^{-16} cm^2. These cross-section values, together with the experimental methods used, and the author references are summarized in Table 9.1. In correspondence to the low thermal Q_m value found here, electron drift velocity determinations were significantly larger than had been estimated at these low E/P values, where no experimental data were previously available. In Fig. 9.5 the drift velocities found in the present study are given by circles, and those values calculated by Lowke and Parker[11] from the best available cross-section estimates are shown by the smooth curve. The initial slope of the w vs E/P curve gives the μP (zero field mobility times pressure) value. Since Lowke and Parker[11] based their low-energy cross-section estimates on the drift velocity data of Pack and Phelps,[12] there is obvious agreement. Correspondingly, the mobility value of 39.4 cm^2 V^{-1} μsec^{-1} torr calculated here from the thermal diffusion value $D_T P$ = 1.04 cm^2 μsec^{-1} torr through the Einstein-Nernst relation gives excellent

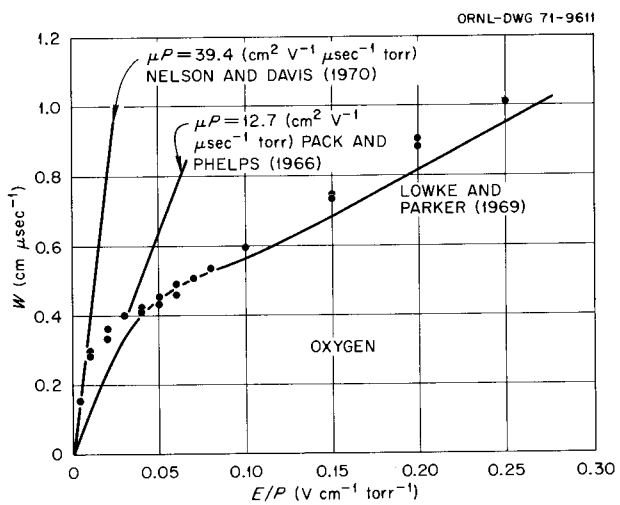

Fig. 9.5. Oxygen drift velocity as a function of E/P.

agreement with the present drift velocity results shown in Fig. 9.5.

A further confirmation of the lack of good low-energy electron Q_m values in O_2 is shown in Fig. 9.6. The calculations of Lowke and Parker[11] for the transverse D_T and longitudinal D_L diffusion coefficients of both O_2 and N_2 are indicated by the solid line curves.

The transverse diffusion coefficient D_T (perpendicular to the direction of the electric field) is measured

11. J. J. Lowke and J. H. Parker, Jr., *Phys. Rev.* **181**, 302 (1969).

12. J. L. Pack and A. V. Phelps, *J. Chem. Phys.* **44**, 1870 (1966).

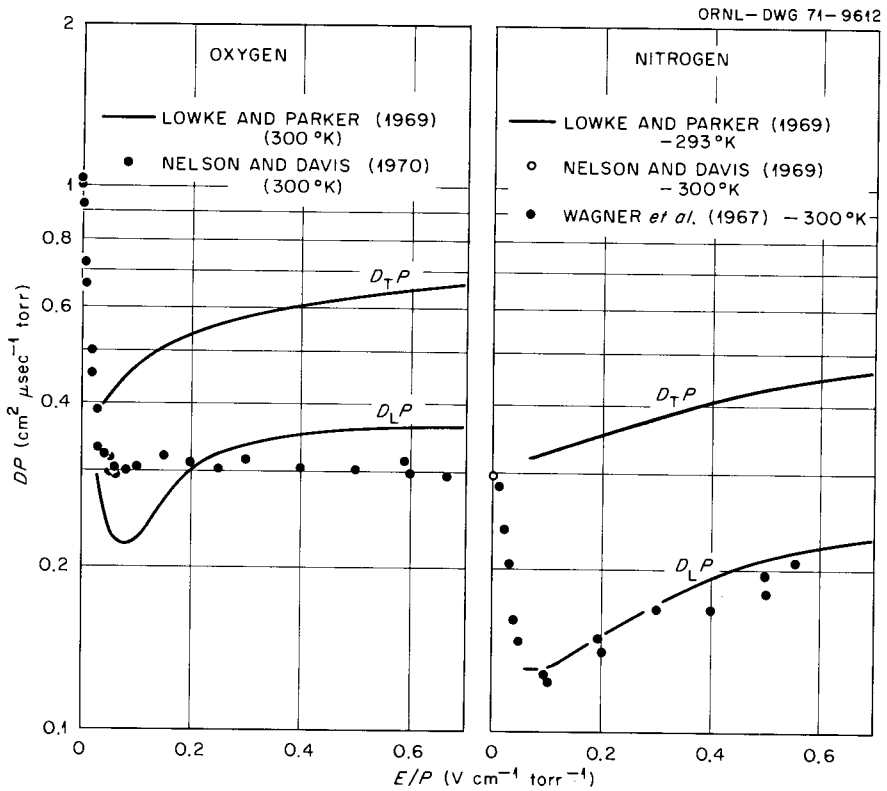

Fig. 9.6. Comparison of transverse and longitudinal diffusion coefficients (D_T and D_L) for O_2 and N_2 as a function of E/P.

with the Townsend-Huxley method. The longitudinal diffusion coefficient D_L (parallel to the direction of the electric field) is measured in the experiment reported here. When $E/P = 0$, then $D_T \equiv D_L$. The agreement between experiment and theory for $D_L P$ is good at all values of E/P in nitrogen but relatively poor for oxygen, especially at low values of E/P. This indicates that the low-energy electron cross sections in O_2 used by Lowke and Parker are in serious doubt.

It is very unlikely that the low thermal energy momentum transfer cross section for electrons in O_2 determined here could be due to impurity molecules. In a previous study of thermal electron diffusion in nine gases,[10] only neon had a higher $D_L P$ value than that found for O_2. Thus, impurities would have increased the momentum transfer cross section. Ultrapure grade of Matheson O_2 was used which was quoted to be 99.95% pure. Two of the most prominent impurities, <2.0 ppm H_2O and 4.5 ppm N_2, would have had a lowering effect on the thermal $D_L P$ value. Therefore, the true thermal energy cross section for electrons in O_2 is probably even lower (i.e., the corresponding $D_L P$ value even higher) than the preliminary value reported here.

ELECTRON INTERACTIONS WITH CARBONYL COMPOUNDS

Carbonyl compounds comprise one of the most widely studied classes of organics. Previously, numerous optical studies have been made of carbonyls, yet surprisingly few definite band assignments have been made in compounds other than formaldehyde. For example, no definite identification of the π-π^* transition in acetone has been made. We have studied electron impact excitation and negative-ion formation for acetone, acetaldehyde, chloroacetone, perfluoroacetone, acetophenone, benzaldehyde, and benzophenone. Both the trapped-electron and SF_6-scavenger techniques were used and essentially identical data were obtained from the two methods. Figure 9.7 shows the SF_6-scavenger spectrum of acetone. An intense temporary negative-ion resonance peaking at 1.6 eV is observed, and, in addition, peaks are observed at 4.15, 6.3, 7.5, and 8.1 eV. The peak at 4.15 eV may be attributed to a n-π^* triplet state, while the 6.3-eV peak is most probably the n-σ^* transition. Recent theoretical treatments predict the π-π^* transition to be around 7.9

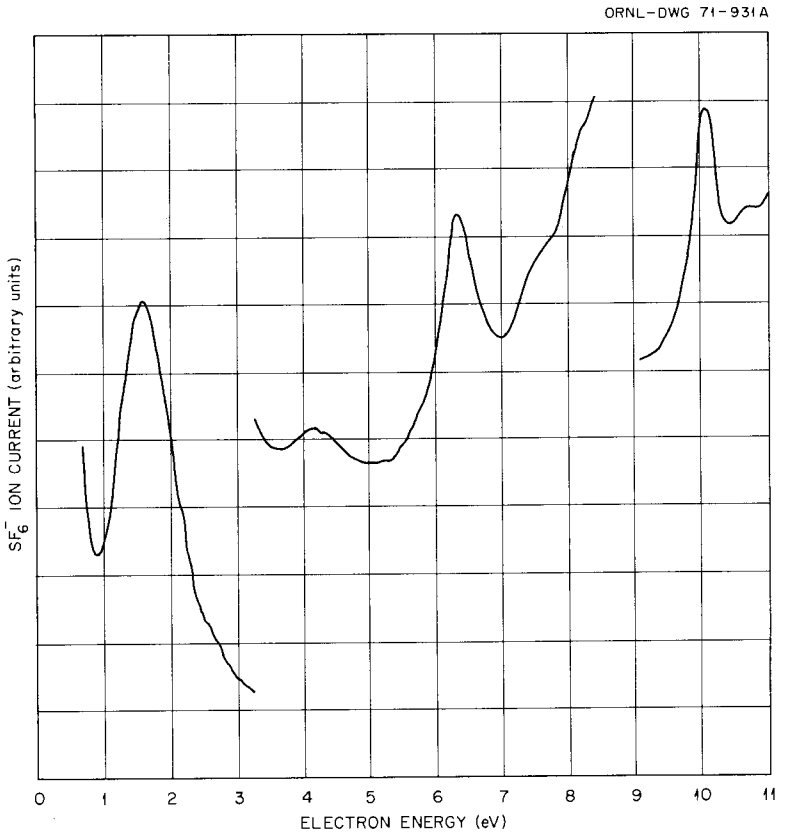

Fig. 9.7. SF_6-scavenger spectrum of acetone.

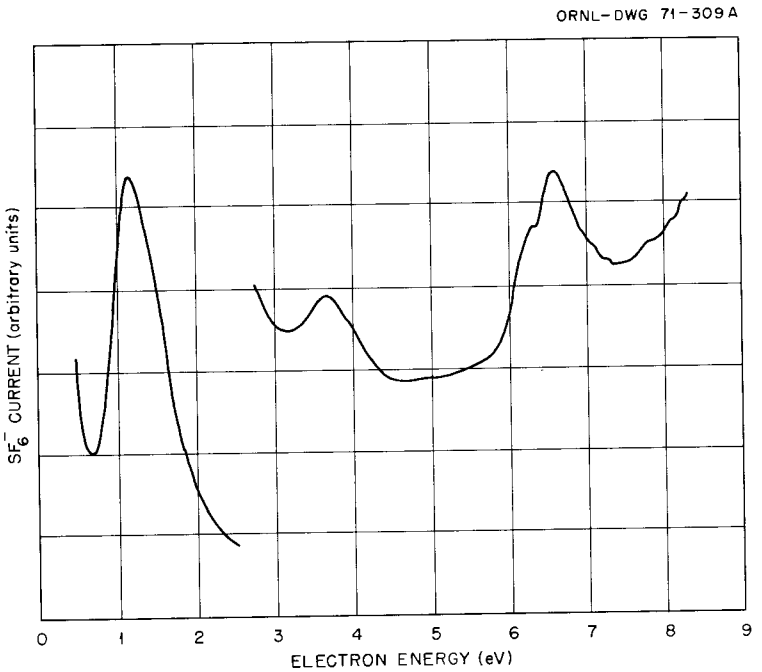

Fig. 9.8. SF_6-scavenger spectrum of acetaldehyde.

± 0.5 eV; thus, the shoulder at 8.1 eV might well be attributed to the π-π^* transition.

An SF_6-scavenger spectrum for acetaldehyde is shown in Fig. 9.8. Peaks were observed at 1.2, 3.8, 6.35, and 6.62 eV, with expected error of ±0.1 eV. Reproducibility was within 0.05 eV, as calibrated with both helium and krypton. The intense peak at 1.2 eV is due to a temporary negative-ion resonance; the peaks at 3.8 and 6.62 eV would seem to correspond to those at 4.15 and 6.3 eV in acetone. Hence it appears that replacing a CH_3 group in acetone by a hydrogen atom shifts the 6.3-eV peak to higher energy by ~0.3 eV, leaving a shoulder at 6.35 eV. The fact that the shoulder appears only in acetaldehyde suggests that two excited states are degenerate in acetone at 6.3 eV, with the degeneracy split in acetaldehyde. This might be expected if one of the states resulted, for example, from a triplet π-π^* transition such that both the π and π^* orbitals were shifted by similar amounts in the course of substitution. Nevertheless, a definite assignment obviously cannot be made at present.

Temporary negative-ion resonances were also observed for acetophenone, benzophenone, and benzaldehyde at energies of 0.95, 0.75, and 0.72 eV, respectively. Figure 9.9 shows all of the carbonyl temporary negative-ion resonances observed to date. The interesting energy shifts in the peak of the cross section are qualitatively explained by the electron acceptor-donor properties of the various carbonyl substituents. Substitution of chlorine to acetone (chloroacetone) lowered the resonance by 1.1 eV, and the dominant decay channel was the production of Cl^- ions. Slow electron collisions with perfluoroacetone resulted in the formation of a metastable long-lived $CO(CF_3)_2^-$ ion with a mean autodetachment lifetime of 65 ± 10 μsec.

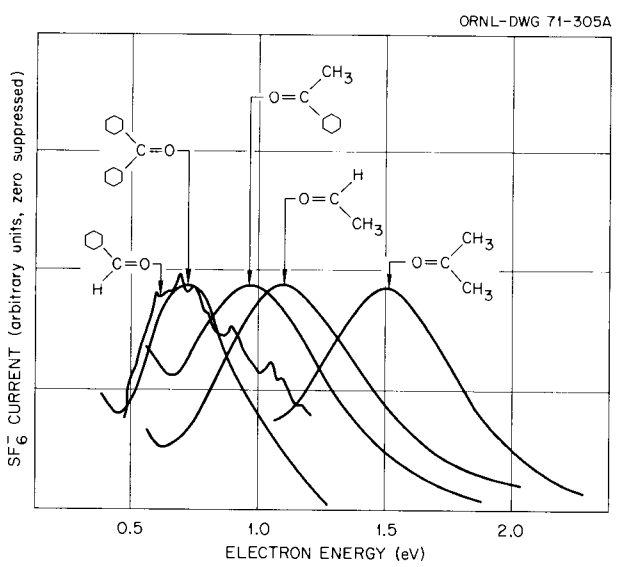

Fig. 9.9. SF_6-scavenger spectra of negative-ion resonances in carbonyls.

IONIC PROCESSES IN BORON HALIDES

Boron trifluoride is an important molecule in theoretical chemistry because of its electron acceptor properties and because of its high symmetry; BF_3 is also of considerable practical importance, as it is used in neutron dosimetry as a counter gas and is the progenitor of a large number of coordination compounds. A complete study of the ionic processes in BF_3 and BCl_3 revealed some interesting anomalies in the negative-ion processes of these gases. The thermal energy attachment rate for BF_3 was found to be quite small (6.6×10^6 sec^{-1} $torr^{-1}$), and the rate of electron attachment to BCl_3 is about a factor of 10 higher (9×10^7 sec^{-1} $torr^{-1}$). The apparent low rate of electron attachment explains why BF_3 is desirable as a neutron counter gas and does not quench the electron avalanche initiated by the alpha particles produced as the boron captures a neutron. Production of F^-, F_2^-, and BF_2^- was observed from BF_3 in the neighborhood of 11.5-eV electron energy, whereas Cl^- and Cl_2^- were observed from BCl_3 near 1 eV. The electronic structures of BF_3 and BCl_3 are such that they are planar in structure; however, Walsh's rules predict that the corresponding negative ion is necessarily pyramidal (e.g., similar to the isoelectronic CF_3 molecule). Thus, the ion is highly distorted in comparison with the neutral and would offer an explanation of the above-mentioned anomalous electron attachment processes.

The SF_6^- ion was observed to react with BF_3 and BCl_3, yielding BF_4^- and BCl_3F^-, respectively; BF_4^- was also produced through the reaction $F_2^- + BF_3 \rightarrow BF_4^- + F$. Rate constants for these reactions were measured by a pulsed source method[13] and were 1.8×10^{-9}, 1.6×10^{-10}, and 6.1×10^{-10} $molecule^{-1}$ cm^3 sec^{-1} in the order above. Attempts to form BF_3^- by simple charge exchange were unsuccessful; however, the reactions $OD^- + BF_3 \rightarrow DF + BF_2O^-$ were observed. The BF_4^- ion observed in this work is the first time this ion has been observed in the gas phase, although its presence in crystals is well accepted. The BF_4^-, in fact, is expected to be quite stable. From our observed ion-molecule reactions we estimate the electron affinity to be ~3.5 eV.

13. J. A. Stockdale, R. N. Compton, and P. W. Reinhardt, *Phys. Rev.* **184**, 81 (1969).

Salts having the structure $Na^+BF_4^-$ are used in molten-salt reactors. The above work will presumably be of interest to reactor chemists considering reaction schemes involving BF_4^- and other compounds such as H_2O and subsequent reactions with tritium.

COLLISIONAL IONIZATION OF CESIUM BY O_2, NO_2, AND N_2O: DETERMINATION OF ELECTRON AFFINITIES

Studies of the collisions of "one-electron atoms," notably the alkali atoms, with neutral gas targets have been the subject of a great number of papers in atomic and molecular physics. Extensive investigations of reactive collisions between alkali atoms and diatomic molecules, especially the halogens, have been made in the thermal energy range. These reactions are believed to proceed via an ionic intermediate state [e.g., $A + MX \rightarrow (A^+MX^-) \rightarrow AM + X$]. At sufficiently high collision energies, ion products should be observed, and a measurement of the threshold for ion-pair production can be related to the electron affinity of the electron acceptor. Specifically, the threshold energy (center-of-mass system) for production of a positive-and-negative-ion pair, that is, $Cs + X \rightarrow Cs^+ + X^-$, would be

$$E_{\text{thres}} = [\text{IP(Cs)} - \text{EA(X)} + E'] \tag{4}$$

where IP(Cs) is the ionization potential of cesium, EA(X) is the electron affinity of X, and E' represents any excitation energy which may reside in X^- plus any activation energy required to make the reaction proceed. Thus, a measurement of E_{thres} affords a determination of the lower limit to the electron affinities of molecules. With the possible exception of O_2 and OH there are *no* accurately known and well-accepted values for electron affinities of molecules. Molecular electron affinities are fundamental quantities which are greatly needed to interpret many chemical, physical, and biological effects.

Our apparatus is made up of three major systems (see Fig. 9.10): a source for producing a neutral cesium

ORNL-DWG 70-1143C

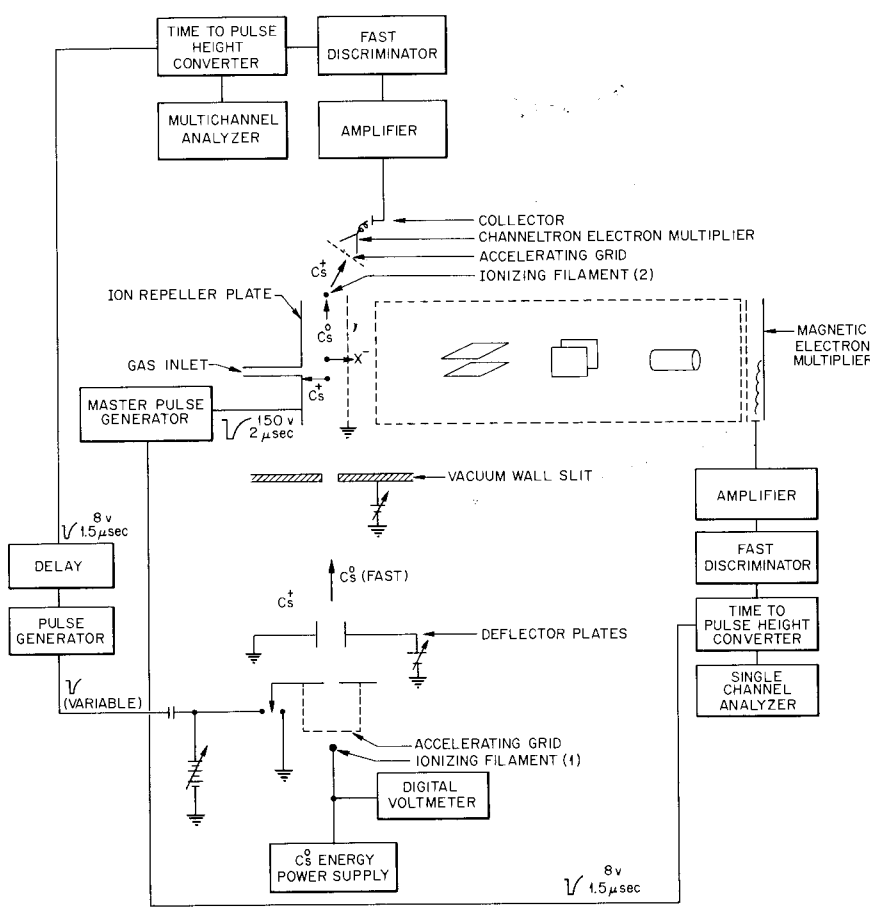

Fig. 9.10. Schematic diagram of fast cesium atom charge transfer apparatus.

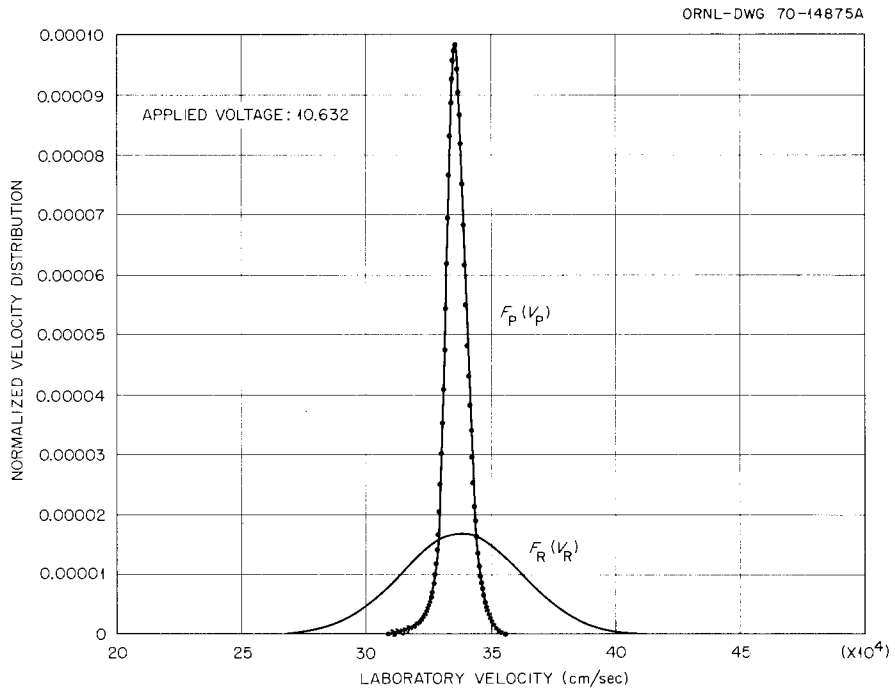

Fig. 9.11. Comparison of the measured velocity distribution function of the incident cesium beam, $F(v)$, with the relative velocity distribution function, $F(v_R)$, for the colliding particles Cs and O_2.

beam with the required energy, a time-of-flight region for velocity analyzing and detecting the Cs^0 beam, and a reaction region with a time-of-flight mass spectrometer for detecting and analyzing the charged products from the collision. All signals are stored in a multichannel analyzer as single counts. The charge-exchange source provides the neutral cesium beam, pulsed on for 1 μsec every 100 μsec and detected by a warm filament and Channeltron electron multiplier in tandem; the time of flight (over a flight path of 44.6 cm) gives the energy. Scattering gas pressure is $\sim 1 \times 10^{-5}$ mm Hg, and background pressures are $\sim 2 \times 10^{-8}$ mm Hg.

A typical velocity distribution measurement $F(v)$ for the cesium beam is shown in Fig. 9.11. Since the relative velocity is important in a collision, the solid line in Fig. 9.11 shows the relative velocity distribution function $F_R(v_R)$ for cesium colliding with O_2 which was computed from the measured Cs beam velocity distribution $F(v)$ by assuming the target O_2 molecule to be at the temperature of the source (300°K).

Figure 9.12 presents the relative cross section for the formation of O_2^- as a function of the center-of-mass energy as Cs and O_2 collide. The laboratory energy of the incident cesium beam is marked at the top of the graph. Although a limited portion of the data is shown, the cross section is seen to continue rising even up to 85 eV (laboratory energy). The relative cross section shown in Fig. 9.12 was found to increase quite linearly up to ~6 eV (c.m.), and O^- was observed for energies above the minimum energy required for its production (7.51 eV). The intensity of the O^- signal at a relative energy of 1 eV (c.m.) above its appearance potential was only ~3% of the O_2^- signal at that energy.

The experimental cross section measured for the production of O_2^- is a convolution of the true cross section with the center-of-mass energy distribution, provided there is no energy discrimination in the collected ion currents. Thus, in order to obtain the threshold for the reaction, the true cross section must somehow be deconvoluted from the experimental measurement. An alternative method is to assume the true cross-section behavior and convolute this with the center-of-mass energy distribution. Because of the very linear nature of the observed cross section above threshold, it was assumed that the true cross section is also linear, and we wished to see if the low-energy tail could be accounted for by the Doppler motion. Chantry[14] has shown that if one assumes a true linear cross section, the shape of the measured cross section ($\mathcal{L}$) is given by

14. P. J. Chantry (submitted to *J. Chem. Phys.*).

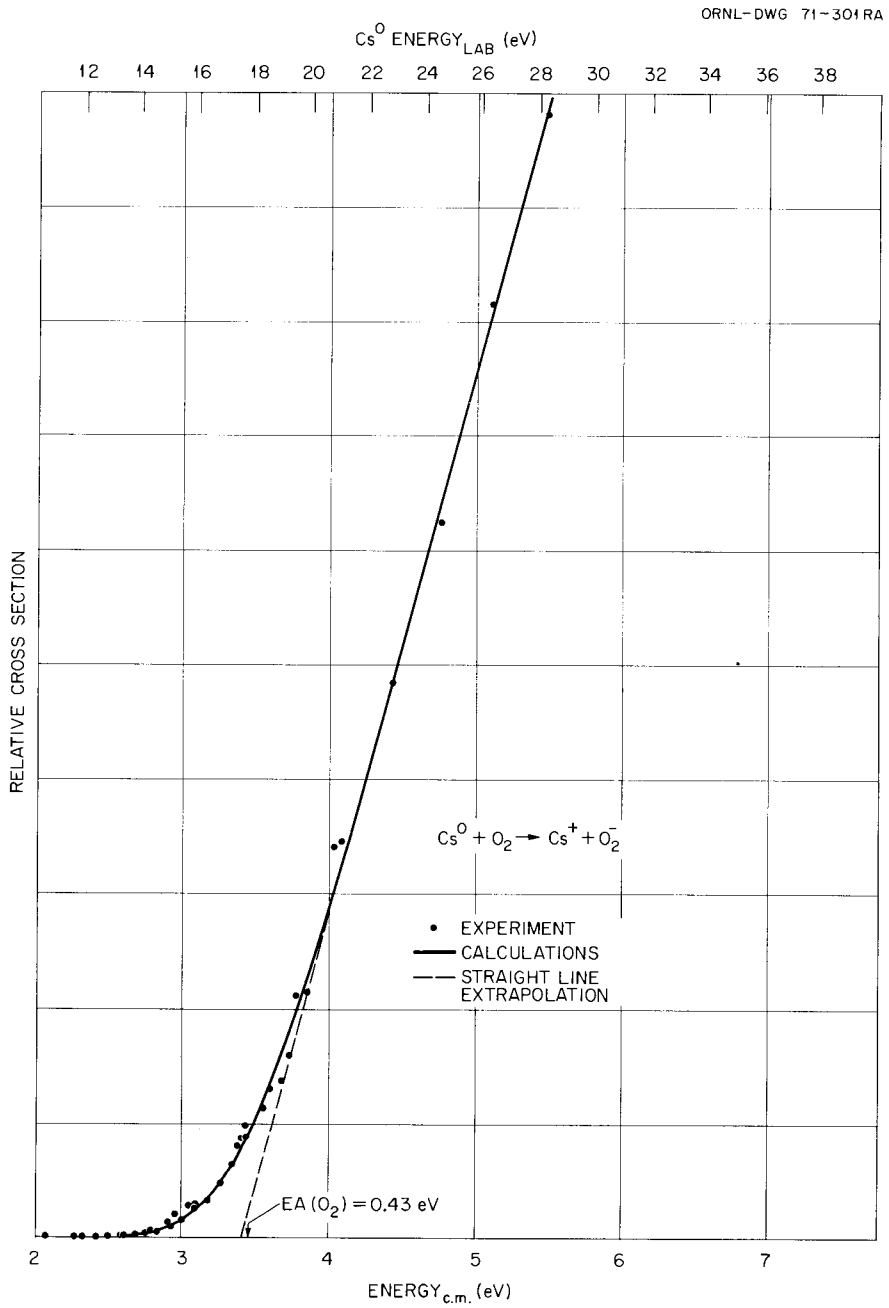

Fig. 9.12. Relative cross section for the formation of O_2^- from the collision of Cs and O_2 vs the laboratory energy of the cesium beam (top) and the center-of-mass energy (bottom).

$$\mathcal{L}(\epsilon_0, \epsilon_T) = \left(\frac{1}{4\pi\epsilon_0}\right)^{1/2} \left[\epsilon_0 + (\epsilon_0\epsilon_T)^{1/2} + \frac{5}{2} + \frac{3}{2}(\epsilon_T/\epsilon_0)^{1/2}\right] e^{-(\epsilon_T{}^{1/2} - \epsilon_0{}^{1/2})^2} + \frac{1}{2}\left[\epsilon_0 - \epsilon_T + 3 - \left(\frac{2\epsilon_T - 3}{4\epsilon_0}\right)\right]\left[1 - \mathrm{erf}\,(\epsilon_T{}^{1/2} - \epsilon_0{}^{1/2})\right], \quad (5)$$

where

$\epsilon_T = E_T/\gamma kT$,

$\epsilon_0 = E_0/\gamma kT$,

E_T = threshold energy (c.m.),

E_0 = c.m. beam energy,

$\gamma = m/(M + m)$,

m = projectile mass,

M = target mass.

The solid curve in Fig. 9.12 represents the calculated result for the case of cesium colliding with O_2. The best fit of the experimental data was found for E_T = 3.43 eV which, subtracted from the ionization potential of cesium (3.89 eV), yields an electron affinity of 0.46 eV for O_2. The uncertainty attached to this number is less than 0.03 eV, allowing for error in energy measurement, and another 0.03 eV should be added to allow for spread in data points which will contribute to uncertainty in the fit of the experiment.

Chantry[14] has also shown that Eq. (5) does become linear for energies somewhat above threshold; however, the linear portion extrapolates back to an apparent threshold which is too low by approximately $3\gamma kT$. The arrow shown in Fig. 9.12 points to the threshold corresponding to $EA(O_2)$ = 0.43 eV and is presented for comparison purposes only. The dashed line shown in Fig. 9.12 is the extrapolation of a least-squares line placed through the data points from 3.6 to 5.5 eV. Adding $3\gamma kT$ (0.06 eV) to the extrapolated onset (3.41 eV) predicts $EA(O_2) \geqslant 0.42$, which is within the limits of uncertainty of the more accurate value quoted above.

In addition, we have analyzed our data for Cs^0 on O_2 to extract the microscopic cross section as follows. The distribution function for relative velocities $F_r(v_r)$ is obtained by convoluting the measured distribution function $F_p(v_p)$ of the cesium projectiles with the Maxwell velocity distribution function $F_t(v_t)$ of the molecules in the target gas. [For example, for Cs^0 on O_2 the spread in the beam (FWHM) is about 0.4 eV at 8 eV lab, or 0.07 eV at 1.55 eV c.m., while the final spread after Doppler broadening is 0.6 eV.] The measured ion counting rate per incident cesium atom is proportional to $\int v_r\ \sigma(v_r)\ F_r(v_r)\ dv_r$; here, of course, $\sigma(v_r)$ is unknown and $F_r(v_r)$ is known numerically (from the above convolution) for each energy of the Cs^0 beam. We solve this integral equation for $\sigma(v_r)$ by an iterative process, with the result shown in Fig. 9.13. $\sigma(v_r)$ is approximately linear from the onset at 3.41 eV [$EA(O_2)$ = 0.48 eV] to ~5 eV, where another process appears. Thus, we conclude that the electron affinity of O_2 is 0.45 ± 0.05 eV. This value is in excellent agreement with the equilibrium value reported by Pack and Phelps[15] and the recent photodetachment value.[16]

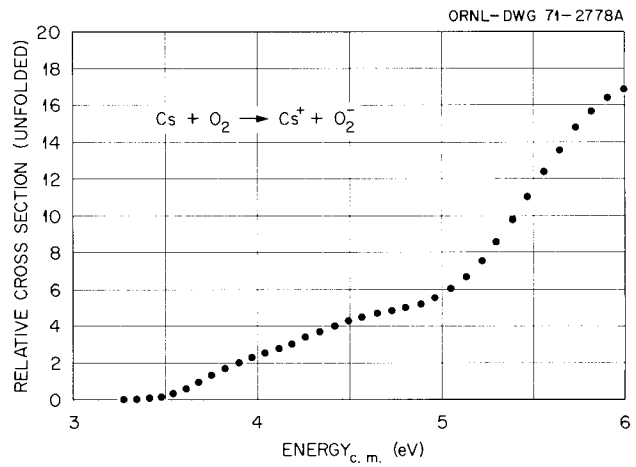

Fig. 9.13. Unfolded cross section for the formation of O_2^- from the collision of Cs and O_2.

Figure 9.14 shows the relative cross section for producing NO_2^- and O^- as Cs and NO_2 collide. Analysis of the threshold for NO_2^- production, taking into account the Doppler motion of NO_2, shows the cross section for ion-pair production to be very close to a step function and yields an electron affinity of NO_2 of 2.0 ± 0.2 eV. O^- production occurs within 0.2 eV of the theoretical onset (calculated from bond dissociation energy of NO–O and the electron affinity of O).

Collision of Cs^0 with N_2O produces N_2O^- as shown in Fig. 9.15. The threshold predicts an electron affinity of ~0 (±0.3 eV). A more intense O^- current appears at 4.1 ± 0.1 eV c.m.; the expected threshold calculated from the electron affinity of O (1.465 eV) and the thermochemical value for the dissociation energy of the N_2–O bond (1.677 eV) is 4.11 eV. A distinct break in

15. J. L. Pack and A. V. Phelps, *J. Chem. Phys.* **44**, 1870 (1966).

16. R. Celotta et al., *Bull. Amer. Phys. Soc.* **16**, 212 (1971).

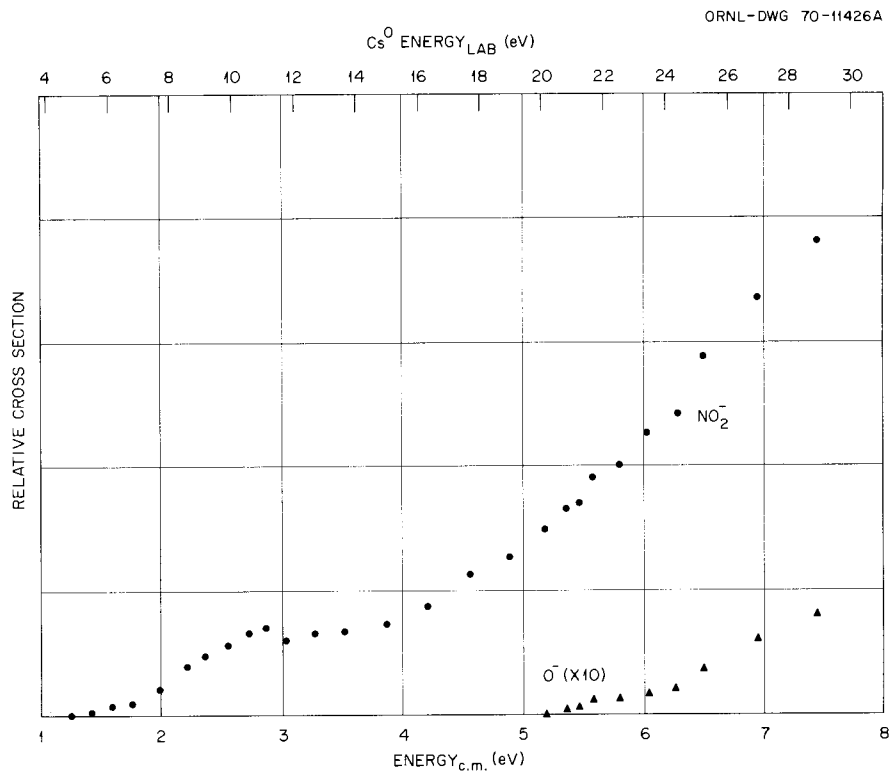

Fig. 9.14. Relative cross section for the production of NO_2^- and O^- from the collision of Cs^0 with NO_2 as a function of the center-of-mass and Cs^0 beam energies.

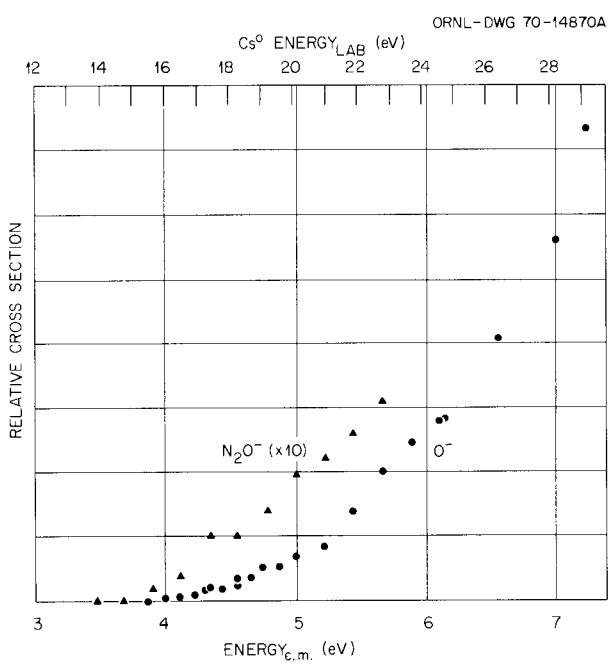

Fig. 9.15. Relative cross section for the production of N_2O^- and O^- from the collision of Cs^0 with N_2O as a function of the center-of-mass energy and the laboratory energy of Cs^0.

the O^- curve occurs at ~5.2 eV and is attributed to the opening of another channel for O^- production.

Present plans are to analyze the energy of the electrons produced in collisions of Cs with molecules at energies above threshold with a double-focusing electrostatic analyzer. This work is being performed in close collaboration with similar work by Datz's group in the Chemistry Division. The data resulting from both sets of experiments, together with theoretical studies under way at ORNL, should greatly increase our understanding of charge exchanging collisions and electron affinities.

FSU-ORNL CHEMICAL ACCELERATOR

A cooperative effort between physicists at ORNL and Florida State University is under way to construct a chemical accelerator for producing fast (500 eV to 10 keV) neutral beams of polyatomic molecules. The idea[17] is to form metastable negative ions by zero-

17. R. N. Compton and R. H. Huebner, p. 281 in *Advances in Radiation Chemistry*, vol. 2, ed. by M. Burton and J. L. Magee, Wiley, New York, 1970.

energy electron attachment, accelerate the ions to the desired energy, and finally allow sufficient flight time for appreciable autodetachment to occur, thus producing a beam of fast neutral particles which are in their ground electronic states. The vibrational-rotational population will be determined by the temperature of the source. The apparatus is being constructed at FSU, and the design includes a 4-m flight path to determine the primary and scattered neutral energies. The experiment is in the initial test stage and appears to have possibilities of being a significant contribution to the area of chemical accelerators.

10. Atomic and Molecular Radiation Physics

L. G. Christophorou

V. E. Anderson[1]
J. B. Birks[2]
R. P. Blaunstein[2]
Ada Carter
J. G. Carter
A. A. Christodoulides[3]
J. T. Cox
C. E. Easterly[4]
R. E. Goans[4]
A. Hadjiantoniou[3]
J. A. Harter
P. D. Kidd[4]
C. E. Klots
D. L. McCorkle[3]
M. N. Pisanias[3]
D. Pittman

SWARM-DETERMINED ELECTRON ATTACHMENT CROSS SECTIONS AS A FUNCTION OF ELECTRON ENERGY[5]

In electron swarm experiments the measured attachment rates αw ($\sec^{-1}$ torr^{-1}) are quantities averaged over the distribution of energies in the electron swarm $f(\epsilon, E/P)$ and are related to $f(\epsilon, E/P)$ and the attachment cross section $\sigma_a(\epsilon)$ by

$$\alpha w = N_0 \left(\frac{2}{m}\right)^{1/2} \int_0^\infty \epsilon^{1/2}\, \sigma_a(\epsilon) f\left(\epsilon, \frac{E}{P}\right) d\epsilon\,, \qquad (1)$$

where α is the attachment coefficient, w is the electron swarm drift velocity, ϵ and m are the electron energy and mass, respectively, and N_0 is the number of attaching gas molecules per cubic centimeter per torr at the temperature of the experiment T. Physically, however, what one is actually after is the *monoenergetic attachment rate*[6] $M(\epsilon)$, from which to determine the cross section as a function of electron energy ϵ from

$$\sigma_a(\epsilon) = \frac{M(\epsilon)}{N_0\,(2/m)^{1/2}\epsilon^{1/2}}\,, \qquad (2)$$

where $M(\epsilon)$ is in units of $\sec^{-1}$ torr^{-1}.

The swarm unfolding method yields $M(\epsilon)$ directly. In this method $F(\langle\epsilon\rangle, \epsilon)$ at each mean electron energy $\langle\epsilon\rangle$ (to each value of E/P corresponds a value of $\langle\epsilon\rangle$) is used as the "smearing out function" at $\langle\epsilon\rangle$ to unfold $M(\epsilon)$ from the experimentally determined electron attachment rate functions $\alpha w(\langle\epsilon\rangle)$ which, for convenience, we write as $R_{\text{exp}}(\langle\epsilon\rangle)$. If we denote by $R(\langle\epsilon\rangle_j)$ the value of the attachment rate at $\langle\epsilon\rangle_j$, by $F(\langle\epsilon\rangle_j, \epsilon)$ the electron energy distribution function that corresponds to $\langle\epsilon\rangle_j$, and by $M(\epsilon)$ the value of the monoenergetic attachment rate at energy ϵ, we have

$$R(\langle\epsilon\rangle_j) = \int_0^\infty M(\epsilon)\, F(\langle\epsilon\rangle_j, \epsilon)\, d\epsilon\,. \qquad (3)$$

To start the iterative procedure $M(\epsilon)$ was approximated[5] either by $R_{\text{exp}}(\langle\epsilon\rangle)$ or by a function which was set equal to a constant value for all energies in the range $0 \leqslant \epsilon \leqslant \epsilon_{\text{max}}$ and 0 for all energies $\epsilon > \epsilon_{\text{max}}$. ϵ_{max} is either an energy well in excess of the highest energy for which the cross section is expected to be significant, or an energy in excess of the highest energy for which nonzero values of $F(\langle\epsilon\rangle, \epsilon)$ exist. This assumed form of $M(\epsilon)$ is introduced into Eq. (3), and $R(\langle\epsilon\rangle_j)$ is calculated for each and every value $\langle\epsilon\rangle_j$ for which attachment rates are experimentally known.

From the experimental rates $R_{\text{exp}}(\langle\epsilon\rangle_j)$ and the calculated rates $R_{\text{cal}}(\langle\epsilon\rangle_j)$ relative weighting factors are defined as

$$w(\langle\epsilon\rangle_j) \equiv \frac{R_{\text{exp}}(\langle\epsilon\rangle_j)}{R_{\text{cal}}(\langle\epsilon\rangle_j)}\,, \qquad (4)$$

1. On loan from Mathematics Division, ORNL.
2. Consultant.
3. Graduate student, University of Tennessee.
4. USAEC Fellow in Radiation Science.
5. L. G. Christophorou, D. L. McCorkle, and V. E. Anderson, *Proc. Phys. Soc., London At. Mol. Phys.* (in press).
6. This is the rate that would be measured if all the electrons in the swarm had the same energy.

with the condition $w(\langle\epsilon\rangle_j) = 1$ when $R_{cal}(\langle\epsilon\rangle_j) = 0$.

A new function $M_{new}(\epsilon)$ is then determined through

$$M_{new}(\epsilon) = M_{old}(\epsilon) \frac{\sum_j w(\langle\epsilon\rangle_j) F(\langle\epsilon\rangle_j, \epsilon)}{\sum F(\langle\epsilon\rangle_j, \epsilon)} . \quad (5)$$

This new function is introduced into Eq. (3), and the procedure is repeated until the residuals are minimized, viz.,

$$\sum_j [R_{exp}(\langle\epsilon\rangle_j) - R_{cal}(\langle\epsilon\rangle_j)]^2 \rightarrow \text{minimum} . \quad (6)$$

When this condition is satisfied the weighting factors $w(\langle\epsilon\rangle_j) \rightarrow 1$, and the function $M(\epsilon)$ does not change with successive iterations. $M(\epsilon)$ is then assumed to be very close to the true monoenergetic rate of electron attachment, and the cross section $\sigma_a(\epsilon)$ is determined from Eq. (2).

The functions $f(\epsilon, E/P)$ are normalized, and the peaks are quite broad. Their full width at half height is of the same order of magnitude as $\langle\epsilon\rangle$, and this requires quite a large number (>100) of iterations for convergence.

To reduce the number of iterations and also to generalize the present unfolding procedure, we expressed Eq. (5) as

$$M_{new}(\epsilon) = M_{old}(\epsilon) \left[\frac{\sum_j w(\langle\epsilon\rangle_j)^n F(\langle\epsilon\rangle_j, \epsilon) w'(\langle\epsilon\rangle_j)}{\sum_j F(\langle\epsilon\rangle_j, \epsilon) w'(\langle\epsilon\rangle_j)} \right]^m , \quad (7)$$

where n and m are real numbers $\geqslant 1$ and $w'(\langle\epsilon\rangle_j)$ are considered as "importance factors," in the sense that one may have reasons to attach a different weight (significance) to each of the experimental data points. In our analysis[5] we set $w'(\langle\epsilon\rangle_j) = 1$ and $n = 1$, but we used periodically values of m greater than 1, namely, integer values between 1 and 10 (in most cases 3). After every few iterations with $m > 1$ it was found necessary to perform a number of iterations with $m = 1$, to "stabilize" the function $M(\epsilon)$. This periodic acceleration (i.e., use of values of $m \geqslant 2$) substantially reduced the number of iterations necessary for convergence.

In Fig. 10.1 cross sections obtained directly from high-pressure swarm experiments through the procedure

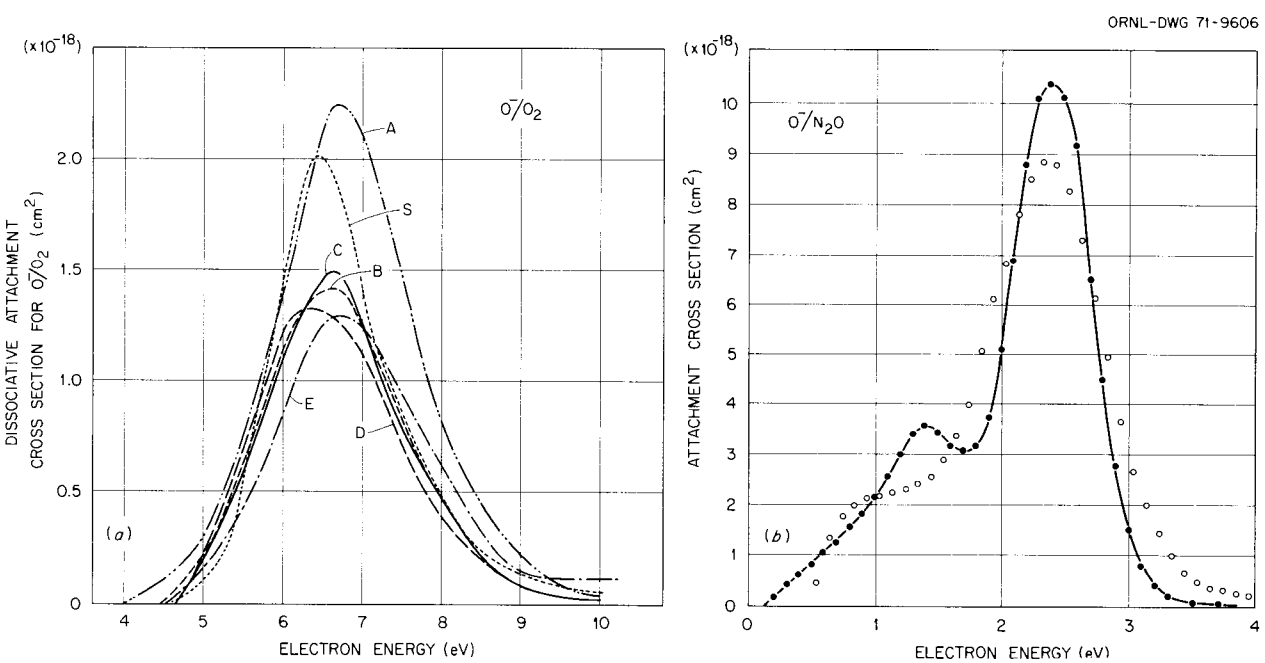

Fig. 10.1. Dissociative attachment cross sections. (*a*) Production of O^- from O_2 as a function of electron energy. Curve: *S* – swarm unfolding (ref. 5); *A* – J. D. Craggs et al., *Proc. Roy. Soc. London* **240A**, 473 (1957); *B* – D. Rapp and D. D. Briglia, *J. Chem. Phys.* **43**, 1480 (1965); *C* – L. G. Christophorou et al., *J. Chem. Phys.* **43**, 4273 (1965); *D* – I. S. Buchel'nikova, *Sov. Phys.-JETP* **8**, 783 (1959); *E* – G. J. Schulz, *Phys. Rev.* **128**, 178 (1962). With the exception of curve *S* all other cross-section functions were determined using electron-beam techniques. (*b*) Production of O^- from N_2O as a function of electron energy. (●) – swarm unfolding (ref. 5); (○) – beam data [D. Rapp and D. D. Briglia, *J. Chem. Phys.* **43**, 1480 (1965)].

just described are presented and are seen to compare well with those determined by the use of quasi-monoenergetic electron-beam methods. For a detailed comparison see Christophorou et al.[5]

CROSS-SECTION FUNCTIONS FOR ELECTRON ATTACHMENT RESONANCES WITH CROSS SECTIONS INCREASING SHARPLY AT THERMAL ENERGIES

The swarm-unfolding technique is uniquely suited for electron attachment resonances with cross-section functions increasing sharply with decreasing energy at thermal and epithermal energies (<0.5 eV). Because these generally strong electron attachment resonances occur at such low energies, they are closer energywise to the conditions prevailing in a condensed environment. They cannot, presently, be determined by other methods. Cross-section functions for such electron attachment resonances obtained by the swarm-unfolding technique are given in Fig. 10.2 (solid points) for four molecules. For all molecules in Fig. 10.2, $M(\epsilon)$ was initially assumed to be constant over the energy range $0 \leqslant \epsilon \leqslant 2$ eV and equal to 0 for $\epsilon > 2$ eV. The cross sections shown in Fig. 10.2 have been found to vary with electron energy ϵ as

$$\sigma_a(\epsilon) = \frac{A_\gamma}{\epsilon^\gamma} \tag{8}$$

over the energy range given in column 4 of Table 10.1, where A_γ and γ are constants. The values of γ for a number of molecules are given in column 3 of Table 10.1 and are seen to vary from ~1 to 1.4.

Prior to the swarm-unfolding technique, Christophorou et al.[7,8] have used Eq. (8) in connection with Eqs. (1) and (6) and have determined the constants A_γ and γ by a least-squares procedure whereby for each set of values of A_γ and γ the attachment rates were calculated as a function of $\langle\epsilon\rangle$ (or E/P) and compared with their experimental values until the residuals [Eq. (6)] were minimized. Their results on γ and $\sigma_a(\epsilon = 0.05$ eV) are given in Table 10.1 and are plotted in Fig. 10.2 (open circles) for some molecules. The agreement seen between the results obtained this way with those of the swarm-unfolding method is gratifying.

7. L. G. Christophorou, D. L. McCorkle, and J. G. Carter, *J. Chem. Phys.* **54**, 253 (1971).
8. A. A. Christodoulides and L. G. Christophorou, *J. Chem. Phys.* **54**, 4691 (1971).

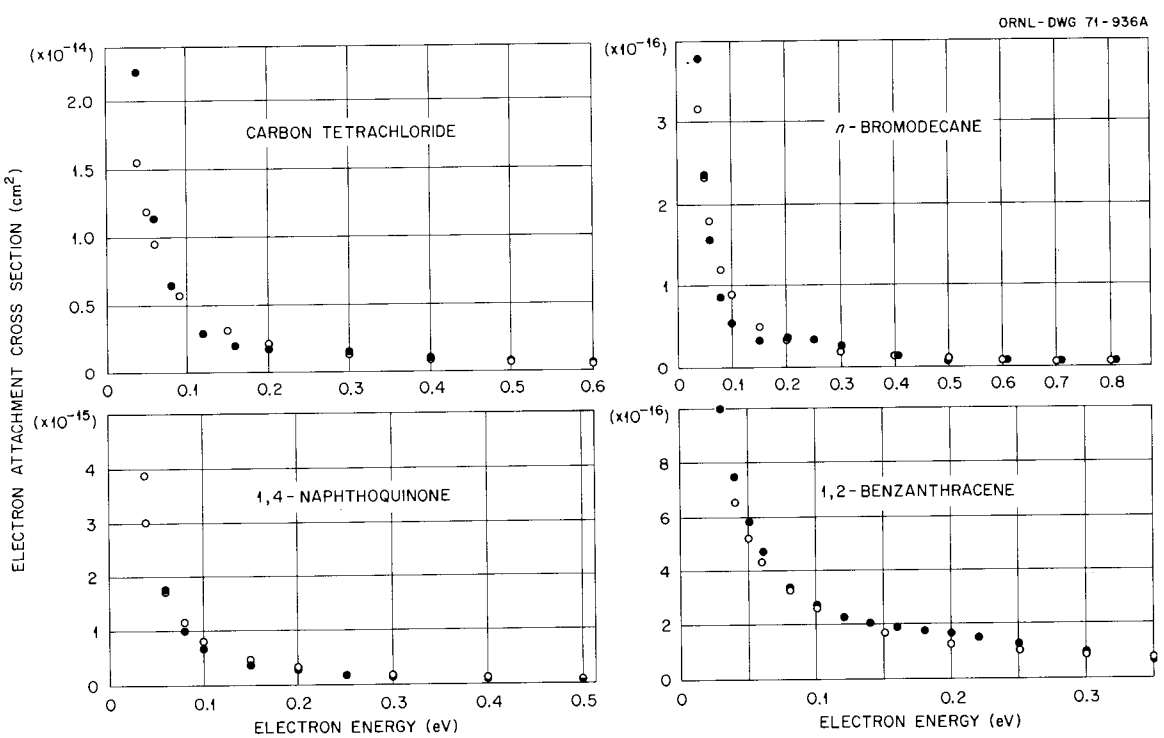

Fig. 10.2. Electron attachment cross section as a function of electron energy for carbon tetrachloride, *n*-bromodecane, 1,4-naphthoquinone, and 1,2-benzanthracene. Solid points are the result of the swarm-unfolding method (ref. 5). Open circles are the result of our earlier studies (refs. 7 and 8), where $\sigma_a(\epsilon)$ was assumed to be equal to A_γ/ϵ^γ at near-thermal energies (see Table 10.1).

Table 10.1. Swarm-determined data on electron attachment resonances with cross sections increasing sharply at thermal energies

Compound	$\sigma_a(0.05\ \text{eV})$ (cm^2)	γ	Energy range[a] (eV)	$(\alpha w)_{th}$[b] ($\text{sec}^{-1}\ \text{torr}^{-1}$)
Carbon tetrachloride	1.4×10^{-14}[c]	1.23[c]	≤0.6	9×10^{9}[d]
	1.2×10^{-14}[e]	1.226[e]		
n-Bromodecane	2.4×10^{-16}[c]	1.38[c]	≤0.85	2.4×10^{8}[f]
	2.3×10^{-16}[e]	1.398[e]		
1,4-Naphthoquinone	2.5×10^{-15}[c]	1.386[c]	≤0.5	1.9×10^{9}[g]
	2.2×10^{-15}[h]	1.412[h]		
1,2-Benzanthracene	5.8×10^{-16}[c]	1.07[c]	≤0.35	6.6×10^{8}[i]
	5.2×10^{-16}[c]	1.03[h]		
Anthracene	1×10^{-16}[h]	1.148[h]	≤0.3	1.5×10^{8}[i]
Sulfur hexafluoride	1.17×10^{-14}[h]	1.12[h]	≤0.11	8.8×10^{9}[h]

[a]This is the energy range in excess of $\frac{3}{2}kT$ for which $\sigma_a(\epsilon)$ can be approximated by Eq. (8).
[b]For 298°K.
[c]Ref. 5; swarm unfolding.
[d]R. P. Blaunstein and L. G. Christophorou, *J. Chem. Phys.* **49**, 1526 (1968).
[e]Ref. 8; assuming $\sigma_a(\epsilon) = A_\gamma/\epsilon^\gamma$.
[f]Ref. 8.
[g]P. M. Collins et al., *Chem. Phys. Lett.* **4**, 646 (1970).
[h]Ref. 7; assuming $\sigma_a(\epsilon) = A_\gamma/\epsilon^\gamma$.
[i]L. G. Christophorou and R. P. Blaunstein, *Radiat. Res.* 37, 229 (1969).

DISSOCIATIVE ELECTRON ATTACHMENT TO HALOGENATED ALIPHATIC HYDROCARBONS[8,9]

A systematic study has been made of a key series of halogenated aliphatic hydrocarbons in an effort to understand fully the process of dissociative electron attachment in polyatomic molecules and to obtain needed gaseous information for comparison with existing data on these molecules in the liquid phase. We have thus completed a swarm-beam study of a series of brominated aliphatic hydrocarbons of the form $n\text{–}C_NH_{2N+1}Br$ (N = 1 to 10) and initiated a similar one on iodine-containing compounds. For the $n\text{–}C_NH_{2N+1}Br$ molecules, the most abundant ion found below ~3 eV is Br^-. The dissociative attachment cross sections peak at energies ranging from 0.8 eV to $\frac{3}{2}\ kT$. A small decrease has been observed in the cross-section width with increasing reduced mass M_r of the $R(=n\text{–}C_NH_{2N+1})$-Br molecules. This and the increase in the dissociative attachment cross section with M_r were discussed within the resonance-scattering-theory treatment of dissociative electron attachment to diatomic molecules. A most interesting conclusion has been reached; namely, that as far as the fast ($\lesssim 10^{-14}$ sec) production of Br^- following electron capture by these molecules is concerned, these molecules can be considered as diatomic-like $R(=C_NH_{2N+1})$-Br systems.

9. L. G. Christophorou, J. G. Carter, P. M. Collins, and A. A. Christodoulides, *J. Chem. Phys.* **54**, 4706 (1971).

ELECTRON CAPTURE BY MOLECULES FORMING "MODERATELY SHORT-LIVED" NEGATIVE IONS UNDER HIGH-GAS-PRESSURE CONDITIONS

The effect of gas density on the nondissociative electron capture by O_2 and CO_2 molecules has been investigated. Both of these molecules are believed to form moderately short-lived ($\sim 10^{-10}$ to 10^{-12} sec) parent negative ions. An indication has been provided from these experiments that CO_2 attaches slow electrons directly at high gas densities. CO_2 does not capture slow electrons at low gas densities, but it is known to capture electrons with a large cross section in the liquid phase. The magnitude and the energy dependence of the capture cross section for O_2 to form O_2^- were found to depend strongly on gas density. These experiments were performed for total pressures of up to 7×10^3 torrs. They are currently being extended to total pressures of up to $\sim 5 \times 10^4$ torrs.

This will allow us to get into areas closer to the radiation effects problem by providing information at an intermediate phase between gaseous and condensed matter. They are part of our effort to bridge the gap in our physical understanding of electron-molecule interactions between gases and liquids.

LIFETIMES OF LONG-LIVED POLYATOMIC NEGATIVE IONS

Our time-of-flight mass spectrometer has been modified and greatly improved. A number of NO_2- and oxygen-containing benzene derivatives have been found[10] to capture electrons forming parent negative ions for times in excess of 10 μsec. Also a long-lived metastable parent negative ion has been found to form in hexafluoroacetone at thermal energies with a lifetime of ~60 μsec. For some of these (such as the nitrophenols) the negative-ion lifetime has been found to decrease drastically with increasing electron energy above $\frac{3}{2}$ kT. For *o*-nitrophenol, for example, the lifetime of the metastable parent negative ion was found to vary from ~350 μsec at ~0.0 eV to ~80 μsec at ~1 eV. These findings are consistent with those previously reported by us[10,11] on 1,4-naphthoquinone and *p*-benzoquinone. Detailed experimental studies are in progress, and an effort is being made to develop a theoretical understanding of the increase in autodetachment with increasing internal energy of the metastable ion. An effort is also under way to unfold the measured $\tau(\epsilon)$ functions using as a smearing-out function the electron pulse profile in order to obtain a better approximation to the true variation of the lifetime with energy. This variation is expected to be more drastic than that measured due to the large width of the electron pulse employed in our experiments.

SCATTERING OF SLOW ELECTRONS BY π-ELECTRON-CONTAINING ORGANIC MOLECULES

Some of the biologically most important molecules contain π electrons. Our earlier studies[12] on the scattering of thermal electrons by polar and nonpolar molecules indicated that π electrons strongly affect the molecular scattering of thermal electrons. A quantitative investigation of the role of π electrons in thermal electron scattering has been initiated, and experiments have been performed on a number of cyclic aromatic and nonaromatic compounds. Preliminary results indicate a profound effect on the magnitude of the cross section, which depends on the number of π electrons in the molecule. This effect is under further experimental and theoretical scrutiny.

THRESHOLD ELECTRON EXCITATION OF MOLECULES; LOCATION OF TRIPLET AND COMPOUND NEGATIVE-ION STATES

A highly improved electron scattering arrangement for studying threshold electron excitation of molecules is in full operation. Threshold electron excitation spectra were obtained for nitrogen, methane, and ethane. Nitrogen is used to calibrate the energy scale. The threshold electron excitation spectrum of methane obtained by us showed clearly a compound negative-ion resonance peak with a maximum at 2.5 eV, in accord with the transmission data of Boness et al.[13] No such resonance was observed in previous[14] threshold electron excitation studies of methane. For ethane, our threshold electron excitation spectrum distinctly evidenced for the first time a compound negative-ion resonance in the energy region between 1.7 and 3.5 eV. In the energy region above the ionization potential, our spectra resemble those obtained by Lassettre and Francis[15] in forward scattering using 390-eV incident electrons, but they are distinctly different from previously reported[14] threshold electron excitation spectra for these molecules in this energy region.

QUASI-EQUILIBRIUM THEORY OF UNIMOLECULAR DECOMPOSITIONS

Calculations of the rate at which an excited molecular species dissociates have suffered from two drawbacks. Conservation of angular momentum has been neglected, and the transition state formalism, with its attendant approximations, has been used. A new formalism based on microscopic reversibility has been developed[16] and applied to the unimolecular dissociation of excited ions.

---

10. L. G. Christophorou, J. G. Carter, E. L. Chaney, and P. M. Collins, *Proceedings of the IVth International Congress on Radiation Research,* Gordon-Breach (Paris), 1971.

11. P. M. Collins, L. G. Christophorou, E. L. Chaney, and J. G. Carter, *Chem. Phys. Lett.* **4,** 646 (1970).

12. See, for example, Christophorou et al., *Proc. Phys. Soc., London (At. Mol. Phys.)* **2,** 71 (1969); **3,** 1252 (1970).

13. W. J. W. Boness, J. W. Larkin, J. B. Hasted, and L. Moore, *Chem. Phys. Lett.* **1,** 292 (1967).

14. C. R. Bowman and W. D. Miller, *J. Chem. Phys.* **42,** 681 (1965); H. H. Brongersma, Ph.D. thesis, Amsterdam (1968).

15. E. N. Lassettre and S. A. Francis, *J. Chem. Phys.* **40,** 1208 (1964).

16. C. E. Klots, *J. Phys. Chem.* **75,** 1526 (1971).

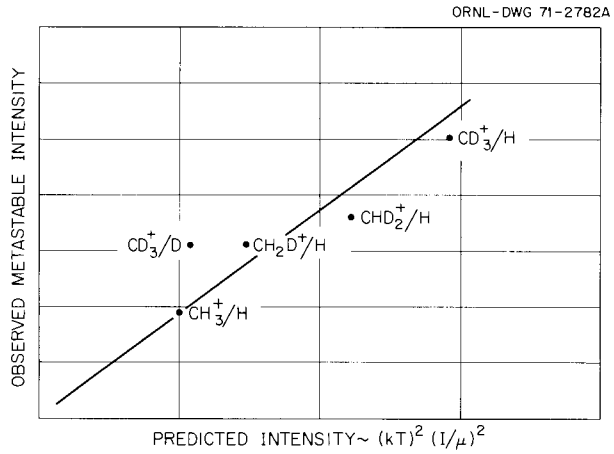

Fig. 10.3. Observed metastable intensity vs predicted intensity for several isotopic variants of methane.

Earlier formulations are shown to represent limiting cases of the present work, and a comparison with experimental data shows generally good agreement.

An especially interesting result of this work has been the demonstration that the delayed "metastable" decompositions of the methane positive ion occur via tunneling through a centrifugal barrier arising from the rotation of the parent ion. Figure 10.3 illustrates the correlation achieved between theory and the observed abundances of these hitherto inexplicable decompositions in several isotopic variants of methane.

IONIC FRAGMENTATION THROUGH CENTRIFUGAL BARRIERS

Quantum mechanical tunneling through a potential energy barrier is usually characterized by a strong dependence on mass. With the recognition[17] that tunneling through centrifugal barriers is important in the unimolecular decomposition of certain ions, it was of interest to calculate the associated mass dependence and hence the isotope effects to be expected. This has been done, using the Gamow theory of barrier penetration. The mass dependence is found to be negligible; the usual mass effect is overridden by the inverse dependence of centrifugal barrier height on mass. This accounts for the experimentally observed fact that tunneling rates do not vary significantly with isotopic substitution.

LINKING OF EXISTING DATA ON ELECTRON ATTACHMENT IN GASES WITH THOSE IN THE LIQUID PHASE[18]

An intense effort has been made to find ways to bridge the gap in our existing knowledge between electron capture processes in gases and those occurring in liquids. Thus we initiated a comprehensive study to evaluate, analyze, and relate gaseous data on electron attachment and data on hydrated-electron–molecule reactions. Some preliminary results of this study show that, indeed, gaseous data can be used for certain groups of molecules to predict liquid behavior very well. Further, there are strong indications that measured physical quantities on electron-molecule collision processes in gases can be used to predict the behavior of hydrated-electron–molecule reactions.

For the purpose of this study we separated the gaseous data into three groups according to the lifetime of the negative ion.

Molecular negative ions are of widely varying lifetimes τ and can be classified broadly[19] as (1) *extremely short-lived* ($\sim 10^{-15} \lesssim \tau \lesssim 10^{-12}$ sec), (2) *moderately short-lived* ($10^{-12} \lesssim \tau \lesssim 10^{-6}$ sec), and (3) *long-lived* ($>10^{-6}$ sec).

1. *Extremely short-lived molecular negative ions.* These show up as resonances in electron scattering experiments and/or in dissociative electron attachment studies and can be formed by electron capture in the field of either the ground or excited electronic states. For molecules for which on energetic grounds it can be argued that they cannot dissociate upon capturing a thermal electron and for which there is no evidence indicating that their electron affinity EA is positive, small electron attachment rates have been reported in the gas phase. These rates are actually about a million times less than the maximum (*s*-wave) thermal attachment rate[20] of 1.62×10^{10} sec^{-1} torr^{-1} and may be

17. C. E. Klots, *Chem. Phys. Letters* (in press).

18. L. G. Christophorou, *Proceedings of the Third Tihany Conference on Radiation Chemistry,* Tihany, Hungary, May 10–15, 1971 (in press).

19. L. G. Christophorou, *Atomic and Molecular Radiation Physics,* Wiley-Interscience, London, 1971.

20. The maximum thermal attachment rate is taken to be equal to

$$N_0 \int_0^\infty v\, \sigma(v)\, f(v)\, dv = 1.62 \times 10^{10}\ \text{sec}^{-1}\ \text{torr}^{-1} ,$$

where

$$\sigma_v = \frac{\pi \hbar^2}{m^2 v^2} = \pi \lambda\!\!\!^{-2} ,$$

$$f(v)\, dv = \left(\frac{m}{2\pi kT}\right)^{3/2} \exp\left(-\frac{mv^2}{2kT}\right) 4\pi v^2\, dv ,$$

$T = 298°$K, and

$N_0 = 3.24 \times 10^{16}$ molecules cm^{-3} torr^{-1} .

due to traces of impurities. The hydrated-electron reaction rates for all such molecules are far below the diffusion-controlled rate of $\sim 10^{10}\ M^{-1}\ \mathrm{sec}^{-1}$, which tends to suggest that even in the liquid phase EA $\lesssim$ $\frac{3}{2}\ kT$ for these systems.

Short-lived negative-ion intermediates (actually metastable negative ions of any lifetime) for which dissociative attachment is energetically possible can lead to molecular disruption, yielding fragment negative ions and free radicals. A number of such reactions have been investigated in both the gas[19] and the liquid phases.[21]

For the purpose of comparison of dissociative electron attachment data in gases with reaction rates with the hydrated electron $[R_{e(\mathrm{aq})}]$, one may separate the gaseous information into three broad groups:[18] (1) those for which $\epsilon_{\max} \leqslant \frac{3}{2}kT$, (2) those for which $\frac{3}{2}kT < \epsilon_{\max} \lesssim 1$ eV, and (3) those for which $\epsilon_{\max} > 1$ eV; $\epsilon_{\max}$ is the electron energy where the electron attachment resonance peaks. This separation is a realistic one since the rates for hydrated-electron reactions depend strongly on $\epsilon_{\max}$ (as do those in gases). For group (1) the attachment rates in gases far exceed those in the liquid, but it should be borne in mind that diffusion-controlled rates for hydrated-electron reactions are very much smaller (by $\sim 3 \times 10^4$) than those corresponding to $\pi\lambda\!\!\!^{-2}$ ($\lambda = \lambda\!\!\!^{-}2\pi$ is the de Broglie wavelength for the electron). Data on a number of molecules belonging to group (1) indicated[18] that the thermal rate of electron attachment in gases varies from one molecule to another much more than $R_{e(\mathrm{aq})}$ does. For this group of molecules $R_{e(\mathrm{aq})}$ attains values close to or in excess of the diffusion-controlled rate, while the thermal values of the gaseous attachment rates are smaller than their theoretical maximum, often by a large factor. This latter difference increases with increasing $\epsilon_{\max}$.

For groups (2) and (3) there are not enough data to allow deduction of realistically valuable conclusions. However, from the data summarized by Christophorou[18] it is indicated that the values of $R_{e(\mathrm{aq})}$ are smaller than the diffusion-controlled rates (but still high; $\sim 10^9\ M^{-1}\ \mathrm{sec}^{-1}$) for molecules in group (2), and are very low (generally $< 10^7\ M^{-1}\ \mathrm{sec}^{-1}$) for molecules in group (3) ($\epsilon_{\max} > 1$ eV). This is because in the liquid not many electrons attain energies far in excess of $\frac{3}{2}kT$ to cause dissociation.

2. *Moderately short-lived molecular negative ions.* These can be stabilized in high-pressure (swarm) experiments, but have not been detected in single-collision (low-pressure) beam experiments. The few inorganic molecules (O_2, NO, N_2O, H_2S, CO_2) on which gaseous information exists have been discussed by Christophorou[18] and indicated that, although these inorganic molecules capture very weakly thermal electrons in the gas phase, their reaction rates with the hydrated electrons are very high, indicating that for all these molecules the electron is captured into a bound state in the liquid environment.

More studies are needed on these systems, especially with respect to the effect of gas density. There is need, also, of a direct measurement of the autoionization lifetimes of such moderately short-lived negative ions. Presently, no method exists for measuring directly negative-ion lifetimes of less than 10^{-6} sec.

The reaction rates $R_{e(\mathrm{aq})}$ for these molecules are comparable with the diffusion-controlled rates. This is also the case for long-lived ($\tau > 10^{-6}$ sec) negative ions as is shown below.

3. *Long-lived molecular negative ions.* Molecules forming long-lived negative ions by electron capture in the field of the ground state (nuclear-excited Feshbach resonances[19]) are generally large, possess positive electron affinities, and are characterized by large electron attachment cross sections sharply increasing with decreasing energy at thermal energies. For all cases for which the functional dependence of the cross section has been determined (see Table 10.1 and refs. 5 and 7), $\sigma_a(\epsilon) \propto \epsilon^{-\gamma}$ with $1 \lesssim \gamma \lesssim 1.5$ within an energy region in excess of $\frac{3}{2}kT$ which varies from 0.1 to $\sim$0.5 eV depending on the molecule. These long-lived polyatomic negative ions can be detected in conventional mass spectrometers and can be studied in high-pressure (swarm) experiments. The two sets of experiments allow determination of the probability for capture and autoionization. Such data have been summarized and discussed[18] and indicated that for all molecules found to form long-lived molecular negative ions in the gas phase for which liquid data are available the hydrated-electron reaction rates are of the order of $2 \times 10^{10}\ M^{-1}\ \mathrm{sec}^{-1}$ and vary very little from molecule to molecule. They seem *not* to depend on the magnitude of EA. On the basis of this study we were tempted to suggest that for all molecules for which it is known that either EA > 0 or $\tau > 10^{-6}$ sec or $\sigma_a(\epsilon)$ is increasing sharply at thermal energies, the rates of reaction of these molecules with the hydrated electron are around $2 \times 10^{10}\ M^{-1}\ \mathrm{sec}^{-1}$. This we suggested to be the case for a number of molecules given in ref. 18.

21. E. J. Hart and M. Anbar, *The Hydrated Electron*, Wiley-Interscience, New York, 1970.

PHOTOPHYSICAL STUDIES OF ORGANIC LIQUIDS AND SOLUTIONS; EMISSION SPECTRA FROM HIGHER EXCITED π-SINGLET STATES OF AROMATIC HYDROCARBONS IN SOLUTION

The first observation of light emission (fluorescence) from the second excited π-singlet state ($S_{1,0}$) of pyrene to the ground state ($S_{0,0}$) in solution has been reported by us over a year ago.[22] Such an observation is of extreme importance in photophysics, radiation physics and chemistry, and development of organic scintillation detectors. A search for similar emissions from other aromatic luminescent molecules in solution has been made. We have observed emission from the second excited π-singlet state from *n*-heptane solutions of 3,4-benzopyrene, 1,2-benzanthracene and some of its methyl derivatives, and 1,12-benzoperylene. All of these molecules are biologically important. Some of them are cancer-inducing chemicals and are quite commonly found in high levels in air impurity analyses. Detailed studies have been made of the normal and second-excited-state fluorescence for 3,4-benzopyrene, 1,2-benzanthracene, and especially for 1,12-benzoperylene. The fluorescence from the second excited π-singlet state depended very strongly on temperature, indicating

22. C. E. Easterly, L. G. Christophorou, R. P. Blaunstein, and J. G. Carter, *Chem. Phys. Lett.* **6**, 579 (1970).

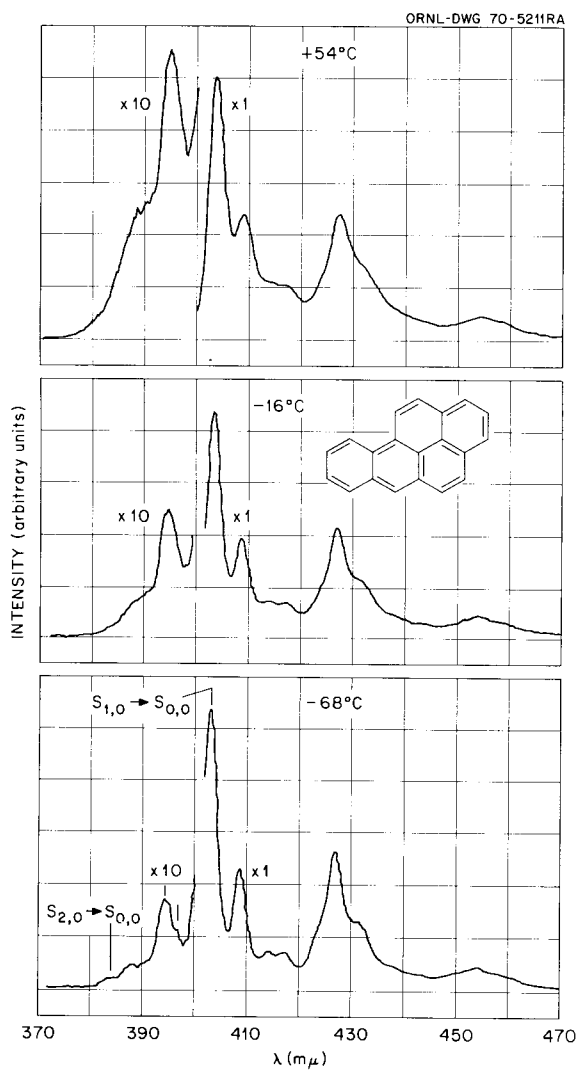

Fig. 10.4. Fluorescence spectra (taken in reflection) of a 10^{-4} *M* solution of 3,4-benzopyrene in *n*-heptane at −73, −18, and +57°C. Exciting wavelength is the 2537-Å Hg line.

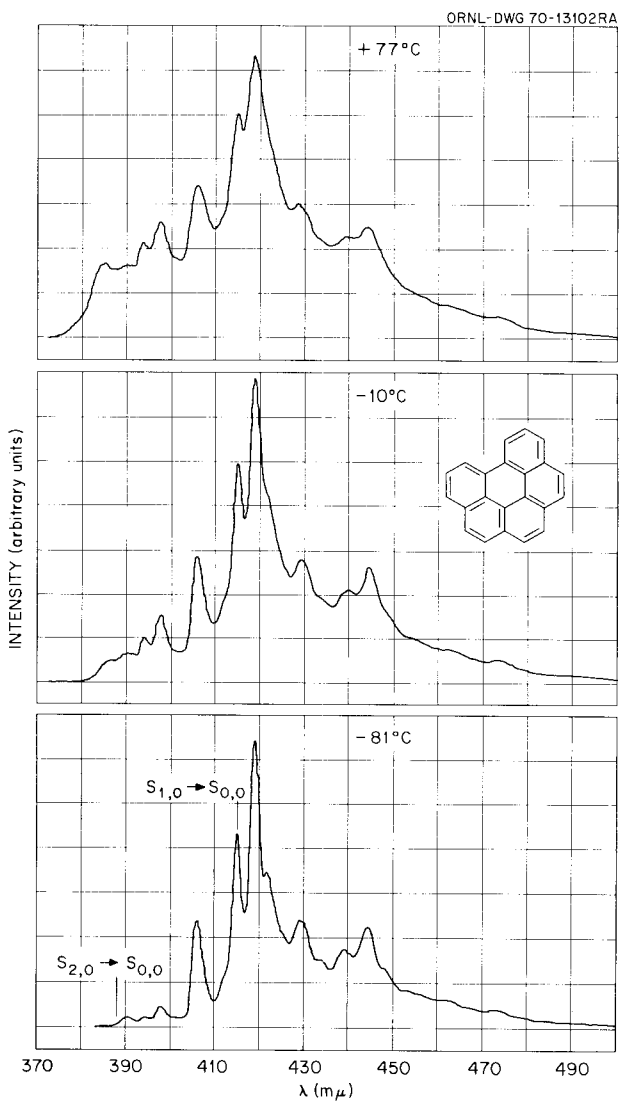

Fig. 10.5. Fluorescence spectra (taken at right angles) of a 5 × 10^{-6} *M* solution of 1,12-benzoperylene in *n*-heptane at +77, −10, and −81°C. Exciting wavelength is the 3030-Å Hg line.

that most of the light emission originating from the second excited state is due to thermal repopulation of the second excited singlet state from the first. A detailed analysis of the spectroscopic data is in progress. Figures 10.4 and 10.5 show examples of the data obtained for 3,4-benzopyrene and 1,12-benzoperylene.

11. Graduate Education and Vocational Training

K. Z. Morgan
M. F. Fair

R. D. Birkhoff
L. G. Christophorou
R. N. Compton
L. C. Emerson
W. R. Garrett
C. E. Klots
R. H. Ritchie
H. C. Schweinler
J. E. Turner
H. A. Wright

The field training program at ORNL during the summer months is open to all AEC Fellowship students who have completed their first academic school year under the fellowship program. In the past most of the Fellows have come from Vanderbilt University and The University of Tennessee; in recent years students have come from other schools participating in the program. The field training consists of two major phases, applied health physics and research health physics. The university program cannot, in itself, produce the desired product. The summer training program is absolutely essential in the education of a health physicist.

Six Fellows participated in the summer training program at ORNL during July and August 1970 – two from Vanderbilt, two from The University of Tennessee, one from Texas A & M, and one from Georgia Institute of Technology. Seven Fellows were in training during May and June 1971.

The summer training began with a three-day orientation program which was followed by five weeks with the applied health physics group and five weeks with the research health physics groups. One week was spent at the Special Training Division (ORAU) doing health physics experiments. Numerous seminars were held throughout the summer highlighting recent advances in health physics and closely allied fields. Many of the seminar speakers were from laboratories and universities from around the world.

In the applied health physics training, the student gains practical experience in all phases of radiation protection under the supervision of a senior health physicist.

In health physics research the students are first given a brief summary of all the research projects in progress in the Division. They then choose the group in which they remain for a five-week period. They become part of the team and are truly engaged in doing health physics research under senior scientist supervision.

The summer program gives the student sufficient experience in applied health physics to enable him to take a position in this field, where with only a little additional experience he will soon qualify for a position of responsibility in radiation protection. Also, he learns of the tremendous breadth in research health physics and is made aware of the diverse problems available for thesis work should he decide to continue his education for the M.S. or the Ph.D. degree.

Ten students were enrolled in the course in General Health Physics (Physics 4710-20-30) taught by a member of the Division at The University of Tennessee. This was a three-quarter course which met 3 hr/week. A course in Applied Radiation Physics (Physics 234) at Vanderbilt University was taken by nine students. This was a one-semester course which met 4 hr/week.

Seventeen universities were visited at which ORNL health physics research and educational activities were discussed.

There were a number of Oak Ridge Graduate Fellows, AEC Fellows, and USPHS students in the Division working on theses for advanced degrees. Their thesis titles are listed at the rear of this report.

The Division provided assistance to the staff of The University of Tennessee in updating and teaching its graduate curriculum in health physics. This included courses in General Health Physics, Radiation Chemical Physics, Physics of Polyatomic Molecules, Interaction of Electrons with Gases, Interaction of Electrons with Solids, and Interaction of Radiation with Matter. This

curriculum has attracted Fellows who desire education to the master's level and also those who wish to pursue the Ph.D. degree. Help was provided The University of Tennessee in conducting the co-op program with ORNL leading to the B.S. degree in Health Physics. This type of assistance and consultation is available to any school desiring to set up a health physics program or institute courses in this field. For example, queries have been received from Georgia Institute of Technology, Southern Technical Institute, Auburn University, Oklahoma State University, Duquesne University, and Wake Forest University with regard to setting up courses in Health Physics. Assistance was given Vanderbilt University and The University of Tennessee in the preparation of qualifying examinations in Health Physics. A visit to ORNL with lectures and tours was provided for students in Health Physics from the University of Arkansas. A series of lectures were given at the University of Alabama.

One member of the Education Group of the Health Physics Division helped in the screening of applicants for the 1970–1971 USAEC Fellowship Program. This work was done at the Oak Ridge Associated Universities (ORAU). Assistance was also given to ORAU in the presentation of a ten-week course in Health Physics.

Four student trainees and two faculty members spent the summer (1970) in the Division as research participants sponsored by ORAU. Three student trainees spent the summer of 1971 in the Division.

Several staff members of the Radiation Physics Section of the Health Physics Division worked with The University of Tennessee faculty in preparing preliminary examinations for the Ph.D. degree and in grading the examinations. Four of our staff hold Ford Foundation appointments at the University and in this capacity participated in student advising on matters of curricula and research. They were also active on the University Committee on Graduate Education. Our staff played prominent roles in the faculty meetings of the UT Physics Staff.

The demands for education in health physics have continued to rise. Although emphasis will be on education to the Ph.D. level to provide personnel for positions of leadership in industrial, academic, and medical institutions, education will continue to be offered during the summer at the master's level to provide vocational training which includes a knowledge of health physics principles and procedures. The needs of the reactor industry must be met by these and other efforts.

A proposal for a cooperative training program for Health Physics Technologists was submitted to the USAEC in May 1971. This program will be open to students who have completed the sophomore year at one of a number of participating colleges and who are majoring in one of the sciences, mathematics, or engineering. They will receive 20 weeks of on-the-job training at ORNL in coordination with their on-campus academic program. Ten weeks of specialized training will be given at a reactor site or hospital depending upon the student's main field of interest.

Part III. Radiation Dosimetry Research

J. A. Auxier

12. Dosimetry for Human Exposures and Radiobiology

J. W. Poston

J. A. Auxier
J. S. Cheka
W. L. Chen[1]
W. F. Fox
H. H. Hubbell, Jr.
J. E. Jackson
T. D. Jones
E. M. Robinson
W. H. Shinpaugh
W. S. Snyder
M. Sohrabi[1]

JAPANESE DOSIMETRY PROGRAM

Heavy Shielding Research

The cooperative program with the Atomic Bomb Casualty Commission (ABCC) in Japan has been concerned the past year with assisting them in computing radiation doses to the last 1100 or so of the survivors for whom shielding histories exist. Dose values had not previously been assigned to these cases. They constitute principally persons in heavy shielding situations, such as reinforced concrete buildings. The liaison representative from ORNL worked out and checked at ABCC a simplification of the procedure for evaluating the shielding effect of concrete walls having variable thickness, because of built-in posts, etc. The average concrete thickness is used in such cases, and calculations show a maximum error introduced in the final dose of only 2 to 3%. This simplification will save considerable time.

In order to refine the techniques and input data for such heavy shielding calculations, a large collimator which had been used in the Nevada Test Site at Operations BREN and HENRE was brought to Oak Ridge and set up on the roof of Building 7710. It will be used to measure the angular distribution of the scattered neutron and gamma radiations reaching the building from the Health Physics Research Reactor (HPRR) on the other side of a hill. From these data the attenuation of the doses by the concrete building and the doses inside will be calculated to check those measured experimentally. It is expected that this work will permit refinement of the shielding calculation techniques used at ABCC and of civil defense calculations.

In Utero Exposure

For the correlation of specific biological responses such as thyroid carcinoma and effects of radiation on those who were in utero survivors in Hiroshima and Nagasaki, a complete description of the internal dose distributions is desirable. In 1970, results were presented for the contribution to dose from (1) the neutron field and from (2) photons produced by neutron interactions inside the phantom, for circular cylinders having heights of 60 cm and radii of 6, 12, and 15 cm, corresponding to the neck and adult human torsi. Dose data for the same phantoms are given here

1. Alien guest.

for gamma rays produced exterior to the phantoms. The photon field, external to the phantoms, was assumed to be isotropic, and its energy spectral distribution[2] is shown in Fig. 12.1. The corresponding dose distributions in the three phantoms are shown in Fig. 12.2. From these distributions and those presented in 1970, it appears that fetal size and directional orientation of the mother are relatively unimportant (except for an extremely late stage of fetal development) because the dose distribution curves are relatively flat across the fetus, ensuring a nearly constant level of exposure. The thyroid gland is not centered in a sagittal plane through the neck, and consequently, unlike the fetus, is not uniformly exposed. Orientation of the survivor is still not very important because contributions to the radiation field are nearly symmetrical with respect to direction.

2. E. A. Straker and M. L. Gritzner, *Neutron and Secondary Gamma-Ray Transport in Infinite Homogeneous Air,* ORNL-4464 (December 1969).

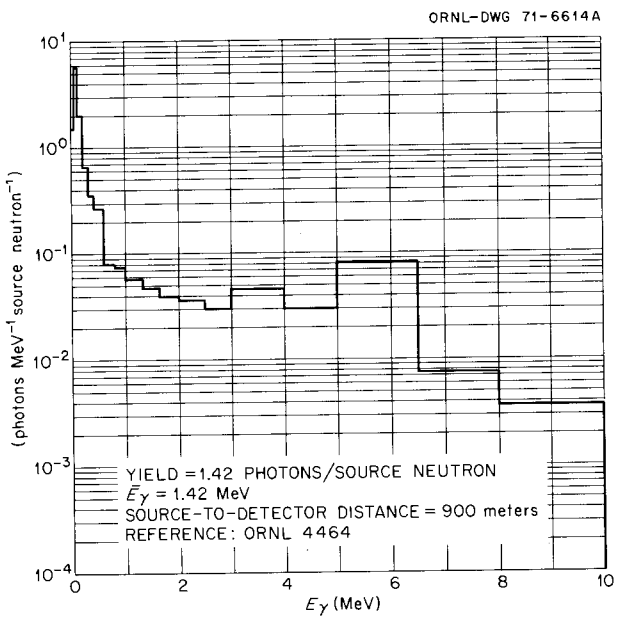

Fig. 12.1. $4\pi R^2$ photon energy spectrum produced by a distant nuclear explosion in an infinite air medium.

CALCULATIONS OF DOSE AND LET DISTRIBUTIONS FOR NEUTRONS AND GAMMA RAYS

Californium-252 – Therapeutic Sources

Distributions of dose equivalent (DE), linear energy transfer (LET), absorbed dose from neutron-produced photons, and absorbed dose from neutron-produced recoil ions from therapeutic implanted and external sources of ^{252}Cf were presented in 1970. The data in Table 12.1 were computed from Barker (1969)[3] and were used in a Monte Carlo sampling technique to choose the source energies of the photons. For internally located sources of ^{252}Cf, the contributions to dose and LET from photons emitted by the spontaneous fission of ^{252}Cf become quite significant. Figure 12.3 shows dose from electrons produced by photons emitted by the spontaneous fission of ^{252}Cf as

3. J. J. Barker (ed.), *Californium-252,* CONF-681032 (1969).

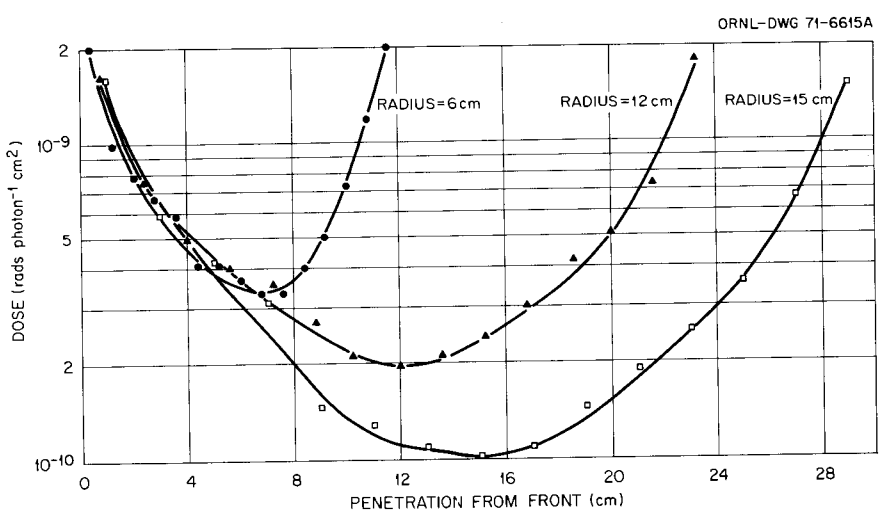

Fig. 12.2. Dose from the photon field external to the phantom.

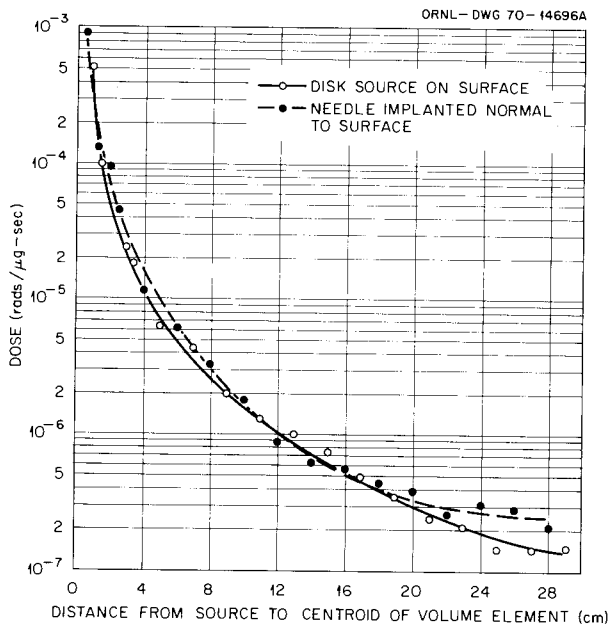

Fig. 12.3. Dose from fission-produced gamma rays as a function of distance from the centroid of a ^{252}Cf source.

Table 12.1. Probability of production of a photon having energy E from the spontaneous fission of ^{252}Cf

Energy (MeV)	Probability
0 to 0.5	0.3479
0.5 to 1.0	0.4312
1.0 to 1.5	0.1286
1.5 to 2.0	0.0582
2.0 to 2.5	0.0166
2.5 to 3.0	0.0083
3.0 to 3.5	0.0042
3.5 to 4.0	0.0022
4.0 to 4.5	0.0012
4.5 to 5.0	0.0006
5.0 to 5.5	0.0003
5.5 to 6.0	0.00014
6.0 to 6.5	0.00008
Total	0.9986

a function of distance from the source to the centroid of the volume element of interest. For internally located therapeutic sources of ^{252}Cf, the contribution from these photons is extremely important and must be taken into account. Earlier work indicated that there is little, if any, air-tissue interface effect on dose for normally oriented needle-implanted sources; however, several therapists recently became concerned about the magnitude of the change in dose to a tumorous region for an implanted source lying parallel to and within a distance of about 0.5 cm of the air-tissue interface.

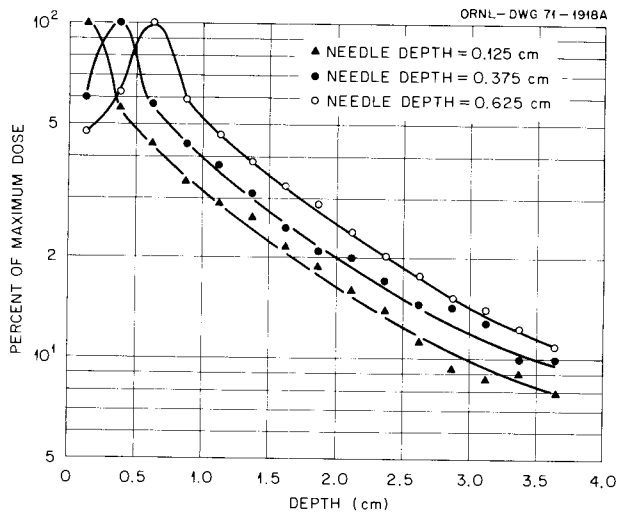

Fig. 12.4. Percent of maximum dose vs depth for ^{252}Cf needles implanted parallel to the surface.

There has even been speculation that the dose to a tumorous region may be decreased by from 4 to 25% relative to the infinite medium geometry.

Figure 12.4 shows the interface effect on dose in a 30-cm cube of tissue-equivalent medium for ^{252}Cf needles, implanted parallel to the surface at depths of 0.125, 0.375, and 0.625 cm. Coefficients of variation for the maximum or peak values (in units of dose) of the three curves shown in Fig. 12.4 were less than 0.05, while the spread of the three maximum values (in units of dose) was only 0.08, and no explainable systematic deviation was apparent. Thus, from these calculations the nearness of an air-tissue interface appears to have no significant effect on the dose from implanted ^{252}Cf needles.

Broad-Beam Neutron Exposures

A recurring problem in dosimetry is the comparison of calculational results to experimental ones and the determination of how closely and over what energy range they should agree. In many exposure situations, one can simply measure dose from either the hydrogen elastic or the $^{1}H(n,\gamma)^{2}H$ reactions and account for about 90% of the dose, but one has to know which reactions to consider for a specified geometry and source energy and under what conditions it is desirable to consider both reactions. Usually these two reactions, either individually or together, depending upon phantom geometry and source energy, account for at least 90% of the dose. At energies below about 2.5 MeV the $^{14}N(n,p)^{14}C^{*}$ reactions account for most of the

remainder, but for higher energies the remainder is usually broken up among several different reactions.

The whole-body contributions to dose from $^1H(n,\gamma)^2H$, $^{14}N(n,p)^{14}C^*$, and hydrogen elastic reactions in cylindrical tissue-equivalent phantoms corresponding in size to a rat, rabbit, and man are given in Fig. 12.5. For low source energies (rat, $E \lesssim 1$ keV; rabbit, $E \lesssim 10$ keV; man, $E \lesssim 100$ keV), most of the contribution to dose comes from the $^1H(n,\gamma)^2H$ reactions with nearly all of the remainder from the $^{14}N(n,p)^{14}C^*$ reactions. Structure characteristic of the curves for fraction of dose from $^1H(n,\gamma)^2H$ appears to occur at an increase in energy by about an order of magnitude for the comparison of rat to rabbit and rabbit to man. Likewise, there appears to be a similar effect for the hydrogen elastic reactions associated with a decrease in energy. Sections of the curves from the $^1H(n,\gamma)^2H$ and the $^{14}N(n,p)^{14}C^*$ reactions have been plotted on the distributions for the hydrogen elastic reactions in order to illustrate which reactions need to be considered for a given source energy and phantom geometry. The fraction of total dose from $^1H(n,\gamma)^2H$ reactions as a function of penetration depth inside the man phantom for various source energies is described in Fig. 12.6. Similar curves were computed for the rabbit and rat phantoms. One must be careful in the use of a single reaction for the description of total dose because of situations like the 100-keV neutron beam incident on the man-sized phantom shown in Fig. 12.6. For this case the $^1H(n,\gamma)^2H$ reactions contribute about 86% of the total dose to the phantom; however, at a penetration depth of 1 cm, it contributes less than 30% of the total local dose. Figure 12.5 indicates that the hydrogen elastic reaction is most important for a wide

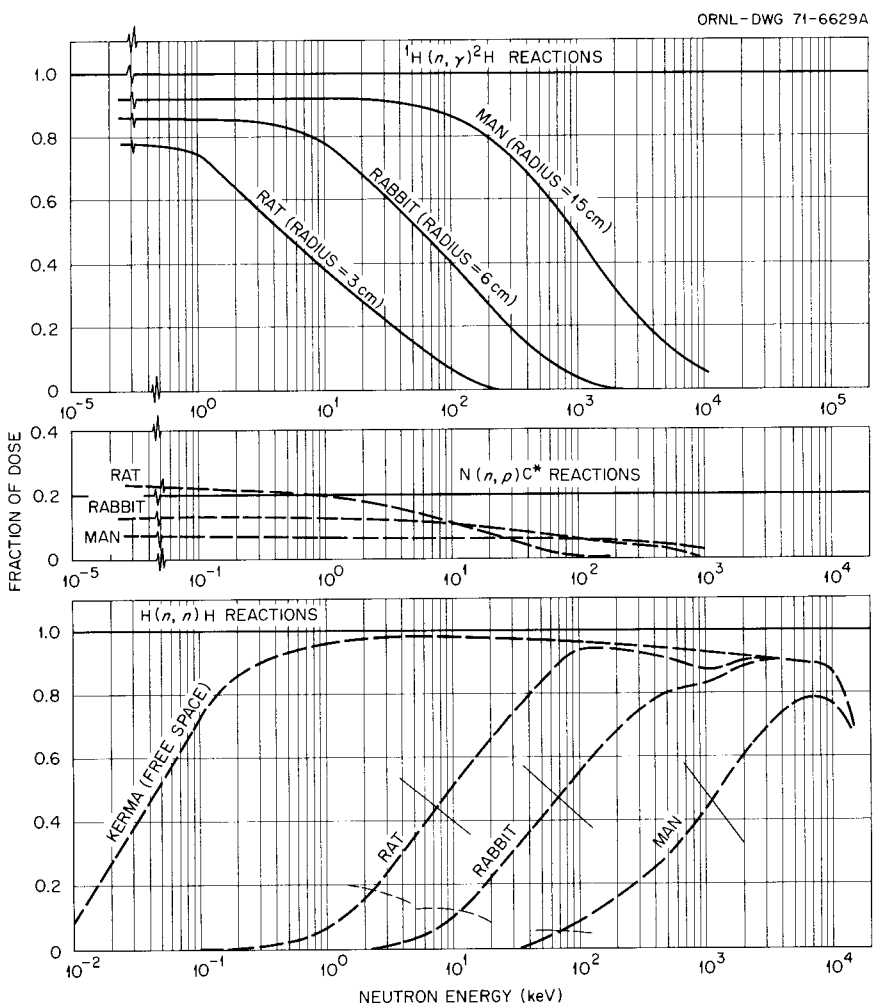

Fig. 12.5. Contributions to dose from important reactions in standard soft tissue from a broad parallel beam of monoenergetic neutrons.

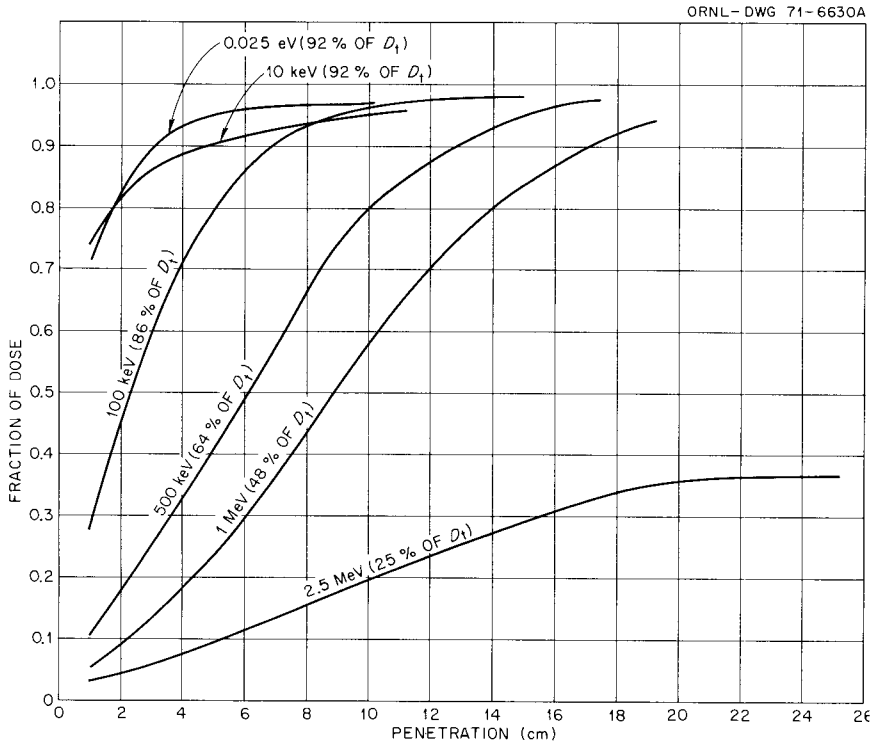

Fig. 12.6. Distribution of dose from $^1H(n,\gamma)^2H$ reactions in a man-sized phantom exposed to a broad parallel beam of monoenergetic neutrons.

range of source energies. Figure 12.7 shows dose as a function of penetration depth in a man-sized cylindrical phantom, exposed to a broad parallel beam of neutrons, having an energy spectral distribution equal to that of the HPRR. Table 12.2 expresses the distribution of the energy of neutrons produced by the HPRR. Column 3 is the probability that a particular neutron is in that specific energy range, and column 4 gives the probability that a given neutron has an energy inside of or greater than that specific energy range. Column 4 shows that about 89% of the neutrons emitted from the HPRR assembly have energies greater than about 160 keV. An energy cutoff of 160 keV was used, and dose from hydrogen elastic reactions only was recorded as a function of depth. This was done because of the response of the recoil proton proportional counter, used in measuring neutron dose, which has such an energy cutoff. It appears that 90% of the spectrum on the high-energy end of the distribution contributes 90% of the total dose from recoil ions, and the distribution does not significantly change from the distribution of the total dose. The change in the distribution of the fraction of dose per unit LET as a function of LET is more notable. The characteristic shape is basically the

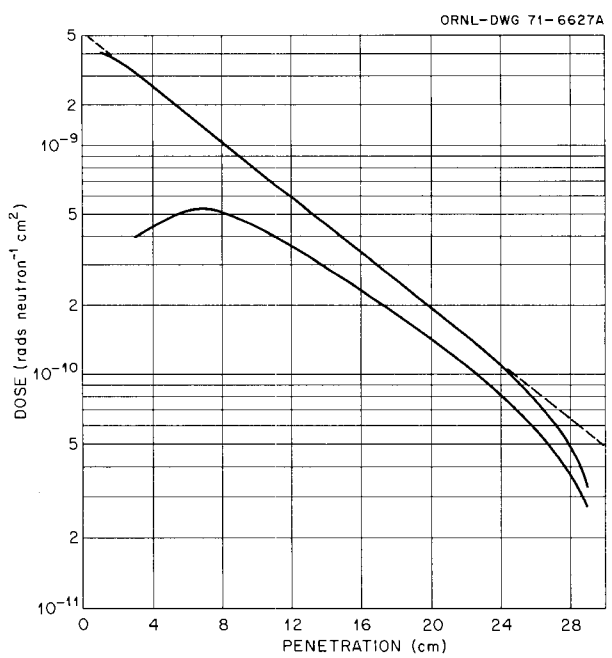

Fig. 12.7. Dose in a man-sized cylindrical phantom exposed to a broad parallel beam of neutrons having an energy spectral distribution equal to that of the HPRR.

Table 12.2. Distribution of the energy of neutrons produced by the HPRR

Group	Energy range $(E_U - E_L)$	$P(E_L < E < E_U)$	$P(E > E_L)$
1	14.92–3.01 MeV	0.0996	0.0996
2	3.01–1.50 MeV	0.179	0.279
3	1.50–0.91 MeV	0.157	0.436
4	0.91–0.41 MeV	0.268	0.704
5	0.41–0.11 MeV	0.188	0.892
6	110–87 keV	0.0123	0.904
7	87–67 keV	0.00907	0.913
8	67–52 keV	0.00679	0.920
9	52–41 keV	0.00539	0.925
10	41–32 keV	0.00438	0.930
11	32–25 keV	0.00372	0.934
12	25–19 keV	0.00321	0.937
13	19–15 keV	0.00285	0.940
14	15–7.1 keV	0.00711	0.947
15	7.1–3.4 keV	0.00596	0.953
16	3.4–1.2 keV	0.00669	0.959
17	1200–580 eV	0.00433	0.964
18	580–214 eV	0.00488	0.969
19	214–101 eV	0.00300	0.972
20	101–48 eV	0.00309	0.975
21	48–29 eV	0.00185	0.976
22	29–18 eV	0.00176	0.978
23	18–11 eV	0.00167	0.980
24	11–5.0 eV	0.00234	0.982
25	5.0–3.1 eV	0.00145	0.984
26	3.1–1.6 eV	0.00185	0.986
27	1.6–1.0 eV	0.00118	0.987
28	1.0–0.66 eV	0.00107	0.988
29	0.66–0.45 eV	0.000886	0.989
30	0.45–0.10 eV	0.00760	0.996
31	Thermal	0.00470	1.000

same, except that the high end of the LET distribution is lost. In addition to this, there is a shift of dose from both high and low LET to the 10-to-40-keV/μ region. For a 14-MeV neutron source and an energy cutoff of 160 keV, Fig. 12.8 shows that dose from hydrogen elastic reactions consists of about 65% of the total and is distributed more uniformly through the phantom than is total dose. Thus under these conditions a dosimeter that is only sensitive to proton recoils should not agree closely with curves for total dose. Figure 12.9 shows that there is also a significant shift toward low LET for the distribution of dose as a function of LET, and LET measurements should take this fact into account.

Photon Exposures

The heterogeneous phantom discussed in ORNL-4584 (ref. 4) was assumed to be unilaterally irradiated by a

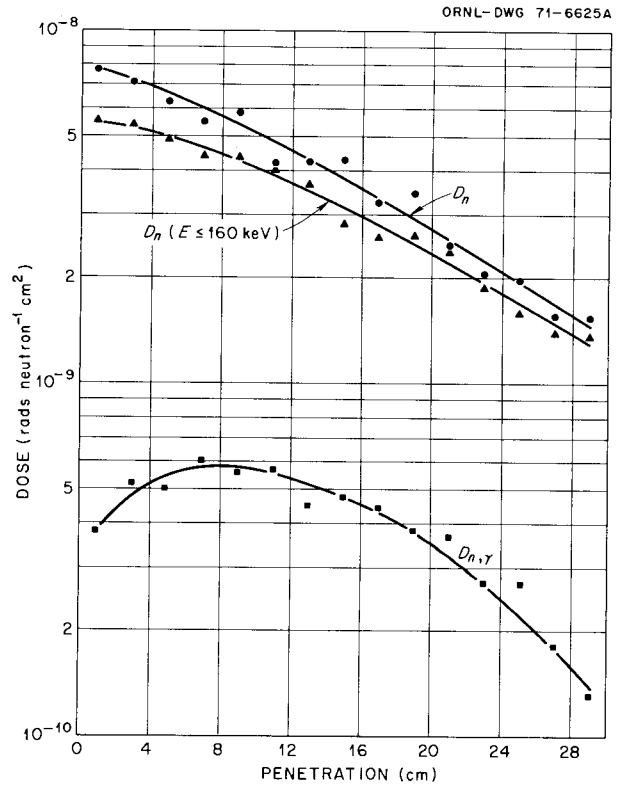

Fig. 12.8. Dose in a man-sized cylindrical phantom exposed to a broad parallel beam of 14-MeV neutrons.

parallel beam of monoenergetic photons limited to incidence on the torso. It contained most of the important organs, and the skeletal approximation included both red and yellow marrow. Photons which entered the phantom were permitted to scatter into the legs and head region and even scatter back into the torso. The extent of the photon beam was determined by the projected area of the torso. Photon source energies were 50, 100, 250, and 660 keV, and 1.25, 3, 6, and 10 MeV.

Since the lower abdomen of the phantom is nearly free of bone, except for a small section of the pelvis which protrudes into tier 1, the results for these irradiations closely approach the homogeneous case and the curves for anterior irradiation. For anterior exposure the nearness of the lungs ($\rho \doteq 0.3$) and the effect of averaging dose to part of the spine into some of the volume elements may be seen in Fig. 12.10. Data for tiers 1, 2, and 3 do not show much "bone effect" for photon energies above 250 keV. At higher energies the "effect" appears to be lost due to (1) the longer mean

4. *Health Phys. Div. Annu. Progr. Rep. July 31, 1970,* ORNL-4584, p. 200.

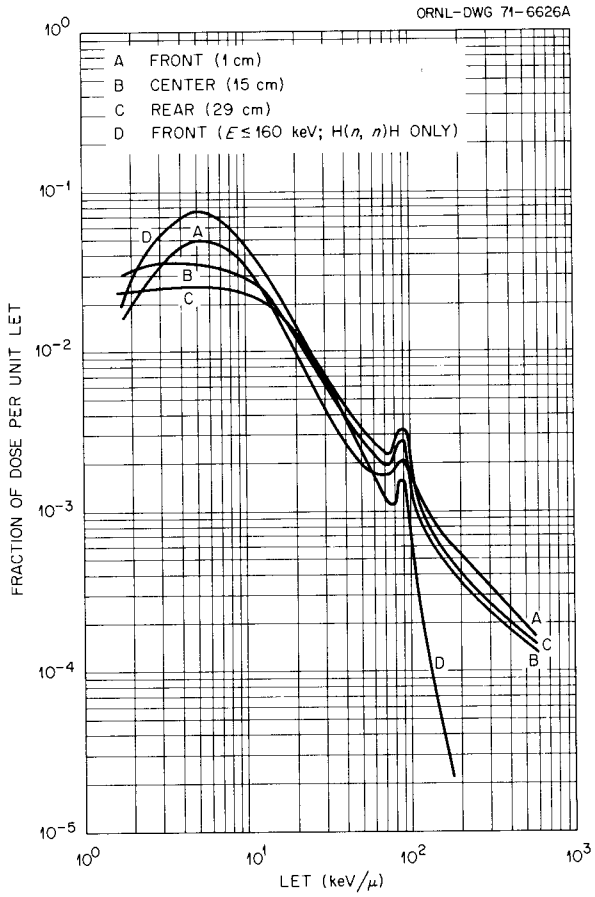

Fig. 12.9. Fraction of dose per unit LET as a function of LET from 14-MeV neutrons.

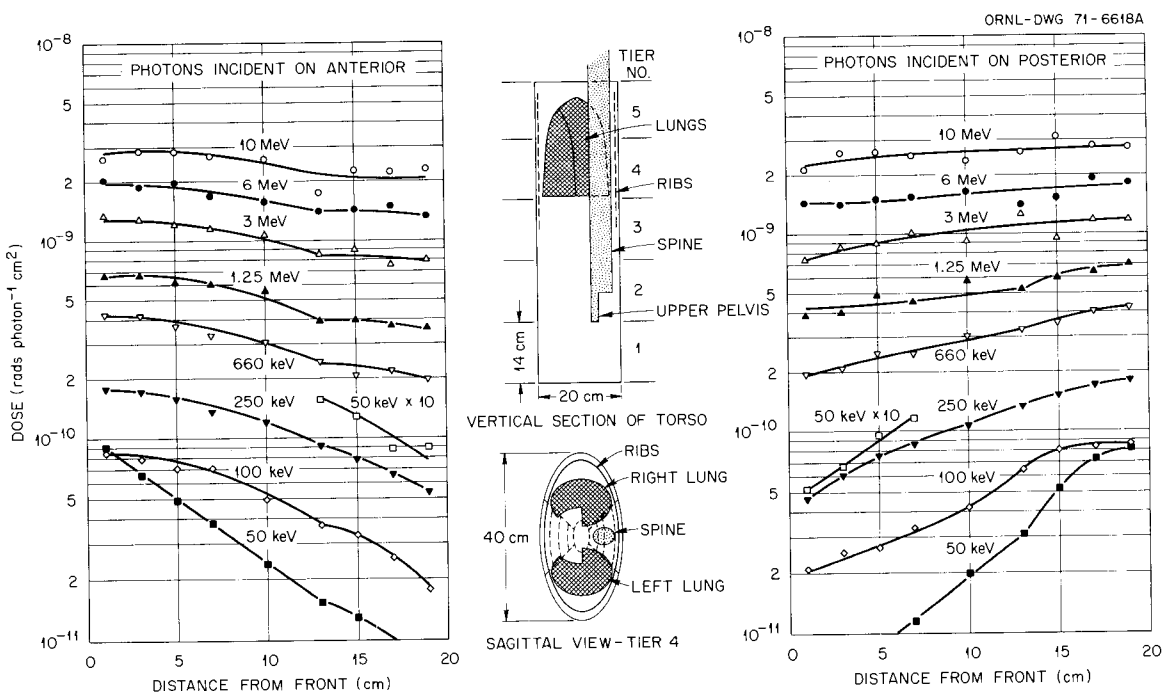

Fig. 12.10. Dose from a broad parallel beam of monoenergetic photons incident unilaterally on the chest of a standard 70-kg human.

collision path length which is inversely proportional to the linear absorption coefficient and to (2) an increase in the variance of the dose contribution to a given volume element.

Tables 12.3, 12.4, and 12.5 give doses to some organs of the human body for anterior, posterior, and left-side irradiation, respectively. Cases where doses have coefficients of variation larger than 0.20 should be checked against the depth-dose data in Figs. 12.10 and 12.11 before any use is attempted. The variations of dose to most organs generally tend to be linear with photon energy; however, the volume of the ovaries is only 8.8 cm^3, and statistical parameters are large enough that under no condition should the data from Tables 12.3, 12.4, and 12.5 be used without first checking them against plotted depth-dose data.

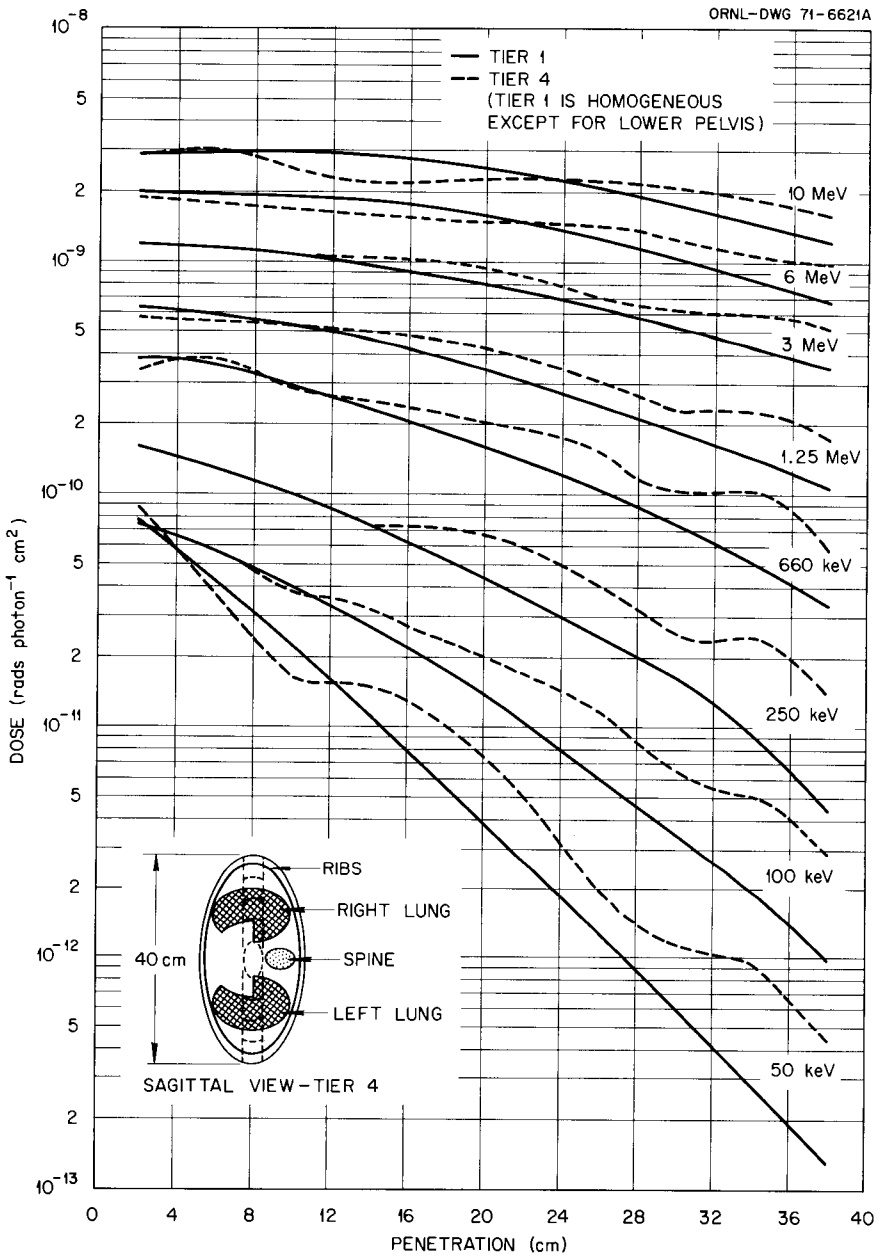

Fig. 12.11. Dose from a broad parallel beam of monoenergetic photons incident unilaterally on the left side of a standard 70-kg human.

Table 12.3. Dose to some organs of the human body irradiated by a broad parallel beam of monoenergetic photons incident on the anterior of the torso

Organ	50 kev		100 kev		250 kev		660 kev		1.25 Mev		3 Mev		6 Mev		10 Mev	
	Dose (rads γ^{-1} cm^2)	C. of V. (%)	Dose (rads γ^{-1} cm^2)	C. of V. (%)	Dose (rads γ^{-1} cm^2)	C. of V. (%)	Dose (rads γ^{-1} cm^2)	C. of V. (%)	Dose (rads γ^{-1} cm^2)	C. of V. (%)	Dose (rads γ^{-1} cm^2)	C. of V. (%)	Dose (rads γ^{-1} cm^2)	C. of V. (%)	Dose (rads γ^{-1} cm^2)	C. of V. (%)
1 Adrenals	6.94-12	34	1.55-11	21	4.16-11	25	6.20-11	29	4.87-10	35	6.31-10	35	1.47-9	38	1.66-9	52
2 Bladder	5.19-11	7	6.90-11	7	1.38-10	10	4.38-10	12	7.62-10	17	1.17-9	19	1.66-9	23	3.70-9	21
3 Contents	5.18-11	4	6.78-11	4	1.42-10	5	3.41-10	6	6.52-10	9	1.14-9	9	1.87-9	10	2.81-9	11
4 Clavicles	9.67-11	6	6.93-11	7	1.20-10	9	2.53-10	12	4.82-10	17	8.76-10	16	1.14-9	21	2.15-9	21
5 G.I. – stomach	5.37-11	4	7.60-11	4	1.67-10	5	4.10-10	6	5.80-10	11	1.01-9	11	1.45-9	13	2.86-9	13
6 G.I. – U.L.I.	3.74-11	4	5.93-11	4	1.43-10	5	3.06-10	6	4.98-10	10	9.72-10	9	1.57-9	11	2.88-9	11
7 G.I. – L.L.I.	2.60-11	5	4.62-11	5	1.26-10	6	3.20-10	7	5.15-10	11	1.02-9	10	1.74-9	12	2.72-9	13
8 G.I. – contents	5.44-11	2	8.72-11	2	2.03-10	2	4.98-10	3	8.43-10	4	1.59-9	4	2.46-9	5	3.88-9	5
9 G.I. – small int & contents	3.10-11	2	5.63-11	2	1.34-10	2	3.44-10	3	5.46-10	4	9.99-10	4	1.76-9	5	2.66-9	5
10 Heart	4.26-11	3	6.46-11	3	1.45-10	3	3.54-10	4	5.46-10	6	1.08-9	5	1.79-9	6	2.68-9	7
11 Kidney – left	8.58-12	11	2.40-11	8	6.46-11	8	2.38-10	9	3.08-10	14	8.55-10	12	1.99-9	12	2.47-9	14
12 Kidney – right	8.28-12	10	2.40-11	8	7.54-11	8	2.08-10	9	4.68-10	12	8.46-10	12	1.19-9	15	2.10-9	15
13 Liver	4.13-11	2	6.14-11	2	1.46-10	2	3.46-10	2	6.08-10	3	1.07-9	3	1.79-9	4	2.68-9	4
14 Lung – left	2.95-11	3	4.74-11	3	1.29-10	3	3.33-10	4	5.60-10	6	1.14-9	6	1.43-9	7	2.20-9	8
15 Lung – right	2.93-11	3	4.78-11	3	1.21-10	3	3.20-10	4	5.54-10	6	1.03-9	6	1.43-9	7	2.40-9	8
16 Ovaries	1.12-11	33	4.21-11	25	1.22-10	29	1.72-10	32	5.43-11	59	6.00-10	63	1.44-9	55	1.04-9	94
17 Pancreas	2.49-11	9	4.88-11	8	1.18-10	9	3.07-10	10	2.91-10	21	1.36-9	15	1.90-9	18	2.27-9	22
18 Pelvis	2.78-11	3	4.92-11	3	8.93-11	3	2.29-10	4	4.03-10	5	8.08-10	5	1.49-9	5	2.22-9	6
19 Ribs	8.26-11	2	7.42-11	2	1.11-10	2	2.89-10	3	4.90-10	5	8.81-10	4	1.55-9	5	2.34-9	5
20 Scapulae	1.97-11	6	3.25-11	5	6.74-11	6	1.96-10	7	3.95-10	9	7.90-10	9	1.46-9	10	2.03-9	11
21 Spine	1.05-11	4	3.02-11	3	5.88-11	3	1.64-10	3	2.88-10	5	6.65-10	4	1.07-9	5	1.81-9	5
22 Skeleton	2.41-11	1	2.79-11	1	4.98-11	1	1.26-10	1	2.14-10	2	4.18-10	2	7.07-10	2	1.08-9	2
23 Skin – trunk	3.90-11	1	4.41-11	2	1.19-10	2	3.18-10	2	5.29-10	4	1.05-9	3	1.75-9	4	2.72-9	4
24 Spleen	1.87-11	7	3.46-11	6	8.92-11	7	2.55-10	8	6.78-10	9	9.43-10	10	1.68-9	12	3.02-9	12
25 Thymus	5.07-11	10	8.70-11	9	2.02-10	11	4.21-10	16	4.70-10	25	1.00-9	25	2.13-9	27	3.19-9	30
26 Trunk – average	3.61-11	0.2	5.08-11	0.3	1.19-10	0.3	3.12-10	0.5	5.43-10	0.7	1.06-9	0.7	1.73-9	0.8	2.58-9	0.7
27 Uterus	2.17-11	9	3.91-11	9	9.84-11	10	2.13-10	14	3.86-10	20	7.61-10	19	1.14-9	28	2.78-9	20

Table 12.4. Dose to some organs of the human body irradiated by a broad parallel beam of monoenergetic photons incident on the left side of the torso

Organ	50 kev		100 kev		250 kev		660 kev		1.25 Mev		3 Mev		6 Mev		10 Mev	
	Dose (rads γ^{-1} cm^2)	C. of V. (%)	Dose (rads γ^{-1} cm^2)	C. of V. (%)	Dose (rads γ^{-1} cm^2)	C. of V. (%)	Dose (rads γ^{-1} cm^2)	C. of V. (%)	Dose (rads γ^{-1} cm^2)	C. of V. (%)	Dose (rads γ^{-1} cm^2)	C. of V. (%)	Dose (rads γ^{-1} cm^2)	C. of V. (%)	Dose (rads γ^{-1} cm^2)	C. of V. (%)
1 Adrenals	6.75-12	23	2.38-11	15	6.77-11	16	1.99-10	20	4.62-10	20	9.58-10	24	1.66-9	29	2.06-9	33
2 Bladder	6.55-12	12	1.44-11	10	4.74-11	11	2.08-10	11	3.52-10	13	9.99-10	13	1.23-9	18	1.83-9	19
3 Contents	4.91-12	9	1.63-11	6	4.85-11	6	1.70-10	6	3.28-10	7	7.35-10	7	1.36-9	9	2.22-9	9
4 Clavicles	2.40-11	7	2.28-11	8	4.36-11	10	1.21-10	11	2.49-10	12	6.51-10	13	1.11-9	15	1.43-9	17
5 G.I. – stomach	2.13-11	4	4.12-11	4	1.10-10	4	2.81-10	5	5.21-10	6	1.01-9	8	1.16-9	10	2.63-9	9
6 G.I. – U.L.I.	4.70-12	7	1.24-11	6	3.76-11	6	1.27-10	6	2.70-10	7	5.46-10	8	1.15-9	9	1.88-9	9
7 G.I. – L.L.I.	7.21-12	6	2.32-11	5	5.94-11	5	2.00-10	6	3.81-10	7	7.85-10	8	1.48-9	9	2.18-9	9
8 G.I. – contents	1.26-11	3	2.80-11	3	7.67-11	3	2.52-10	3	5.08-10	3	1.13-9	4	2.09-9	4	2.86-9	4
9 G.I. – small int & contents	7.48-12	3	2.01-11	3	5.98-11	2	1.81-10	3	3.47-10	3	8.24-10	3	1.37-9	4	2.05 9	4
10 Heart	1.06-11	4	2.24-11	3	7.06-11	3	2.33-10	3	4.36-10	3	9.28-10	4	1.49-9	5	2.46-9	5
11 Kidney – left	2.19-11	5	3.89-11	5	9.63-11	5	2.91-10	6	5.30-10	6	8.94-10	8	1.59-9	9	2.48-9	10
12 Kidney – right	1.43-12	21	5.36-12	12	2.71-11	9	1.11-10	9	2.68-10	9	6.78-10	9	1.12-9	11	2.05-9	10
13 Liver	1.42-12	6	6.20-12	4	2.34-11	3	9.85-11	3	2.26-10	3	5.72-10	3	1.16-9	3	1.73-9	3
14 Lung – left	1.79-11	2	3.38-11	2	9.73-11	3	2.67-10	3	4.82-10	4	9.04-10	4	1.51-9	5	2.43-9	5
15 Lung – right	1.05-12	9	5.28-12	5	2.60-11	5	1.02-10	5	2.74-10	5	6.16-10	5	1.13-9	6	1.79-9	6
16 Ovary	1.40-12	49	9.88-11	27	1.06-11	34	1.04-10	36	1.46-10	47	4.62-10	42	9.79-10	46	4.74-10	97
17 Pancreas	1.10-11	9	2.45-11	7	7.00-11	8	2.02-10	9	3.81-10	11	8.78-10	13	1.79-9	13	2.28-9	16
18 Pelvis	1.98-11	2	3.12-11	2	5.93-11	2	1.75-10	3	3.20-10	3	6.42-10	4	1.26-9	4	1.96-9	4
19 Ribs	4.43-11	1	4.20-11	2	8.12-11	2	2.14-10	2	3.81-10	3	7.99-10	3	1.44-9	4	2.12-9	4
20 Scapulae	5.68-11	3	4.24-11	3	7.63-11	4	2.00-10	5	3.53-10	5	7.59-10	6	1.31-9	7	1.89-9	8
21 Spine	8.65-12	3	2.12-11	3	4.98-11	2	1.46-10	2	2.78-10	3	6.18-10	3	1.11-9	4	1.66-9	4
22 Skeleton	1.75-11	0.7	1.83-11	0.8	3.43-11	1	9.01-11	1	1.62-10	1	3.42-10	2	6.07-10	2	9.21-10	2
23 Skin – trunk	3.12-11	1	3.64-11	1	9.63-11	2	2.72-10	2	4.88-10	2	9.59-10	3	1.65-9	3	2.50-9	3
24 Spleen	2.94-11	4	5.15-11	4	1.22-10	4	3.00-10	5	5.50-10	6	1.02-9	7	1.67-9	8	2.20-9	9
25 Thymus	3.78-12	21	1.46-11	16	4.98-11	15	1.27-10	19	4.12-10	17	6.62-10	22	1.74-9	21	2.31-9	24
26 Trunk – average	1.78-11	0.2	2.62-11	0.3	6.82-11	0.2	2.03-10	0.2	3.87-10	0.2	8.26-10	0.3	1.44-9	0.4	2.22-9	0.4
27 Uterus	3.23-12	16	1.09-11	10	3.49-11	11	1.78-10	12	2.69-10	13	5.13-10	16	7.26-10	20	1.31-9	20

Table 12.5. Dose to some organs of the human body irradiated by a broad parallel beam of monoenergetic photons incident on the posterior of the torso

	Organ	50 kev		100 kev		250 kev		660 kev		1.25 Mev		3 Mev		6 Mev		10 Mev	
		Dose (rads γ^{-1} cm^2)	C. of V. (%)	Dose (rads γ^{-1} cm^2)	C. of V. (%)	Dose (rads γ^{-1} cm^2)	C. of V. (%)	Dose (rads γ^{-1} cm^2)	C. of V. (%)	Dose (rads γ^{-1} cm^2)	C. of V. (%)	Dose (rads γ^{-1} cm^2)	C. of V. (%)	Dose (rads γ^{-1} cm^2)	C. of V. (%)	Dose (rads γ^{-1} cm^2)	C. of V. (%)
1	Adrenals	4.74-11	12	7.82-11	12	1.39-10	16	3.35-10	19	4.35-10	25	1.12-9	31	1.54-9	39	4.04-9	35
2	Bladder	1.16-11	13	2.72-11	10	7.45-11	12	2.21-10	14	4.86-10	16	1.40-9	17	1.83-9	20	2.54-9	24
3	Contents	9.02-12	10	2.46-11	7	7.43-11	7	2.19-10	8	3.94-10	9	9.47-10	10	1.51-9	11	2.69-9	11
4	Clavicles	9.03-12	17	1.74-11	12	3.25-11	15	9.64-11	18	3.27-10	16	4.32-10	22	1.05-9	21	1.85-9	21
5	G.I. stomach	1.38-11	7	3.51-11	6	8.11-11	7	2.45-10	8	4.90-10	9	1.07-9	10	2.17-9	11	2.39-9	14
6	G.I. U.L.I.	1.32-11	6	3.38-11	5	8.02-11	6	2.61-10	7	4.99-10	7	8.17-10	10	1.58-9	11	2.23-9	12
7	G.I. – L.L.I.	1.74-11	6	4.12-11	5	1.11-10	6	2.95-10	7	4.63-10	9	1.10-9	10	1.59-9	12	2.72-9	13
8	G.I. contents	2.15-11	3	4.96-11	3	1.31-10	3	3.70-10	3	6.81-10	4	1.42-9	4	2.43-9	5	3.35-9	6
9	G.I. small int & contents	1.88-11	3	4.40-11	3	1.14-10	3	2.97-10	3	5.34-10	3	1.03-9	4	1.49-9	5	2.61-9	5
10	Heart	1.14-11	5	3.03-11	4	7.79-11	4	2.50-10	4	4.43-10	5	8.80-10	6	1.29-9	7	2.38-9	7
11	Kidney – left	6.19-11	4	7.69-11	5	1.83-10	5	4.42-10	7	6.21-10	9	9.41-10	12	1.61-9	13	2.56-9	14
12	Kidney – right	5.87-11	5	7.52-11	5	1.83-10	5	4.08-10	7	6.67-10	8	1.14-9	11	1.95-9	12	3.99-9	11
13	Liver	2.54-11	2	4.43-11	2	1.07-10	2	3.15-10	2	5.41-10	3	9.81-10	3	1.63-9	4	2.65-9	4
14	Lung – left	2.60-11	3	4.60-11	3	1.23-10	3	3.28-10	4	5.22-10	5	9.26-10	6	1.64-9	7	2.80-9	7
15	Lung – right	2.70-11	3	4.30-11	3	1.25-10	3	3.24-10	4	5.67-10	5	1.04-9	6	1.52-9	7	2.33-9	8
16	Ovaries	1.54-11	25	4.68-11	22	7.93-11	29	2.53-10	32	3.39-10	43	1.29-9	41	8.08-10	59	1.85-9	62
17	Pancreas	2.16-11	10	5.13-11	8	1.18-10	9	3.16-10	11	4.43-10	15	1.09-9	16	1.56-9	20	2.31-9	22
18	Pelvis	8.27-11	2	9.01-11	2	1.46-10	2	3.25-10	3	5.43-10	4	9.74-10	5	1.57-9	5	2.28-9	6
19	Ribs	7.97-11	2	7.15-11	2	1.15-10	2	2.91-10	3	5.10-10	3	9.49-10	4	1.57-9	5	2.20-9	5
20	Scapulae	1.27-10	3	9.83-11	3	1.67-10	4	3.44-10	5	6.23-10	6	9.88-10	8	1.64-9	9	3.00-9	9
21	Spine	6.57-11	2	8.35-11	2	1.36-10	2	3.02-10	3	4.53-10	3	9.18-10	4	1.41-9	5	2.08-9	5
22	Skeleton	3.74-11	0.7	3.96-11	0.8	6.66-11	1	1.50-10	1	2.57-10	2	4.66-10	2	7.84-10	2	1.12-9	2
23	Skin – trunk	3.93-11	1	4.60-11	2	1.16-10	2	3.15-10	2	6.01-10	3	1.03-9	4	1.68-9	4	2.79-9	4
24	Spleen	4.65-11	5	7.12-11	5	1.57-10	5	3.60-10	7	5.68-10	8	1.13-9	10	2.00-9	11	2.14-9	14
25	Thymus	8.48-12	22	2.32-11	18	7.82-11	18	1.88-10	23	3.67-10	25	4.67-10	35	8.50-10	42	1.81-9	36
26	Trunk – average	3.66-11	0.2	5.10-11	0.3	1.19-10	0.3	3.12-10	0.4	5.44-10	0.4	1.04-9	0.5	1.70-9	0.6	2.56-9	0.7
27	Uterus	1.04-11	13	2.97-11	9	8.08-11	11	2.00-10	14	2.88-10	17	7.58-10	18	1.45-9	20	1.53-9	25

Table 12.6. Effective Z for photon interactions in skeleton, lung, and soft tissue

Medium$_i$	i	Photoelectric		Compton		Pair production	
		$Z_{\mathrm{eff}(i)}$	$Z_{\mathrm{eff}(i)}/Z_{\mathrm{eff}(1)}$	$Z_{\mathrm{eff}(i)}$	$Z_{\mathrm{eff}(i)}/Z_{\mathrm{eff}(1)}$	$Z_{\mathrm{eff}(i)}$	$Z_{\mathrm{eff}(i)}/Z_{\mathrm{eff}(1)}$
Soft tissue	1	6.41	1.00	3.34	1.00	4.58	1.00
Lung	2	6.59	1.03	3.44	1.03	4.75	1.04
Skeleton	3	7.58	1.18	3.88	1.16	5.21	1.14

The variation of dose for unilateral exposure to the left side of the body is shown in Fig. 12.11 for a traverse through the lower abdomen and a traverse through the chest region of the body. It may be noted that there is a leveling effect of dose across the lungs because of the low density there and the long mean flight paths of photons. It appeared that there was a slight increase in dose to tissue behind the right lung for several energies, and, since the lungs had an atomic composition slightly different from that of soft tissue, it was assumed that the increase was due to greater absorption coefficient values in tissue. According to Evans,[5] Compton scattering varies with atomic number, the photoelectric effect varies according to the fifth power of the atomic-number, and pair production varies with the square of the atomic number. From this and the atomic composition of the different media, effective Z's for photoelectric, Compton, and pair production reactions in skeleton, lung, and soft tissue were computed, with the results shown in Table 12.6. Important reactions were Compton and photoelectric, which contribute equal amounts for $Z = 5$ and $E = 20$ keV; for energies below about 3 MeV, pair production is insignificant; however, effective Z's were computed for all reactions for the sake of completeness.

From Table 12.6, one would not expect a dose buildup in the tissue behind the right lung; therefore, the number of photon histories was increased by a factor of 4 in order to decrease the coefficient of variation by a factor of 2. The 660-keV case, the worst offender (as seen in Fig. 12.11), was recomputed. This calculation indicated that the dose curve was very flat across this region and that the previous apparent increase was purely a statistical phenomenon. For cases where the coefficients of variation are greater than about 0.20, problems indicate the existence of a nonnormal distribution because of the limited number of contributions. This is especially true for very small volumes such as the ovaries, where there are few contributing photon interactions.

5. R. D. Evans, *The Atomic Nucleus,* McGraw-Hill, New York, 1955.

Table 12.7 contains doses to red and yellow marrow in the human torso for the three exposure situations. Ribs of the skeletal approximation are closed and symmetrical; hence, doses to marrow of this region for anterior and posterior exposure are nearly identical. A depth-dose value equal to that for a penetration depth of 5 cm is commonly used by therapists for the dose to red marrow. Table 12.8 compares this assumption with the exposure situations from these calculations, and the assumption does not seem to be acceptable according to these results.

MEASUREMENTS OF DOSE DISTRIBUTIONS

Dose as a Function of Depth in a Tissue-Equivalent Phantom

A study was made of the dose deposited by fast neutrons at various depths in a tissue-equivalent phantom 30 cm in diameter and 60 cm high to simulate the human body. These measurements were intended to overcome several shortcomings in previous work as outlined by Hubbell and Auxier.[6]

The radiation sources used were the HPRR and a 14-MeV neutron generator. Doses due to recoil ions from neutron interactions and to gamma rays were measured separately. The gamma-ray doses measured for 14-MeV neutrons incident were those produced by neutron interactions in the phantom. For the HPRR case, the gamma-ray doses measured were due to neutron interactions in the phantom plus gamma rays from fission in the reactor core. In both cases, the doses due to neutrons and gamma rays scattered into the phantom from the surroundings were separately measured and subtracted. A gamma-ray dosimeter[7] having low neutron sensitivity was used, and the neutron detector was a small cyclopropane-filled proportional counter[8] of special design. Curves were plotted of the

6. H. H. Hubbell, Jr., and J. A. Auxier, "Review of Neutron Depth Dose Theory and Experiments," Health Physics Annual Meeting, Pittsburgh, Pennsylvania, June 1969.

7. E. B. Wagner and G. S. Hurst, *Health Phys.* 5, 20 (1961).

8. W. A. Mills and G. S. Hurst, *Nucleonics* 12(8), 33 (1954).

Table 12.7. Dose to bone marrow in the human torso irradiated by a broad parallel beam of monoenergetic photons incident on the anterior of the torso

		50 kev		100 kev		250 kev		660 kev		1.25 Mev		3 Mev		6 Mev		10 Mev	
		Dose (rads γ^{-1} cm^2)	C. of V. (%)	Dose (rads γ^{-1} cm^2)	C. of V. (%)	Dose (rads γ^{-1} cm^2)	C. of V. (%)	Dose (rads γ^{-1} cm^2)	C. of V. (%)	Dose (rads γ^{-1} cm^2)	C. of V. (%)	Dose (rads γ^{-1} cm^2)	C. of V. (%)	Dose (rads γ^{-1} cm^2)	C. of V. (%)	Dose (rads γ^{-1} cm^2)	C. of V. (%)
	Red and yellow marrow																
1	arm – left	7.21-11	4	6.60-11	5	1.26-10	5	3.21-10	6	5.35-10	9	8.27-10	9	1.37-9	11	2.56-9	10
2	arm – right	6.87-11	4	6.87-11	5	1.21-10	5	3.47-10	6	5.15-10	9	1.10-9	8	1.76-9	10	2.55-9	10
3	clavicles	9.67-11	6	6.93-11	7	1.20-10	9	2.53-10	12	4.82-10	17	8.76-10	16	1.14-9	21	2.15-9	21
4	pelvis	2.78-11	3	4.91-11	3	8.93-11	3	2.29-10	4	4.03-10	5	8.08-10	5	1.49-9	5	2.22-9	6
5	ribs	8.26-11	2	7.42-11	2	1.11-10	2	2.89-10	3	4.90-10	5	8.81-10	4	1.55-9	5	2.34-9	5
6	scapulae	1.97-11	6	3.25-11	5	6.74-11	6	1.96-10	7	3.95-10	9	7.90-10	9	1.46-9	10	2.03-9	11
7	spine – lower	1.07-11	8	3.50-11	6	7.09-11	6	2.04-10	6	3.58-10	10	8.50-10	8	1.27-9	10	2.44-9	10
8	spine – middle	1.25-11	5	3.39-11	4	6.52-11	4	1.81-10	4	3.30-10	6	7.47-10	5	1.25-9	6	2.01-9	6
	Yellow marrow only																
9	arm – lower left	8.37-11	3	7.48-11	3	1.49-10	4	3.64-10	4	5.85-10	6	1.21-9	6	1.92-9	7	2.87-9	7
10	arm – lower right	7.67-11	3	7.28-11	3	1.32-10	4	3.31-10	4	5.68-10	7	1.06-9	6	1.78-9	7	2.50-9	8
	Dose to Bone Marrow in the human Torso irradiated by a broad, parallel, beam of monoenergetic photons incident on the posterior of the torso																
	Red and yellow marrow																
1	arm – left	7.09-11	4	6.62-11	5	1.21-10	5	3.22-10	6	6.01-10	7	1.01-9	9	1.53-9	10	2.34-9	11
2	arm – right	6.70-11	4	6.62-11	5	1.12-10	5	3.01-10	6	4.70-10	7	1.08-9	8	1.94-9	9	2.59-9	11
3	clavicles	9.03-12	17	1.74-11	12	3.25-11	15	9.64-11	18	3.27-10	16	4.32-10	22	1.05-9	21	1.85-9	21
4	pelvis	8.27-11	2	9.01-11	2	1.46-10	2	3.24-10	3	5.43-10	4	9.74-10	5	1.57-9	5	2.29-9	6
5	ribs	7.98-11	2	7.16-11	2	1.15-10	2	2.91-10	3	5.10-10	3	9.50-10	4	1.57-9	5	2.20-9	5
6	scapulae	1.27-10	3	9.83-11	3	1.67-10	4	3.44-10	5	6.23-10	6	9.88-10	8	1.64-9	9	3.00-9	9
7	spine – lower	8.25-11	3	9.72-11	3	1.62-10	4	3.77-10	5	5.39-10	6	1.02-9	8	1.78-9	9	2.54-9	10
8	spine – middle	7.40-11	2	9.56-11	2	1.54-10	3	3.41-10	3	5.27-10	4	1.09-9	5	1.61-9	6	2.42-9	6
	Yellow marrow only																
9	arm – lower left	8.01-11	3	8.65-11	3	1.52-10	3	3.14-10	4	6.66-10	5	9.30-10	7	2.00-9	7	2.45-9	8
10	arm – lower right	7.34-11	3	6.89-11	3	1.29-10	4	3.01-10	5	5.55-10	5	1.07-9	6	1.98-9	7	2.69-9	8
	Dose to Bone Marrow in the human Torso irradiated by a broad, parallel, beam of monoenergetic photons incident on the left side of the torso																
	Red and yellow marrow																
1	arm – left	1.15-10	2	9.43-11	3	1.54-10	3	3.57-10	4	5.83-10	5	1.04-9	6	1.64-9	7	2.44-9	7
2	arm – right	2.29-13	38	1.84-12	16	7.13-12	13	4.60-11	10	1.34-10	9	4.57-10	9	7.40-10	10	1.18-9	10
3	clavicles	2.40-11	7	2.28-11	8	4.36-11	10	1.21-10	11	2.49-10	13	6.51-10	13	1.11-9	15	1.43-9	17
4	pelvis	1.98-11	2	3.12-11	2	5.93-11	3	1.75-10	3	3.20-10	3	6.42-10	4	1.26-9	4	1.96-9	4
5	ribs	4.43-11	1	4.21-11	2	8.12-11	2	2.14-10	2	3.81-10	3	7.99-10	3	1.44-9	4	2.12-9	4
6	scapulae	5.68-11	3	4.24-11	3	7.63-11	4	2.00-10	5	3.53-10	5	7.59-10	6	1.31-9	7	1.89-9	8
7	spine – lower	9.58-12	6	2.38-11	5	5.75-11	5	1.51-10	5	3.01-10	6	7.67-10	6	1.38-9	7	1.79-9	8
8	spine – middle	1.00-11	4	2.38-11	3	5.71-11	3	1.76-10	3	3.30-10	3	7.06-10	4	1.25-9	4	2.01-9	4
	Yellow marrow only																
9	arm – lower left	1.26-10	1	9.93-11	2	1.54-10	2	3.41-10	3	5.54-10	4	1.05-9	4	1.78-9	5	2.69-9	5
10	arm – lower right	2.06-13	31	1.48-12	14	7.31-12	10	3.65-11	8	1.15-10	8	3.86-10	7	7.73-10	7	1.37-9	7

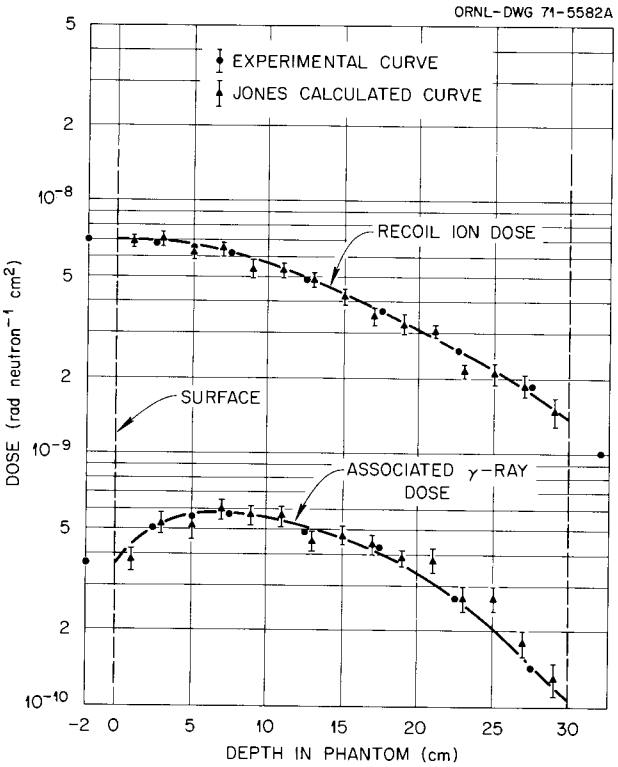

Fig. 12.12. Comparison of experimental depth-dose distributions for 14-MeV neutrons with calculations of T. D. Jones.

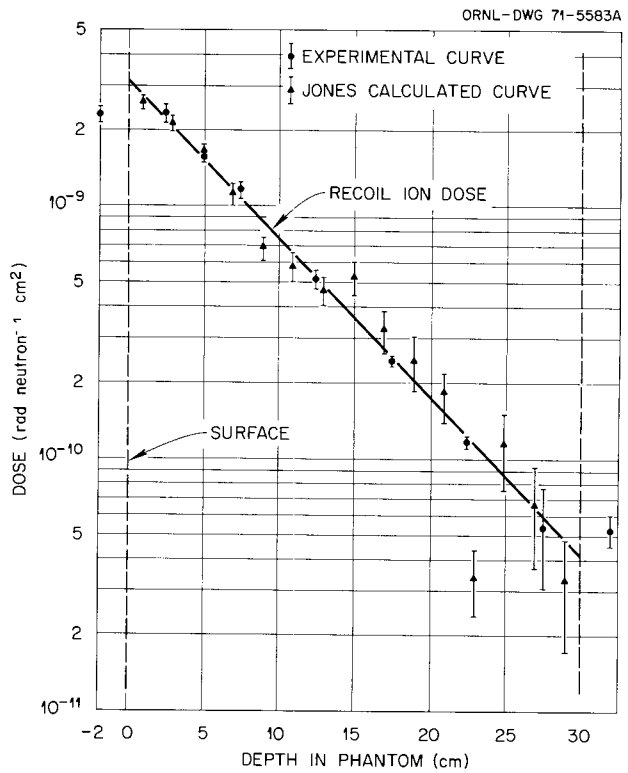

Fig. 12.13. Comparison of experimental depth-dose distribution for HPRR neutrons with calculations of T. D. Jones.

Table 12.8. Ratio of dose at a depth of 5 cm to average red marrow dose

Energy	Anterior	Posterior	Left side
6 MeV	1.3	~1	1.3
1.25 MeV	1.6	0.7	1.8
250 keV	2.0	0.5	2.0
50 keV	2.5	0.1	3.0

dose as a function of depth along the center line of the phantom perpendicular to its axis. The experimental data were analyzed by the "least-squares" method and fitted to an empirical equation of the form

$$D(X) = \frac{D(r)\, r^2 B^{-X/L}}{(r+X)^2} ,$$

where $D(X)$ is the dose rate at a depth of X centimeters in the phantom, $D(r)$ is the dose rate in air at the front surface of the phantom, r centimeters from the source, X is the depth in centimeters in the phantom measured from the front surface, B is the dose buildup at the surface of the phantom, that is, the ratio of the dose measurement at the front surface of the phantom to the measurement in air at that point without the phantom, and L is the relaxation length in centimeters. For the HPRR fission neutrons, the value of B was found to be 1.60, and the value of L was found to be 7.27 cm. For 14-MeV neutrons, B was found to be 1.88, and L was found to be 15.97 cm. The experimental results were compared with dose distribution curves which were calculated by the Monte Carlo statistical method.[9] The experimental results agreed with calculations within the standard deviations of either method (see Figs. 12.12 and 12.13).

Dose Distributions at Bone-Tissue Interfaces

Detectors[10] which facilitate the measurement of dose distributions at subcutaneous bone-tissue interfaces in a tissue-equivalent phantom have been described. The detectors rely upon the extrapolation ionization principle suggested by Failla.[11] These detectors have been

9. J. A. Auxier et al., *Health Phys. Div. Annu. Progr. Rep. July 31, 1965,* ORNL-3849, p. 171.
10. J. W. Poston et al., *Health Phys. Div. Annu. Progr. Rep. July 31, 1970,* ORNL-4584, pp. 152–55.
11. G. Failla, *Radiology* **29**, 202–15 (1937).

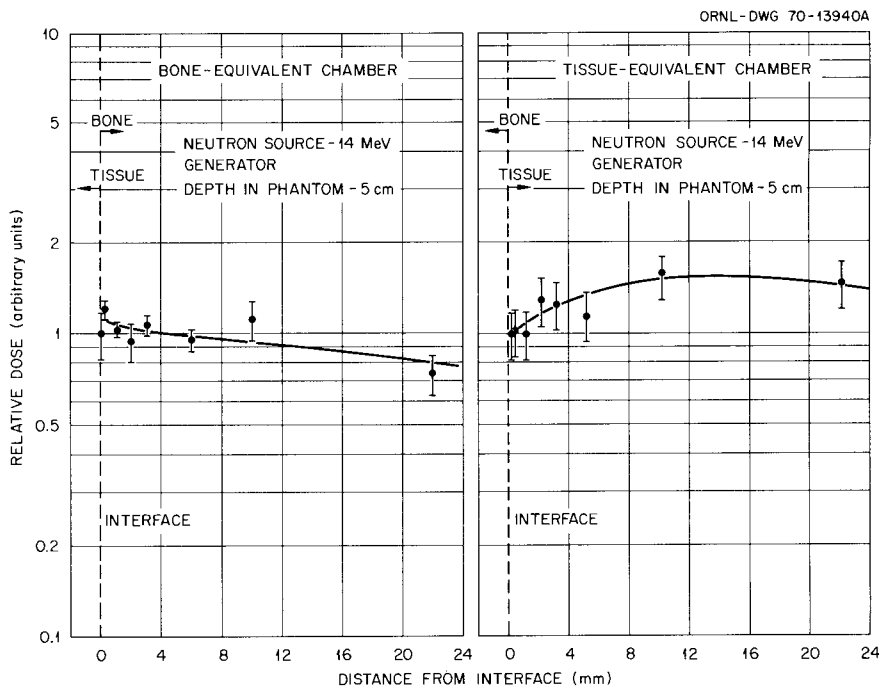

Fig. 12.14. Dose distribution in bone; dose distribution in tissue.

employed for measurement of dose distributions at bone-tissue interfaces due to incident fission neutrons from the HPRR.[10] The use of these detectors has been extended to measurements of distributions due to 14-MeV neutrons.

The DOSAR Low Energy Accelerator (DLEA) was the source of monoenergetic 14-MeV neutrons for this study. The experimental arrangement consisted of a standard[12] 30-cm cubical phantom filled with tissue-equivalent liquid[13] and located 0.50 m from the accelerator target. The center line of the phantom and the target were 0.96 m above the building floor. A Lucite tube, 5 cm in inside diameter with 0.635-cm-thick walls, was located along the center line of the phantom. This tube, which passes through the two parallel faces of the phantom, allows the movement of the ionization chambers through the phantom while isolating the detector from the liquid. Space in the tube not occupied by the detector is filled with tissue-equivalent material. Measurements were made only with the interface located at a depth of 5 cm. The interface was formed by use of tissue- and bone-equivalent plastics.[14,15]

Dose distributions near the interface resulting from a 14-MeV monoenergetic neutron source are shown in Fig. 12.14. These results are essentially as expected; there is an increase in the dose as the interface is crossed from bone into tissue. The buildup is about 50% at a depth of 9 to 10 mm in the tissue. In the bone environment, there is a reduction of about 20% at a depth of 20 mm. These distributions actually represent a summation of the neutron and gamma dose distributions near the interface since the ionization chambers have essentially equal sensitivity to both radiations. Comparison of these results to calculated neutron dose distributions will not be possible until the components of the distribution can be separated.

Initial Nuclear Radiation

Over the past decade the Radiation Shielding Subcommittee of the National Academy of Sciences' Advisory Committee on Civil Defense has developed extensive criteria and engineering methods for protection against fallout radiations. However, for the initial radiations, both neutrons and gamma rays, such

12. "Clinical Dosimetry," *Natl. Bur. Stand. (U.S.) Handb.* 87, U.S. Department of Commerce, 1963.

13. H. H. Rossi and G. Failla, *Nucleonics* **14**, 32–37 (1956).

14. F. R. Shonka, J. E. Rose, and G. Failla, "Conducting Plastic Equivalent to Tissue, Air, and Polystyrene," pp. 160–66 in *Progr. Nucl. Energy, Ser. XII*, vol. I, Pergamon, New York, 1959.

15. C. L. Wingate, W. Gross, and G. Failla, *Radiology* **79**, 984–99 (1962).

criteria have been delayed because of the complexities of the problem and the lack of some important input data. Now it appears that the problem is manageable if the criteria are chosen properly. Two staff members of the Radiation Dosimetry Research Section were members of a "working group" picked by the subcommittee and given the responsibility of writing the criteria to be used as input in shielding calculations for the initial radiations from nuclear weapons.

A report of this study is published elsewhere[16] and is intended primarily for persons who are concerned with shielding for civil defense purposes and who are assumed to have a high degree of familiarity with this field. Typical of the recommendations and criteria given are:

1. A fission to fusion yield (energy) ratio of 50/50.
2. A "typical" intermediate thermonuclear neutron spectrum leaking from the weapon.
3. Because the direction to the detonation cannot be known in advance, the detonation is assumed to have occurred in a ring around the observer (equal probabilities in all directions).
4. The angular distribution of radiation at the shield be chosen such that the source would appear at an angle of elevation of 45° above the horizontal plane.
5. A source-detector distance of 1200 m in an infinite medium of air.

Information presented included source leakage spectra (neutron), neutron and gamma-ray spectra incident at the shield, energy and angular distributions and intensity relationships such as dose as a function of distance and source height, and peak overpressure as a function of weapon yield, height of burst, and distance.

16. J. A. Auxier, Z. G. Burson, R. L. French, F. F. Haywood, L. G. Mooney, and E. A. Straker, *Recommended Standard Free-Field Environment for Initial Radiation Shielding Calculations,* ORNL-TM-3396 (to be published).

13. Applied Dosimetry Research

Klaus Becker
J. S. Cheka
K. W. Crase[1]
R. B. Gammage
F. E. Gillespie[2]
A. Moreno-Moreno[3]
M. Sohrabi[3]

TSEE RESEARCH

TSEE Instrumentation

A new routine reader of the pulse-counting variety has been designed and built to facilitate rapid loading and readout of ceramic BeO disks of the type to undergo testing in a new personnel dosimeter. The disk is placed on a floating base which is then raised against a conducting ductile gold ring set on a solid roof. The object is to obtain good electrical contact when the faces of the BeO disk might be uneven in areas where electrical contact is desired. This is expected to result in a more convenient faster readout procedure and in better reproducibility of response.

Most of our earlier TSEE research has involved the use of conventional gas-flow G-M counters. Such counters have recently been used in the proportional region with the incorporation of a channel analyzer. Noise signals can be largely eliminated by use of the proper discrimination level. The advantages of this system are an eightfold increase in sensitivity due to an increased counting efficiency, better peak resolution, and a larger dynamic range due to reduced dead-time losses. For most TSEE research, the G-M counter has, therefore, been replaced by proportional counting equipment.

Another counter based on an ionization chamber and electrometer, as described in the last annual report, has been improved and used to investigate the response characteristics of ceramic BeO. The heater is enclosed in a stainless steel beaker flushed with helium to prevent filament oxidation and to increase the operational lifetime of the heater. A newly designed slide drawer allows more uniform heating of the surface of the sample and minimizes heat losses to the walls of the chamber. The modified heater control compensates for the increased thermal lag of the system and minimizes electrometer noise pickup from the heater. This results in better peak resolution and measurability of smaller emission currents. The TSEE response of 995 BeO to gamma doses between 0.3 and 10^7 rads has been measured with electrometer currents in the range of 10^{-14} to 10^{-10} A being produced. Similar response vs dose measurements were made for alpha and beta radiations (discussed later). The dynamic range of this detector is such that it provides overlap with the ranges of the G-M and proportional counters, and it easily allows measurement of radiation doses up to and beyond the saturation dose.

A low-energy electron accelerator was utilized to study the response characteristics of ceramic BeO to monoenergetic electrons, including energy response, LET dependence, and dose dependence. Acceleration properties provide monoenergetic beams of electrons with variable energy between 0.2 and 20 keV, with a maximum current of approximately 1 μA. Currents collected on the Faraday cup are measured by means of a low-leakage-current digitizer and scaler.

Detector Development

The effect of thin inert metal films, vacuum-deposited onto the ceramic BeO detector, has been discussed in the last annual report. It has since been discovered that sensitization can also be brought about by heat treatment without the presence of these metals. Heat treatment alone is more convenient, and there are no complications such as undesirable energy response due to the presence of a high-Z material. Scanning electron micrographs (Fig. 13.1) reveal the fate of the Au or Pt

1. AEC Fellow.
2. On loan from Instrumentation and Controls Division.
3. Alien guest.

PHOTO 1754 - 71

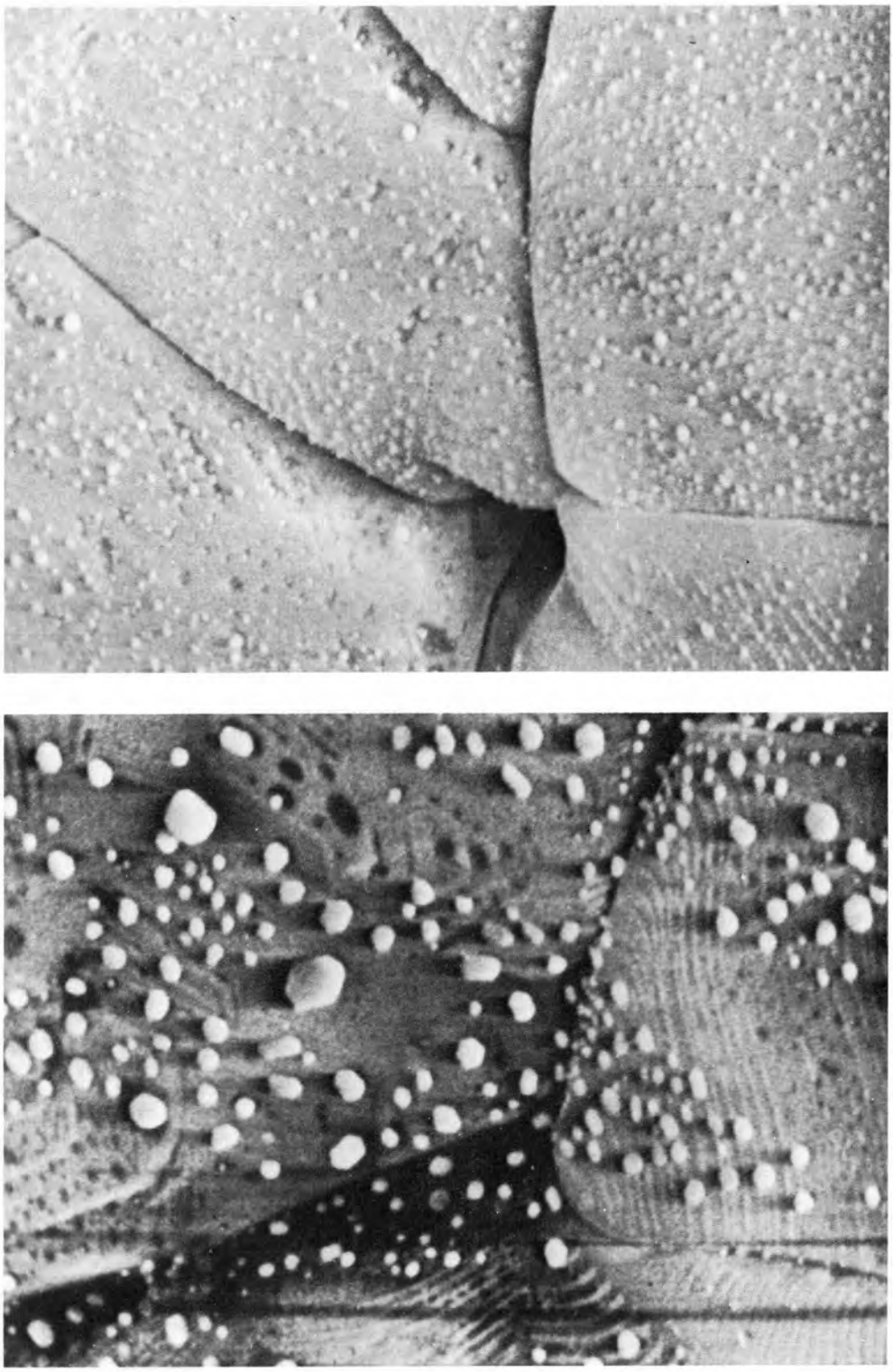

Fig. 13.1. Scanning electron micrographs of BeO 995 coated with gold and heated at 1000°C (bottom), and BeO 995 coated with platinum and heated at 1200°C (top).

film after high-temperature treatment: The originally continuous film breaks up into microcrystals preferentially aligned along growth steps.

Heat Sensitization

By heating Thermalox 995 BeO disks in air at 1400°C, the sensitivity and reproducibility between detectors can be maximized. For the main peak at about 325°C, the response increases by a factor of between 5 and 8 compared with the response in the "as-received" condition from the manufacturer (Brush Beryllium Company). The sensitization as a function of temperature is shown in Table 13.1, while in Fig. 13.2 the development of the sensitivity with time of heating is shown for temperatures between 800 and 1400°C. While the intensity of the ~325°C peak is markedly affected by thermal treatment, the two small peaks at higher temperatures show little, if any, change in intensity. Considerable effort has been expended in finding answers to two questions: In what way is the BeO conditioned at 1400°C, and what activator is responsible for the peak at ~325°C?

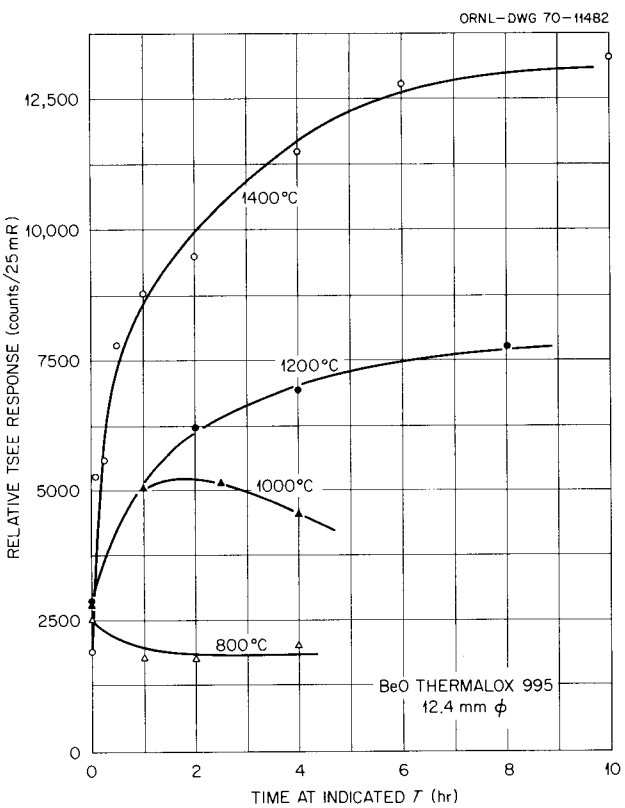

Fig. 13.2. Relative TSEE response (in counts per 25 mR) of a ceramic BeO as a function of preheating in air at different temperatures.

Table 13.1. Relative sensitivity (maximum = 1) of Thermalox 995 after heating for 4 hr at various temperatures

T (°C)	Relative sensitivity
650	0.17
800	0.17
1000	0.38
1200	0.6
1400	1.0
1400[a]	1.0
1500	0.12
1600	0.0
1800	0.0

[a]Sample reheated at 1400°C following the heating at 1500°C.

Silicon Activator[4]

Two types of ceramic BeO have been studied, the highly sensitive Thermalox 995 and the much less sensitive Thermalox 998. The response of 998 is quite erratic and lacks the pronounced ~325°C peak which is characteristic of 995. The major difference in these two ceramics lies in the silica impurity content. Silicon is the major impurity in 995 (2150 ppm); in 998 its concentration is reduced nearly thirtyfold.

The distribution of silicon in 995 was examined by electron microprobe analysis. Compared to the bulk, the concentration of silicon in the surface is some sixfold higher (~10^4 ppm). The surface scan shows peaks in the silicon concentration every few microns which probably correspond to silica segregated at imperfections such as growth steps and grain boundaries.

Etching the 995 in 48% HF leaches SiO_2 out of the nearly insoluble BeO. By this treatment, the dominant TSEE peak at 325°C as shown in Fig. 13.3 could be eliminated without affecting the smaller high-temperature peaks. Two methods have been used to enhance the concentration of silicon in the surface layer of the etched 995 in order to restore the peak at ~325°C. First, the ceramic was heated at 1400°C to promote diffusion of silicon from the bulk to the surface. Second, a thin layer (350 Å) of silicon was vacuum-evaporated onto the etched surface, oxidized, and then diffused into the BeO at 1400°C. In the former case the intensity of the TSEE peak was only partially restored, while in the latter case it was fully restored to the normal response of the unetched 995. These effects of

4. R. B. Gammage, K. W. Crase, and K. Becker, "Role of Silicon Activator in Exoelectron Emission from BeO," *Health Physics* (in press).

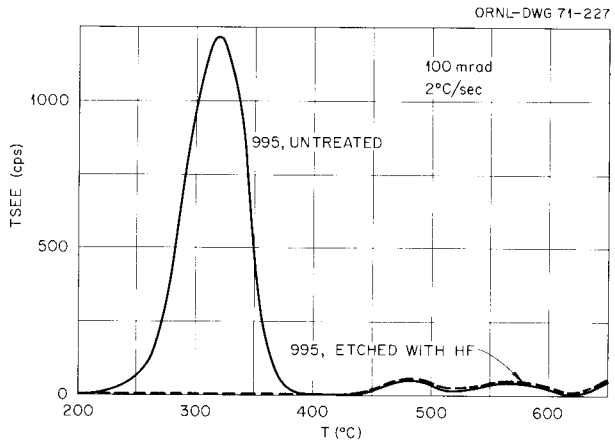

Fig. 13.3. Radiation-induced TSEE in Thermalox 995 before and after removal of SiO_2 by etching with concentrated HF.

etching and reimpregnation are reversible. For the relatively insensitive 998, silicon coating, oxidation, and heat treatment at 1400°C also induced, as expected, a strong TSEE peak at ~325°C. Thus 998 was made almost identical to 995 with regard to sensitivity.

Silica itself did not give appreciable TSEE signals. A coating of silicon (870 Å) was evaporated onto a brass plate and then oxidized; there was no TSEE even following radiation to a much higher dose. Obviously, the presence of silicon in BeO gives rise to strong exoelectron emission at ~325°C. It is suggested that within the exoelectron-emitting region, substitutional Si^{4+} in place of Be^{2+} acts as an electron trap because of its excess positive charge with respect to the normal lattice sites. Si^{4+} (0.41 Å) is a particularly suitable candidate for substitution because of its preference for tetrahedral coordination and its closeness in size to the Be^{2+} ion (0.31 Å).

The observed changes in exoelectron emission with heat treatment appear to be related to the phase diagram[5] for bulk $BeO\text{-}SiO_2$. Compound formation of phenacite ($2BeO \cdot SiO_2$) occurs below ~1560°C. Above ~1560°C and below the eutectic temperature (1670°C), the phenacite decomposes into solid BeO and solid SiO_2. By alternately heating Thermalox 995 at 1400 and 1600°C, the TSEE activity can be maximized and eliminated in a back and forth fashion. Thus it seems that in addition to substitutional silicon, the presence of phenacite is required for exoelectron activity. Heating above the eutectic temperature (e.g., at 1800°C to give solid BeO + liquid) permanently deactivates the 995. Possibly in the presence of liquids, macroscopic separation of SiO_2 and BeO can occur to make reformation of phenacite at 1400°C much more difficult. Thermalox 995 is not at maximum sensitivity after manufacture, because the original firing at 1560 to 1580°C produced an intimate mixture of BeO + SiO_2 (no TSEE response); presumably some phenacite formed as the 995 was cooled slowly through 1400°C with the development of some latent TSEE response.

5. E. M. Levin, C. R. Rolskins, and H. F. McCurdie, *Phase Diagrams for Ceramists*, American Ceramic Society, Columbus, Ohio, 1964.

Lithium Activator

Several other potential activators were examined for their influence on exoelectron emission. Cations studied were those known to go into solid solution from EPR studies (e.g., B, Al, and Li) and those suspected to do so because of their similarity in ionic radius to Be^{2+} (e.g., P^{5+}). Thus far we have only been successful in diffusing Li^{+} into the BeO and influencing the TSEE spectra. Lithium activation has the effect of increasing the intensity of the TSEE peaks at ~450 and ~550°C, up to fifty- and twentyfold, respectively. As can be seen from Fig. 13.4, maximum sensitization occurs at a diffusion temperature for the Li_2O of 1000°C. Unfortunately, the response is erratic. Perhaps the lithium

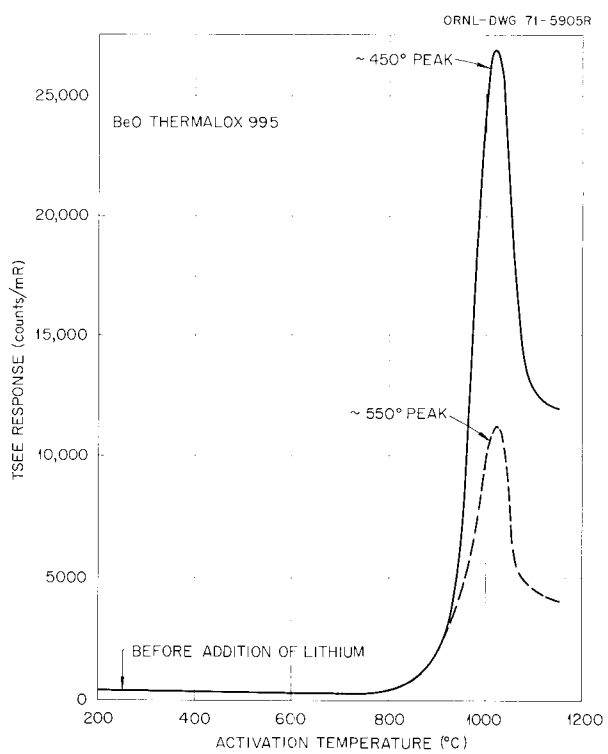

Fig. 13.4. Sensitization of BeO 995 by lithium diffused into the surface during heat treatment in air.

imparts hydrophilic character to the surface because of its highly polar nature, and this makes the surface of doped BeO more prone to chemical attack by atmospheric constituents, resulting in instability. Substitutional Li^+ is a hole trap in BeO, not contributing directly to any electron emission. Oxygen vacancies, formed to preserve charge neutrality as the Li^+ substitutes for Be^{2+}, are electron traps (F^+ centers), and these might be acting as the exoelectron emitter at high temperatures.

Radiation Damage

Exposure to high doses of alpha radiation also increased the relative intensity of the high-temperature TSEE peak as shown in Fig. 13.5. Believing that heavy-particle radiation damage would also be creating oxygen vacancies (as in lithium doping), the damage effects of an intense beam of deuterons on the TSEE properties have been studied. Intense bombardment of ceramic BeO by deuterons (10^{14} deuterons/cm^2) has a twofold action. First, the TSEE peak at 325°C is largely destroyed. After heating to 1400°C, however, the peak is restored to full intensity (1000 counts/mR). Second, the TSEE peak at 450°C is enhanced as a result of deuteron damage. Annealing at 950°C maximizes the intensity of this peak (80 counts/mR) without any redevelopment of the peak at 325°C. In this condition the ceramic BeO will record and store radiation effects in a high-temperature environment with a sensitivity of about 1 mR. The effects of deuteron irradiation and annealing are shown in Fig. 13.6, while the results of annealing as a function of temperature are contained in

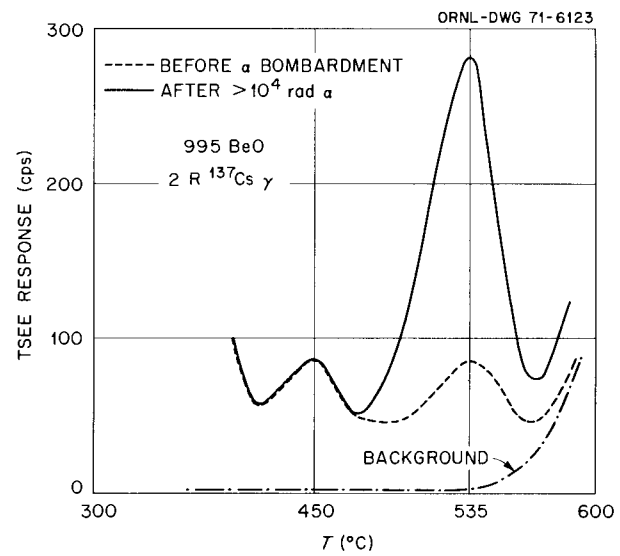

Fig. 13.5. High-temperature TSEE peak before and after alpha irradiation of BeO 995.

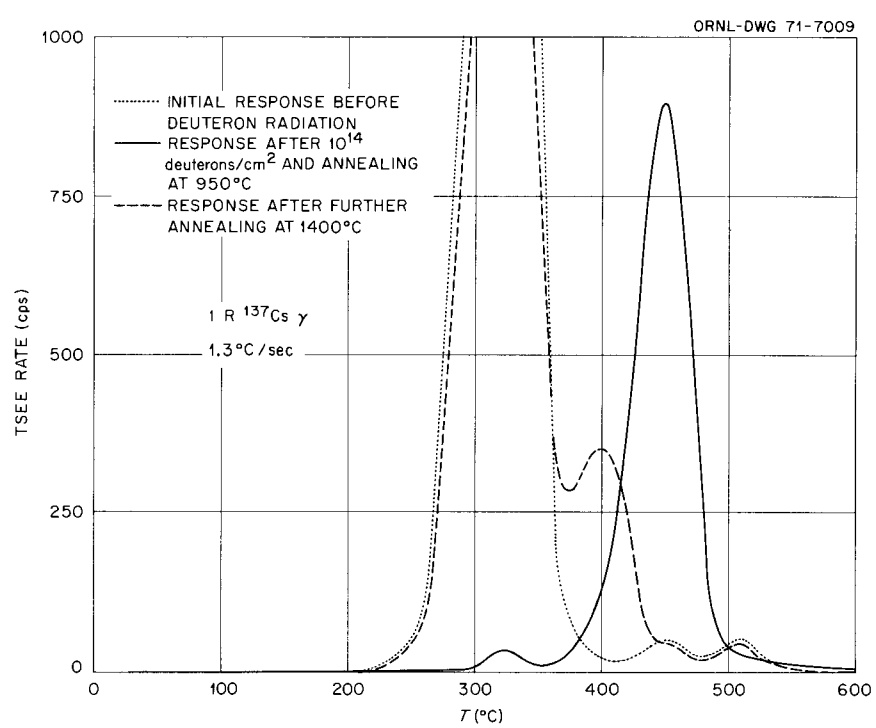

Fig. 13.6. Effects of deuteron radiation and annealing on the TSEE characteristics of ceramic BeO.

Table 13.2. These effects are explainable in terms of silicon impurity and damage sites of the oxygen-vacancy type.

The sensitivity of the deuteron-irradiated BeO was stable during storage in air at 80% relative humidity with no fading of the response. A day's storage in liquid water reduced the sensitivity 30%, but thereafter there was no fading or further decrease in sensitivity. The stability of the BeO ceramic showing the strong peak at 450°C makes it a candidate for radiation measurements in hot gaseous environments (e.g., in the gas stacks of power plants burning tritium-containing natural gas).

Electron Response

Thermalox 995 samples were exposed to monoenergetic beams of electrons in the energy range of 0.2 to 18 keV in order to investigate the energy response and stopping-power dependence. The response to 10-keV electrons was measured from fluences of 1.25×10^8 to 6.25×10^{13} electrons per square centimeter, corresponding to doses of 38.3 to 1.91×10^6 rads. Since exoelectron emission occurs from a thin surface layer of the sample, the absorbed dose is given by $D = k\,S(E)\phi$. Thus the energy response as a function of energy (E) at constant fluence (ϕ) is a measure of the stopping power (S) in BeO. The energy response of BeO is given in Fig. 13.7.

The result that the form of the Bethe stopping-power theory gives a good fit to the energy response implies that the energy response varies in the same manner as the stopping power and hence is a rough measure of it. This can be of interest below 10 keV, where the Bethe formula breaks down and stopping-power values must be determined experimentally.

Table 13.2. Relative peak intensities of deuteron-irradiated and annealed BeO 995

Annealing temperature (°C)	325°C peak[a]	450°C peak[b]
25[c]	1.000	0.103
650	0.053	0.313
700	0.028	0.293
750	0.023	0.310
800	0.014	0.321
900	0.014	0.370
950	0.004	1.000
1000	0.369	0.117
1400	0.971	0.082

[a]Unit intensity after initial sensitization at 1400°C.

[b]Unit intensity after annealing treatment at 950°C.

[c]Sensitized at 1400°C but not deuteron-irradiated.

Saturation at High Dose Levels

The effects of alpha, beta, and gamma radiations, up to and above saturation, on the TSEE response at ~325°C are illustrated in Fig. 13.8. Utilizing the ionization chamber and electrometer, the saturation doses were found to be 2×10^4 and 3×10^5 rads for gamma and beta radiations, respectively. After alpha exposure, however, no plateau was seen for doses up to 10^5 rads. A peak shift to lower temperatures occurs as the dose is increased (Fig. 13.9). The maximum shift is approximately 50°C and possibly represents a measure of the energy width of the trapping levels, the lower energy levels being filled preferentially. At saturation all traps are filled, and the position of the peak is at minimum temperature.

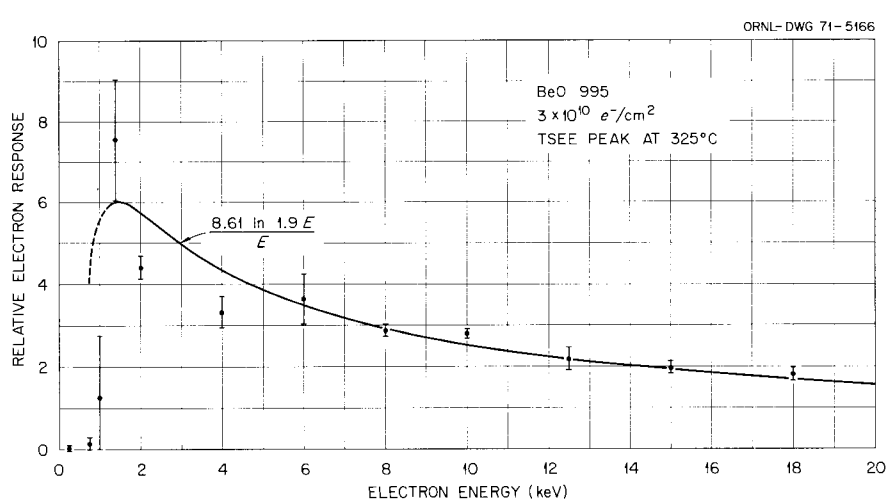

Fig. 13.7. TSEE response of BeO 995 to beta particles in the energy range 0.2–18 keV.

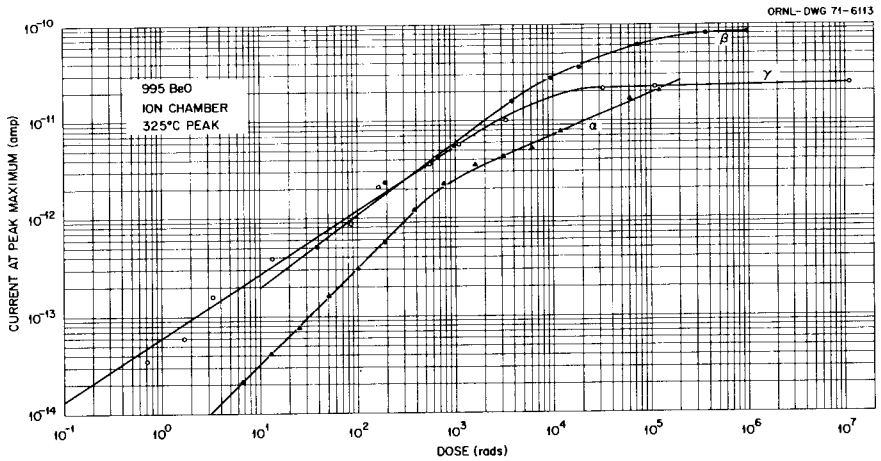

Fig. 13.8. Response of ceramic BeO (325°C peak) to alpha, beta, and gamma radiation.

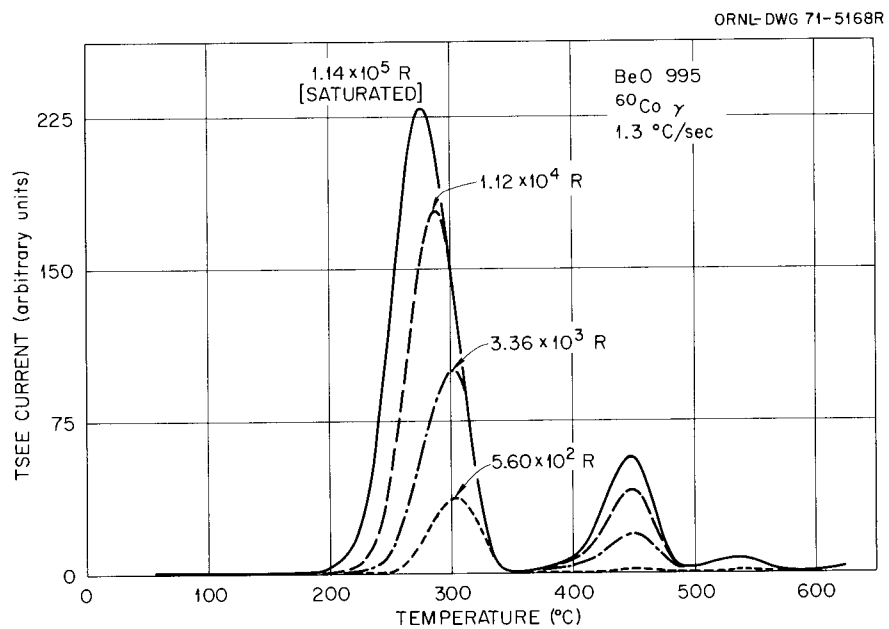

Fig. 13.9. TSEE response of BeO showing saturation and peak shifts for high gamma exposure.

Neither gamma nor beta exposure to very high dose levels was seen to have any permanent effect on the exoelectron-emitting properties of the 995. Higher doses ($>10^3$ rads) of alpha radiation, however, caused permanent changes due to lattice damage.

Reproducibility and Stability of Detector Response

Heating of the ceramic BeO 995 to 1400°C not only maximizes the sensitivity but also improves the reproducibility (in one experiment, the standard deviation in response decreased from 20 to 6%). Microscopic examination of occasional "mavericks" will usually detect some mechanical damage of the surface, or such a disk is warped which prevents good electrical contact during readout. The response is not a strictly linear function of dose due to local charge buildup at the surface during readout (Fig. 13.10).

The high heat-induced sensitivity is stable over extended periods of time, other than for a ~15% drop within the first few days to an equilibrium value, even in atmospheres of 80% relative humidity (Fig. 13.11). No humidity-induced "chemical" fading of stored radiation effect has been observed over a storage period

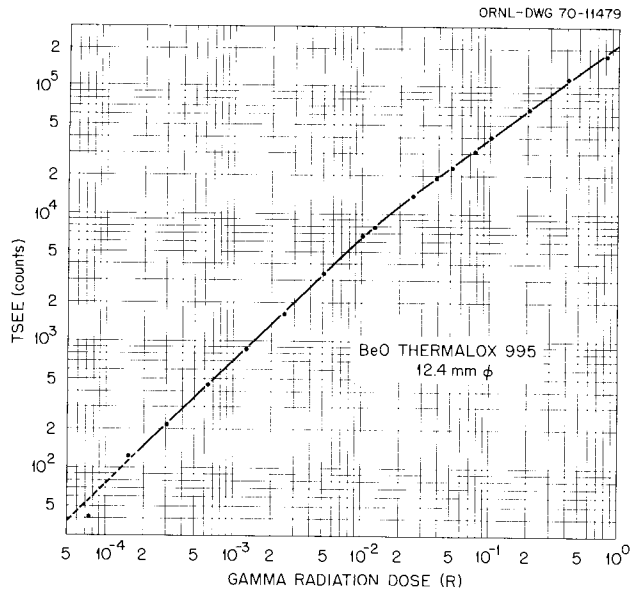

Fig. 13.10. Response of a heat-sensitized ceramic BeO detector (net counts between 200 and 450°C) as a function of ^{60}Co gamma radiation dose.

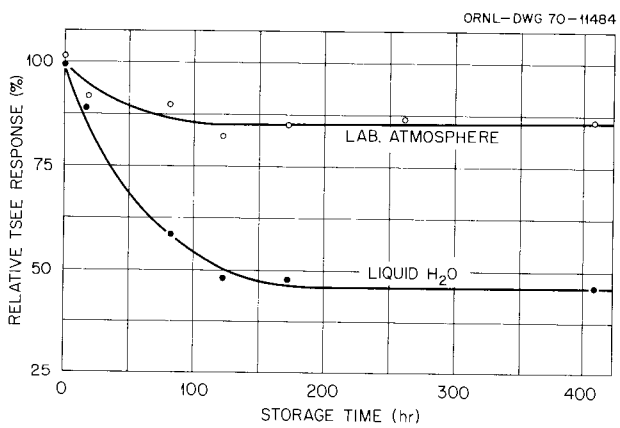

Fig. 13.11. Decrease in sensitivity of BeO 995 as a function of storage time in normal lab atmosphere and in liquid water.

of one month, nor did any "physical" fading occur at temperatures below 150°C. Treatment of a sensitized disk with liquid water causes a reduction in sensitivity over a few days of ~50%, but thereafter has reached a stable equilibrium with regard to hydration. This opens the way for radiation measurements with the bare ceramic in aqueous environments. Experiments with ^{3}H-containing solutions have been carried out and showed promising results.

Early incorporation of ceramic BeO TSEE detectors into personnel dosimeters seems feasible now, and construction of such badges is presently under way. There is also a contract being sought (RANN) for low-level radiation monitoring in several problem areas of environmental monitoring (smokestacks of fossil and nuclear power plants, aqueous effluents, etc.). The extreme sensitivity and versatility of the BeO dosimeter make it suitable for such studies.

Thermal Neutron Response

The inherent thermal neutron response of BeO is small. If the BeO disk is covered with a thermal neutron absorber/converter, the resulting thermal neutron sensitivity is 38 times greater than the gamma sensitivity (on a tissue rad/rad basis) for BN, if the ~325°C peak is measured. The factor is 34 for LiF and 29 for Cd. If the ~450°C peak is used, however, the sensitivity for the (n,α) converters becomes much larger due to the LET dependence of BeO (e.g., 187 for LiF). This is not the case for Cd.

Lunar Materials

Lack of space does not permit us to discuss in any depth the results of exhaustive studies on the natural and artificial TSEE of lunar fines and rocks. The interested reader is referred to this NASA-sponsored work in our current reports,[6,7] which can be summarized as follows: The search for exoelectron emission from Apollo 12 materials usually produced negative results, suggesting that the concentration of naturally occurring traps is very low. Weak exoelectron activity was found scattered inhomogeneously within a pigeonite basalt rock and in a deep-core-tube sample. Its erratic appearance and intensity make any interpretation of radiation history difficult and are attributed to the activity being carried by only a few scattered crystals. The thermally stimulated emission of exoelectrons is judged an unsuitable technique for tracing the natural radiation histories of these samples.

The reverse is true for detecting artifically induced changes in these materials. Several intense artificial TSEE peaks located between about 130 and 550°C have been induced by preheating of samples in air. Corresponding heat treatment in vacuum or hydrogen fails to develop TSEE. These processes have been linked

6. R. B. Gammage and K. Becker, "Search for Exoelectrons in Apollo 12 Materials," *Earth and Interplanetary Science Letters* (in press).

7. R. B. Gammage and K. Becker, "Exoelectron Emission and Surface Characteristics of Lunar Materials," *Proceedings, of the Second Lunar Science Conference,* M.I.T. Press (1971) (in press).

with the oxidation state of iron ions through parallel studies with iron powder. Other reduced species play important roles, and adsorbed atmospheric species (O_2) also affect the TSEE characteristics. In general, TSEE is a sensitive diagnostic tool for detecting and investigating several subtle changes occurring at the surface in terrestrial environments.

THERMOLUMINESCENCE DOSIMETRY[8]

For many years, thermoluminescence dosimetry (TLD) could not be used for precise measurements in the milliroentgen range because the available detectors were either too insensitive or subject to rapid thermal fading. Only recently did some newly developed phosphors such as $CaSO_4$:Dy, $CaSO_4$:Tm, and CaF_2:Dy appear to be sufficiently sensitive. Little is known, however, about their fading kinetics. The sensitivities of CaF_2:Dy, $CaSO_4$:Dy (both made by Harshaw Chemical Company, Cleveland), and $CaSO_4$:Tm (Matsushita Electric Ind., Osaka) turned out to be, if aliquots of ~30 mR each are compared in an Isotopes TLD 7100 reader, 30 to 38 times higher than that of LiF:Mg,Ti (Harshaw TLD 100). The signal-to-background (freshly annealed phosphor) reading ratio, which is an even better indicator of the usability at low dose levels, is by factors of 5 to 15 larger in $CaSO_4$:Tm and $CaSO_4$:Dy than in CaF_2:Dy. Doses as low as 0.1 mR can be measured with $CaSO_4$:Dy or Tm.

Fading measurements at various temperatures clearly show (Fig. 13.12) that the fading rate in CaF_2:Dy is intolerably high at increased ambient temperatures. Of the phosphors compared in this study, CaF_2:Mn was the most stable. Even at 120°C, less than 30% fading occurred in three days, as compared with the same amount of fading in LiF:Mg,Ti at 100°C within a few minutes.

Both $CaSO_4$:Tm and $CaSO_4$:Dy are substantially more stable than LiF:Mg and CaF_2:Dy, but somewhat less stable than CaF_2:Mn. Twenty percent fading may be considered tolerable for most field applications such as personnel and environmental monitoring. It can be seen from the extrapolation in Fig. 13.13 that at a temperature of 40°C, which is close to the upper limit in both applications, 20% fading occurs within half a day in CaF_2:Dy. The same fading would require more than one month in LiF:Mg,Ti, many years in $CaSO_4$:Tm, and even longer in $CaSO_4$:Dy. The extrapolation is admittedly based on somewhat simplified assumptions about the fading kinetics, but is probably not grossly misleading. From these and the sensitivity data, it can be concluded that Tm- and Dy-activated

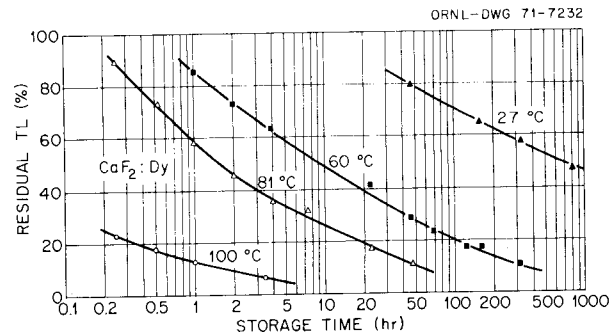

Fig. 13.12. Fading of TL in irradiated CaF_2:Dy as a function of storage temperature.

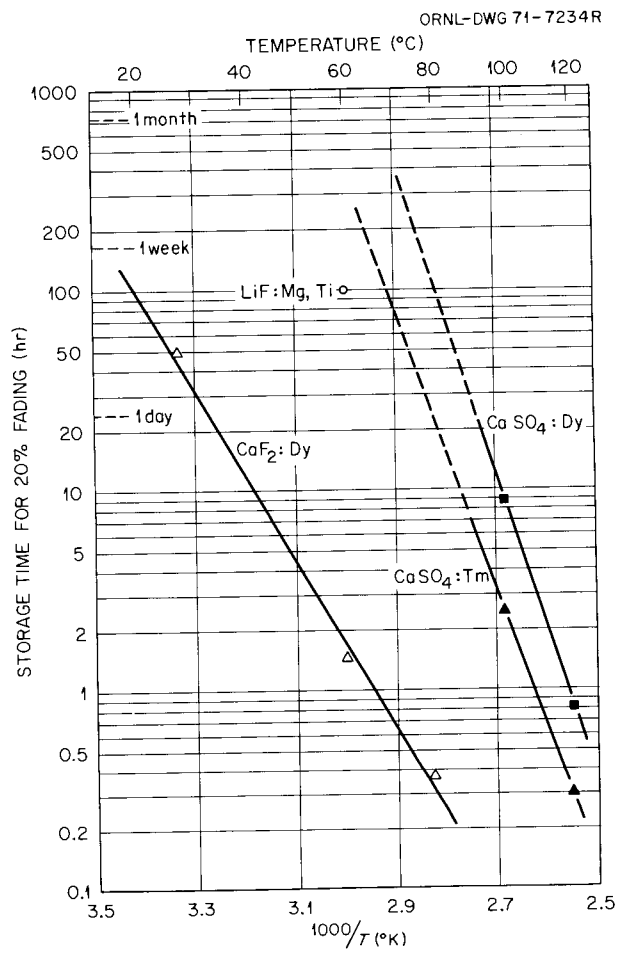

Fig. 13.13. Schematical presentation of fading rate (storage time required for 20% fading) as a function of storage temperature for various TL phosphors.

8. Part of this work is sponsored by IAEA.

9. K. Becker, R. Lu, and P. S. Weng, "Environmental and Personnel Dosimetry in Tropical Countries," Third International Conference on Luminescence Dosimetry, Risö (1971).

$CaSO_4$ are most suitable for measurements requiring high sensitivity, when energy dependence does not pose a problem.

Field experiments in a tropical country (Taiwan) confirmed this result. Detectors have been exposed 1 m above the ground in specially designed bamboo sticks for one month in a climate of 25 to 35°C and 75 to 95% relative humidity. Only in CaF_2:Dy has a substantial fading been observed. Area monitoring experiments around different research reactors and at the site of a 500-MW(e) nuclear power station in northern Taiwan resulted in excellent agreement in the readings of different detectors.[9] Dose levels of 9 to 22 mR/month have been measured at various locations with both energy-independent (LiF) and energy-dependent ($CaSO_4$) detectors, indicating that the energy dependence can be neglected in area monitoring. It should be noted that no meaningful data could be obtained under those conditions with photographic films.

NUCLEAR TRACK ETCHING STUDIES

A scanning electron microscope was employed for studies of the track etching kinetics in different materials. As an example, Fig. 13.14 shows tracks of different sizes resulting from a fractioned exposure of a polycarbonate film to ^{252}Cf fission fragments and subsequent etching in KOH. The samples had to be coated with a thin gold film in order to improve electrical conductivity and reduce damage by the intense electron beam.

In extensive laboratory and mine tests,[10] the radon progeny personnel dosimeter, as described in previous reports, was found to perform in a superior manner compared with systems whose operation is based on different principles such as TLD. Their use is being extended to the measurements of radon daughter products attached to aerosols in the air of salt mines, in homes in which natural gas is burned, etc.

Among the factors which limit the use of fissile materials in fast-neutron personnel dosimetry, the most important ones are cost and toxicity of the materials, fast-neutron fission cross section (sensitivity), energy dependence, background increase due to spontaneous fission, and exposure of the environment of the fissile material (skin, gamma radiation detectors) to beta and gamma radiation. These problems can be minimized by the use of ^{237}Np. Regarding spontaneous fission, ^{232}Th is somewhat superior to ^{237}Np. However, ^{237}Np emits less penetrating radiation than ^{232}Th, which is impossible to shield sufficiently in a small detector unit. As the cross section and energy response of ^{237}Np are superior to the other fissile materials, it has been used for extensive tests.

One major problem was coating the carriers (Ni foils) with sufficient amounts (2–5 mg/cm^2) of ^{237}Np to obtain optimum sensitivity. Both electroplated and vacuum-deposited samples were not easy to prepare and had to be protected from ruboff of alpha activity by a thin protective plastic layer and/or spacer rings. After optimizing the spark-counting conditions (a "plateau" in the spark-count vs etching-time curve is obtained after ~2 hr at 60°C in 28% KOH with Kimfoil 10 μm thick), results such as given in Fig. 13.15 are obtained for HPRR fission neutrons and different foils. As can be seen, a dose range from 0.01 to 10 rads can be covered with a single ^{237}Np foil of ~2.8 mg/cm^2. This sensitivity can be doubled by sandwiching the detector foil between two fissile layers, and the range can be extended to much higher doses by visual track counting.

The system has been used for a number of studies concerning their possible future use in personnel dosimeters. For example, the response of different detectors has been measured as a function of orientation on the surface of a water-filled elliptical thorax phantom for different neutron energies. A typical result is given in Fig. 13.16. In other experiments, such factors as the effect of distance from the body (backscattering) on the dosimeter reading have been investigated. Fading studies did not reveal any fading and/or effect of humidity around room temperature. At higher temperatures (60–100°C), however, high humidity seems to accelerate the fading rate in the polycarbonate.

A newly developed commercial track detector film (LR 115 by Kodak Pathe, France) consists of an 8-μm-thick, intensely red-dyed cellulose nitrate layer on a thick polyester carrier. It has been tested for possible use in sensitive alpha-particle measurements. After etching, transparent holes appear on a red background. The contrast can be amplified by the use of the proper wavelength of light used in the density measurement. After about 90 min of etching in 10% NaOH at 60°C, optimum contrast was obtained. The sensitivity of this method is, however, not as high as that of alpha track spark counting.

10. O. White, Jr., *Evaluation of MIT and ORNL Radon Daughter Dosimeters*, HASL-70-3 (1970).

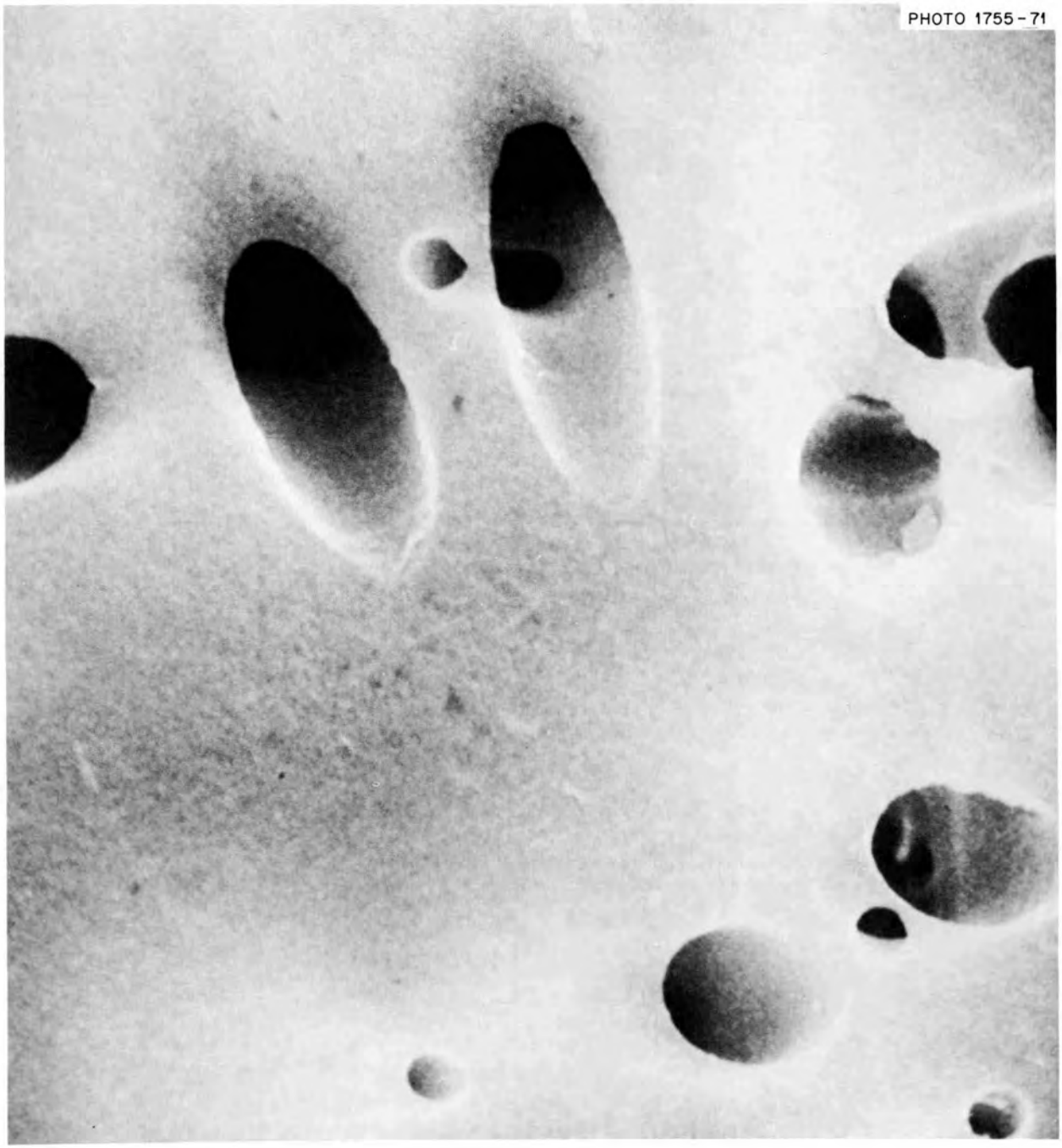

Fig. 13.14. Scanning electron micrograph of etched fission fragment tracks in polycarbonate. Different diameters are due to different etching times.

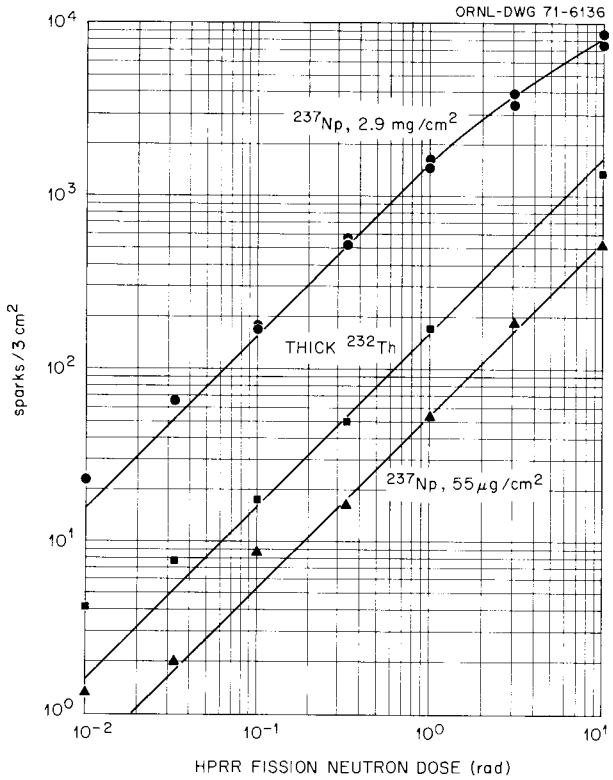

Fig. 13.15. Track density vs dose of HPRR fission neutrons using different fission foils.

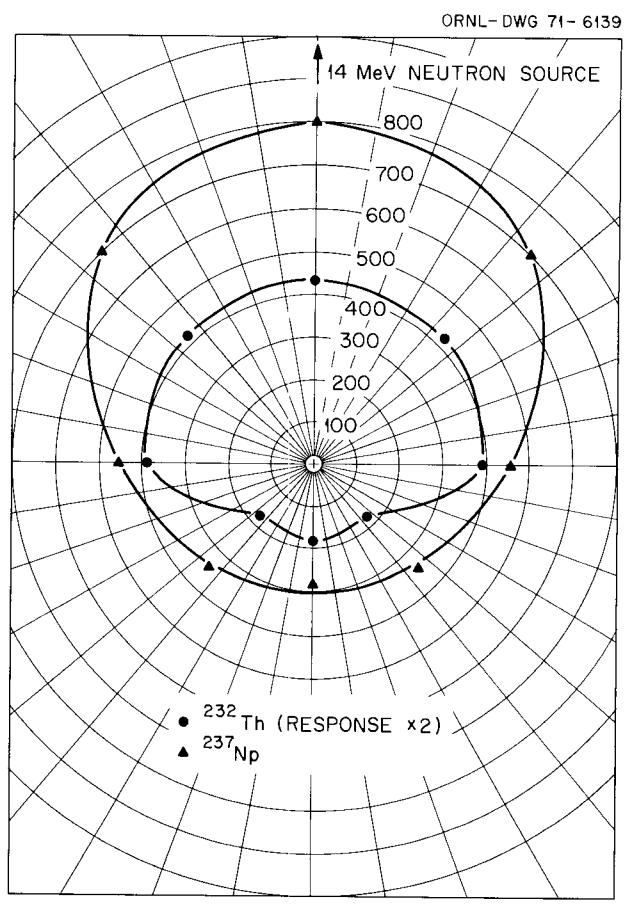

Fig. 13.16. Directional dependence of Kimfoil fission detector exposed (on a water phantom) to 14-MeV neutrons.

14. Interaction of Charged Particles with Matter

G. S. Hurst

D. M. Bartell[1] T. E. Bortner[2]

E. B. Wagner

To determine the energy pathways involved when charged particles interact with gases, the following experimental quantities are measured using a single facility, the ORNL 3-MV Van de Graaff accelerator:

1. radiation intensities as a function of wavelength and pressure for pure noble gases,
2. quenching of electromagnetic radiation by additive gases,
3. W values for the pure gases,
4. W values for the gas mixture (Jesse effects),
5. lifetimes of continuous and resonance radiations,
6. absolute intensities of radiation into the vacuum ultraviolet region.

In addition to these, theoretical inputs involving the transport of resonance photons and the slowing down of secondary electrons are utilized to test energy pathway models. The basic experimental measurements are illustrated in the diagram of the annual report for the previous year.[3] We have now incorporated a computer-based multichannel analyzer which facilitates greatly the accumulation and processing of experimental data, and it is useful also for some of the theoretical work.

Vacuum ultraviolet studies were made (at the University of Kentucky) of the emission from helium gas excited by 4-MeV protons under conditions where the gas purity was monitored by concomitant total ionization measurements. The relative intensity of the 584-Å resonance line was studied from 0.01 to 100 torrs. Three continua, near 600, 675, and 800 Å, respectively, were investigated from a few torrs to 800 torrs. Studies of

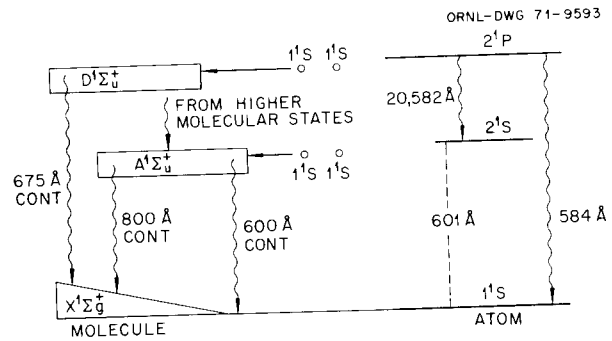

Fig. 14.1. Schematic diagram of continuous emission from helium showing three-body conversion of the atomic states 2^1S and 2^1P to molecular states $A^1\Sigma_u^+$ and $D^1\Sigma_u^+$, respectively. The molecular A state is also populated by radiation from higher molecular states. Not shown is two-body depletion of the 2^1S state.

intensity as a function of pressure are consistent with the interpretation[4] that the 675-Å continuum is the bound-continuum transition $D^1\Sigma_u^+ \rightarrow X^1\Sigma_g^+$ in the helium diatomic molecule, where the D state is in a high state of vibration and is formed by three-body collisions involving the atomic 2^1P state, Fig. 14.1. Some of the 800-Å continuum, as well as the narrow continuum near 600 Å, is produced, most likely, from a similar process involving emission from the $A^1\Sigma_u^+$ molecular state, created from three-body conversion of a 2^1S atomic state. Recent studies made of emission spectra in liquid helium,[5,6] where an intense continuum was observed near 750 Å, appear from our studies to be the bound-free transitions $D^1\Sigma_u^+ \rightarrow X^1\Sigma_g^+$ from low-lying vibrational levels in the D state. Lifetime studies (over a wide pressure range) of resonance lines and of the

1. University of Kentucky Summer Fellowship.
2. Consultant.
3. *Health Phys. Div. Annu. Progr. Rep. July 31, 1970*, ORNL-4584, p. 199.
4. T. E. Stewart et al., *Phys. Rev.* **A3**, 1991 (1971).
5. C. M. Surko et al., *Phys. Rev. Lett.* **24**, 657 (1970).
6. M. Stockton, J. W. Keto, and W. A. Fitzsimmons, *Phys. Rev. Lett.* **24**, 654 (1970).

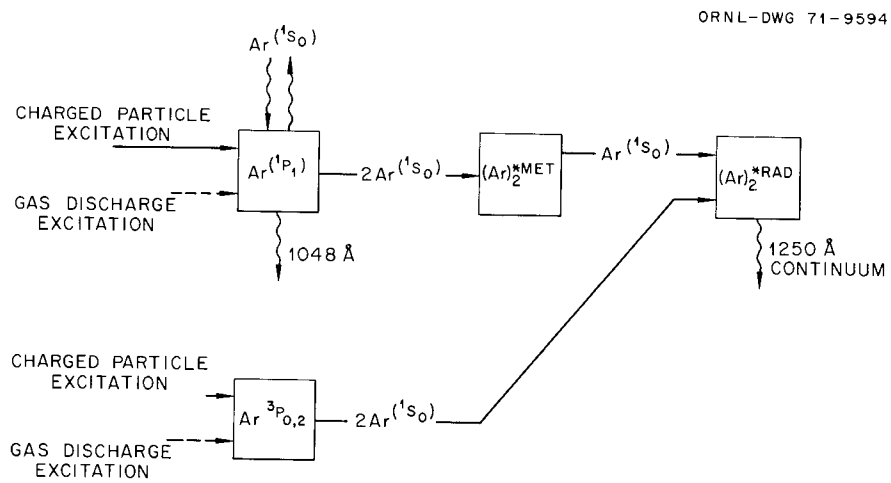

Fig. 14.2. Model for emission from argon molecules.

continua have been completed at ORNL; some quenching studies are now in progress. These inputs will be tested with W measurements with particular interest in explaining the Jesse effects in helium.

In the case of helium, important theoretical input is already available, and we are making a calculation of the number of states excited in helium gas in the following way. The primary particles (2- to 3-MeV protons) are assumed to excite atomic states and the ionization continuum according to the optical approximation which involves only the optical oscillator strengths. Quantum mechanical calculations[7] of the distribution in energy of secondary electrons will then be folded into the slowing-down calculations already performed by Alkhazov.[8] In the course of time only trapped resonance states and metastable states will be left behind for the production of continua through atomic collisions. Thus, one may estimate, independent from experiment, the number of the types of various states which could contribute significantly to observed continuous emission.

For argon gas, most of the necessary input data (1–6) were obtained at the University of Kentucky. However, the lifetime data obtained by N. Thonnard,[9] using a pulsed electron accelerator, were repeated here with protons. The main features of the lifetime data obtained with 250-keV electrons and with 2-MeV protons are very similar. The complex time behavior of the 1250-Å continuum in argon has led to the very interesting emission process shown in Fig. 14.2. Here one sees that the Ar ($^1P_1$) states emit resonance photons at 1048 Å, which are trapped many times. At high pressure virtually all of the $^1P_1$ states are converted to metastable argon molecules by three-body (eigenizing) collisions. Two-body collisions convert argon metastable molecules to molecules which radiate with a lifetime of about 3 μsec. The same (or a similar) radiating molecule is formed out of triplet excited states in a more direct process. Since triplet states are preferentially excited by the low-energy electrons of a gas discharge, this channel is relatively more important than in the case of proton excitation. With protons the singlet channel dominates because of the larger oscillator strength of the $^1P_1$ state.

The emission mechanism above also contains some of the richness needed to interpret Jesse effects. In particular, Parks[10] and Parks and Hurst[11] observed that the Jesse effects (at a given concentration) decrease with increases in the total pressure. This can be understood if one assumes that Jesse effects are due to

$$\mathrm{Ar}^*(^1P_1) + XY \rightarrow XY^+ + e + \mathrm{Ar}(^1S_0)$$

and that the competing process is

$$\mathrm{Ar}^*(^1P_1) + 2\mathrm{Ar}(^1S_0) \rightarrow (\mathrm{Ar})_2{}^{*\mathrm{Met}} + \mathrm{Ar}(^1S_0)\,.$$

7. Prof. A. E. Kingston, Queens College, Belfast, private communication.

8. G. D. Alkhazov, *Ioffe Institute of Physics and Technology, Leningrad*, Preprint FTI-108 (1968).

9. N. Thonnard, Ph.D. thesis, University of Kentucky, 1971.

10. J. E. Parks, Ph.D. thesis, University of Kentucky, 1970.

11. J. E. Parks et al., "Ionization of the Noble Gases by Protons" (to be published).

Jesse effects from the atomic state can evidently occur with ionization efficiencies approaching (or equal to) that observed in photoionization. In the process

$$(\mathrm{Ar})_2{}^{*\mathrm{Met}} + XY \rightarrow XY^+ + e^- + 2\mathrm{Ar}\,(^1S_0)\,,$$

one expects a much lower ionization efficiency mainly because less energy is available for ionization.

The emission model also appears to explain the fact that quenching of the 1250-Å emission involves a kinetic scheme which is more complicated than the Jesse effect. The interpretation of the detailed ways in which quenching collisions intercept the energy flow, as illustrated in Fig. 14.1, is made possible by separate studies of the resolved radiation at 1048 Å, the 1100-Å continuum, and the 1250-Å continuum. These measurements have been made, and interpretation is well advanced.

15. Spectrometry Research and Development

J. H. Thorngate
M. D. Brown[1] G. D. Kerr
P. T. Perdue

ORGANIC SCINTILLATOR RESEARCH

It has been shown in earlier studies[2] that there is an upper limit to the light output per unit energy imparted to organic scintillators. However, for the *para*-polyphenyl oligomers, there is evidence[3-5] that this upper limit has not yet been reached. The principal obstacle to evaluation is obtaining pure materials. In the case of *para*-quaterphenyl synthesized by the Grignard process, zone refining[6] is sufficient to remove most of the impurities that limit light output. The purified material has about the same emission for gamma photons as anthracene.

For *para*-sexiphenyl, purification is much more difficult. It is a function of the melting point, which, in this case, is close to 465°C. There are no known solvents for *para*-sexiphenyl; therefore, solvents must be found for the impurities. Working in cooperation with the ORNL Chemistry Division, a method for growing single crystals approximately 8 μ thick and greater than 1 cm^2 in area was evolved. Aside from the research permitted by such crystals directly, recrystallization is a preferred method for removing impurities. Further zone refining of these crystals will permit evaluation of the scintillation properties of this material.

Preliminary measurements made on the single crystals of *para*-sexiphenyl show that the optical index of refraction lies above 1.64 (the density is 1.26); the thin crystals are completely transparent to visible light and are quite strong. Mass spectroscopy done in the ORNL Chemistry Division revealed the principal mass at 458.6 amu with traces at 425 and 610 amu. The fluorescence spectrum of the single crystals was measured in the ORNL Biology Division, and a single large peak was found at 450 nm. For better purification the peak should shift to near the theoretical maximum of 430 nm.[4] The infrared spectrum for *para*-sexiphenyl is in the literature,[7] and many measurements of the IR spectrum have been made in KBr disks. These measurements agree reasonably well with the published data. Only small differences were found in the IR spectrum between the brown starting material and the clear single crystals; however, the single-crystal spectra are closest to the published spectrum for the material.

It is hoped that a technique employing "seed" crystals will permit the growth of crystals thick enough for proton and alpha stopping-power studies, as well as measurements of dL/dE.

A VOLTAGE-TO-FREQUENCY CONVERTER

Many dosimetry experiments require the accumulation of data using an electrometer with a strip-chart recorder to transcribe the data. This leads to problems in obtaining a mean value from the irregular recorder tracing. One way to overcome short-term variations in the data is to integrate the area of the trace. To facilitate such a reading, an electrometer that has a digital output with integration is desirable. While such instruments are commercially available, their operating ranges and price are not always compatible with experimental conditions. A second approach would be to digitize the output of an existing electrometer and to

1. Part time.
2. J. B. Birks, "Organic Crystal Scintillators," p. 244 in *The Theory and Practice of Scintillation Counting*, Pergamon, London, 1964.
3. I. B. Berlman, *Mol. Cryst.* 4, 157–63 (1968).
4. H. O. Wirth, F. U. Herrman, G. Herrman, and W. Kern, *Mol. Cryst.* 4, 321–42 (1968).
5. T. Nozaki, M. Tamura, Y. Harada, and K. Saito, *Bull. Chem. Soc. Japan* **10**, 1329–32 (1960).
6. P. T. Perdue and M. D. Brown, *Nucl. Instrum. Methods* 71, 113–16 (1969).
7. J. A. Cade and A. Pilbeam, *J. Chem. Soc. London*, 114–21 (January 1964).

record the digital signal with a scaler. Such an approach is possible with a simple voltage-to-frequency converter that was designed and built for use with depth-dose and TSEE experiments at the DOSAR. A unijunction-transistor relaxation oscillator is the basic voltage-to-frequency conversion unit. This simple approach has some drawbacks, but none are excessive for an instrument designed for laboratory use. Temperature sensitivity is a major problem with relaxation oscillators, but well-known techniques are available to decrease this effect when a unijunction transistor is used. An integrated-circuit operational amplifier amplifies the input voltage so that adjustable input voltages from 10 mV to 1 V will produce the maximum frequency output. A second integrated-circuit amplifier is used as a variable current source for the relaxation oscillator. Output pulses are shaped by a third integrated circuit. Both zero and span of the instrument are adjustable by front panel controls. The nominal maximum output frequency is 1 kHz with 50% overranging possible. Precision is 0.2% for input values above 10% of full scale. Below 10%, this value drops to 1%, which is an effect of zero shifts in the circuit that arise due to component leakage currents. The present unit was designed to operate in an NIM power unit. Commercial voltage-to-frequency converters are available, but are generally prohibitive in cost and not well-suited for direct application to this type of measurement.

HEALTH PHYSICS RESEARCH REACTOR TIMER

The precision of timing irradiation intervals is one of the factors affecting the precision of the dose delivered during an experiment using the HPRR. To improve timing precision, a timer was built to terminate reactor runs automatically.[8] Some of the features of the timer were its ability to terminate reactor runs after operating times adjustable from 1 to 99,999 sec in 1-sec units, timing precision of 1/60 sec, and a means whereby immature termination of the reactor run would stop the timer. Two registers were used; one counted down from the desired time and terminated the reactor run when it reached zero, via a relay in the reactor slow-scram line, and the second recorded elapsed time in seconds. Manual start, stop, and reset of the timer was provided by front panel control. A means whereby the timer could be run to measure elapsed time without controlling the reactor was also included.

Problems encountered with the original unit, constructed with discrete solid-state components, led to the design of a new timer that utilizes integrated circuits. Since integrated logic circuits perform the switching and control functions of the timer, a considerable increase in reliability was obtained. All of the features of the original unit have been retained, but to improve the serviceability of the unit, a new housing is used that is compatible with the modular design of other HPRR instrumentation.

8. J. H. Thorngate, *An Interval Timer for Use During Irradiations at the Health Physics Research Reactor,* ORNL-TM-1559 (August 1966).

16. HPRR and Accelerator Operations

F. F. Haywood
H. E. Banta[2]
C. P. Littleton[3]
D. R. Ward[1]
J. W. Poston
E. M. Robinson

HEALTH PHYSICS RESEARCH REACTOR OPERATIONS

The HPRR is used extensively as a source of fission neutrons for health physics and radiobiological research activities. The reactor was employed, not only by the Health Physics Division, but by other Laboratory divisions (e.g., Biology and Ecological Sciences), representatives of several foreign countries, many colleges and universities, and other Federal contractors and agencies. In addition to standing experiment categories reported earlier, a summary of other experiments is as follows:

1. long-term effects of acute nonlethal doses of fission neutrons in mice;
2. study of crypt cell survival in the intestine of laboratory mice;
3. determination of neutron and gamma-ray depth-dose distributions in homogeneous tissue-equivalent phantoms;
4. in support of the Second IAEA Intercomparison Study and NAD Coordination Meeting;
5. the effectiveness of radioprotectants applied in vivo and in vitro to bone marrow cells;
6. testing of criticality monitors for use in fuel processing facilities;
7. determination of the HPRR fission gamma-ray spectrum as a function of operating history.

No major modifications or changes in the reactor have been made in the past year. The annual inspection of the fuel and associated equipment showed no significant change in the condition of the reactor components.

INTERCOMPARISON STUDIES

In 1964, a series of studies was begun to provide facilities for comparing the response of nuclear accident dosimeters used by dosimetrists throughout the world. It was considered to be a worthwhile program because of:

1. wide interest at ORNL in the field of dosimetry for human exposure;
2. a lack of adequate dose determinations for persons exposed during criticality accidents;
3. the necessity for developing guidelines in instrumentation and procedures; and
4. the need for standardized radiation fields whose characteristics, such as energy spectrum, intensity, and uniformity, had been determined using widely accepted instruments and techniques (such radiation fields to be used to simulate nuclear accidents).

1970 Intercomparison

The seventh intercomparison study was held July 20–31, 1970. Participating laboratories included those from four foreign countries, as well as ten U.S. laboratories.

Personnel monitoring badges and detectors used as area monitors were compared. Three different spectra were used to simulate nuclear accidents. Results of the experiment are given in Tables 16.1 and 16.2. Reported values of dose were within ±22% for all pulses. It should be noted that for the unshielded reactor environment, measurements were within ±5% for neutron dose and ±9% for gamma dose at one standard deviation. The uncertainty of values for neutron fluence in several energy groups was slightly higher than those for dose.

1. On loan from Neutron Physics Division.
2. Consultant.
3. On loan from Instrumentation and Controls Division.

Table 16.1. Seventh intercomparison of nuclear accident dosimetry systems, July 20–31, 1970

Stations in air at 3 m

Pulse No.	Neutron dose[a] (rads)	Gamma dose[a] (rads)	n/γ[a]	Neutron fluence × 10^{-10} (neutrons/cm^2)						
				Thermal	$E > 1$ keV	$E > 750$ keV	$E > 1.5$ MeV	$E > 2.5$ MeV	$E > 2.9$ MeV	$E > 3.0$ MeV
1	310[b] ±5%	44.8 ±9%	6.8 ±9%	0.58 ±12%	12.73 ±11%	8.12 ±12%	4.39 ±11%	2.37 ±13%	1.96 ±11%	1.78 ±9%
2	42.6 ±17%	33.7 ±16%	1.42 ±37%	1.43 ±25%	1.54 ±27%	1.01 ±11%	0.62 ±10%	0.34 ±24%	0.31 ±13%	0.24 ±8%
3	106 ±14%	11.5 ±21%	9.8 ±18%	0.35 ±26%	5.44 ±18%	2.64 ±31%	0.99 ±29%	0.33 ±15%	0.31 ±22%	0.24 ±12%

[a]Numbers given represent the average of all values presented.
[b]Errors given in this table represent the error of the mean value at one standard deviation.

Table 16.2. Seventh intercomparison of nuclear accident dosimetry systems, July 20–31, 1970

Phantom studies

Pulse No.	Neutron dose[a] (rads)	Gamma dose[a] (rads)	Na activity (μCi ^{24}Na/mg ^{23}Na)	^{23}Na concentration of phantom facing (mg Na/ml)
1	323 ± 18.3%[b]	89 ± 19%	8.47 × 10^{-4} ± 13%	1.50
2	45 ± 14%	51 ± 19%	1.40 ± 19%	1.50
3	116 ± 21%	34 ± 22%	4.03 ± 18%	1.48

[a]Numbers given represent the average of all values presented for dose except for measurements on the rear surface. See tables for interpretation of dose.
[b]Errors given in this table represent the error of the mean value at one standard deviation.

1971 Intercomparison

The eighth intercomparison study was held May 3–15, 1971. There was a slight departure from previous experiments in that the International Atomic Energy Agency was cosponsor. In addition, this intercomparison was primarily for the benefit of laboratories from emerging European nations. Only two U.S. laboratories participated: Oak Ridge National Laboratory and Savannah River Laboratory. There were representatives from 11 foreign countries as follows:

Canada	Germany	Poland
Czechoslovakia	Hungary	Russia
England	India	Yugoslavia
France	Italy	

As in recent intercomparisons, three different radiation fields from the HPRR were utilized: (1) bare, (2) 13-cm steel shield, and (3) 12-cm Lucite shield. The shields in (2) and (3) above were positioned at 2 m between the HPRR and detector station which was located at 3 m.

Table 16.3. Preliminary results of 1971 intercomparison study

Pulse no.	Shield	Neutron dose (rads)	Gamma-ray dose (rads)
1	None	373 ± (8)	57 ± (18)
2	13-cm steel	142 ± (19)	17 ± (25)
3	12-cm Lucite	47 ± (18)	44 ± (10)

Only preliminary results are available at this time; however, the data appear to be very acceptable as shown in Table 16.3. Mean values of neutron and gamma-ray dose (for air stations) are presented. The numbers in parentheses represent the percent accuracy at one standard deviation.

ACCELERATOR OPERATIONS

Use of the Physics Division's 3-MV Van de Graaff by the Radiation Dosimetry Section was limited by failures of the accelerator to a total running time less than the six-month period for which this Section was responsible for machine operation. As a result, only limited irradiations using charged particles were made as part of the TSEE research program. The remainder of the available operating time was used to study interactions of charged particles with matter. During this period, the Physics Division announced its intent to discontinue operation of this accelerator, and a plan was worked out whereby prime responsibility for the operation of the machine would pass to this Section.

The DOSAR Low-Energy Accelerator has been used successfully in support of several dosimetry programs. In particular, these have been related to measurements of dose as a function of depth in tissue-equivalent phantoms. Depth-dose measurements have been made for both broad and collimated beams of 14-MeV neutrons and for broad beams of 2.5-MeV neutrons. The accelerator has also been used to provide neutrons for some activation studies and irradiation of seeds and to provide intense beams of deuterons to study radiation damage in ceramic BeO TSEE detectors. One of the major applications of the accelerator has been in support of studies related to the development of a long-lived tritium target.

A SELF-REPLENISHING TRITIUM TARGET

In order to extend the lifetime of conventional nonrotating tritium targets (say, TiT_2), a new design concept for neutron-generator targets has been tested successfully. It consists of a device which allows the target area to be replenished during operation.

Experiments were performed with the target assembly mounted on the beam tube of a small positive-ion accelerator. An unanalyzed 1-mA beam whose diameter at the target was 1 cm provided deuterons. An overall view of the assembly, which is mostly copper, is shown in Fig. 16.1. It is $2\frac{1}{2}$ in. long, $1\frac{3}{4}$ in. wide, and $\frac{1}{4}$ in. thick, and is made up of two end-cap headers (*A*) and a

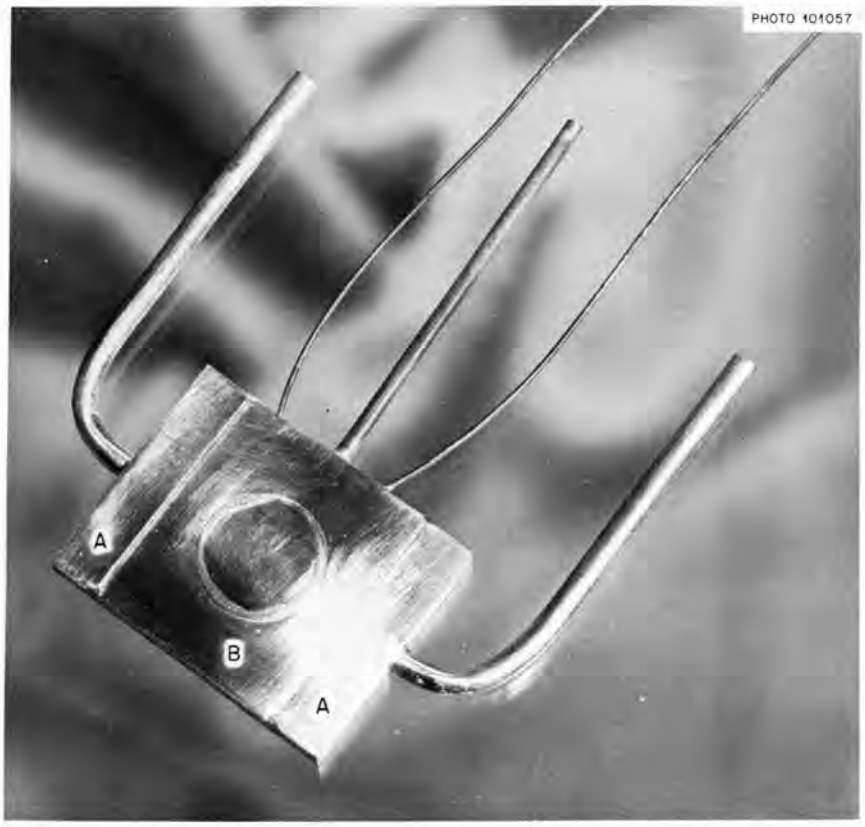

16.1. Overall view of the prototype self-replenishing tritium target. A Pd-Ag foil is shown brazed into position in the center of the assembly.

larger centerpiece (*B*) in which a shallow gas reservoir was machined. Six holes 0.040 in. in diameter were drilled the length of *B* just under the gas reservoir for circulating coolant. A foil of Pd-Ag alloy (0.80 Pd) 0.875 in. in diameter was brazed in an inert atmosphere to form the top cover of the gas cell. Tritium was supplied through a $^1/_8$-in. stainless steel tube to the cell from a uranium trap. A layer of titanium was deposited over the palladium so that tritium diffusing through the foil could form a hydride target. Neutron yields were determined using foil activation techniques; a moderated BF_3 counter was used to monitor yield as a function of time.

Several self-diffusing target assemblies were fabricated and tested. The first of these was for a palladium thickness of 0.030 in. and 0.303 mg/cm^2 of titanium. Although the results did not represent optimum parameters, feasibility was again demonstrated as in an earlier case. The next assembly tested incorporated a 0.020-in. palladium substrate and a 1.0-mg/cm^2 layer of titanium. A maximum yield of 2×10^{10} neutrons/mA-sec was observed over a period of 2 hr. During this time, the tritium pressure was varied from 8 to 24.5 in. vacuum (Hg). A decrease of about 35% in neutron yield was noticed; however, it was concluded that neutron output was not strongly related to tritium pressure. The third and final target was made with a 0.030-in. palladium foil and titanium thickness of 0.445 mg/cm^2. Tritium pressure in the cell was maintained at 10 in. vacuum. The results of this run are also shown in Fig. 16.2. There was an initial buildup in 20 min to a yield of 4.5×10^{10} neutrons/mA-sec. This level continued for a period of 3 hr; thereafter a half-life of 2.5 hr was observed. After 4.8 hr, the accelerator was shut down

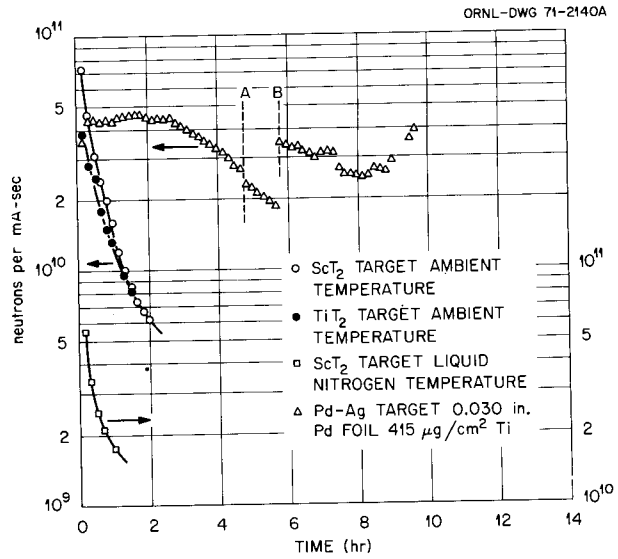

Fig. 16.2. Comparison of neutron yield per mA-sec as a function of operating time for three "standard" tritium targets and for the self-replenishing (Pd-Ag) target.

overnight (Fig. 16.2, position *A*). The following 1 hr of operation indicated the yield was offset lower and declined at near the previous half-life. As predicted, a slight beam displacement to fresh hydride (Fig. 16.2, position *B*) resulted in an increase by a factor of 2 in neutron output. The average yield for 10 hr was greater than 2×10^{10} neutrons/mA-sec. For application to radiobiology research and cancer therapy, for which a neutron yield of 10^{12} neutrons/sec is required, this system used on a low-voltage accelerator (200–300 kV) with 50–100 mA beam currents would provide the required output.

Part IV. Internal Dosimetry

W. S. Snyder

17. Preliminary Indications of the Age Variation of the Specific Absorbed Fraction for Photons

W. S. Snyder M. J. Cook

For the situation where a monoenergetic photon source is uniformly distributed in an organ S (termed the source organ) and an estimate of the total energy absorbed in a target organ T is desired, the specific absorbed fraction is defined by

$$\Phi(T \leftarrow S) = \frac{\text{energy absorbed in } T}{(\text{energy emitted in } S) \times (\text{mass of } T)} \ (\text{g}^{-1}) \ . \quad (1)$$

In most practical situations, there will be photons emitted of a variety of energies and intensities, and the concept of the specific absorbed energy can be extended to include such cases (see ref. 1); but for simplicity, we consider here only the simple case of a monoenergetic source. Absorbed dose is closely related to Φ since

$$\text{absorbed dose in target organ } T = 1.6 \times 10^{-8} \times (\text{disintegrations in } S) \times E \times (T \leftarrow S) \text{ rads} \ , \quad (2)$$

provided E is in MeV. In (2), the energy E is to be in MeV, and the constant represents the g-rad/MeV. Values of Φ for a "standard man" may be obtained from the absorbed fractions published in ref. 2 by dividing by the mass of the target organ. These estimates approximately take account of the size, shape, location, composition, and density of the organ or tissue. However, no similar estimates for other ages are available.

It seems clear that a large variation of Φ with age is to be expected if only on the basis of the inverse square law. In fact, for a point source at distance x from an infinitesimal mass element dV, the specific absorbed fraction for dV is given by

$$\Phi(x) = \frac{\mu_{ab}\, e^{-\mu x}}{4\pi x^2} B(\mu x) \ , \quad (3)$$

where μ is the mass attenuation coefficient of the medium, assumed to have unit density, μ_{ab} is the mass absorption coefficient, and $B(\mu x)$ is the buildup factor. An accurate estimate of Φ for individuals of various ages by the Monte Carlo method used for the adult (see ref. 2) requires the development of phantoms representing these individuals. An examination of data on the

1. Robert Loevinger and Mones Berman, "A Schema for Absorbed-Dose Calculations for Biologically Distributed Radionuclides," MIRD Pamphlet No. 1, Suppl. No. 1, *J. Nucl. Med.* (February 1968).

2. W. S. Snyder et al., "Estimates of Absorbed Fractions for Monoenergetic Photon Sources Uniformly Distributed in Various Organs of a Heterogeneous Phantom," MIRD Pamphlet No. 5, Suppl. No. 3, *J. Nucl. Med.* (August 1969).

ORNL-DWG 66-6436

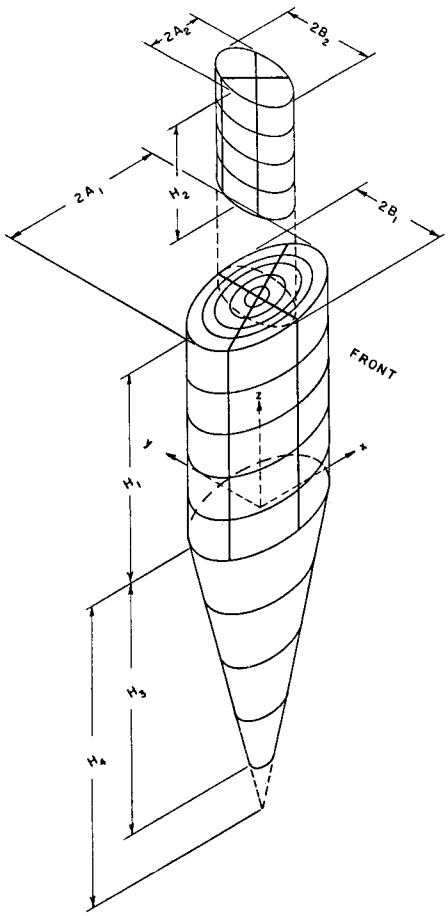

PHANTOM DIMENSIONS AND DOSE REGIONS

Age (yr)	Weight (kg)	H_1 (cm)	H_2 (cm)	H_3 (cm)	H_4 (cm)	A_1 (cm)	B_1 (cm)	A_2 (cm)	B_2 (cm)
0	3.473	23	13	15	20	5.5	5	4.5	5
1	10.171	33	16	27	36	8	7	6.5	7
5	19.654	45	20	46	57.5	11	7.5	6.5	7.5
10	31.902	54	22	64	80	14	8	6.5	8
15	54.041	65	23	78	97.5	18	9	7	9
20	70.037	70	24	80	100	20	10	7	10

Fig. 17.1. Dose regions of phantom.

total body as well as on various organs reveals that individuals of the younger age groups are not merely adults reduced proportionately by a constant factor. This is common knowledge which had been pointed out previously in the context of health physics by Henry Fisher[3] and J. G. Kereiakes.[4] However, designing phantoms for a series of ages is a formidable task, particularly when data on certain ages are sparse. It was thought that some preliminary calculations should be made to document that the expected changes in specific absorbed fractions with age do occur and that the range of variation is quite large.

3. H. L. Fisher, Jr., and W. S. Snyder, "Variation of Dose Delivered by ^{137}Cs as a Function of Body Size from Infancy to Adulthood," *Health Phys. Div. Annu. Progr. Rep. July 31, 1966*, ORNL-4007, pp. 221–28.

4. J. G. Kereiakes et al., "Radionuclide Doses to Infants and Children: A Plea for a Standard Child," *Health Phys.* **11**, 999 (1965).

For this purpose, the adult phantom was reduced by scale factors selected separately for the head section, the trunk section, and the leg section of the phantom (see Fig. 17.1). All organs and tissues within these sections were reduced by the scale factors for that section. The explicit transformation formulas which apply are given below.

Let (x, y, z) be the coordinates of a point in the adult phantom (see Fig. 17.1 where the coordinate system is indicated). Let (x', y', z') be the coordinates of the corresponding point in the transformed phantom (with coordinate system similarly placed), and primes are used also to designate the corresponding dimensions of the transformed phantom. Then for (x, y, z) in the trunk section we have

$$x' = A'_1\, x/A_1 \;, \quad y' = B'_1\, y/B_1 \;, \quad z' = H'_2\, z/H_2 \;. \qquad (4)$$

Similarly, for (x, y, z) in the leg section of the adult

phantom, the corresponding point (x', y', z') is given by

$$x' = A'_1 x/A_1 \ , \quad y' = B'_1 y/B_1 \ , \quad z' = H'_1 z/H_1 \ . \qquad (5)$$

Finally, for (x, y, z) in the head section, the corresponding point is given by

$$x' = A'_1 x/A_2 \ , \quad y' = B'_2 y/B_2 \ ,$$
$$z' = H'_2 + H'_3 \ (z - H_2)/H_3 \ . \qquad (6)$$

It is clear that these transformations are similitudes, and hence volumes V in the head, trunk, or leg section of the adult phantom are transformed into volumes

$$V' = KV \text{ when } K = A'_2 B'_2 H'_3 / (A_2 B_2 H_3) \ ,$$
$$A'_1 B'_1 H'_2 / A_1 B_1 H_2 \ , \quad A'_1 B'_1 H'_1 / A_1 B_1 H_1 \ , \qquad (7)$$

respectively. Moreover, loci (organs) which are nonintersecting in one phantom are nonintersecting in the other phantom.

Using the transformation, it is easy to adapt the computer program for the new phantom. Indeed, whenever one needs to determine whether a point in the transformed phantom is in an organ of that phantom, one simply applies the inverse transformation and tests the corresponding point in the adult phantom. Thus this part of the computer code is not changed, and this is advantageous since it constitutes a major complexity of that code. Photon histories are then computed for the transformed phantom as before (see ref. 2).

For these preliminary test cases, dimensions of the phantom were taken to be those selected by Fisher[3] to correspond to individuals of ages 0, 1, 5, 10, and 15 years, the 20-year-old being the adult phantom. The dimensions are listed in Fig. 17.1. A monoenergetic source of photons has been programmed in the stomach. The estimates of the specific absorbed fraction obtained by the Monte Carlo method are shown in Figs. 17.2 and 17.3 for liver and for lungs as the target organs. As will be noted, there is an increase of an order of magnitude or more in Φ as the age decreases. Since dose is proportional to Φ, it follows that the use of the

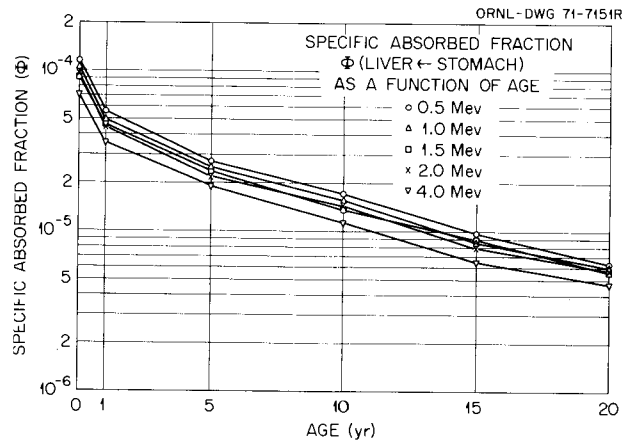

Fig. 17.2. Specific absorbed fraction as a function of age. Liver as target organ.

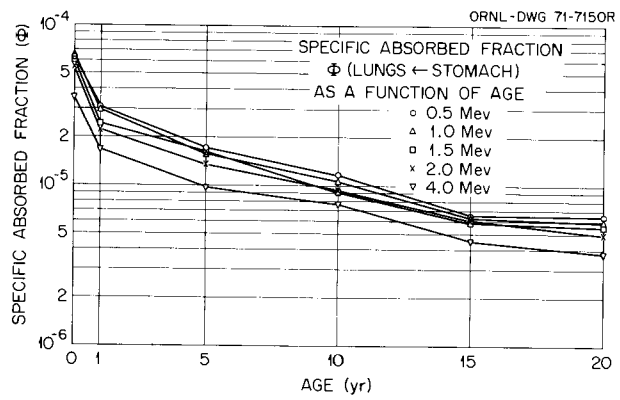

Fig. 17.3. Specific absorbed fraction as a function of age. Lungs as target organ.

estimates of Φ for the adult will lead to a gross underestimate of the dose. We hope to redesign the phantoms to approximate more closely to the organ and body dimensions of the individuals and to publish tables of Φ which will meet the needs of health physicists who have occasion to estimate doses for infants and children, whether from medical use of radiopharmaceuticals or in the context of exposure of the population for reactor siting or other peaceful uses of radiation.

18. Dose to a Developing Fetus from a Gamma Emitter in the Bladder

W. S. Snyder R. J. Cloutier[1] S. Smith[2]

In this study, we have undertaken to estimate dose to the developing fetus. The work of designing the fetus model and placing it appropriately in the phantom is largely due to Smith.

A schematic representation of the fetus is shown in Fig. 18.1. Since it is practically in contact with the bladder, a series of bladders (representing various stages of filling) was designed also. The dimensions selected are shown in Fig. 18.2 as functions of fetal age as well as a comparison of weight of the uterus of the model and some data of Williams[3] and Gillespie.[4] The Monte Carlo type computer program reported in MIRD Pamphlet 5 was adapted for the phantom plus fetus model described above but was otherwise unchanged. The source was placed in the bladder since this organ was not greatly altered, except that the maximum size was limited to 300 ml. For each estimate 3000 photons were sampled.

Results for sources of energies 1, 0.5, and 0.1 MeV are shown in Fig. 18.3. The source was programmed for a bladder of changing size – a "dynamic bladder." Source photons were selected according to the relative volume of the bladder during a period of filling, thus assuming that the concentration remained constant and that the bladder fills at a constant rate to a maximum content of 300 g. The dose estimates are expressed as rads per photon emitted during a complete filling of the bladder. It is evident that average dose to geometrical subdivisions of the fetus tends to decrease as the fetus grows and as the average distance from the source increases. Also, compartment 5, which is in contact with the bladder during pregnancy, gets rather more dose.

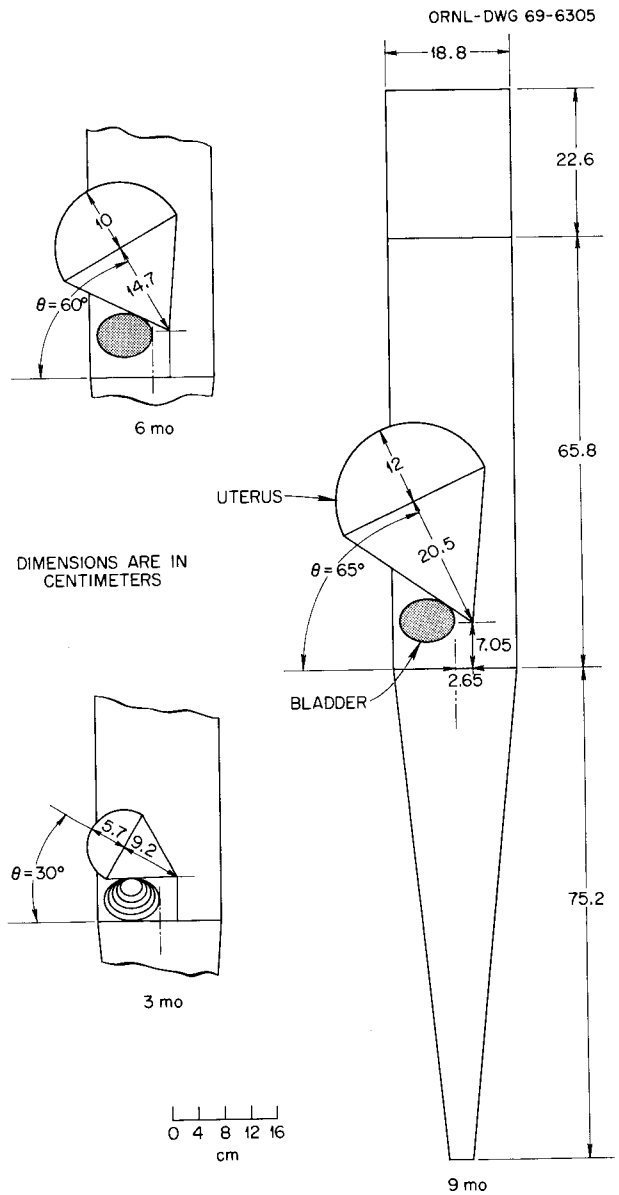

Fig. 18.1. Model of pregnant woman.

1. Oak Ridge Associated Universities.
2. Research participant, Oak Ridge Associated Universities.
3. J. W. Williams, *Obstetrics,* 11th ed., N. J. Eastman (ed.), Appleton-Century-Croft, Inc., New York, 1956.
4. E. C. Gillespie, "Principles of Uterine Growth in Pregnancy," *Amer. J. Obstet. Gynecol.* 59(5), 949 (1950).

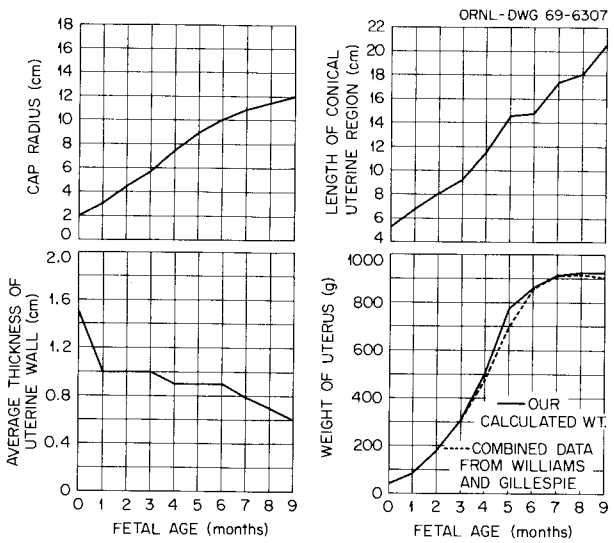

Obviously, dose in a small volume about the point of contact essentially will be constant during all stages of the pregnancy.

We are hoping to place the source in other locations near the fetus, but this awaits redesigning the model of the gastrointestinal tract, kidneys, and perhaps other organs which are displaced somewhat as the fetus grows.

Fig. 18.2. Dimensions and volume of the uterus during pregnancy.

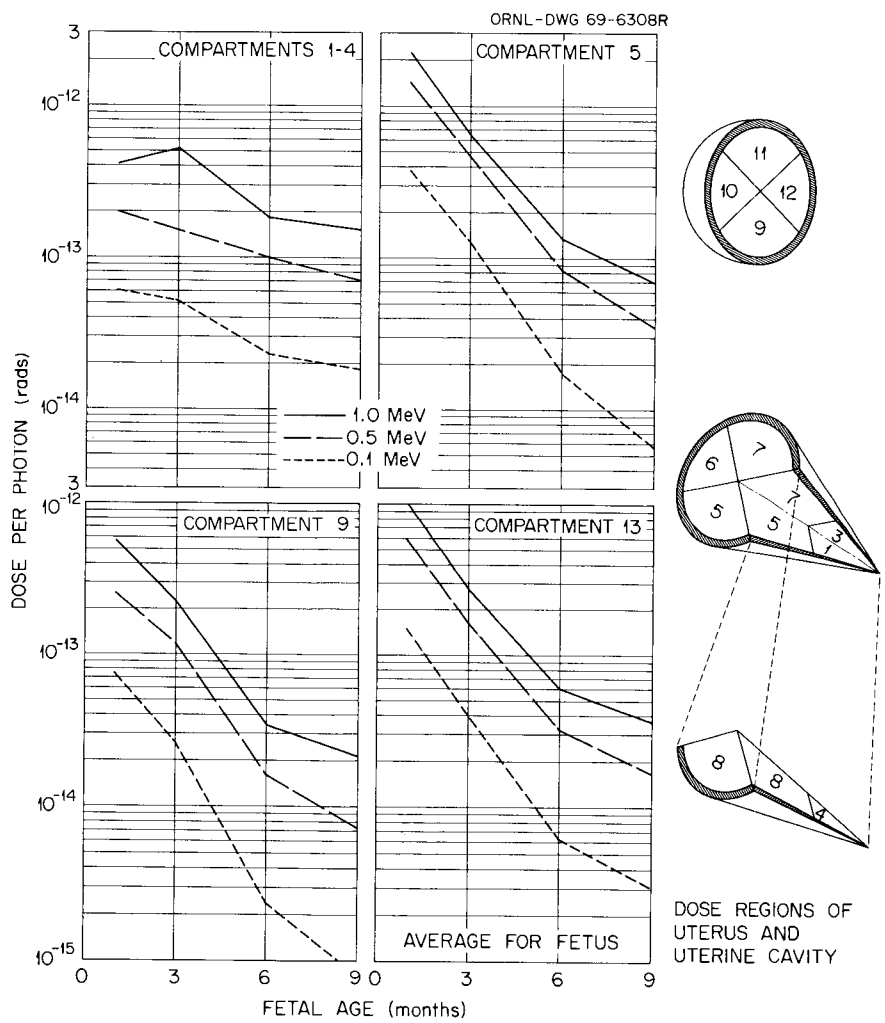

Fig. 18.3. Dose per photon in certain fetal regions.

19. Absorbed Fractions for Internal Emitters

W. S. Snyder Mary R. Ford G. G. Warner[1] P. Brindza[2]

The estimation of genetic dose is a problem of particular interest for radiation protection because of the possibility of accumulation of effects of radiation during many generations. Thus, it is important to provide accurate estimates of genetic dose for the many uses of radiation, even though the dose to the gonads may be far less than the dose to some other organ. For example, the genetic doses from fallout, or from occupational exposure, or from diagnostic use of radioactive pharmaceuticals are of interest even though some other organ may be receiving a higher dose than the gonads. Some estimates of genetic dose are implicit in ICRP Publication 2,[3] but, in general, these estimates of dose do not include dose to the gonads from photons emitted in other organs of the body, for example, bladder, gastrointestinal tract, etc. In this paper a method of obtaining estimates of genetic dose is developed which, while not highly accurate, is generally conservative and does include dose from all photon sources in the body without being unrealistically high.

Three of the present authors have published estimates of absorbed fraction of energy for various source and target organs.[4] The estimates are obtained by a Monte Carlo type calculation using a phantom design which allows size, shape, location, density, and elemental composition of the organs to be represented in an approximate sense. See Fig. 19.1 where the general form of the phantom, as well as a sketch of some of the organs, is shown. Unfortunately, the estimates obtained are subject to large statistical uncertainty in many cases, particularly whenever the target organ is far from the source or when the target organ is small. In the case of the gonads, the coefficient of variation of the estimate (CV = $100\sigma/m$) is nearly always large. Thus absorbed fractions for the gonads are not given in ref. 4. Similarly, the absorbed fractions of small organs such as the thyroid and spleen frequently will have an unacceptably high CV.

Berger[5] has published a tabulation of the buildup factor for a point source of monoenergetic photons in an infinite medium of soft tissue. He also has provided polynomial formulas which approximate the tabulated data. Using the notation of MIRD Pamphlet No. 1,[6] the specific absorbed fraction $\Phi(x)$ and the buildup factor $B(\mu x)$ in an infinite homogeneous medium are related by

$$\Phi(x) = \frac{\mu_{ab}\, e^{-\mu x}}{4\pi x^2} B(\mu x) . \qquad (1)$$

In Eq. (1) x is the distance (cm) of the target point from the point source, μ and μ_{ab} are the mass attenuation and mass absorption coefficients ($cm^2\ g^{-1}$), and Φ (g^{-1}) is the fraction of energy emitted by the point photon source which is absorbed per gram of medium at distance x from the source point. A density of 1 is assumed.

One may use (1) to obtain an estimate of specific absorbed fraction for a target region T in the presence of a source distributed in a region S, both S and T being subregions of an infinite and homogeneous space with

1. Mathematics Division.
2. ORAU summer student, 1970.
3. *Report of Committee II on Permissible Dose for Internal Radiation (1959)*, ICRP Publication 2, Pergamon, London, 1959.
4. W. S. Snyder, Mary R. Ford, G. G. Warner, and H. L. Fisher, Jr., "Estimates of Absorbed Fractions for Monoenergetic Photon Sources Uniformly Distributed in Various Organs of a Heterogeneous Phantom," MIRD Pamphlet No. 5, Suppl. No. 3, *J. Nucl. Med.* **10**, 7 (1969).
5. Martin J. Berger, "Energy Deposition in Water by Photons from Point Isotropic Sources," MIRD Pamphlet No. 2, Suppl. No. 1, *J. Nucl. Med.*, 15 (1968).
6. Robert Loevinger and Mones Berman, "A Schema for Absorbed-Dose Calculations for Biologically Distributed Radionuclides," MIRD Pamphlet No. 1, Suppl. No. 1, *J. Nucl. Med.*, 7 (1968).

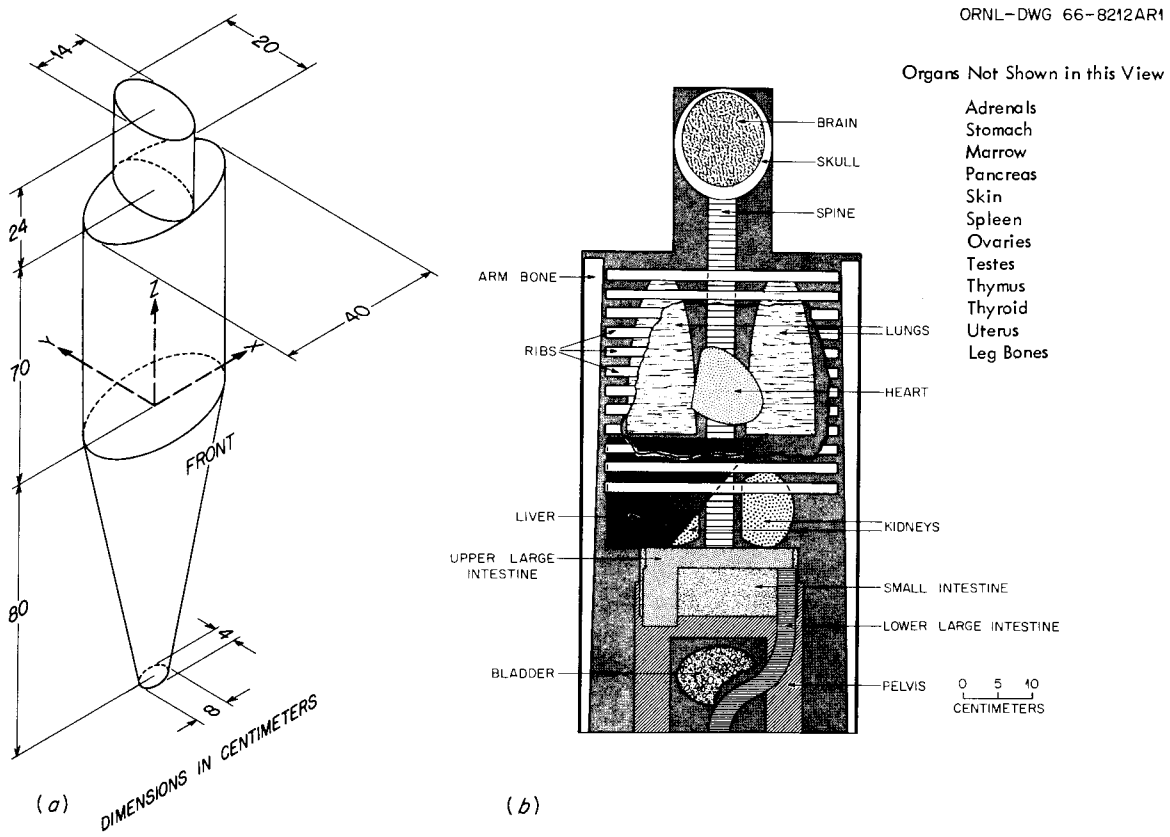

Fig. 19.1. (*a*) **The adult human phantom;** (*b*) **anterior view of the principal organs in the head and trunk of the phantom.**

the composition of tissue. For definiteness, suppose that the photons all have energy E and that source strength in S is 1 photon per gram. Then, the energy emitted from volume element dx of S (see Fig. 19.1) is $\rho E\, dx$, and the energy absorbed in a volume element dy of the target region T from this source in dx is given by

$$\Phi(dy \leftarrow dx)\, E\, dx\, dy = \frac{\mu_{ab}\, e^{-\mu|y-x|}}{4\pi|y-x|^2} B(\mu|y-x|)\, E\, dx\, dy\,, \quad (2)$$

the medium being of density 1. Integration of (2) over S yields the energy absorbed in dy from the source region S, namely,

$$E\, dy \int_S \frac{dx\, \mu_{ab}\, e^{-\mu|y-x|}}{4\pi|y-x|^2} B(\mu|x-y|)\,. \quad (3)$$

It follows by integration over T that the energy absorbed in region T is given by

$$E \int_T dy \int_S dx \frac{\mu_{ab}\, e^{-\mu|y-x|}}{4\pi|y-x|^2} B(\mu|y-x|)\,, \quad (4)$$

and hence

$$\Phi(T \leftarrow S) = \frac{1}{|S|\,|T|} \times \int_T dy \int_S dx \frac{\mu_{ab}\, e^{-\mu|y-x|}}{4\pi|y-x|^2} B(\mu|y-x|)\,. \quad (5)$$

The integral in (5) is difficult to evaluate in most cases for it requires an integration over the product space $S \times T$, that is, in a subregion of six-dimensional space. However, it is easy to devise a Monte Carlo sampling scheme for evaluating (5).

Let x_i and y_i denote points selected randomly in S and in T, respectively, the subscript i denoting the ith selection in a sequence of such pairs of points. The

value of the integral in (5) is then only the "average value" of the function

$$I(x, y) = \frac{\mu_{ab}\, e^{-\mu|x-y|}}{4\pi|x-y|^2} B(\mu|x-y|) \tag{6}$$

over the six-dimensional locus $S \times T$. It follows readily that (5) is the average value of (6) as usually defined, and thus the sample mean

$$\frac{1}{N}\sum_{i=1}^{N} I(x, y) \tag{7}$$

tends toward (5) as N is increased.[7] Formula (7) was easy to program for pairs of organs S and T since the subroutines for random selection of points in S and T were available from the calculations reported in ref. 4. The running time is small, in most cases being only a few minutes, and the coefficient of variation is generally small.

Some results are presented in Figs. 19.2 and 19.3 and are typical of results at other energies where the Compton or photoelectric processes of scattering predominate, respectively. The specific absorbed fraction $\Phi(T \leftarrow S)$ as estimated by (7) is plotted as the ordinate, and the value of Φ obtained by the Monte Carlo calculation in the finite phantom is plotted as the abscissa. Thus each point represents a comparison of the values of Φ for an organ pair, the organ pair being considered as subregions of an infinite homogeneous medium of tissue in the one case and as subregions of the finite heterogeneous phantom in the other. Most of the points fall close to the line representing equal estimates by the two methods, and a band representing a factor of 2 about the line would contain most of the points. If one allows for the uncertainty present in the estimate for the finite heterogeneous phantom, this conclusion is strengthened. The points with skeleton as target organ tend to lie on the lower side of the line for the lower energies, indicating that the estimate of Φ by use of the buildup factor for water or muscle is too low. This is understandable since the mass absorption coefficient $\mu_{ab} = (\mu - \sigma)/\rho$, sometimes referred to as μ_{en}, is greater for skeletal tissue than for muscle at these low energies. The magnitude of the ratio

$$\mu_{ab}{}^{\text{skeleton}}/\mu_{ab}{}^{\text{muscle}}$$

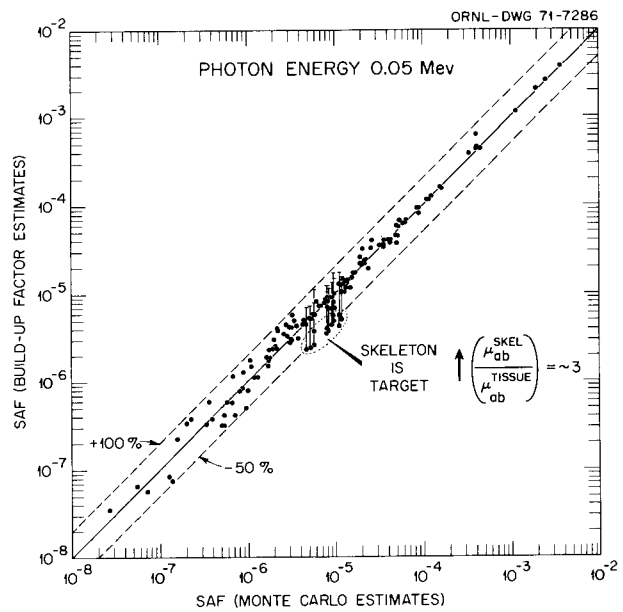

Fig. 19.2. Monte Carlo estimates of specific absorbed fractions compared with buildup factor estimates. 0.05 Mev.

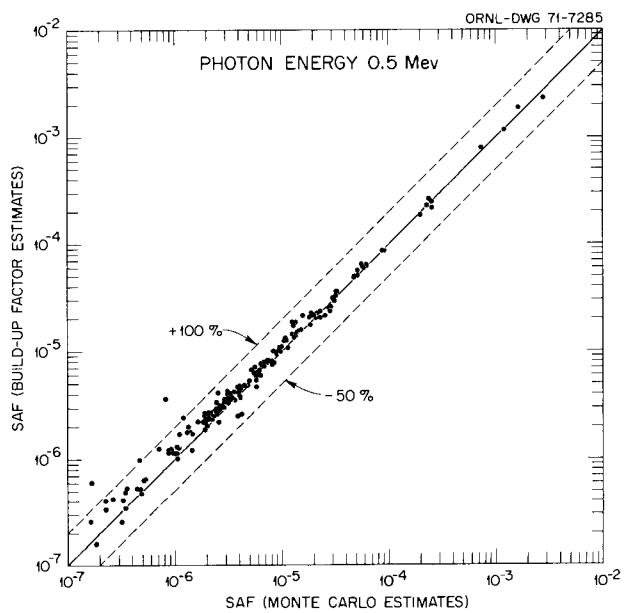

Fig. 19.3. Monte Carlo estimates of specific absorbed fractions compared with buildup factor estimates. 0.5 Mev.

is indicated on Fig. 19.3 for photon energies of 200 keV or less, and the estimates of Φ for the skeleton as target plausibly might be increased by this factor. If this is done, it will be noticed that most of the points lie above the line, indicating that the estimate of Φ for subregions of the infinite space is generally higher than for the finite heterogeneous phantom. If the phantom

7. J. M. Hammersley and D. C. Handscomb, *Monte Carlo Methods* (Methuen and Co., Ltd., London, 1964).

were homogeneous and composed of muscle, this would always be true, but the exceptions here are probably due to the heterogeneity or to poor statistics, or both.

In sum, the use of the buildup factor for an infinite homogeneous medium of tissue (muscle), or water, may be used to obtain estimates of the specific absorbed fraction for organs of the body composed of soft tissue. The estimates (B) tend to be high but generally not by more than a factor of 2. When skeletal tissue (bone plus marrow) is the target tissue, the results obtained by use of the buildup factor for muscle (or water) tend to be low at energies below 200 keV, but when they are multiplied by the correction factor

$$\mu_{ab}^{bone}/\mu_{ab}^{muscle} ,$$

these adjusted values seem to correspond as well with the Monte Carlo estimates as for organs composed of soft tissue. Thus, these estimates of specific absorbed fraction based on the buildup factor for an infinite homogeneous medium appear to provide accuracy within a factor of 2 or better, and the methods apply for those cases where the Monte Carlo calculations are statistically unreliable.

20. Depth-Dose Rates in Reference Man from Electrons and Beta Particles in a Radioactive Cloud

L. T. Dillman[1]

A dosimetry problem of current interest is immersion of a person in a radioactive cloud. Problems of this type can arise around accelerator and reactor installations. In this work we shall confine our attention to the beta and electron components of the radioactivity. Our purpose is to present a method for calculating radiation dose rates as a function of depth in the standard man phantom[2] representing the human body.

The energy span of beta particles and electrons ejected from radioactive atoms is such that the range of these particles in tissue is less than 1 cm in most cases. Hence, it is customary to neglect the slight curvature of the reference man phantom over dimensions of the order of 1 cm and treat the air-tissue boundary as flat. The most widely adopted technique for calculating the depth-dose rate to the standard man phantom from a beta emitter in the air is to use the semiempirical equation developed by Loevinger[3] for a semiinfinite slab geometry. However, Loevinger's equation has several distinct disadvantages. First of all it applies only to beta spectra and is not applicable to monoenergetic electron sources. Second, the formula tends to underestimate the true absorbed energy at small distances from the air-tissue boundary (e.g., a few percent of the range and less) and tends to overestimate the true absorbed energy at depths near the range of the betas. Indeed, examination of the comparative data given at the end of this paper shows that the Loevinger formula can be in error by an order of magnitude or more at positions near the end of the range.

Recently Martin J. Berger has published[4] scaled absorbed dose tables for point sources of monoenergetic electrons immersed in an infinite homogeneous medium. Berger's work uses the spatial moments method developed by Spencer,[5] which is considered to be the most accurate theoretical framework presently available for electron transport problems in infinite homogeneous media. Berger cites experimental measurements which indicate an agreement with Spencer's theory to within 4% or better for a wide variety of beta spectra. Furthermore, Berger states that the agreement was found to hold for all distances from the source up to that within which 95% of the emitted energy is absorbed. According to Berger's work the absorbed dose rate $R(r, E_0)$ in rads per second at distance r centimeters from a point monoenergetic electron emitter of energy E_0 MeV is given by

$$R(r, E_0) = \frac{AnkE_0\, F(\xi, E_0)}{4\pi\rho r^2 r_{90}}, \tag{1}$$

where A is the source activity in disintegrations per second, n is the number of electrons of energy E_0 emitted per disintegration, k is a constant equal to 1.6×10^{-8} g-rad/MeV, ρ is the density of the medium in grams per cubic centimeter, r_{90} is the distance in centimeters from the source within which 90% of the energy is absorbed, ξ is the ratio r/r_{90}, and $F(\xi, E_0)$ is the scaled absorbed fraction. Berger tabulates $F(\xi, E_0)$ for water for ξ = 0.0, 0.05, 0.1, ..., 1.15 for nine energies E_0 ranging from 0.025 to 4.0 MeV. Berger also tabulates r_{90} as a function of energy. In addition, Berger suggests the scaling techniques which must be employed to find $F(\xi, E_0)$ and r_{90} for media other than water. We have used the scaling methods to find $F(\xi, E_0)$ and r_{90} for tissue.

The point-source formula given in Eq. (1) may be integrated to find the dose rate at distance h below a semiinfinite radioactive half space. This is the configura-

1. Consultant to ORNL from Ohio Wesleyan University.
2. H. W. Fisher, Jr., and W. S. Snyder, ORNL-4168, p. 245 (1967).
3. G. J. Hine and G. L. Brownell, *Radiation Dosimetry,* chap. 16, Academic, New York, 1956.
4. M. J. Berger, "Distribution of Absorbed Dose around Point Sources of Electrons and Beta Particles in Water and Other Media," *J. Nucl. Med.,* Suppl. No. 5, March 1971.
5. L. V. Spencer, "Energy Dissipation by Fast Electrons," *Nat. Bur. Stand. (U.S.) Monogr.* No. 1, 1959.

tion of interest for finding depth doses in a human phantom. As illustrated in Fig. 20.1 a volume element dV of the radioactive space may be expressed as $2\pi r'\,dr'\,dx$. The activity A of such a volume element is $A_v\,dV$, where A_v is the disintegration rate per unit volume. Thus the dose rate at depth h is

$$R(h, E_0) = \frac{A_v n k E_0}{2\rho r_{90}}$$

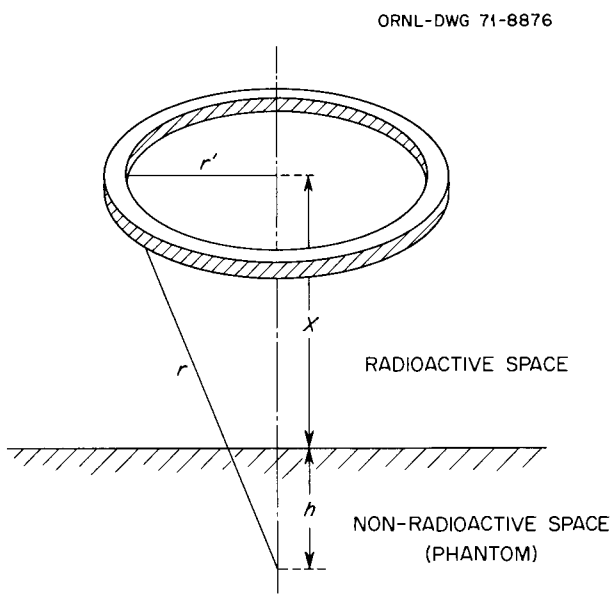

Fig. 20.1. Illustration of geometric parameters involved in numerical integration of point-source dose-rate formula.

$$\times \int_0^{R_0-h} \left[\int_0^{f(x)} F(\xi, E_0)\, r^{-2}\, r'\, dr' \right] dx\,, \quad (2)$$

where $f(x) = [R_0^2 - (x + H)^2]^{1/2}$, $r = [r'^2 + (x + h)^2]^{1/2}$, $\xi = r/r_{90}$, and R_0 is the range of the electrons of energy E_0 in the tissue medium of the phantom. Treating the radioactive air space as tissue for purposes of the above integration is equivalent to assuming that there is no boundary effect at the air-tissue interface and that the entire space may be considered as if it were infinite and homogeneous (which is the situation for which Berger's scaled absorbed fraction tabulations are valid). Since the point-source kernels for air and tissue are quite similar, there is reason to believe that this approximation will not significantly alter the results.

We have carried out the double integration of Eq. (2) numerically using the Romberg method. This has been done at the nine energies for which Berger gives tabulated information of scaled absorbed fractions, and by interpolation or extrapolation for 42 other energies ranging from 0.001 to 4.0 MeV. Since the scaled absorbed fractions are a very slowly varying function of energy, linear interpolations or extrapolations have been used. If the ratio of the absorbed dose rate to the infinite medium equilibrium dose rate is plotted as a function of the ratio of the depth h to the depth, h_{max}, where the dose rate becomes zero, the results are nearly independent of the energy E_0 as illustrated in Fig. 20.2.

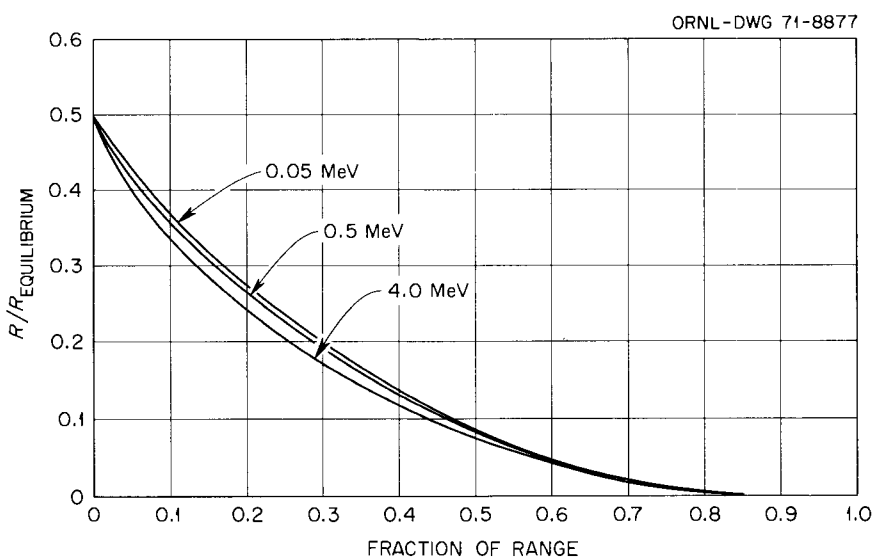

Fig. 20.2. Ratio of absorbed dose rate to infinite medium absorbed dose rate as a function of the depth in the phantom measured as a fraction of the range of the electrons in tissue. The curves are for a semiinfinite slab geometry with zero fraction of range corresponding to the air-tissue interface.

Table 20.1. Beta and electron dose rates as a function of depth in reference man

Assumed source strength is 1 μCi per gram of air

Depth (cm)	Dose rate (rads/day)						
	1-MeV monoenergetic electrons, this work	^{15}O source		^{13}N source		^{28}Al source	
		This work	Loevinger formula	This work	Loevinger formula	This work	Loevinger formula
0.0	25.57	18.43	18.43	12.48	12.48	31.69	31.69
0.007	24.00	16.71	16.50	10.66	10.22	30.11	29.79
0.02	21.09	14.18	14.19	8.358	7.860	27.40	27.42
0.05	16.73	10.37	10.52	5.177	4.735	22.67	23.33
0.1	11.20	6.369	6.597	2.366	2.188	17.30	18.35
0.15	7.125	3.876	4.152	1.014	1.019	13.32	14.60
0.2	4.036	2.300	2.614	0.3871	0.474	10.38	11.65
0.27	1.264	1.009	1.367	0.0728	0.1627	7.017	8.508
0.5	0.0	0.0218	0.1625	0.0	0.0048	1.778	3.026
0.75	0.0	0.0	0.016	0.0	0.00010	0.202	0.9839
1.0	0.0	0.0	0.0016	0.0	0.00000	0.0068	0.3199
Skin av	11.4	6.898	7.335	3.079	2.989	17.38	18.85

This fact is made use of in order to find the absorbed dose rate as a function of depth h for any desired energy other than the 51 energies for which data are tabulated. First a linear interpolation of $R(h, E_0)/R_{\text{equilibrium}}$ vs $h/h_{\max}$ is made on energy, and then the resulting curve is linearly interpolated on the tabulated values of $h/h_{\max}$ to give $R(h, E_0)$ for any desired h and any desired E_0.

The author of this report has developed previously a computer code for calculating the spectral energy distribution $W(E)$ for beta sources.[6] This computer code has been combined with the present work to obtain $R(h, E_{\max})$ for a beta source for any desired h and any end-point energy $E_{\max}$. We have simply

$$R(h, E_{\max}) = \frac{\int_0^{E_{\max}} W(E)\, R(h, E)\, dE}{\int_0^{E_{\max}} W(E)\, dE}. \tag{3}$$

The integrations in Eq. (3) have been carried out numerically using Simpson's rule. In addition we have calculated the average dose rate to the skin of standard man by averaging the function of Eq. (3) for betas, or the function of Eq. (2) for monoenergetic electrons, over depths from 0.007 to 0.2 cm.

Typical results for both monoenergetic electrons and betas are given in Table 20.1. Comparison with the Loevinger formula is also given in Table 20.1.

6. L. T. Dillman, "Average Particle Energy in Beta Decay," *Health Phys.* **19**, 385 (1970).

21. Estimates of Microcurie-Days Residence, Dose Equivalent, and $(MPC)_W$ for Thorium-232 in Man Using a Mammillary Model

S. R. Bernard C. F. Holoway

In two previous progress reports[1,2] application of a mammillary compartment model was made to the problem of estimating microcurie-days residence of ^{232}Th, ^{228}Ra-^{228}Ac, ^{228}Th, and ^{224}Ra in organs and tissues of man following a single intake of the parent into the bloodstream. This problem is difficult because of the lack of information on the metabolic behavior of the radium daughters produced in the chain. The metabolic behavior of the radium daughters, that is, the fractions of the radium daughters which are recycled to blood or which undergo radioactive decay in the tissue where they are formed and their retention there, has a pronounced effect on the residence times accumulated in the organs and tissues and, subsequently, on the dose equivalent and the $(MPC)_w$ calculated from the model.

Fortunately, some data have been made available on this recycling by Stover et al.[3] who administered single intravenous doses of ^{228}Th citrate to beagle dogs and measured (or estimated) levels of ^{224}Ra and ^{228}Th and other daughters in various organs and tissues and body fluids out to 1400 days. Stover et al. have defined and discussed $F_T(t)$, the fraction of ^{224}Ra daughters undergoing translocation in the body, by the equation

$$F_T(t) = \frac{1 - (^{224}Ra/^{228}Th)_{body}}{0.3} . \qquad (1)$$

Here, ^{224}Ra and ^{228}Th represent the level of ^{224}Ra daughter and ^{228}Th parent present in the body at various times, and $(^{224}Ra/^{228}Th)_{body}$ is the ratio of daughter to parent in the body at various times. The numerator of Eq. (1) corresponds roughly to the measured fraction of radium daughter which is released from the body, while the denominator is the calculated fraction assuming that all of the radium daughter is recycled to blood where it behaves as freshly injected material. The level of ^{224}Ra present in the body was estimated by Stover et al.[3] from urine and fecal excretion data. Any errors present in these estimates (and there usually are losses in collection and analyses of excreta) will affect the value of $F_T(t)$. In the period 100 to 1400 days, $(^{224}Ra/^{228}Th)_{body}$ ranges from 0.88 to 0.92, and thus $F_T(t)$ changes from 0.12/0.3 (=0.4) to 0.08/0.3 (=0.11), thus decreasing by a factor of about 4 for only a 4% change in the ratio $(^{224}Ra/^{228}Th)$. Thus small changes in the ratio $(^{224}Ra/^{228}Th)$ may produce a large percentage change in $F_T(t)$.

We have employed the four-compartment mammillary model (see Fig. 21.1) studied previously in refs. 1 and 2. The model consists of a blood compartment, two bone compartments (one short-term and one long-term), and a soft tissues compartment, with the further constraint that the half-lives for short-term bone and soft tissues are the same. We showed previously that only three exponential terms are required for each compartment of this four-compartment system to obtain the total-body retention equations given by Stover et al.[3] Also, we gave equations for calculating the rate transfer constants in the mammillary compartment model from the total-body retention function.

In this study we have computed $F_T(t)$ from a different set of assumptions. These can be made explicit from the following mathematical considerations. Let $A^k(t)$ denote a column vector $a_i^k(t)$ of the amounts of

1. S. R. Bernard and C. F. Holoway, "Application of a Mammillary Compartment Model to the Estimation of Microcurie-Days Residence of ^{232}Th Parent and ^{228}Ra Daughter in Man," *Health Phys. Div. Annu. Progr. Rep. July 31, 1969,* ORNL-4446, pp. 285–95.

2. S. R. Bernard and C. F. Holoway, "Application of a Mammillary Compartment Model to Estimation of Microcurie-Days Residence of ^{232}Th, ^{228}Ra-^{228}Ac, ^{228}Th, and ^{224}Ra in Man," *Health Phys. Div. Annu. Progr. Rep. July 31, 1970,* ORNL-4584, pp. 214–16.

3. B. J. Stover et al., "The ^{228}Th Decay Series in Adult Beagles: ^{224}Ra, ^{212}Pb, and ^{212}Bi in Blood and Excreta" *Radiat. Res.* **26**, 226 (1965).

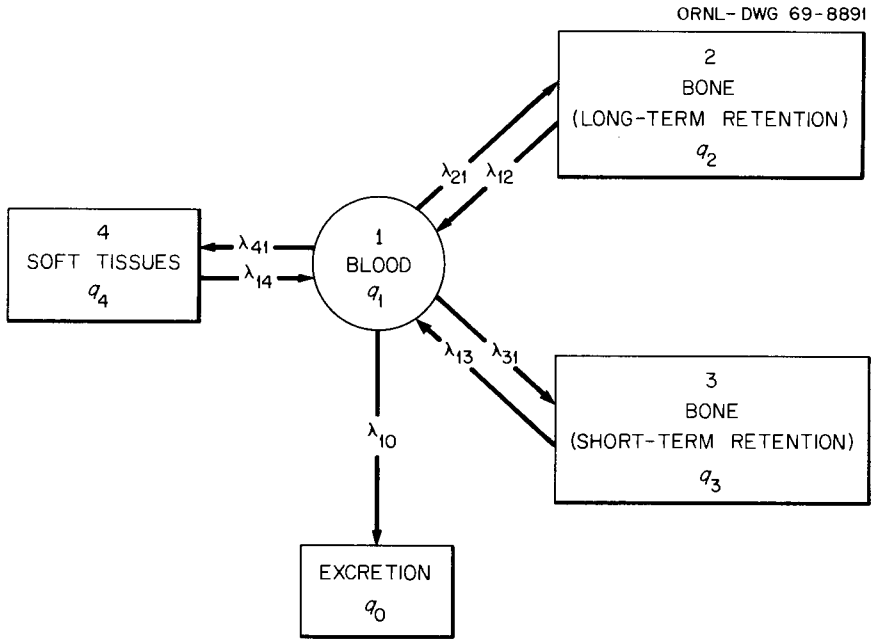

Fig. 21.1. Mammillary model for distribution and excretion of radium and thorium in dogs and man.

radioactivity of the kth ($k = 0, 1, \ldots, n$) daughter (or a parent) present in the ith ($i = 1, 2, 3, 4$) compartment of the mammillary model at time t. Let $(\lambda_{ij}{}^k)$ denote the matrix of rate transfer constants for passage of the kth radionuclide from compartment j ($j = 1, 2, 3, 4$) to compartment i and denote by $\lambda_r{}^k$ the radioactive decay constant, a scalar, of the kth radionuclide of the chain. The differential equations for the rate of change of the kth isotope are, in matrix notation:

$$\dot{A}^k(t) = \lambda_r{}^k R^k A^{k-1}(t) - (\lambda_{ij}{}^k) A^k(t), k = 0, 1, \ldots, n , \quad (2)$$

where $A^{-1}(t) \equiv 0$ and

$$R^k \equiv \begin{pmatrix} 1 & r_2{}^k & r_3{}^k & r_4{}^k \\ 0 & 1 - r_2{}^k & 0 & 0 \\ 0 & 0 & 1 - r_3{}^k & 0 \\ 0 & 0 & 0 & 1 - r_4{}^k \end{pmatrix} \quad (3)$$

is a matrix which indicates the details of recycling; that is, $r_i{}^k$ is a scalar ($0 \leqslant r_i{}^k \leqslant 1$) representing the fraction of the kth daughter produced in compartment i that recycles from compartment i to blood, which is compartment 1. Note that the solution is independent of $r_i{}^0$ since $A^{-1}(t) \equiv 0$. For $r_2{}^k = r_3{}^k = r_4{}^k = 1$, we say 100% of the kth daughter is recycled from compartments 2, 3, and 4 to 1. When $r_2{}^k = r_3{}^k = r_4{}^k = 0$, we say 0% or none of the kth daughter is recycled to blood.

In this report we treat three cases – A, B, and C – in which we allow different recycling for the compartments. In case A, we assume $r_2{}^1 = 0$, $r_3{}^1 = r_4{}^1 = 1.0$; that is, long-term bone recycles none of the Ra, while both short-term bone and soft tissues recycle all of it. In case B we assume $r_2{}^1 = 0$, $r_3{}^1 = 0.2$, and $r_4{}^1 = 1.0$. In case C we assume $r_2{}^1 = 0 = r_3{}^1$, $r_4{}^1 = 1.0$. Calculations of Eq. (1) were made using the solutions of Eq. (2), and a plot of Eq. (1) vs time is shown in Fig. 21.2. As can be noted, case B is closest to the experimental data on dogs labeled "all dogs studied." (We also mention that a "dose effect" was noted by Stover et al., but for purposes of clarity we do not show nor discuss that here.)

Now that the $F_T(t)$ is estimated fairly closely, we have to look at the predicted values for individual organs and ratios of ^{224}Ra to ^{228}Th in the separate organs and compare these with the data on the beagle dogs. Table 21.1 presents the retention equations for the two radionuclides present in the various compartments for the initial condition of unit intake of ^{228}Th to blood. From these equations the ratios of ^{224}Ra to ^{228}Th can be computed for each organ. We do not give these detailed computations here, but instead we merely state the results. In the interval 100 to 1400 days, we find the ratio in total bone increases from 0.86

Table 21.1. Retention equations for each compartment and ^{228}Th and ^{224}Ra contained therein[a]

Isotope	Organ									
^{228}Th	Blood	0.00107	0.00199	0.0	0.0	0.0	0.0	0.997	0.0	$e^{-0.00389t}$
	Long-term bone	0.498	−0.342	0.0	0.0	0.0	0.0	−0.156	0.0	$e^{-0.00114t}$
	Short-term bone	0.124	0.338	0.0	0.0	0.0	0.0	−0.462	0.0	$e^{-0.00200t}$
	Soft tissues	0.0669	0.182	0.0	0.0	0.0	0.0	−0.249	0.0	$e^{-0.191t}$
^{224}Ra	Blood	0.0315	0.0851	−0.000334	−0.0511	−0.0511	0.0	0.643	−0.709	$e^{-0.260t}$
	Long-term bone	0.508	−0.325	−0.359	0.127	0.128	0.0	−0.00000376	0.0473	$e^{-0.257t}$
	Short-term bone	0.0928	0.253	−0.000762	−0.163	−0.163	−0.293	−0.0593	0.169	$e^{-0.694t}$
	Soft tissues	0.0370	0.100	−0.00152	−0.325	−0.325	0.293	−0.442	0.339	$e^{-0.885t}$

[a]Initial condition: unit input of ^{228}Th to blood; nothing initially present in other organs.

Table 21.2. Microcurie-days in various organs and tissues for ^{232}Th and its daughters in man and microcurie-days in bone and approximate effective energies of the radionuclide[a]

Isotope	Organ	Microcurie-days	Microcurie-days in bone	Effective energies (MeV)	
				Bone	Soft tissues
^{232}Th	Blood	12.7	11,561	206	41.2
	Long-term bone	10,136			
	Short-term bone	1,425			
	Soft tissues	623			
^{228}Ra-^{228}Ac[a]	Blood	37.3	7,074	2.7	0.7
	Long-term bone	6,963			
	Short-term bone	1,110			
	Soft tissues	4.3			
^{228}Th	Blood	1.43	6,560	279	55.7
	Long-term bone	6,416			
	Short-term bone	144			
	Soft tissues	49.1			
^{224}Ra-^{208}Pb	Blood	71.2	6,514	1386	278
	Long-term bone	6,400			
	Short-term bone	114			
	Soft tissues	0.154			

[a]It is assumed that ^{228}Ac has the same microcurie-days as ^{228}Ra due to the short half-life of 0.26 day.

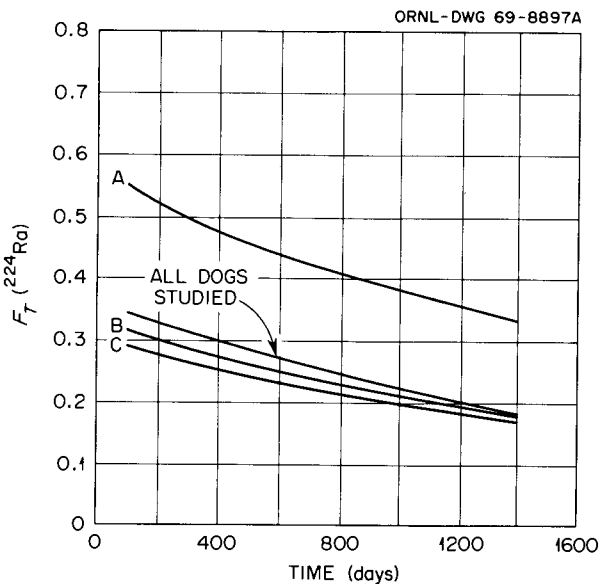

Fig. 21.2. Stover et al.'s estimate of fraction of ^{224}Ra formed in the dog which translocates. All-dogs-studied curve derived from all the dog excretion data. At 20 to 30 days, F_T (^{224}Ra) = 0.79. A: 100% recycle in soft tissues, 100% recycle in short-term bone, 20% recycle in long-term bone. B: 100% recycle in soft tissues, 20% recycle in short-term bone, 0% recycle in long-term bone. C: 100% recycle in soft tissues, 0% recycle in short-term bone, 0% recycle in long-term bone.

at 100 days to 0.93 at 1400 days. This is to be compared with Stover et al.'s data which yielded the single value of 0.9 for $100 \leqslant t \leqslant 1400$ days.[4] For blood, the ratio drops from 39 at 100 days to 36 at 1400 days. Stover et al.[4] have found the ratio to be a single value of 24 in plasma for $100 \leqslant t \leqslant 1400$ days. For soft tissues, the calculated ratio is ~0.55 at 100, 700, and 1400 days. Stover et al. have found a ratio of 1.3 for liver, 1.1 for spleen, and about 0.3 for kidney. However, the variability in the retention is large for all of the above organs, and the time dependency is masked by this variability.

In our calculations for the ^{232}Th chain in man, we assume that the radium daughters behave similarly as case B in the dogs, that is, $R^1 = R^3$. For the ^{228}Th daughter, $r_j^3 = 0$ for all j. The estimated microcurie-days at 50 years were calculated using the rate transfer constants in the previous report (p. 287 of ref. 1) and for case B in Fig. 21.2. These appear in Table 21.2, together with the approximate effective energies for bone and soft tissues (where liver is assumed to be the critical organ as an approximate size for the soft tissues). The dose equivalent for bone from these data is

$$(\mathrm{DE})_{\mathrm{bone}} = 0.966 \times 10^5 \text{ rem}/\mu\text{Ci into blood},$$

and the $(\mathrm{MPC})_w$ computed from this DE and for the case of 30 rems/year as the permissible level is

$$(\mathrm{MPC})_w = 3.88 \times 10^{-6}\ \mu\text{Ci/cc (168-hr week)}.$$

In this calculation f_1 is taken as 10^{-4} as indicated from the human data of Maletskos et al.[5] on thorium in mock dial paint. This is to be compared with the ICRP Publication 2 $(\mathrm{MPC})_w$ of 2×10^{-5} μCi/cc for soluble compounds based on bone as the critical organ. As can be noted, a factor of 5 reduction in the $(\mathrm{MPC})_w$ is indicated.

The authors acknowledge, with gratitude, the programmer John Carpenter who assembled the code DESCP which they used in solving the differential equations arising in this work.

4. B. J. Stover et al., "The ^{228}Th Decay Series in Adult Beagles: ^{224}Ra, ^{212}Pb, and ^{212}Bi in Selected Bones and Soft Tissues," *Radiat. Res.* **26**, 132 (1965).

5. C. J. Maletskos et al., "Metabolic Data on Injected and Ingested ^{234}Th in Human Beings," *Proc. 12th Annual Bioassay and Analytical Chemistry Meeting, Gatlinburg, Tenn., October 13–14, 1966*, pp. 191–207.

Theses, Papers, Publications, and Lectures

Theses

Gerald Alton
Study of Low-Energy Electron Molecule Interactions (in preparation).

A. J. Braundmeier, Jr.
Radiative Decay of Coulomb-Stimulated Plasmons in Al, Mg, and Be, ORNL-TM-3158 (October 1970).

Barbara Brooks
The Technique of Ellipsometry in the Determination of the Optical Constants of Indium and Tin, ORNL-TM-3307 (May 1971).

W. L. Chen
Dose Distributions from Neutrons Incident on a Tissue-Equivalent Phantom, ORNL-TM-3425 (June 1971).

A. A. Christodoulides
Electron Attachment to Polyatomic Molecules, ORNL-TM-3163 (December 1970).

P. M. Collins
Low-Energy Electron Attachment to Polyatomic Molecules, ORNL-TM-2614 (September 1970).

C. E. Easterly
Study of Aromatic Hydrocarbons in Relation to Carcinogenesis, ORNL-TM-2616 (in preparation).

J. M. Elson
Collective Excitations in Inhomogeneous Plasmas (in preparation).

T. F. Gesell
Photoelectric Determination of Electron Attachment Lengths in Magnesium and Aluminum, ORNL-TM-2617 (May 1971).

R. E. Goans
Dissociative Electron Attachment to Polyatomic Molecules (in preparation).

A. Hadjiantoniou
Electron Attachment to and Autoionization of Long-Lived Negative Ions of Polyatomic Molecules (in preparation).

W. F. Hanson
Optical Properties of Solids in the Extreme Ultraviolet (in preparation).

Paul D. Kidd
Electron Capture and Drift in Organic Liquids (in preparation).

D. L. McCorkle
Interaction of Low-Energy Electrons with Polyatomic Systems (in preparation).

W. T. Naff
Electron Attachment and Excitation Processes in Selected Organic Molecules, ORNL-TM-3410 (May 1971).

S. J. Nalley
Collisional Ionization between Cesium and Selected Molecules, ORNL-TM-2620 (May 1971).

M. N. Pisanias
Inelastic Scattering of Slow Electrons by Organic Molecules (in preparation).

J. W. Poston
Neutron Depth Dose Distributions in Heterogeneous Phantoms, ORNL-TM-3329 (April 1971).

B. L. Sowers
Optical Properties of Organic Liquids in the Vacuum Ultraviolet (in preparation).

R. B. Vora
Optical Model Studies of Ion Molecule Interactions (in preparation).

R. B. Vora
Calculation of Stopping Power at Extreme Relativistic Energies, ORNL-TM-2621 (October 1970).

J. F. Wilson
Mass Analysis of Ions Formed in Electron Swarm Experiments (in preparation).

J. F. Wilson
The Effects of Radiation Energy, Dose Level, and the Atomic Number of the Immediate Environment on the Thermally Stimulated Exoelectron Emission from Beryllium Oxide and Lithium Fluoride, ORNL-TM-3325 (May 1971).

Papers

E. T. Arakawa
Experimental Studies of Surface Plasmas, American Physical Society, March 29–April 1, Cleveland, Ohio.

J. A. Auxier and J. Neufeld
What and Where Should We Measure?, Special Symposium on the Future of Personnel Dosimetry, Health Physics Society Annual Meeting, July 12–16, 1971, New York (presented by J. Neufeld).

C. J. Barton, D. G. Jacobs, M. J. Kelly, and E. G. Struxness
Radiological Considerations in the Use of Natural Gas from Nuclearly Stimulated Wells, Atomic Industrial Forum 1970 Annual Conference, November 17, 1970, Washington, D.C.

K. Becker
Exoelectron Emission as a Research Tool, Seminar at Drexel University, November 16, 1970, Philadelphia, Pennsylvania.

Some Applications of Nuclear Track Etching in Polymers, American Nuclear Society, November 15–19, 1970, Washington, D.C.

Etched Film Techniques, Argonne National Laboratory Symposium on Autoradiography, February 18, 1971, Chicago, Illinois.

K. Becker, J. S. Cheka, K. W. Crase, and R. B. Gammage
New Exoelectron Dosimeters, Symposium on New Developments in Physical and Biological Radiation Detectors, November 23–27, 1970, Vienna, Austria (presented by F. H. Attix).

K. Becker and R. B. Gammage
Exoelectron Emission and Surface Characteristics of Lunar Materials, Second Annual Lunar Science Conference, January 11, 1971, Houston, Texas (presented by K. Becker).

Exoelectron Emission and Surface Characteristics of Lunar Materials, American Chemical Society, April 2, 1971, Los Angeles, California (presented by K. Becker).

S. R. Bernard and C. F. Holoway
Application of a Mammillary Compartment Model to the Estimation of Microcurie-Days Residence of ^{232}*Th Parent and* ^{228}*Ra Daughter in Man,* Health Physics Society Annual Meeting, July 11–15, 1971, New York.

W. P. Bonner
Application of Zonal Centrifugation in Environmental Studies, 26th Industrial Waste Conference, May 4–6, 1971, Lafayette, Indiana.

A. J. Braundmeier and E. T. Arakawa
Plasma Radiation from Mg and Be, American Physical Society, Southeastern Section, November 23–25, 1970, New Orleans, Louisiana.

B. G. Brooks and L. C. Emerson
Optical Properties of Indium, Tin, and Gold between 270 and 800 nm, American Physical Society, Southeastern Section, November 23–25, 1970, New Orleans, Louisiana.

J. B. F. Champlin, J. W. Poston, and J. A. Lake
An Interior Seaway for Northern Africa, Symposium on Engineering with Nuclear Explosives, January 14–16, 1970, Las Vegas, Nevada (presented by J. B. F. Champlin).

A. A. Christodoulides, L. G. Christophorou, P. M. Collins, and J. G. Carter
Dissociative Electron Attachment to Brominated Aliphatic Hydrocarbons, 23rd Annual Gaseous Electronics Conference, October 21–23, 1970, Hartford, Connecticut.

L. G. Christophorou
Electron Attachment Processes, Gordon Conference, July 13–17, 1970, New Hampton, New Hampshire.

R. N. Compton, S. J. Nalley, H. C. Schweinler, and V. E. Anderson
Ions from Collisions of Cs with O_2, NO_2, and N_2O, VIIth International Conference on the Physics of Electronic and Atomic Collisions, July 26–30, 1971, Amsterdam, Holland.

M. J. Cook, W. S. Snyder, and G. G. Warner
Age Dependence of Dose in Anthropomorphic Phantoms Corresponding to Ages 0, 1, 5, 10, 15, and 20 Years, Health Physics Society Annual Meeting, July 11–15, 1971, New York.

H. Dickson, E. Roberts, Jr., H. M. Butler, R. J. Cloutier, G. Smithwick,
E. E. Watson, F. F. Haywood, and J. D. Berger
Radiation Safety in the Operation of a Low-Energy Accelerator, Second Conference on Applications of Small Accelerators, March 23–25, 1970, Oak Ridge, Tennessee (presented by R. J. Cloutier).

J. L. Durham, B. R. Fish, J. Wagman, and F. G. Seeley
Radiochemical Analysis of $^{35}SO_2$ Absorbed on PbO_2, 14th Conference on Analytical Chemistry in Nuclear Technology, October 13–15, 1970, Gatlinburg, Tennessee.

J. L. Durham, B. R. Fish, and Jack Wagman
Effect of Submicron Fe_3O_4 Particles on the Transport of SO_2, American Chemical Society Meeting, March 28–April 4, 1971, Los Angeles, California.

C. E. Easterly, L. G. Christophorou, R. P. Blaunstein, and J. G. Carter
Fluorescence from the Second Excited π-Singlet State of Aromatic Hydrocarbons in Solution, American Physical Society, Southeastern Section, November 23–25, 1970, New Orleans, Louisiana.

J. M. Elson and R. H. Ritchie
Interaction of Photons at a Rough Metal Surface, American Physical Society, Southeastern Section, November 23–25, 1970, New Orleans, Louisiana.

L. C. Emerson and R. D. Birkhoff
Electron Spectrum in Irradiated Silicon, IEEE Conference on Nuclear and Space Radiation Effects, July 20–23, 1970, Durham, New Hampshire.

B. R. Fish
Air Pollution Effects of SO_2 Compared with Radioactivity, Southeastern Industrial Health Conference, September 30–October 2, 1970, Gatlinburg, Tennessee.

Electrical Generation of Natural Aerosols from Vegetation, 45th National Colloid Symposium of American Chemical Society, June 21–23, 1971, Atlanta, Georgia.

M. R. Ford and W. S. Snyder
Absorbed Fractions for Internal Emitters, Health Physics Society Annual Meeting, July 11–15, 1971, New York.

C. W. Francis and Tsuneo Tamura
Methodological Parameters in Zonal Centrifugation of Soil Clays and Clay Minerals, Annual Meeting of the American Society of Agronomy, August 23–28, 1970, Tucson, Arizona.

Cesium-137 Soil Inventory of a Tagged Liriodendron Forest, 1962 and 1969, Third National Symposium on Radioecology–Radionuclides in Ecosystems, May 10–12, 1971, Oak Ridge, Tennessee.

E. L. Fuller, Jr., H. F. Holmes, R. B. Gammage, and K. Becker
The Interaction of Gases with Lunar Materials, Second Annual Lunar Science Conference, January 13, 1971, Houston, Texas (presented by E. L. Fuller, Jr.).

The Interaction of Gases with Lunar Materials, American Chemical Society, April 2, 1971, Los Angeles, California (presented by R. B. Gammage).

R. B. Gammage and K. Becker
Potentials of Exoelectron Dosimetry, Health Physics Society Annual Meeting, July 12–16, 1971, New York (presented by R. B. Gammage).

R. B. Gammage, K. W. Crase, and K. Becker
Role of Activators in the Exoelectron Emission from Ceramic BeO, Health Physics Society Annual Meeting, July 12–16, 1971, New York (presented by K. Becker).

R. B. Gammage, E. L. Fuller, Jr., and H. F. Holmes
Heats of Immersion in the Zirconia-Water System, American Chemical Society, March 29, 1971, Los Angeles, California (presented by R. B. Gammage).

Adsorption on Porous Thorium Oxide Modified by Water, Symposium in Honor of Stephen Brunauer, April 16, 1971, Bethlehem, Pennsylvania (presented by H. F. Holmes).

W. R. Garrett
Elastic Scattering of Electrons by a Freely Rotating Electric Dipole: Effect of Closed Channels, 23rd Annual Gaseous Electronics Conference, October 21–23, 1970, Hartford, Connecticut.

T. F. Gesell and E. T. Arakawa
Evidence for Short Electron Mean Free Paths in Aluminum and Magnesium, American Physical Society, Southeastern Section, November 23–25, 1970, New Orleans, Louisiana.

Duncan Grant and R. H. Ritchie
The Interaction of Slow Electrons with Surface Plasmons, American Physical Society, Southeastern Section, November 23–25, 1970, New Orleans, Louisiana.

J. T. Grissom, W. T. Naff, W. R. Garrett, R. N. Compton, and J. A. Stockdale
Electron Impact Excitation and Ionization of the Rare Gases; Production of Slow Electrons in the Ionization Continuum, Second International Conference on Atomic Physics, July 21–24, 1970, Oxford, England.

F. F. Haywood
Low-Energy X-Ray Spectrometry, DASA Aerospace Systems Division Annual Review, May 5–6, 1970, Palo Alto, California.

L. D. Hulett, T. A. Carlson, B. R. Fish, and J. L. Durham
Studies of Sulfur Compounds Adsorbed on Smoke Particles and Other Solids by Photoelectric Spectroscopy, Symposium on Air Quality, 161st National Meeting of American Chemical Society, April 1–2, 1971, Los Angeles, California.

D. G. Jacobs
Survey of Tritium Problems in the United States, IAEA Consultants Meeting on Tritium, November 14–18, 1970, Vienna, Austria.

D. G. Jacobs and E. G. Struxness
Radiological Safety Considerations in the Distribution of Natural Gas Containing Radionuclides, Second International Atomic Energy Agency Panel on Plowshare, January 17–22, 1971, Vienna, Austria.

G. D. Kerr, R. D. Birkhoff, M. W. Williams, and L. R. Painter
Extreme Vacuum UV Optical Properties of DC-704 and DC-705 Diffusion Pump Oils, American Physical Society, Southeastern Section, November 23–25, 1970, New Orleans, Louisiana.

C. E. Klots
Reformulation of the Quasi-Equilibrium Theory of Ionic Fragmentation, 19th Annual Conference on Mass Spectrometry and Allied Topics, May 2–7, 1971, Atlanta, Georgia.

V. Krishan and R. H. Ritchie
Damping of Volume Plasmons in Polycrystalline Metals, American Physical Society, Southeastern Section, November 23–25, 1970, New Orleans, Louisiana.

W. C. McClain
Demonstration Repository for Solidified Radioactive Wastes, 16th Annual Meeting of Health Physics Society, July 11–15, 1971, New York.

W. T. Naff and R. N. Compton
Electron Impact Studies of Acetone and Halogenated Acetone, 23rd Annual Gaseous Electronics Conference, October 21–23, 1970, Hartford, Connecticut.

W. T. Naff, P. W. Reinhardt, and R. N. Compton
Temporary Attachment of Electrons to Some Organic Molecules, American Physical Society, Southeastern Section, November 23–25, 1970, New Orleans, Louisiana.

S. J. Nalley, R. N. Compton, and P. W. Reinhardt
Charge Exchanging Collisions between Cs and NO_2, 23rd Annual Gaseous Electronics Conference, October 21–23, 1970, Hartford, Connecticut.

D. R. Nelson and F. J. Davis
Determination of Thermal Electron Diffusion (D) and Attachment Rate (αw) *Coefficients for Oxygen,* 23rd Annual Gaseous Electronics Conference, October 21–23, 1970, Hartford, Connecticut.

Jacob Neufeld
Revised Formulation of the Kinetic Plasma Theory, American Physical Society, February 1–4, 1971, New York.

Health Physics Metrology, Consultants' Meeting on the Practical Application of Quantities, Units and Measurement Methods in Radiation Dosimetry for Radiological and Protection Purposes (Sponsored by International Atomic Energy Agency), April 19–23, 1971, Geneva, Switzerland.

J. W. Poston
A Detector for the Measurement of Dose Distributions at a Bone-Tissue Interface, Symposium on New Developments in Physical and Biological Radiation Detectors, November 23–27, 1970, Vienna, Austria.

R. H. Ritchie
Plasma Effects in Solids, Gordon Conference on Particle Solid Interaction, August 10–14, 1970, Plymouth, New Hampshire.

Low-Energy Electron Inelastic Processes in Metals, Low-Energy Electron Diffraction Seminar, March 18–19, 1971, Washington, D.C.

Collective Electron Resonances in Solids, U.S.-Japan Seminar on Wave and Plasma Effects in Solids, June 8–10, 1971, Ithaca, New York.

R. H. Ritchie and V. E. Anderson
Electron Slowing-Down Cascade Spectra in Solids, IEEE Conference on Nuclear Space and Radiation Effects, July 20–23, 1971, Durham, New Hampshire.

P. S. Rohwer, R. S. Booth, S. V. Kaye, M. J. Kelly, and E. G. Struxness
Evaluation of Potential Exposure to Environmental Radioactivity, 3rd Session of U.S.–U.S.S.R. Technical Talks on Plowshare, Washington, D.C., July 12–23, 1971.

P. S. Rohwer and E. G. Struxness
Development of Radiation Safety Devices for Environmental Releases of Radioactivity, 16th Annual Meeting of the Health Physics Society, July 11–15, 1971, New York.

H. C. Schweinler and J. W. McKeever
A New Way to Get Potential Energy Curves, Molecular Spectroscopy Symposium, June 14–18, 1971, Columbus, Ohio.

W. S. Snyder
General Principles of Internal Exposure; Dosimetry of the ICRP Model for the Lung; Dosimetry of the ICRP Model for the Gastrointestinal Tract; Estimation of Absorbed Fraction of Energy from Photon Sources in Body Organs; Depth Dose in an Anthropomorphic Phantom for Neutron Beams of Energies up to 14 Mev; Calculations of Depth-Dose Curves for High-Energy Neutrons and Protons and Their Interpretation for Radiation Protection; International Summer School on Radiation Protection, September 21–30, 1970, Cavtat, Yugoslavia.

Standard Models for Metabolism and Dosimetry, 16th Annual Bioassay and Analytical Chemistry Conference, October 8–9, 1970, Bethesda, Maryland.

B. L. Sowers and E. T. Arakawa
Optical Properties of Six-Membered Ring Liquids in the Vacuum UV, American Physical Society, Southeastern Section, November 23–25, 1971, New Orleans, Louisiana.

J. A. D. Stockdale, R. N. Compton, and P. W. Reinhardt
Electron Impact Studies of Excitation, Negative Ion Formation, and Negative Ion Molecule Reactions in Boron Trichloride, Negative Ion Meeting, March 23–26, 1971, Liverpool, England.

E. G. Struxness
External and Internal Doses to Man from Natural Background Radiation and Deposited Artificial Radioactivity, Prepared for Presentation 3rd Session of U.S.–U.S.S.R. Technical Talks on Plowshare, Washington, D.C., July 1971.

Tsuneo Tamura
Radioactive Waste Disposal by Hydraulic Fracturing, American Nuclear Society Meeting, June 13–17, 1971, Boston, Massachusetts.

J. H. Thorngate and J. A. Auxier
Advances in Dosimetric Instrumentation, American Nuclear Society Annual Meeting, June 13–17, 1971, Boston, Massachusetts (presented by J. H. Thorngate).

J. E. Turner
Meaning and Assessment of Radiation Quality for Radiation Protection, Symposium on Biophysical Aspects of Radiation Quality, March 8–12, 1971, Lucas Heights, New South Wales, Australia.

J. E. Turner, H. A. Wright, and R. N. Hamm
Pion Beam Dosimetry: Comparison of Experiment and Theory and Other Studies, International Congress on Protection against Accelerator and Space Radiation, April 26–30, 1971, Geneva, Switzerland.

R. B. Vora, V. N. Neelavathi, T. S. Subramanian, M. A. Prasad, and J. E. Turner
Semi-Classical Calculation of the Effect of Magnetic Moment (Spin) on the Slowing Down of Heavy Particles, American Physical Society, Southeastern Section, November 23–25, 1970, New Orleans, Louisiana.

U. S. Whang, E. T. Arakawa, and T. A. Callcott
Optical Constants of Rubidium for Photon Energies from 3 to 9.6 eV, American Physical Society, March 29–April 1, 1971, Cleveland, Ohio.

M. W. Williams, B. L. Sowers, and E. T. Arakawa
Optical Properties of Heterocyclic Liquids in the Vacuum UV, American Physical Society, Southeastern Section, November 23–25, 1970, New Orleans, Louisiana.

H. A. Wright, R. N. Hamm, and J. E. Turner
Effect of Lateral Scattering on Absorbed Dose from 400 MeV Neutrons and Protons, International Congress on Protection against Accelerator and Space Radiation, April 26–30, 1971, Geneva, Switzerland.

Publications

H. H. Abee, W. D. Cottrell, K. E. Cowser, and D. J. Nelson
"Environmental Monitoring Significance of the Clinch River Study," pp. 388–93 in *Proceedings of a Symposium on Environmental Surveillance in the Vicinity of Nuclear Facilities,* C. C. Thomas, Springfield, Illinois, 1970.

G. A. Andrews and F. F. Haywood
"Clinical and Biological Consequences of Nuclear Explosions," to be published in *The Practitioner.*

J. C. Ashley and R. H. Ritchie
"The Mean Free Path of Relativistic Electrons for Plasmon Excitation," *Phys. Status Solidi* **40**, 623–30 (1970).

"Contribution of Surface Losses to the Stopping Power of Matter for Charged Particles," submitted for publication in *Health Physics.*

J. C. Ashley, R. H. Ritchie, and Werner Brandt
"Z_1^3 Effect in the Stopping Power of Charged Particles in Matter," submitted for publication in *The Physical Review.*

J. A. Auxier
"Multilaboratory Intercomparisons and Standardization of Nuclear Accident Dosimetry Systems," pp. 153–64 in *Nuclear Accident Dosimetry Systems,* IAEA, Vienna, 1970.

Health Physics Division–ORNL–ABCC Liaison Pool Activities, Period August 17 thru September 18, 1969, August 27, 1970.

"The Outcry over Exposure Guidelines," to be published in *Nuclear Safety.*

Book Review: "Personnel Dosimetry Systems for External Radiation Exposures," IAEA Technical Report Series No. 109, to be published in *Health Physics.*

J. A. Auxier and Barbara G. Auxier
Book Review: "The Story of Radioactivity," *Health Phys.* **21**, 129 (1971).

J. A. Auxier, K. Becker, E. M. Robinson, D. R. Johnson, R. H. Boyett, and C. H. Abner
"A New Radon Progeny Personnel Dosimeter," *Health Phys.* **21**, 126–28 (1971).

J. A. Auxier, Z. G. Burson, R. L. French, F. F. Haywood, L. G. Mooney, and E. A. Straker
Recommended Standard Free-Field Environment for Initial Radiation Shielding Calculations, ORNL-TM-3396 (in publication).

J. A. Auxier, T. D. Jones, and H. H. Hubbell, Jr.
"Review of Depth-Dose Calculation and Experimentation," pp. 73–94 in *Proceedings of the Symposium on Neutrons in Radiobiology, November 11 thru 14, 1969,* Oak Ridge, Tennessee, CONF-691106, USAEC-DTI, 1970.

H. E. Banta, F. F. Haywood, and Z. G. Burson
A Self-Replenishing Tritium Target for Neutron Generators, ORNL-TM-3397 (in publication).

C. J. Barton
Radiological Considerations in the Use of Natural Gas from Nuclearly Stimulated Wells, ORNL-CF-71-1-12.

Radon in Air, Natural Gas and Houses: A Preliminary Literature Survey and Evaluation, ORNL-CF-71-5-48.

C. J. Barton, D. G. Jacobs, and M. J. Kelly
Quarterly Progress Report on Radiological Safety of Peaceful Uses of Nuclear Explosives: Consumer Products from Nuclearly Stimulated Gas Wells, ORNL-TM-3123 (September 1970).

Quarterly Progress Report on Radiological Safety of Peaceful Uses of Nuclear Explosives: Hypothetical Population Exposures in Metropolitan Areas, ORNL-TM-3338 (March 1971).

C. J. Barton, D. G. Jacobs, M. J. Kelly, and E. G. Struxness
"Radiological Considerations in the Use of Natural Gas from Nuclearly Stimulated Wells," *Nucl. Technol.* **11**, 335–44 (July 1971).

K. Becker
"Application of the Track Etching Process in Radiation Protection," *Proceedings of International Topical Conference on Nuclear Track Registration in Insulating Solids, May 6–9, 1969,* Clermont-Ferrand, France (to be published).

"Recent Progress in Neutron Solid-State Dosimetry," pp. 30–45 in *Proceedings of the Symposium on Neutrons in Radiobiology, November 11 thru 14, 1969,* Oak Ridge, Tennessee, CONF-691106, USAEC-DTI, 1970.

"Principles and Basic Dosimetric Properties of Radiophotoluminescence in Silver-Activated Glasses," pp. 153–92 in *Solid-State Dosimetry* (S. Amelickx, ed.), Gordon and Breach, 1970.

"Principles of Thermally Stimulated Exoelectron Emission (TSEE) Dosimetry," *At. Energy Rev.* **8**(1), 173–218, IAEA, Vienna, 1970.

"Solid-State Dosimetry," *Critical Rev. Radiol. Sci.* **1**(3), 363–433 (1970).

Book Review: "Festkorperdosimetrie ionisierender Strahlung," Leipzig, 1969, *Health Phys.* **19**, 837–38 (1970).

Book Review: "The Photographic Action of Ionizing Radiation in Dosimetry and Medical, Industrial Neutron, Auto- and Microradiography," R. H. Herz, Wiley, 1969, to be published in *Review of Scientific Instruments.*

K. Becker and K. W. Crase
"A Sensitive Integrating Fast Neutron Dosimeter Based on TSEE," *Nucl. Instrum. Methods* **82**, 297–98 (1970).

K. Becker and R. B. Gammage
"Exoelectron Emission and Surface Characteristics of Lunar Materials," *Proceedings of the Second Lunar Science Conference, January 11 to 14, 1971,* Houston, Texas (to be published).

K. Becker, M. Oberhofer, and J. S. Cheka
"Thermally Stimulated Exoelectron Emission, Thermoluminescence, and Impurities in LiF and BeO," *Health Phys.* **19**, 391–403 (1970).

R. D. Birkhoff
"Electron Flux Spectra and Radiation Yields in Solids Irradiated by Beta Rays," pp. 1–15 in *Penetration of Charged Particles in Matter: A Symposium,* National Academy of Sciences, Washington, D.C., 1970.

J. O. Blomeke and W. C. McClain
"A Salt Mine Repository for Radioactive Wastes," *Nucl. News,* 35–38 (April 1971).

W. J. Boegly, Jr., and W. L. Griffith
Feasibility of Retrieving Utility System Capital and Maintenance Costs from Annual Reports, ORNL-HUD-16 (June 1970).

The Potential Use of Utility Tunnels in Urban Areas, the American Society of Mechanical Engineers, United Engineering Center, 345 East 47th Street, New York, 1970.

W. J. Boegly, Jr., W. L. Griffith, and W. C. Ulrich
System Requirements for Underground Utility Installation, ORNL-HUD-19 (February 1971).

W. P. Bonner and Tsuneo Tamura
"Determination of the Forms and Distribution of Phosphorus in Soils and Calcareous Sediments Using Zonal Centrifugation," to be published in *Environmental Science and Technology* (1971).

W. P. Bonner, Tsuneo Tamura, C. W. Francis, and J. W. Amburgey, Jr.
"Zonal Centrifugation – a Tool for Environmental Studies," *Environ. Sci. Technol.* 4, 821–25 (October 1970).

R. S. Booth, S. V. Kaye, and P. S. Rohwer
"A Systems Analysis Methodology for Predicting Dose to Man from a Radioactively Contaminated Terrestrial Environment," *Proceedings of the Third National Symposium on Radioecology, May 10–12, 1971,* Oak Ridge, Tennessee.

R. H. Boyett and K. Becker
"LET Effects on the Chemical Resistance of Irradiated Polymers," *J. Appl. Polym. Sci.* **14**, 1654–56 (1970).

R. L. Bradshaw and T. F. Lomenick
"Rheology of Salt in Mine Workings," pp. 109–23 in *Proceedings of the Symposium on the Geology and Technology of Gulf Coast Salt, May 1–2, 1967,* Louisiana State University, Baton Rouge, Louisiana (September 1970).

R. L. Bradshaw and W. C. McClain
"Roof Bolt Test and Application in Supporting a Two-Foot-Thick Roof Bed," pp. 466–70 in *Third Symposium on Salt,* vol. II, April 21–25, 1969, Cleveland, Ohio, The Northern Ohio Geological Society, Inc., Cleveland, Ohio.

Project Salt Vault: A Demonstration of the Disposal of High-Activity Solidified Wastes in Underground Salt Mines, ORNL-4555 (April 1971).

A. J. Braundmeier, Jr., and E. T. Arakawa
"Observed Radiation from 'Nonradiative' Surface Plasmons in Aluminum," *Z. Physik* **239**, 337–42 (1970).

"Plasma Radiation from Electron Bombarded Be Films," *Optics Commun.* **2**, 257–58 (1970).

A. J. Braundmeier, Jr., E. T. Arakawa, and M. R. Williams
"Intrinsic Damping Rate and Volume Plasmon Energy in Mg from Radiative Decay Measurements," *Phys. Lett.* **32A**, 241–42 (1970).

D. G. Brown and F. F. Haywood
"14-MeV Neutron Irradiation of Swine," to be published in *Health Physics.*

D. G. Brown, D. F. Johnson, and J. A. Auxier
"Unilateral and Bilateral Exposure of Swine to Fission Neutrons," to be published in *Health Physics.*

Z. G. Burson
Radiation Output Description from the $T(d,n)^4He$ Reaction in a Large Target (1000 cm^2) – Operation HENRE, CEX-65.04 (March 1971).

H. M. Butler and F. F. Haywood
Radiation Safety Practices – Operation HENRE, CEX-65.05 (January 1971).

J. S. Cheka
Report of Trip to Japan August 22, 1970–October 4, 1970, CF-70-11-35 (November 16, 1970).

J. S. Cheka, E. M. Robinson, L. Wade, Jr., and W. A. Gramly
"The UT-AEC Agricultural Research Laboratory Variable Gamma Dose Rate Facility," *Health Phys.* **20**, 339–43 (1971).

W. L. Chen, W. H. Shinpaugh, H. H. Hubbell, Jr., and J. W. Poston
Dose Distributions from Neutrons Incident on a Tissue-Equivalent Phantom, ORNL-TM-3425 (June 1971).

A. A. Christodoulides and L. G. Christophorou
"Electron Attachment to Aliphatic Hydrocarbons of the Form n-$C_NH_{2N+1}Br$ (N = 1 to 6, 8, and 10). Part I: An Electron Swarm Study," *J. Chem. Phys.* (in press).

L. G. Christophorou
"Cross Section Functions for Slow Electron–Molecule (Atom) Collision Processes," pp. 95–120 in *Progress and Problems in Contemporary Radiation Chemistry,* vol. 1 (Proceedings of Tenth Czechoslovak Meeting on Radiation Chemistry, Marianske Lazne, Czechoslovakia, June 22–25, 1970), Prague, March 1971.

"Recent Studies on Electron Attachment," to be published in *Proceedings Third Tihany Conference on Radiation Chemistry.*

L. G. Christophorou, J. G. Carter, E. L. Chaney, and P. M. Collins
"Long-Lived Parent Negative Ions Formed by Capture of Low-Energy Electrons (0 to 3 eV) in the Field of the Ground and Excited Electronic States of Organic Molecules," to be published in *Proceedings IVth International Congress of Radiation Research,* Gordon and Breach, Paris.

L. G. Christophorou, J. G. Carter, P. M. Collins, and A. A. Christodoulides
"Electron Attachment to Aliphatic Hydrocarbons of the Form n-$C_NH_{2N+1}Br$ (N = 1 to 6 and 8). Part II: A Swarm Beam Study," *J. Chem. Phys.* (in press).

L. G. Christophorou, D. L. McCorkle, and V. E. Anderson
"Swarm-Determined Electron Attachment Cross Sections as a Function of Electron Energy," submitted for publication in the *Journal of Physics B.*

L. G. Christophorou, D. L. McCorkle, and J. G. Carter
"Cross Sections for Electron Attachment Resonances Peaking at Subthermal Energies," *J. Chem. Phys.* **54**, 253–60 (1971).

L. G. Christophorou and D. Pittman
"Thermal Electron Scattering by Polar Molecules," *J. Phys. B* **3**, 1252–59 (1970).

R. N. Compton and R. H. Huebner
"Collisions of Low-Energy Electrons with Molecules: Threshold Excitation and Negative Ion Formation," pp. 281–381 in *Advances in Radiation Chemistry,* vol. 2 (ed. by J. L. Magee and M. Burton), Wiley, New York, 1970.

R. N. Compton, D. R. Nelson, and P. W. Reinhardt
"Negative Ion Mass Analysis of Swarm Experiments: Sulphur Hexafluoride," *Int. J. Mass Spectrom. Ion Phys.* **6**, 117–23 (1971).

J. J. Cowan and E. T. Arakawa
"Dispersion of Surface Plasmons in Multiple Metal and Dielectric Layers on Concave Diffraction Gratings," *Phys. Status Solidi* **1**, 695–705 (1970).

J. J. Cowan, E. T. Arakawa, and R. H. Ritchie
"Dispersion of Surface Plasmons in Dielectric-Metal Coatings on Concave Diffraction Gratings," *Z. Physik* **235**, 97–109 (1970).

F. J. Davis and D. R. Nelson
"Attachment Rate of Thermal Electrons to SF_6," *Chem. Phys. Lett.* **6**, 277–78 (1970).

Wallace de Laguna
"Radioactive Waste Disposal by Hydraulic Fracturing," *Health Phys.* **11**(5), 391–400 (1970).

"Radioactive Waste Disposal by Hydraulic Fracturing," *Ind. Water Eng.* 7(10), 32–37 (October 1970).

H. Dickson, E. Roberts, Jr., H. M. Butler, R. J. Cloutier, G. Smithwick, E. E. Watson, F. F. Haywood, and J. D. Berger
"Radiation Safety in the Operation of a Low-Energy Accelerator," pp. 441–58 in *Proceedings of the Second Oak Ridge Conference on the Use of Small Accelerators for Teaching and Research, March 23 thru 25, 1970,* CONF-700322, USAEC-DTI, 1970.

C. E. Easterly, L. G. Christophorou, R. P. Blaunstein, and J. G. Carter
"Fluorescence from the Second Excited π-Singlet State of 1,2-Benzanthracene and 3,4-Benzopyrene in Solution," *Chem. Phys. Lett.* **6**, 579–82 (1970).

J. M. Elson and R. H. Ritchie
"Photon–Surface Plasmon Coupling at a Dielectric Solid," *Phys. Lett.* **33A**, 255 (1970).

"Photon Interactions at a Rough Metal Surface," submitted for publication in *The Physical Review.*

L. C. Emerson
"Induced Radioactivity" (book review), *Health Phys.* **19**, 701 (1970).

F. M. Empson, R. L. Bradshaw, W. C. McClain, and B. L. Houser
"Results of the Operation of Project Salt Vault: A Demonstration of Disposal of High-Level Radioactive Solids in Salt," pp. 455–62 in *Third Symposium on Salt,* vol. I, April 21–25, 1969, Cleveland, Ohio, The Northern Ohio Geological Society, Inc., Cleveland, Ohio.

Kenneth Fox
"Simple Approximate Eigenfunctions for an Electron in a Finite Dipole Field," *Phys. Rev. A* **3**, 13–15 (1971).

C. W. Francis
Plutonium Mobility in Soil and Uptake in Plants: A Review, ORNL-CF-71-5-62 (June 1971).

C. W. Francis, W. P. Bonner, and Tsuneo Tamura
"An Evaluation of Zonal Centrifugation as a Research Tool in Soil Science, Part 1: Methodology," to be published in *Proceedings of Soil Science Society of America.*

C. W. Francis, Gordon Chesters, and Larry A. Haskin
"Determination of Lead-210 Mean Residence Time in the Atmosphere," *Environ. Sci. Technol.* **4**, 586–89 (July 1970).

C. W. Francis and D. F. Grigal
"A Rapid and Simple Procedure Using ^{85}Sr for Determining Cation Exchange Capacities of Soils and Clays," to be published in July 1971 issue of *Soil Science.*

C. W. Francis and Tsuneo Tamura
"An Evaluation of Zonal Centrifugation as a Research Tool in Soil Science, Part 2: Characterization of Soil Clays," to be published in *Proceedings of Soil Science Society of America.*

R. B. Gammage and K. Becker
"Search for Exoelectrons in Apollo 12 Materials," to be published in *Earth and Interplanetary Science Letters.*

Research on Stimulated Exoelectron Emission from Lunar Materials, ORNL-TM-3131 (October 1970).

F. W. Garber, M. Y. Nakai, J. A. Harter, and R. D. Birkhoff
"Low-Energy Electron Beam Studies in Thin Aluminum Foils," *J. Appl. Phys.* **42**, 1149–58 (1971).

W. R. Garrett
"Comment on the Critical Dipole Moments for Electron Binding to a Freely Rotating Electric Dipole," *Mol. Phys.* **20**, 751–52 (1971).

"Critical Binding of an Electron to a Rotationally Excited Dipolar System," *Phys. Rev. A* **3**, 961–72 (1971).

"Variational Method for Elastic Scattering Involving Long Range Forces," *J. Phys. B* **4**, 643–51 (1971).

T. F. Gesell and E. T. Arakawa
"Attenuation Length for Photoelectrons in Aluminum Excited by 21.2 eV Photons," *Phys. Rev. Lett.* **26**, 377–80 (1971).

A. H. Haber, L. L. Triplett, F. F. Haywood, and D. R. Ward
"RBE of Fast Neutrons in Growth Inhibition: Evidence for a Component Requiring Cell Division," *Radiat. Res.* **44**(2) (1970).

W. F. Hanson, E. T. Arakawa, and M. W. Williams
"Optical Properties of MgO and MgF_2 in the Extreme Ultraviolet Region," submitted to the *Journal of Applied Physics.*

F. F. Haywood
1970 Intercomparison of Nuclear Accident Dosimetry Systems at the Oak Ridge National Laboratory, unpublished data, 1970.

Report of Trip to England, France, and Italy during the Period June 8 thru July 2, 1970, CF-70-9-45 (September 28, 1970).

"High Yield, Long-Lived Tritium Targets," *Proceedings of the 1971 Particle Accelerator Conference, March 1–3, 1971* (to be published).

Book Review: "Nuclear Accident Dosimetry Systems," IAEA, Vienna, 1970, STI/PUB/241, to be published in *Health Physics.*

F. F. Haywood and J. A. Auxier
"Unusual and Unexpected Radiation Sources," *Safety Newsletter,* National Safety Council, Chicago, Illinois (March 1971).

H. H. Hubbell, Jr.
Book Review: "Colloque International sur la Dosimetrie des Irradiations Dues a des Sources Externes," le Service Central de Protection contre les Rayonnements Ionisants, 1967, *Health Phys.* **19**, 838–39 (1970).

Book Review: "Radiation Dosimetry: X Rays Generated at Potentials of 5 to 150 kV, ICRU Report 17," to be published in *Health Physics.*

G. S. Hurst, T. E. Bortner, and T. D. Strickler
"Proton Excitation of the Argon Atom," *Phys. Rev.* **178**, 4–10 (1969).

G. S. Hurst and J. E. Parks
"An Electrical Sensor of Plane Coordinates," *Rev. Sci. Instrum.* **41**, 1846 (1970).

G. S. Hurst, T. D. Stewart, and J. E. Parks
"Vacuum Ultraviolet Radiation and Jesse Effects in the Noble Gases," *Phys. Rev.* **A2**, 1717 (1970).

G. S. Hurst, N. Thonnard, and K. Schneider
"A Recording Exposure Control for X-Ray Machines," *Health Phys.* **21**, 91–95 (1971).

G. S. Hurst and J. E. Turner
Elementary Radiation Physics, Wiley, New York, 1970.

S. Jablon, S. Fujita, K. Fukushima, T. Ishimaru, and J. A. Auxier
"RBE of Neutrons in Japanese Survivors," pp. 547–79 in *Proceedings of the Symposium on Neutrons in Radiobiology, November 11 thru 14, 1969,* Oak Ridge, Tennessee, CONF-691106, USAEC-DTI, 1970.

D. G. Jacobs
"Tritium," pp. 423–25 in *McGraw-Hill Yearbook of Science and Technology,* McGraw-Hill, New York, 1971.

(Book Review), "Proceedings of the Symposium on Public Health Aspects of Nuclear Explosives Sponsored by the Southwestern Radiological Health Laboratory, Bureau of Radiological Health, Las Vegas, Nevada, April 7–11, 1969," *Health Phys.* **20**, 671 (1971).

D. G. Jacobs et al.
"Public Health," pp. 71–86 in *Nuclear Power in the South,* Sect. V (A Report of the Southern Governors' Task Force for Nuclear Power Policy) (September 22, 1970).

D. G. Jacobs and E. G. Struxness
"A Preliminary Assessment of the Radiological Implications of Commercial Utilization of Natural Gas from a Nuclearly Stimulated Well," *Symposium on Engineering with Nuclear Explosives, January 14–16, 1970, Las Vegas, Nevada, Proceedings,* CONF-700101, vol. 1, pp. 831–49.

D. R. Johnson and K. Becker
Mechanisms and Applications of Nuclear Track Registration in Polymers, ORNL-TM-2826 (June 1970).

D. R. Johnson, R. H. Boyett, and K. Becker
"Some Studies on the Chemical Damage Mechanism along Charged Particle Tracks in Polymers," *Proceedings of International Topical Conference on Nuclear Track Registration in Insulating Solids, May 6–9, 1969,* Clermont-Ferrand, France (to be published).

Larry D. Johnson
"Molecular Orbitals and Oscillator Strengths for Magnesium Porphin," submitted for publication in the *Journal of Chemical Physics.*

T. D. Jones
"Dose and LET in a Rabbit and a Rat," to be published in *Health Physics.*

T. D. Jones and J. A. Auxier
"Neutron Dose, Dose Equivalent, and Linear Energy Transfer from ^{252}Cf Sources," *Health Phys.* **20**, 253–58 (1971).

"Absorbed Dose and Linear Energy Transfer Distributions from Therapeutic Sources of ^{252}Cf," to be published in *Physics in Medicine & Biology.*

T. D. Jones, W. S. Snyder, and J. A. Auxier
"Absorbed Dose, Dose Equivalent, and LET Distributions in Cylindrical Phantoms Irradiated by a Collimated Beam of Monoenergetic Neutrons," to be published in *Health Physics.*

S. V. Kaye and P. S. Rohwer
Dose Estimation Studies Related to Proposed Construction of an Atlantic-Pacific Interoceanic Canal with Nuclear Explosives: Phase III, ORNL-4579 (December 1970).

G. D. Kerr, J. T. Cox, L. R. Painter, and R. D. Birkhoff
"A Reflectometer for Studying Liquids in the Vacuum Ultraviolet," submitted to *Review of Scientific Instruments.*

G. D. Kerr, M. W. Williams, R. D. Birkhoff, and L. R. Painter
"Optical Properties of Some Silicone Diffusion Pump Oils in the Vacuum Ultraviolet, Using an Open Dish Technique," to be published in the *Journal of Applied Physics.*

C. E. Klots
"Bimolecular Association Reactions and Microscopic Reversibility," *J. Chem. Phys.* **53**, 1616–17 (1970).

"Comparison of Direct and Photosensitized Ionization Efficiencies," to be published in *Proceedings IVth International Congress of Radiation Research,* Gordon and Breach, Paris.

"Energy Partition in Irradiated Mixtures," pp. 120–25 in *Progress and Problems in Contemporary Radiation Chemistry,* vol. 1 (Proceedings of Tenth Czechoslovak Meeting on Radiation Chemistry, Marianske Lazne, Czechoslovakia, June 22–25, 1970), Prague, March 1971.

"Reformulation of the Quasi-Equilibrium Theory of Ionic Fragmentation," *J. Phys. Chem.* **75**, 1526 (1971).

"Reformulation of the Quasi-Equilibrium Theory of Ionic Fragmentation," to be published in *Proceedings 19th Annual Conference on Mass Spectrometry and Allied Topics.*

"Ionic Fragmentation through Centrifugal Barriers," submitted for publication in *Chemical Physics Letters.*

C. E. Klots and P. W. Reinhardt
"Energy-Loss Rates of Slow Electrons in Hydrocarbons," *J. Phys. Chem.* **74**, 2848–50 (1970).

C. E. Klots and Harvel Wright
"Aspects of Degradation Spectra," *Int. J. Radiat. Phys. Chem.* **2**, 191 (1971).

W. C. McClain
On Earthquakes Induced by Underground Fluid Injection, ORNL-TM-3154 (October 1970).

"The Mechanics of Hydraulic Fractures in Shales," pp. 410–20 in *Third Symposium on Salt,* vol. II, April 21–25, 1969, Cleveland, Ohio, The Northern Ohio Geological Society, Inc., Cleveland, Ohio.

W. C. McClain and R. L. Bradshaw
"Deformation and Stress Transference in a Salt Mine Resulting from the Application of Heat," *Second International Congress of International Society for Rock Mechanics, Belgrade, September 21–26, 1970,* pp. 1–7.

"Status of Investigations of Salt Formations for Disposal of Highly Radioactive Power-Reactor Wastes," *Nucl. Safety* **11**(2), 130–41 (1970).

W. C. McClain and O. H. Myers
Indexed Bibliography of Literature on Seismic Considerations in the Siting of Nuclear Facilities-1, ORNL-NSIC-88 (June 1971).

K. Z. Morgan

"Excessive Medical Diagnostic Exposure," *Proceedings of the Third Annual National Conference on Radiation Control, May 3, 1971,* Scottsdale, Arizona (to be published).

"President's Report to the General Assembly of IRPA," *Health Phys.* **20**(5) (1971).

"Radiation Exposure to the General Population" (retitled "Never Do Harm"), *Environment* **13**(1), 28–38 (1971).

"History of Radiation Protection," *Mat. Eval.* **29**(3), 19A (1971).

"Adequacy of Present Standards of Radiation Exposure," *Environ. Affairs* **1**(1), 91 (1971).

"Welcoming Address," *Proceedings of the International Summer School on Radiation Protection, September 20–30, 1970,* Cavtat, Yugoslavia, *Radiat. Dosimetry* **1**, 4 (1971).

"Maximum Permissible Levels of Exposure to Ionizing Radiation," *Proceedings of the International Summer School on Radiation Protection, September 20–30, 1970,* Cavtat, Yugoslavia, *Radiat. Dosimetry* **1**, 7, Boris Kidrič Institute of Nuclear Sciences, Beograd, 1971.

"Criteria for the Control of Radioactive Effluents," *Proceedings of the IAEA Symposium on Environmental Aspects of Nuclear Power Stations, August 11, 1970,* UN Building, New York.

"Criteria for the Control of Radioactive Effluents," to be published in *International Journal of Environmental Studies,* 1971.

"Why the 1968 Act for Radiation Control for Health and Safety Is Required," to be published in *Radiology,* 1971.

"History of the Health Physics Society," to be published as part of *The RSNA Symposium on the Critical History of American Radiology, November 1970.*

"History of the International Radiation Protection Association," to be published as part of *The RSNA Symposium on the Critical History of American Radiology, November 1970.*

K. Z. Morgan and J. E. Turner

"Health Physics," to be published in *American Institute of Physics Handbook,* McGraw-Hill, New York.

O. H. Myers

The ORNL Seismograph Station ORT: Operation from March 1, 1969, through August 31, 1969, ORNL-CF-70-8-42.

W. T. Naff, C. D. Cooper, and R. N. Compton

"Attachment of Electrons to Substituted Benzenes," *J. Chem. Phys.* **54**, 212–22 (1971).

S. J. Nalley and R. N. Compton

"Collisional Ionization of Cesium by Oxygen: The Electron Affinity of O_2," *J. Chem. Phys.* (in press).

Jacob Neufeld

"Dosimetric Field Quantities in Health Physics," to be published in *Health Physics.*

"Metrology in Health Physics and the ICRU," to be published in *Health Physics.*

"Radiation Quantities and Their Significance in Health Physics," *Health Phys.* **19**, 253–79 (1970).

"Reply to a Letter of H. J. Dunster on 'Quality Factor – a Sound Concept,' " *Health Phys.* **20**, 530–31 (1971).

"What Is Energy Imparted?" to be published in *Health Physics.*

J. E. Parks, G. S. Hurst, and H. F. Holzer

"A Binary Current Integrator Logic," *Rev. Sci. Instrum.* **40**, 496 (1969).

J. E. Parks, G. S. Hurst, T. E. Stewart, and H. L. Weidner

"Ionization of Noble Gases by Protons," to be published in *Physical Review.*

J. W. Poston

Report of Trip to the Netherlands, Austria, and Italy during Period November 7, 1970–December 2, 1970, ORNL-CF-71-1-3.

Neutron Depth Dose Distributions in Heterogeneous Phantoms, ORNL-TM-3329 (April 1971).

Book Review: "Fast Burst Reactors," *AEC Symposium Series 15,* Clearinghouse for Federal Scientific and Technical Information, Springfield, Virginia 22151, 646 pp., 1969, *Health Phys.* **19**, 588 (1970).

"A Detector for the Measurement of Dose Distributions at a Bone-Tissue Interface," *Proceedings of the Symposium on New Developments in Physical and Biological Radiation Detectors, November 23–27, 1970.*

Book Review: "Protection against Neutron Radiation, NCRP Report No. 38," January 4, 1971, to be published in *Nuclear Safety.*

E. M. Robinson and M. Oberhofer

"A Sensitive Ceramic BeO-TSEE Dosimeter," *Health Phys.* **18**, 434–37 (1970).

P. S. Rohwer, K. E. Cowser, W. S. Snyder, and E. G. Struxness

"An Approach for Assessing Potential Population Exposures," pp. 217–25 in *Proceedings of a Symposium on Environmental Surveillance in the Vicinity of Nuclear Facilities,* C. C. Thomas, Springfield, Illinois, 1970.

K. J. Schneider, R. L. Bradshaw, A. G. Blasewitz, J. O. Blomeke, and W. C. McClain

"Status of Solidification and Disposal of Highly Radioactive Liquid Wastes from Nuclear Power in the USA," *Proceedings of IAEA Symposium on Environmental Aspects of Nuclear Power Stations, August 10–14, 1970, New York,* STI/PUB/261, IAEA, 1971.

H. C. Schweinler and E. P. Wigner

"Orthogonalization Methods," *J. Math. Phys.* **11**, 1693–94 (1970).

S. Y. Shieh and R. H. Ritchie

"Simultaneous Generation of Transition Radiation and Bremsstrahlung from a Thin Foil. I," *Phys. Rev. B* **2**, 1646–51 (1970).

W. S. Snyder

"General Principles of Internal Exposure," p. 87 in *Radiation Dosimetry,* ed. by I. Mirić, Boris Kidrič Institute of Nuclear Sciences, Beograd, 1971, vol. 1.

"Estimation of Absorbed Fraction of Energy from Photon Sources in Body Organs," ibid., p. 108.

"Dosimetry of the ICRP Model for the Gastrointestinal Tract," ibid., p. 136.

"Dosimetry of the ICRP Model for the Lung," ibid., p. 147.

"Depth Dose in an Anthropomorphic Phantom for Neutron Beams of Energies up to 14 MeV," ibid., p. 160.

W. S. Snyder, M. R. Ford, and G. G. Warner

"Estimation of Dose to Gonads from Gamma Emitters Present in the Body," *Radioprotection* **5**(4), 271 (1970).

W. S. Snyder, H. A. Wright, J. E. Turner, and J. Neufeld

"Calculation of Depth Dose from Neutrons and Protons of High Energy and Their Interpretation for Radiation Protection," p. 185 in *Radiation Dosimetry,* ed. by I. Mirić, Boris Kidrič Institute of Nuclear Sciences, Beograd, 1971, vol. 1.

B. L. Sowers, E. T. Arakawa, and R. D. Birkhoff

"Optical Properties of Six-Member Carbon Ring Organic Liquids in the Vacuum Ultraviolet," *J. Chem. Phys.* **54**, 2319–24 (1971).

B. L. Sowers, M. W. Williams, R. N. Hamm, and E. T. Arakawa

"Optical Properties of Some Silicon Diffusion Pump Oils in the Vacuum Ultraviolet, Using a Closed Cell Technique," submitted for publication in the *Journal of Chemical Physics.*

"Optical Properties of CCl_4, C_6H_{14}, and C_6H_{12} in the Vacuum Ultraviolet," submitted for publication in the *Journal of Chemical Physics.*

T. E. Stewart, G. S. Hurst, T. E. Bortner, J. E. Parks, F. W. Martin, and H. L. Weidner
"Proton Excitation of Continuous Emission in the Noble Gases," *J. Opt. Soc. Amer.* **60**, 1290 (1970).

T. E. Stewart, G. S. Hurst, J. E. Parks, and D. M. Bartell
"Vacuum Ultraviolet Emission from Proton Excited Helium Gas," to be published in *Physical Review.*

J. A. D. Stockdale, R. N. Compton, and P. W. Reinhardt
"Reactions of O^- with Some Hydrocarbons in the Energy Region between 0 and 2 eV," *Int. J. Mass Spectrom. Ion Phys.* **4**, 401–14 (1970).

J. A. D. Stockdale, R. N. Compton, and H. C. Schweinler
"Negative Ion Formation in Selected Hexafluoride Molecules," *J. Chem. Phys.* **53**, 1502–7 (1970).

Jacob Tadmor and K. E. Cowser
Deposition of Krypton-85 and Tritium Released from a Nuclear Fuel Reprocessing Plant, ORNL-CF-71-7-34.

T. Tamura, W. J. Young, and M. M. Yarosh
Data Obtained on Several Possible Locales for the Agro-Industrial Complex, ORNL-4293 (February 1971).

N. Thonnard and G. S. Hurst
"A Sequential Neutron and Gamma Ray Monitor," *Health Phys.* **19**, 671 (1970).

J. H. Thorngate
Book Review: "Neutron Capture Gamma Ray Spectroscopy," *Proceedings of the International Symposium on Neutron Capture Gamma Ray Spectroscopy, August 11 thru 15, 1969, Studsvik,* organized by Chalmers University of Technology and the University of Gothenburg, IAEA, Vienna, 1969, to be published in *Health Physics.*

J. E. Turner
"Calculations of the Penetration of Charged Particles through Matter at Very High Energies," pp. 48–58 in *Penetration of Charged Particles in Matter: A Symposium,* National Academy of Sciences, Washington, D.C., 1970.

"Current Topics in Radiation Research" (book review), *Health Phys.* (in press).

"Meaning and Assessment of Radiation Quality for Radiation Protection," to be published in *Proceedings of Symposium on Biophysical Aspects of Radiation Quality.*

J. E. Turner and V. E. Anderson
"Relativistic Ground-State Energy Eigenvalues of the Electron-Dipole System," *Il Nuovo Cimento* **1B**, 149–54 (1971).

J. E. Turner, R. D. Birkhoff, V. E. Anderson, E. B. Wagner, and H. A. Wright
"Monte Carlo Method of Determining LET Spectra from Pulse-Height Measurements," p. 373 in *Microdosimetry* (ed. by H. G. Ebert), Commission of the European Communities, Brussels, Belgium, 1970.

J. E. Turner and H. A. Wright
"Calculation of Dose from High Energy Nucleons," pp. 146–58 in *Accelerator Dosimetry and Experience,* CONF-691101, U.S. Atomic Energy Commission, Washington, D.C., 1970.

Judith A. Varga and D. G. Jacobs
Dissolution of Calcium-Strontium Carbonate and Its Subsequent Movement in the Ground, ORNL-TM-3130 (November 1970).

R. B. Vora, V. N. Neelavathi, J. E. Turner, T. S. Subramanian, and M. A. Prasad
"Semiclassical Estimation of Neutron Stopping Power," *Phys. Rev. B* **3**, 2929–33 (1971).

B. V. Waddell and G. S. Hurst
"Collisional Destruction of the 6^3P_1 State of Mercury," *J. Chem. Phys.* **53**, 3892 (1970).

U. S. Whang, E. T. Arakawa, and T. A. Callcott
"Collective Effects in the Optical Properties of Cs above the Plasma Frequency," *Phys. Rev. Lett.* **25**, 646–49 (1970).

"Optical Properties of Cs for Photons of Energy 3.6 to 9.6 eV," *J. Opt. Soc. Amer.* (in press).

D. G. Willhoit and T. D. Jones
"Dose and LET Distributions in Small Animal-Sized Cylinders for a Fission Neutron Spectrum," *Radiat. Res.* **44**, 263–72 (1970).

J. F. Wilson
The Effects of Radiation Energy, Dose Level, and the Atomic Number of the Immediate Environment on the Thermally Stimulated Exoelectron Emission from Beryllium Oxide and Lithium Fluoride, ORNL-TM-3325 (May 1971).

H. A. Wright and J. E. Turner
"Free-Nucleon Target Model Applied to Penetration and Dose Calculations for 200 and 400 MeV Protons and Neutrons," *Health Phys.* **18**, 711–20 (1970).

Harvel Wright and W. S. Snyder
"On the Differentiability of Arbitrary Real-Valued Set Functions. II," *Trans. Amer. Math. Soc.* (in press).

Lectures

C. J. Barton
Radiological Considerations in the Use of Natural Gas from Nuclearly Stimulated Wells, Environmental Aspects of Radiation Sciences, Topical Institute for College and University Faculty, Oak Ridge Associated Universities, January 14, 1971, Oak Ridge, Tennessee.

W. P. Bonner
Properties of Clays and Their Uses in Environmental and Industrial Processes, University of Tennessee, Geology Department, April 20, 1971, Knoxville, Tennessee.

J. S. Cheka
Glass Dosimetry, ORAU-ORNL Ten-Week Course in Health Physics, March 9, 1971, Oak Ridge, Tennessee.

L. G. Christophorou
Resonance Electron Attachment Processes in Gases, Department of Physics, University of Tennessee, January 26, 1971, Knoxville, Tennessee.

Recent Studies on Electron Attachment, Central Research Institute for Physics, May 17, 1971, Budapest, Hungary.

K. E. Cowser
Research in the Radioactive Waste Disposal Section, Health Physics Division, The Environment and ORNL Seminar Series, Oak Ridge National Laboratory, January 12, 1971, Oak Ridge, Tennessee.

Health Physics and Geohydrological Considerations in Waste Management, Staff Members of ORNL-NSF Environmental Program, Oak Ridge National Laboratory, April 7, 1971, Oak Ridge, Tennessee.

Résumé of Research in Radioactive Waste Disposal, University of Arkansas Students, Oak Ridge National Laboratory, April 8, 1971, Oak Ridge, Tennessee.

Radioactive Waste Disposal Research, Students from the University of North Carolina, School of Public Health, Oak Ridge National Laboratory, July 21, 1971, Oak Ridge, Tennessee.

Wallace de Laguna
ORNL Waste Disposal, ORAU-ORNL Ten-Week Health Physics Course, Oak Ridge National Laboratory, March 30, 1971, Oak Ridge, Tennessee.

ORNL Waste Disposal, University of Arkansas Students, Oak Ridge National Laboratory, April 8, 1971, Oak Ridge, Tennessee.

F. M. Empson
Waste Disposal in Geologic Formations, University of Arkansas Students, Oak Ridge National Laboratory, April 8, 1971, Oak Ridge, Tennessee.

Radioactive Waste Disposal in Salt, Students from the University of North Carolina, School of Public Health, Oak Ridge National Laboratory, July 21, 1971, Oak Ridge, Tennessee.

B. R. Fish

Present State of the Atmosphere, Oak Ridge Associated Universities, August 10, 1970, and March 29, 1971, Oak Ridge, Tennessee.

Effects of Air Pollution on Man and His Ecosystem, Oak Ridge Associated Universities, August 14, 1970, Oak Ridge, Tennessee.

Air Pollution, West Hills Garden Club, August 20, 1970, Knoxville, Tennessee; Society for Nondestructive Testing, October 13, 1970, Oak Ridge, Tennessee; Webb School, March 8, 1971, Knoxville, Tennessee; Mary Starr TV Show, October 26, 1970, Knoxville, Tennessee.

Air Pollution Aerosol Technology, Department of Environmental Engineering, University of Texas, September 11–25 and November 2–18, 1970, Austin, Texas (36 lectures during two 3-week periods).

Emergency Guidelines – Exposure Limits for Personnel – Contamination Guides, Seventh AEC-Sponsored Seminar on Medical Planning and Care in Radiation Accidents, September 29, 1970, Oak Ridge, Tennessee.

Environmental Pollution Problems, Panel discussion at UT Space Institute, November 21, 1970, Tullahoma, Tennessee.

Proposed Air Pollution Legislation in Tennessee, League of Women Voters, December 1, 1970, Oak Ridge, Tennessee.

How Clean Is the Air We Breathe and What Do We Do About It, American Society of Civil Engineers, December 9, 1970, Knoxville, Tennessee.

Program for Citizen Action, Workshop on Air Quality Control for Memphis–Shelby County Federal Air Quality Control Region, January 23, 1971, Jackson, Tennessee.

The Lung Model, ORAU Ten-Week Training Course in Health Physics, March 18, 1971, Oak Ridge, Tennessee.

The Role of the Air Pollution Control Board in Tennessee's Program, League of Women Voters Air Quality Project for Tennessee Kickoff Workshop, March 30, 1971, Nashville, Tennessee.

Instrumentation in the Measurement of Pollution, Short Course at UT Space Institute, May 20, 1971, Tullahoma, Tennessee.

C. W. Francis

Use of Zonal Centrifugation in Environmental Research, Department of Soils, University of Wisconsin, December 11, 1970, Madison, Wisconsin.

F. F. Haywood

A Program of Intercomparison and Standardization of Nuclear Accident Dosimetry Systems, June 30, 1970, Servizio Protezione, Euratom C.C.R., Ispra, Italy.

Nuclear Accident Dosimetry, ORAU-ORNL Ten-Week Course in Health Physics, March 11, 1971, Oak Ridge, Tennessee.

D. G. Jacobs

Waste Disposal and Releases of Radionuclides from Nuclear Facilities, ORAU Summer Training Program for Teacher-Demonstrators, Old Jefferson Junior High School, August 3, 1970, Oak Ridge, Tennessee.

Containment and Disposal of Radioactive Material, Great Lakes Colleges Association, ORAU Seminar Program, Oak Ridge National Laboratory, October 14, 1970, Oak Ridge, Tennessee.

T. F. Lomenick

Waste Disposal, Environmental Aspects of Radiation Sciences, Topical Institute for College and University Faculty, Oak Ridge Associated Universities, January 14, 1971, Oak Ridge, Tennessee.

Advanced Waste Disposal, ORAU-ORNL Ten-Week Health Physics Course, Oak Ridge National Laboratory, March 30, 1971, Oak Ridge, Tennessee.

Waste Disposal Concepts, ORAU Health Physics Certification Course, Oak Ridge Associated Universities, June 22, 1971, Oak Ridge, Tennessee.

K. Z. Morgan

Patient Exposure to Radiation Hazards and Responsibility for Control of Exposure, Loyola University School of Medicine, "Ground Rounds," March 23, 1971, Maywood, Illinois.

Energy Pollution of the Environment, Regional Junior Science and Humanities Symposium, March 25, 1971, Fort Knox, Kentucky.

Health Physics Tolerance Levels, Connecticut Chapters of the American Nuclear and Health Physics Societies, March 30, 1971, Hartford, Connecticut.

Commencement Address, Oak Ridge Associated Universities Ten-Week Health Physics Course, April 8, 1971, Oak Ridge, Tennessee.

Comments on Radiation Hazards and Risks, American Physical Society, April 29, 1971, Washington, D.C.

Excessive Medical Diagnostic Exposure, Third Annual National Conference on Radiation Control, May 3, 1971, Scottsdale, Arizona.

History of Development of Radiation Protection Standards, Radiation Research Society, May 9–13, 1971, Boston, Massachusetts.

Adequacy of Present Standards of Radiation Protection, Sigma Xi Society, University of Virginia, May 11, 1971, Charlottesville, Virginia.

Health Physics and the Environment, International Symposium of Rapid Methods for Measurement, July 5–9, 1971, Neuherberg, Germany.

Relationship of Science and Religion, Lutheran Theological Southern Seminary, January 27–28, 1971, Columbia, South Carolina.

Adequacy of Present Standards of Radiation Protection, Allen University, January 28, 1971, Columbia, South Carolina.

Principles of Radiation Protection, Nuclear Power Reactor Engineering Fundamentals, Sponsored by the University of Alabama, Marshall Space Flight Center, January 29, 1971, Huntsville, Alabama.

Adequacy of Present Standards of Radiation Protection, Georgia Institute of Technology, February 8, 1971, Atlanta, Georgia.

Maximum Permissible Levels of Ionizing Radiation, Nuclear Power – a Review and Assessment, Oak Ridge National Laboratory Seminar, February 18, 1971, Oak Ridge, Tennessee.

Internal Dose Lectures, University of Tennessee, February 10–26, 1971, Knoxville, Tennessee.

Internal Dose Lectures, Vanderbilt University, March 15–16 and April 5–6, 1971, Nashville, Tennessee.

Population Exposure to Ionizing Radiation, University of Washington Radiological Sciences Graduate Students, March 2, 1971, Seattle, Washington.

How and Why Reduce Medical X-Ray Exposure, Baltimore-Washington Chapter of the Health Physics Society, March 18, 1971, McLean, Virginia.

President's Report to the General Assembly of IRPA, International Radiation Protection Association Congress II, May 1970, Brighton, England.

Health Physics Tolerance Levels, Physics Division Seminar, Oak Ridge National Laboratory, October 30, 1970, Oak Ridge, Tennessee.

History of Radiation Protection, 75th Anniversary of Discovery of X-Rays Symposium, Milwaukee School of Engineering, November 13–14, 1970, Milwaukee, Wisconsin.

Health Physics Tolerance Levels, Chemical Technology Division Seminar, Oak Ridge National Laboratory, December 2, 1970, Oak Ridge, Tennessee.

Health Physics Tolerance Levels, ORAU Symposium on Environmental Aspects of Radiation Science, January 20, 1971, Oak Ridge, Tennessee.

Adequacy of Present Standards of Radiation Exposure, Environmental and Ecological Forum, January 20, 1971, Silver Spring, Maryland.

Health Physics Tolerance Levels, Davidson College, January 26, 1971, Davidson, North Carolina.

Adequacy of Present Standards of Radiation Protection, Johnson C. Smith University, January 26, 1971, Charlotte, North Carolina.

Adequacy of Present Standards of Radiation Exposure, Testimony before Subcommittee on Air and Water Pollution of the Senate Committee on Public Works, August 4, 1970, Washington, D.C.

Criteria for the Control of Radioactive Effluents, IAEA Symposium on Environmental Aspects of Nuclear Power Stations, August 11, 1970, UN Building, New York, N.Y.

Adequacy of Current Radiation Standards, Lecture before the Salt Project Briefing, Oak Ridge National Laboratory, August 27, 1970, Oak Ridge, Tennessee.

Energy Pollution of the Environment, Lecture for Euratom, October 9, 1970, Ispra, Italy.

Welcoming Address, International Summer School on Radiation Protection, September 20–30, 1970, Cavtat, Yugoslavia.

Maximum Permissible Levels of Exposure to Ionizing Radiation, International Summer School on Radiation Protection, September 20–30, 1970, Cavtat, Yugoslavia.

P. S. Rohwer

Environmental Aspects of Radiation Sciences – Nuclear Explosives, ORAU Topical Institute for College and University Faculty, January 21, 1971, Oak Ridge, Tennessee.

W. S. Snyder

Health Physics Organizations and Journals, ORAU Ten-Week Course in Health Physics, February 12, 1971, Oak Ridge, Tennessee.

Tsuneo Tamura

Waste Disposal by Hydraulic Fracturing, University of Tennessee, Geology Department, February 10, 1971, Knoxville, Tennessee.

J. E. Turner

Calculation of Depth-Dose Curves for Pion Beams and Comparison with Experiment, Department of Physics, University of Nebraska, May 19, 1971, Lincoln, Nebraska.

Interaction of Low-Energy Electrons with Polar Molecules, Department of Physics, University of Nebraska, May 20, 1971, Lincoln, Nebraska.

General Concepts in Radiation Dosimetry, Department of Physics, University of Nebraska, May 21, 1971, Lincoln, Nebraska.

HEALTH PHYSICS DIVISION

SEPTEMBER 1, 1971

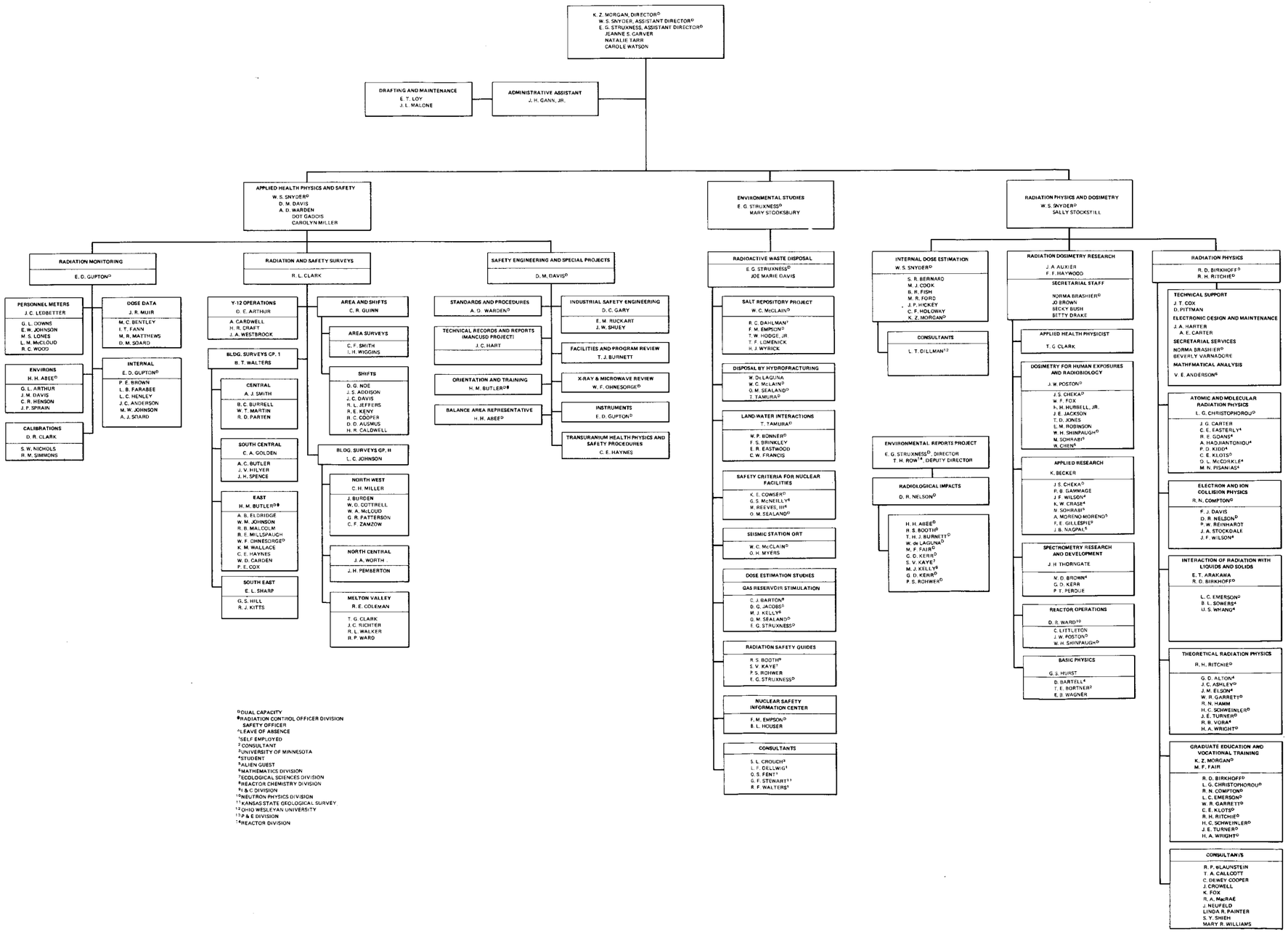

[D] DUAL CAPACITY
[9] RADIATION CONTROL OFFICER DIVISION SAFETY OFFICER
[4] LEAVE OF ABSENCE
[1] SELF EMPLOYED
[2] CONSULTANT
[3] UNIVERSITY OF MINNESOTA
[5] STUDENT
[6] ALIEN GUEST
[8] MATHEMATICS DIVISION
[7] GEOLOGICAL SCIENCES DIVISION
[9] REACTOR CHEMISTRY DIVISION
[10] I & C DIVISION
[11] NEUTRON PHYSICS DIVISION
[12] KANSAS STATE GEOLOGICAL SURVEY
[13] OHIO WESLEYAN UNIVERSITY
[14] P & E DIVISION
[15] REACTOR DIVISION

ORNL-4720
UC-41 – Health and Safety

INTERNAL DISTRIBUTION

1. Biology Library
2–4. Central Research Library
5. Laboratory Shift Supervisor
6. ORNL Y-12 Technical Library, Document Reference Section
7. MIT Practice School
8–62. Laboratory Records Department
63. Laboratory Records, ORNL RC
64. H. H. Abee
65. H. I. Adler
66. E. T. Arakawa
67. D. E. Arthur
68. J. C. Ashley
69. S. I. Auerbach
70–76. J. A. Auxier
77. C. J. Barton
78. S. E. Beall
79. K. Becker
80. S. R. Bernard
81. R. D. Birkhoff
82. W. P. Bonner
83. P. E. Brown
84. F. R. Bruce
85. T. H. J. Burnett
86. J. G. Carter
87. H. P. Carter
88. J. S. Cheka
89. L. G. Christophorou
90. R. L. Clark
91. T. G. Clark
92. W. E. Cohn
93. W. C. Colwell
94. R. N. Compton
95. M. J. Cook
96. K. E. Cowser
97. J. T. Cox
98. F. L. Culler
99. J. W. Curlin
100. Roger Dahlman
101. D. M. Davis
102. F. J. Davis
103. Wallace de Laguna
104. P. B. Dunaway
105. L. C. Emerson
106. F. M. Empson
107. M. F. Fair
108. L. B. Farabee
109. B. R. Fish
110. M. R. Ford
111. C. W. Francis
112. J. A. Gabbard
113. W. R. Garrett
114. D. C. Gary
115. J. H. Gillette
116. W. R. Grimes
117. C. R. Guinn
118. E. D. Gupton
119. R. N. Hamm
120. C. S. Harrill
121. J. C. Hart
122. J. A. Harter
123. F. F. Haywood
124. R. F. Hibbs
125. L. B. Holland
126. C. F. Holoway
127. H. H. Hubbell
128. G. S. Hurst
129. D. R. Johnson
130. L. C. Johnson
131. T. D. Jones
132. W. H. Jordan
133. M. T. Kelley
134. M. J. Kelly
135. R. F. Kimball
136. C. E. Klots
137. T. A. Lincoln
138. J. L. Liverman
139. R. S. Livingston
140. T. F. Lomenick
141. H. G. MacPherson
142. F. C. Maienschein
143. W. C. McClain
144. W. J. McConnell
145. A. J. Miller
146. K. Z. Morgan
147. O. H. Myers
148. D. J. Nelson
149. D. R. Nelson
150. J. S. Olson
151. R. V. O'Neill

152–153. R. B. Parker
154. G. R. Patterson
155. R. W. Peelle
156. J. W. Poston
157. M. L. Randolph
158. D. E. Reichle
159. P. W. Reinhardt
160. R. H. Ritchie
161. E. M. Robinson
162. P. S. Rohwer
163. H. C. Schweinler
164. H. E. Seagren
165. M. J. Skinner
166. W. S. Snyder
167. E. G. Struxness
168. D. A. Sundberg
169. T. Tamura
170. E. H. Taylor
171. J. H. Thorngate
172. D. B. Trauger
173. J. E. Turner
174. E. B. Wagner
175. B. T. Walters
176. D. R. Ward
137. A. D. Warden
178. A. M. Weinberg
179. J. P. Witherspoon
180. H. A. Wright
181. Gale Young
182. John C. Frye (consultant)
183. Edward Gerjuoy (consultant)
184. John B. Hursh (consultant)
185. R. P. Blaunstein (consultant)
186. W. Brandt (consultant)
187. Thomas Calcott (consultant)
188. C. D. Cooper (consultant)
189. J. Crowell (consultant)
190. Charles Eisenhauer (consultant)
191. R. J. Lovell (consultant)
192. Linda R. Painter (consultant)
193. S. Y. Shieh (consultant)
194. G. E. Thoma (consultant)
195. I. H. Tipton (consultant)
196. Neil Wald (consultant)
197. M. R. Williams (consultant)

EXTERNAL DISTRIBUTION

198–434. Given external distribution
435. J. A. Swartout, Union Carbide Corporation, New York, N.Y. 10017
436. Laboratory and University Division, AEC, ORO
437. Patent Office, AEC, ORO
438–697. Given distribution as shown in TID-4500 under Health and Safety category (25 copies – NTIS)